The Fluid Dynamics of Climate:
General Circulation Models and Applications to Past, Present and Future Climatic Changes

Luca Filippi

The Fluid Dynamics of Climate:
General Circulation Models and Applications to Past, Present and Future Climatic Changes

Luca Filippi

Tutor: Antonello Provenzale

Contents

Motivation and outline

The research activity presented in this thesis concerns the optimization and use of global climate models, and in particular of coupled atmosphere-ocean general circulation models, to investigate a series of issues of interest in the framework of climate dynamics with applications to past, present and future climatic changes.

Climate changes on all time scales. As weather varies from hour to hour, from day to day and from year to year, the past history of the Earth reveals that the same occurs on longer time scales, from decades to centuries, millennia and million years. In the future this will surely hold true. Constraining uncertainties about the future evolution of the Earth's climate and the attribution of changes to natural and anthropogenic forcings is of crucial importance for economies and societies worldwide. Policy makers increasingly demand accurate climatic information from the scientific community to develop adequate adaptation strategies. Projections of future climate necessarily rely on coupled atmosphere-ocean general circulation models, the most sophisticated global climate models existing today. Despite the huge progresses achieved in recent years, climate models are not flawless. A number of issues exist regarding both computational resources as well as our present understanding of the climate system, which inevitably affect model skills and reliability. Understanding past climatic changes is essential to test the robustness of climate models and discern how climate varies and may vary in the future.

Most of the research presented in this thesis is conducted with the EC-Earth model, a state-of-the-art global climate model developed by a consortium of European research institutions. Part of my thesis work concerns the optimization of the EC-Earth model and in particular the tuning of the model. Model tuning is an integral part of the model development process and consists in the practice of calibrating model parameters in order to improve its performance in reproducing some selected features of the climate system. The tuning activity presented here includes efforts devoted to the solution of some known issues affecting the original version of EC-Earth, including problems related to the energy balance of the atmosphere and the advection of water vapour. This work has actively contributed to the release of the latest version of the EC-Earth model (EC-Earth version 3.1).

In addition to model optimization, this thesis presents modelling studies addressing climatic issues covering different time scales of the Earth's climate, from

the far to the recent past and to future projections.

During the Earth's history there have been periods much warmer than today, such as the late Cretaceous (about 100 to 65 million years ago) and the Early Eocene (about 56 to 48 million years ago), characterized by roughly equal temperatures throughout the globe: polar temperatures were much closer to the tropical ones and seasonality was deeply reduced, with above freezing winter temperatures also over high-latitude continental areas. These periods have been called equable climates. While warm equable climates of the past show similarities with the expected climate under increasing greenhouse gas concentrations, climate models consistently fail in reproducing such climatic conditions, an issue that is referred to as the "equable climate problem". In the first modelling study presented here I investigate the equable climate problem using numerical simulations performed with the EC-Earth model. The ability of the model in reproducing equable climate conditions with appropriate boundary conditions is tested and new hypotheses are advanced in order to throw light on the equable climate problem. Results indicate that issues related to model inadequacies in representing tropical low clouds may be at the heart of the equable climate problem.

The other two modelling studies presented in this thesis refer to issues related to mountain regions. Mountains are hotspots of biodiversity and play a central role in the Earth's hydrological cycle, being crucial for human activities worldwide. As such, mountains have received growing attention within the climate community in recent years. In particular, I focus on the Tibetan Plateau-Himalayan region, one of the most important mountain areas in the world, which is often referred to as the "Third Pole" of the Earth because it hosts the largest amount of snow and ice outside the polar regions.

The first of the two modelling studies addressing mountains concerns the analysis of winter precipitation in the western Himalayas, which is primarily responsible for the build-up of seasonal snow cover representing an essential water reservoir and a vital source for some of the major rivers in the region. I investigate its teleconnection with the North Atlantic Oscillation, the dominant pattern of atmospheric variability in the North Atlantic sector affecting climate across much of the Northern Hemisphere during winter. In this study I use an ensemble of currently available observational datasets, including gridded archives based on in-situ precipitation measurements, satellite precipitation estimates and atmospheric reanalyses, as well as model simulations run with EC-Earth. Results indicate that the North Atlantic Oscillation significantly affects the amount of precipitation in this area, regulating its variability on the interannual time scales, and the processes responsible for this behavior are explored. Additionally, I address the multi-decadal variations that occurred in the relationship between the North Atlantic Oscillation and precipitation in the western Himalayas during the 20th century, showing that changes in the spatial structure of the pattern of the North Atlantic Oscillation are crucial in determining the way it regulates other climatic

parameters, with consequences for precipitation in this region. Simulation results from EC-Earth are consistent with observational data, attesting that the model is a valuable tool to investigate these processes and further corroborating conclusions drawn from observations.

There is growing evidence that the rate of temperature change with increased levels of greenhouse gases in the atmosphere is amplified with elevation. In other words, mountain regions are warming faster than adjacent lowlands, similarly to the warming amplification observed in the Arctic. This phenomenon has been referred to as "elevation dependent warming". In the second mountain-oriented modelling study, I use an ensemble of global climate models participating in the Coupled Model Intercomparison Project phase 5 (CMIP5) to investigate the elevation dependent warming in the Tibetan Plateau-Himalayan region, considering both historical model simulations and future projections. Results indicate that during the past century the Tibetan Plateau-Himalayan region has experienced an elevation dependent warming, which is expected to exacerbate in future decades. The possible drivers for the amplification of warming rates at higher altitudes are investigated, showing that changes in surface albedo and atmospheric humidity are of importance. The elevation dependent warming may accelerate the rate of change in mountain ecosystems, glaciers, hydrological regimes and biodiversity, with significant repercussions on human activities.

This thesis is structured as follows. Chapter 1 provides an overview on existing climate models, with a particular focus on coupled atmosphere-ocean general circulation models. Furthermore, it provides a description of the EC-Earth model, which will be extensively used in the following chapters. Model optimization and the tuning activity aimed at improving the EC-Earth model is presented in chapter 2. In chapter 3 I discuss the model experiments performed with EC-Earth to investigate the equable climate problem, advancing new hypotheses to address one of the great unsolved problems in paleoclimatology. The study of winter precipitation in the western Himalayas and its teleconnection with the North Atlantic Oscillation over interannual and multi-decadal time scales is presented in chapter 4. Evidences of elevation dependent warming in the Tibetan Plateau-Himalayan region during the last century and future projections for the next decades are explored in chapter 5. Final considerations and concluding remarks are given in the last chapter.

Chapter 1

Modelling the climate system

1.1 The climate system and a hierarchy of climate models

Climate in a narrow sense is usually defined as *the average weather, or more rigorously, as the statistical description in terms of the mean and variability of relevant quantities over a period of time* (definition from the Fifth Assessment Report of the Intergovernmental Panel on Climate Change, IPCC AR5). A climate state is the result of the complex network of interactions occurring between the different components of the climate system, including the atmosphere, the hydrosphere (oceans, lakes, underground water, etc.), the cryosphere (ice sheets of Greenland and Antarctica, continental glaciers and snow fields, sea ice and permafrost), the lithosphere (soils) and the biosphere (both marine and terrestrial). Processes influencing climate act on a variety of spatial and time scales, and as a consequence climate varies on all time scales — from one year to the next, as well as from one decade, century or millennium to the next — and all spatial scales — from the regional to the global (Ghil, 2002). Recently, a growing attention has been given to the role of the climate system components and their interactions, to highlight the highly complex nature of such a system. Following this perspective, a wider definition of climate has been introduced by the IPCC AR5, as *the state, including a statistical description, of the climate system, the highly complex system consisting of five major components [...] and the interactions between them.*

The high complexity of the climate system makes it impossible to be physically reproduced in laboratory. Hence the need for climate models to answer a number of questions of interest for the global community, such as *"What is the effect of increasing (doubling, tripling or quadrupling) atmospheric CO_2? What is the impact of removing the tropical forests? What are the social and economical implications?"*

Because of the hugeness of the processes and scales (both temporal and spatial) involved in the climate system, a great variety of models with different features exist. These models are hierarchically organized, starting from the simplest
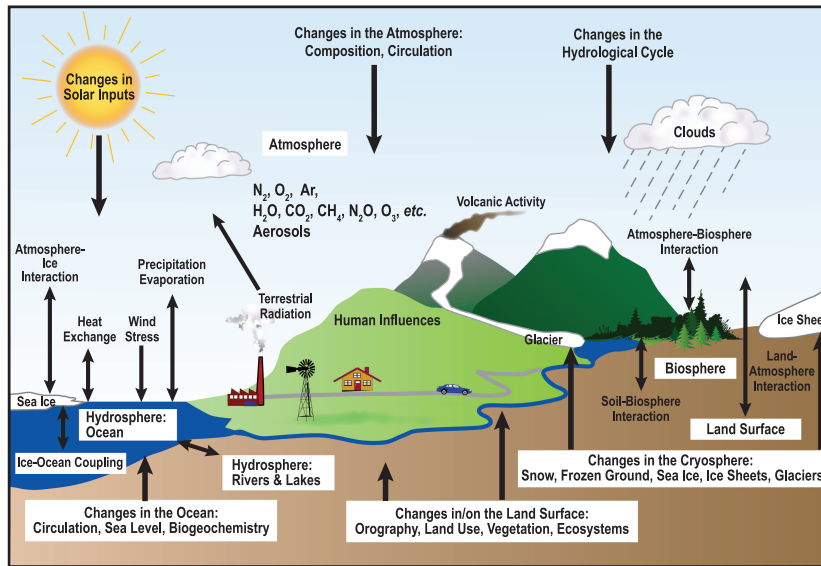
Figure 1.1: Schematic view of the components of the climate system, their processes and interactions. FAQ 1.2, figure 1 from IPCC (2007) published in: Climate Change 2007: The Physical Science Basis. Contribution of Working Group I to the Fourth Assessment Report of the Intergovernmental Panel on Climate Change, Cambridge University Press, copyright IPCC 2007.
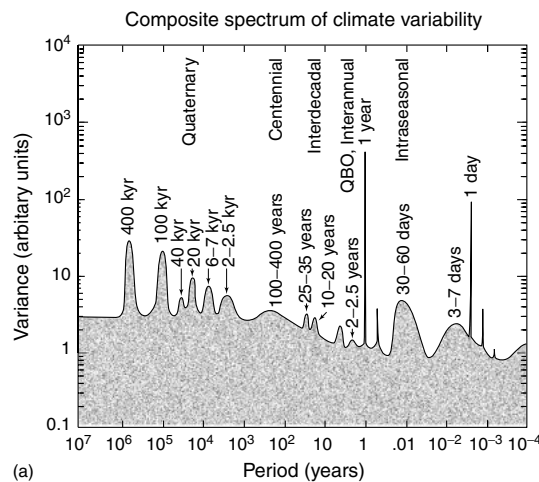
Figure 1.2: Composite power spectrum of climate variability over the last 10 Myr obtained by analyzing the many different climatic series, reflecting the types of variability: sharp lines correspond to periodically forced variations; broader peaks arise from internal modes of variability; the continuous portion of the spectrum reflects stochastically forced variations, as well as deterministic chaos (irregular variations that result from the deterministic interplay of non-linear feedbacks). Figure 1(a) from Ghil (2002).
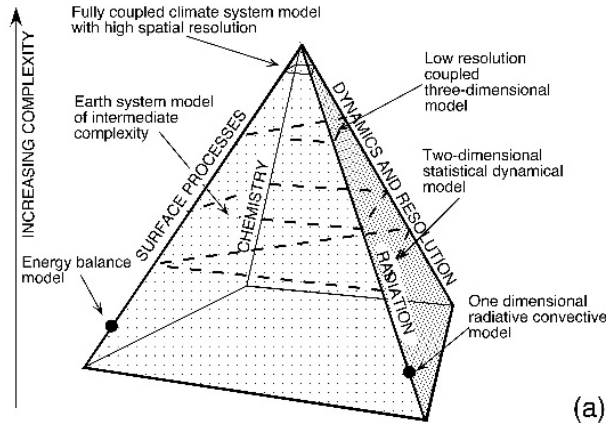
Figure 1.3: The climate modelling pyramid. The position of a model on the pyramid indicates the complexity with which the four primary processes introduced by McGuffie and Henderson-Sellers (2005) (dynamics, radiation, surface and oceans and chemistry) interact. Progression up the pyramid leads to greater interaction between each primary process. The vertical axis is not intended to be quantitative. Figure 2.1(a) from McGuffie and Henderson-Sellers (2005).

zero-order models and reaching the most comprehensive three-dimensional coupled atmospheric-oceanic-soil-vegetation-ice and chemistry models. All the steps of such a hierarchy of models are fundamental to fully study and understand climate and its different processes, and the reader should not get into the error of deprecating the simplest ones and magnifying the most complex. The simpler models are useful to isolate a single process or few processes and help us to analyze the mechanisms and variables involved, providing insights that might otherwise be hidden by the complexity of larger models. As an example, we can build the simplest energy balance model for the Earth considering only the solar radiation absorbed and the planetary radiation emitted, and then try to improve it taking account of other processes we know (or we think) are of importance for the problem in question. The greenhouse effect, for instance, can be introduced at several levels of complexity, starting with a single atmospheric layer that is homogeneous in absorbing/emitting terrestrial and solar radiation; then moving to multiple homogeneous layers; then considering different absorption/emission properties of gas molecules in the atmosphere; then adding clouds, and so on. Each step makes our model a bit closer to reality and allows us to better understand the relative importance of the different processes involved and the interactions and feedbacks between the various components. More comprehensive models attempt to run realistic simulations taking into account the most important processes involved in the whole climate system and can be used, for example, to make projections of the response of the Earth system under different future scenarios (see section 1.4).

6
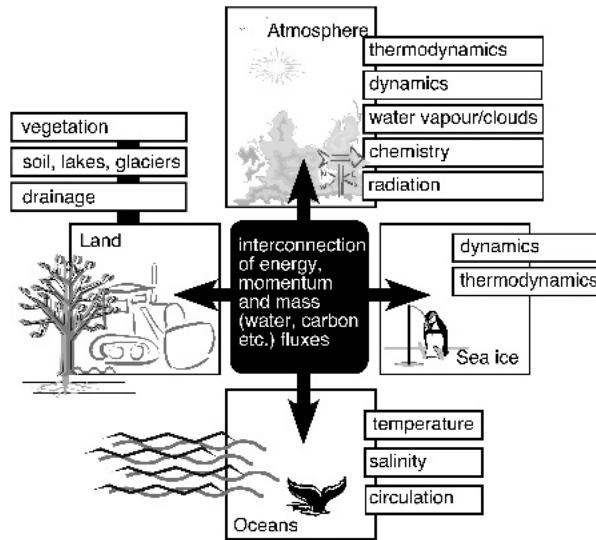
Figure 1.4: Schematic view of the structure of modern ESMs. They are constructed as modular components connected by a coupler (black), a program that transfers fluxes between the model components. Figure 5.1 from McGuffie and Henderson-Sellers (2005).

1.2   General Circulation Models and Earth System Models

The most complex atmospheric and oceanic models are the so called General Circulation Models (GCMs), which simulate the time evolution on planetary scale of a series of variables for the atmosphere (AGCMs) and the oceans (OGCMs) in three spatial dimensions. AGCMs and OGCMs are coupled together in coupled Atmosphere-Ocean General Circulation Models (AOGCMs). An Earth System Model (ESM) is a coupled AOGCM in which additional components — such as soil, vegetation, ice, chemistry and possibly other modules — are included. Modern fully-coupled, three-dimensional ESMs are actually a collection of models simulating the main components of the climate system introduced above, connected by a coupler module. A schematic view of this structure is given in Fig. 1.4. To give an idea of the complexity of these models, McGuffie and Henderson-Sellers (2005) estimated that a fully-coupled AOGCM takes about 25-30 person-years to code, and the code requires constant updating in parallel with the development of new ideas as well as advances in computer science. In this section I briefly describe some aspects of GCMs, mainly focusing on atmospheric models.

1.2.1   Fluid dynamics of GCMs

The atmosphere and the oceans are shallow layers of stratified fluids on a rotating sphere. They are shallow, in the sense that their thickness is much less than the horizontal extent; they are stratified, meaning that the mean vertical gradient of

density is often large compared with the horizontal one; finally they are rotating, i.e. their motion is strongly influenced by Earth's rotation.

The fundamental equations governing the motions of the oceans and of the atmosphere are derived from the same basic laws of physics, including the conservation laws of momentum (Newton's second law of motion), mass (continuity equation) and energy (first law of thermodynamics), plus an additional equation of state relating several parameters in the other equations. The specific characteristics of the two systems, then, make the final equations for the ocean and the atmosphere to be significantly different. For example, the equation of state for the atmosphere relates pressure, density and temperature, while for the ocean also salinity is included. Time and space scales differ: dominant time scales are much longer in the ocean than in the atmosphere due to the higher thermal inertia of the ocean, while ocean spatial scales are smaller by about one-tenth than atmospheric ones, with implications for discretization choices (Washington and Parkinson, 2005). Air is compressible for large-scale atmospheric motions, while seawater is nearly incompressible, so that changes of density can be neglected in the ocean; Ocean water motions are greatly constrained by bottom topography. Radiative processes are more complex in the atmosphere. The atmosphere is mostly heated by the Earth's surface below, while oceans are heated only at the top surface, and so on.

The fundamental equations for the atmosphere can be written in the following form (McGuffie and Henderson-Sellers, 2005):

1. Conservation of momentum

$$\frac{D\mathbf{v}}{Dt} = -2\mathbf{\Omega} \times \mathbf{v} - \rho^{-1}\nabla p + \mathbf{g} + \mathbf{F} \tag{1.1}$$

2. Conservation of mass

$$\frac{D\rho}{Dt} = -\rho\nabla \cdot \mathbf{v} + C - E \tag{1.2}$$

3. Conservation of energy

$$\frac{DI}{Dt} = -p\frac{D\rho^{-1}}{Dt} + Q \tag{1.3}$$

4. Ideal gas law

$$p = \rho R T$$

Where:
$\mathbf{v}$ = velocity relative to the rotating Earth,
t = time,
$\frac{D}{Dt}$ = total time derivative [= $\frac{\partial}{\partial t} + \mathbf{v} \cdot \nabla$],
$\mathbf{\Omega}$ = angular velocity vector of the Earth,

ρ = atmospheric density,
$\mathbf{g}$ = apparent gravitational acceleration,
p = atmospheric pressure,
$\mathbf{F}$ = force per unit mass,
C = rate of creation of atmospheric constituents,
E = rate of destruction of atmospheric constituents,
I = internal energy per unit mass $[= c_p T]$,
R = gas constant,
T = temperature,
c_p = specific heat of air at constant pressure.

This set of equations is called the primitive equation system, referring to the full set of basic equations prior to its simplification by various approximations. An analogue set of primitive equations can be defined for the ocean, taking into account the differences mentioned above. Starting from the primitive equations, several approximations of varying complexity have been introduced for both ocean and atmospheric models.

A common assumption that is introduced for both the atmosphere and the ocean is the hydrostatic approximation, since both fluids are nearly always close to hydrostatic balance (i.e. balance between buoyancy forces and vertical pressure gradients) with regard to large-scale motions. Under the hydrostatic approximation, the vertical component of the momentum equation (1.1) can be written as:

$$\frac{\partial p}{\partial z} = -\rho g \tag{1.4}$$

where we have neglected all terms but the gravitational and the pressure ones, which are order of magnitudes larger than the others for most large-scale motion in the atmosphere and in the oceans.

Primitive equations are then complemented by equations describing other constituents of interest. In the case of the atmosphere, the most important is the moisture equation, which is introduced similarly to the mass continuity equation (1.2) and describes the conservation of water vapour mixing ratio q (i.e. the ratio of the density of water vapor to the density of dry air):

$$\frac{Dq}{Dt} = P_q - D_q \tag{1.5}$$

where P_q and D_q denote production and destruction of q.

Appendix A reports the equations corresponding to 1.1–1.5 used by the Integrated Forecasting System, the atmospheric component of the EC-Earth ESM described in section 1.3. I refer to Vallis (2006); Trenberth (1992); McGuffie and Henderson-Sellers (2005); Washington and Parkinson (2005) for further details on GCM equations of motion and their implementations.

1.2.2   Physics and parameterizations

In addition to the dynamics, which is governed by the equations described in section 1.2.1, GCMs include a set of schemes to represent other processes of importance in the climate system. These processes constitute the *physics* of the model, as opposed to the *dynamics*. For the atmosphere, they include the radiation scheme, the boundary layer scheme, the surface parameterization scheme, the convection scheme (including convective clouds and precipitation) and the large-scale precipitation scheme. A description of the basics of these modules can be found in Trenberth (1992); McGuffie and Henderson-Sellers (2005).

The climate system has infinite degrees of freedom. Any approach to climate modelling requires to neglect some parts of the complete system and/or reproduce others by imprecise or semi-empirical mathematical expressions. This process of neglect/semi-empirical representation is called parameterization. Also, a common feature of all GCMs, even the most complex, is the limitation in the spatial detail they can resolve. Since it is impossible to solve equations and evaluate climatic variables everywhere on the Earth, in the oceans and the atmosphere, even with the most powerful computers available today, calculations are executed over three dimensional grids with finite resolution. The horizontal resolution of modern coupled AOGCMs and ESMs is typically of about one hundred kilometers in the atmosphere ($\sim$70 km at most, see also section 1.3 and table 5.1). This creates problems, since many climatic phenomena act over smaller scales. These phenomena acting over scales smaller than the grid resolution cannot be incorporated explicitly but through parameterization. A parameterization is a statistical relation between variables which are resolved and others that are not, and so starting from the former an average estimation of the latter is done. In terms of equations a parameter is introduced, which links together these variables. Such a parameter and the statistical relation between the variables in question are empirically derived from data. Of course, modellers try to make parameterizations as physical as possible, but they always contain an empirical part. Thus, the overall performance of a model also depends on the empirical statistical parameterizations included in the model itself (Trenberth, 1992).

1.3   The Earth System Model EC-Earth

Weather and climate predictions are often considered as different disciplines. While meteorologists face the problem of forecasting the atmosphere state on relatively short time scales (from few days to a season), the temporal scales of interest in climatology vary from some decades to centuries (and even more if we look at paleoclimatology). The biggest difference between the two kinds of predictions is that the former is an initial condition problem, while the latter is a boundary condition problem. In spite of this remark, meteorology and climatology actually
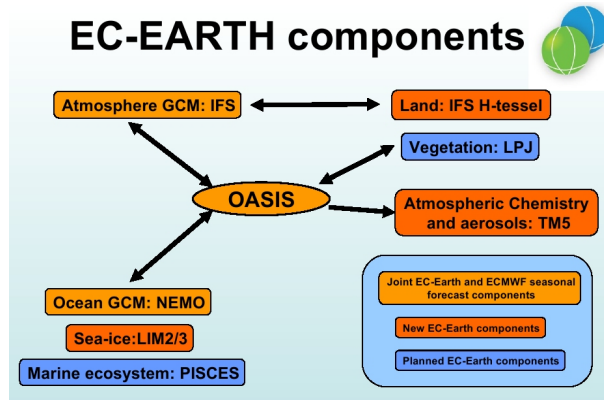
Figure 1.5: Schematic view of EC-Earth components and their interconnections. Modules actually included in the EC-Earth configurations used in this thesis are the atmosphere, land, ocean and sea-ice modules, connected through the coupler OASIS. Fig. 1 from Brandt (2010).

build on the same physical principles. The concept of seamless prediction is a new emerging challenge that forges weather and climate predictions into a unitary framework. At the same time, in the field of climate modeling, a recent trend is to extend global climate models into Earth System Models, explicitly including new modules which take into account biogeochemical processes and converging to a more comprehensive description of the Earth system as a whole. Starting from these considerations, EC-Earth is a new ESM developed by the EC-Earth consortium (currently 28 institutions from 12 European countries) at ECMWF (European Centre for Medium-range Weather Forecast) that integrates the concept of seamless prediction (`www.ec-earth.org`). The model is designed to encompass all the mentioned temporal scales, performing from weather to interannual to multi-decadal scales. A mutual advantage is expected from this strategy for both numerical weather prediction (NWP) and Earth System Models. NWP models generally have more developed atmospheric models, which are designed to capture atmospheric fluctuations and fast feedbacks accurately, and ESMs can take advantage of it. On the other hand, NWP models increasingly include modules, such as atmospheric composition and land modules, that are generally developed by Earth system modellers.

EC-Earth is an ESM based on state-of-the-art models for the atmosphere, the ocean, land, sea ice and the biosphere. Consistently with the idea of seamless prediction, the model is based on the NWP system of ECMWF. Some differences between the latter and the EC-Earth ESM exist because of the different goals they are used for. For example, EC-Earth has interactive atmosphere-ocean-sea ice coupling across the entire globe, while the ocean wave model in use at ECMWF is not included. Different sea ice and land modules are used. However, the main

difference is the use of a different ocean model. EC-Earth versions used throughout this thesis are model Version 2 (V2 — chapters 4 and 5) and Version 3 (V3 — chapters 2 and 3). EC-Earth components are briefly described below and its different modules with their interconnections are shown in figure 1.5. More information can be found in Hazeleger and Bintanja (2014) and a description and validation of the model is presented by Hazeleger et al. (2012).

The atmosphere model of EC-Earth is the Integrated Forecasting System (IFS), which is a primitive-equation model with fully interactive cloud and radiation physics. The dynamical core of IFS is hydrostatic, semi-implicit, semi-Lagrangian and applies spectral transforms between the grid-point space (where the physical parameterizations and advection are calculated) and the spectral space to compute large-scale atmospheric motions. In the vertical the model is discretised using a finite-element scheme on hybrid coordinates. A reduced Gaussian grid is used in the horizontal. The model allows for different resolutions. EC-Earth V2 uses IFS cycle 31r1, with a standard spectral resolution of T159 (corresponding to $\sim$ 125 km) and 62 vertical layers. EC-Earth V3 uses a newer version of IFS — cycle 36r4 — with a standard resolution of T255 ($\sim$ 80 km) and 91 vertical layers. Model fundamental equations are reported in appendix A. A detailed documentation on the physics and the dynamics of the model is available at ECMWF (`https://goo.gl/mTfwRe`).

The land surface module is the Hydrological extension of the Tiled ECMWF Surface Scheme for Exchange processes over Land (H-TESSEL). The model has 4 soil layers and 6 land tiles (bare ground, low and high vegetation, intercepted water, shaded and exposed snow) and is directly linked with the atmospheric model.

The ocean model of EC-Earth is the Nucleus for European Modelling of the Ocean (NEMO) developed by the Institute Pierre Simon Laplace (IPSL). NEMO is a primitive equation model with a free surface. It uses a tri-polar grid with poles over northern North America, Siberia and Antarctica. The standard configuration of EC-Earth uses the so called ORCA1-configuration with a non-constant horizontal resolution of about 1° and higher resolution near the equator (of up to 1/3°). EC-Earth V2 employs version 2 of the NEMO model with 42 vertical levels in the standard configuration. EC-Earth V3 uses NEMO Version 3 with 46 vertical levels in the standard configuration. More information about the model are available at `http://www.nemo-ocean.eu/About-NEMO`.

EC-Earth uses the Louvain-la-Neuve sea ice model (LIM) as part of the NEMO system. LIM is a thermodynamic-dynamic sea ice model and it is run on the same grid as the ocean model NEMO. EC-Earth V2 and V3 use the LIM version 2 (LIM2) and 3 (LIM3) respectively.

The atmosphere/land model and the ocean/sea-ice model are coupled together through the coupler OASIS 3. No direct communication occurs between these components, but all communications pass through the coupler. The coupling frequency between the ocean and atmosphere is every 3 hours.

EC-Earth configurations used in my thesis work include the four components described above (IFS, H-TESSEL, NEMO and LIM). Other components are planned to be coupled in the near future, including atmospheric chemistry, terrestrial and marine ecosystem modules, and there is an on-going work within the EC-Earth community to this aim. In particular, the atmospheric chemistry model Tracer Model 5 (TM5), describing the atmospheric chemistry and transport of reactive and inert tracers, and the vegetation and biogeochemistry model LPJ-GUESS, combining the General Ecosystem Simulator (GUESS) and the Lund-Potsdam-Jena Dynamic Global Vegetation Model (LPJ), have already been included in a preliminary version of the model (V2.4) and are planned to be permanently implemented in the next releases.

EC-Earth (V2.3) has contributed to CMIP5, the coupled model intercomparison project that fed into the 5th IPCC report (see section 1.4). Also, it has provided data to downscale global climate change information to regional levels and it has been used to study feedbacks and predictability of the climate system. EC-Earth is becoming a prominent model within the European framework and as such it is involved in many European projects, including projects on high performance computing.

1.4   Practical climate modelling: experiments and applications

Most of the experiments presented and discussed throughout this thesis refer to coupled atmosphere-ocean simulations performed with the ESM EC-Earth or other state-of-the-art ESMs and coupled AOGCMs. Coupled AOGCMs and ESMs (hereafter referred to as coupled GCMs for conciseness) are the preferred tools for studying climate change for a number of reasons. They make fewer model assumptions than simpler models and simulate the physical climate system given only a small number of external boundary conditions, such as the solar "constant" and atmospheric concentrations of radiatively active gases and aerosols. Also, they can be compared directly with the observed climate and the geographical distribution of the climatic variables can be studied.

Probably the most popular application of coupled GCMs is the study of current climate change, that is during the recent past (since the end of the 19th century) and the next decades (up to 2100). In this framework, the Coupled Model Intercomparison Project (CMIP) is a standard experimental protocol for studying the outputs of coupled GCMs that was first established in 1995 by the Working Group on Coupled Modelling (WGCM) of the World Climate Research Programme (WCRP) with the aim of analyzing GCMs in a systematic fashion. The most recent phase of the CMIP (phase 5 – CMIP5) has promoted a standard set of model simulations in order to 1) evaluate how realistic the models are in simulating the

recent past, 2) provide projections of future climate change on two time scales, near term (out to about 2035) and long term (out to 2100 and beyond), and 3) understand some of the factors responsible for differences in model projections. CMIP5 experiments are described in detail by Taylor et al. (2012). It is important to introduce here two main sets of CMIP5 experiments:

- *historical experiments*: simulations driven by changing conditions reconstructed from available observations for the period 1850-2005, including atmospheric composition (radiatively active gases and aerosols) due to both anthropogenic and volcanic influences and solar forcing;

- *future projections*: simulations of future climate under different emission scenarios taking into account various levels of mitigation of anthropogenic emissions for the period 2006-2100. These scenarios are called Representative Concentration Pathways (RCPs – Moss et al. (2008)). They are labeled according to the approximate target radiative forcing at year 2100 (e.g., RCP4.5 identifies a concentration pathway that approximately results in a radiative forcing of 4.5 Wm^{-2} at year 2100, relative to pre-industrial conditions).

Before running any experiment with coupled GCMs, included the ones mentioned above, long *spin-up runs* are needed to set the model in the appropriate conditions to start the simulation (statistical equilibrium). This procedure can be interpreted as a way to build initial conditions for model simulations, and it is a necessary step because 1) observational data are usually not enough to provide accurate initial conditions for both the atmosphere and the ocean and 2) observation-derived initial conditions can be far from the model solution. Spin-up runs are relatively long (hundreds of simulated years) for modern coupled GCMs because of the slow dynamics of the deep ocean components. These runs are performed using perennial boundary conditions (i.e. fixed atmospheric composition and solar constant) until any climatic trend is extinguished and the statistical equilibrium is reached.

Once the statistical equilibrium is reached, *perennial experiments* (i.e. experiments driven by perennial boundary conditions and showing no climatic trends) can be useful to study the natural variability of climate. They are so called in opposition to *transient experiments*, which are driven by changing boundary conditions and include, among the others, the CMIP5 historical experiments and future projections discussed above.

In chapter 3 we will discuss the equable climate problem, one of the longstanding problems in paleoclimatology. Paleoclimate studies refer to past climates on geological time-scales ($10^2 - 10^6$ years), covering periods when the Earth was quite different from today, not only in terms of atmospheric composition and solar forcing, but also concerning geography, vegetation and so on. Modelling experiments to investigate paleoclimate issues must take these differences into account,

by using appropriate boundary conditions and expedients. *Paleoclimate experiments* offer the opportunity to test models on climatic conditions far beyond the "present-day" range (for which they are usually constructed) and thereby increase confidence in models themselves. On the other hand, paleoclimate experiments help us to better understand past climates, especially for periods and regions where few or no proxy data are available.

Coupled GCMs are useful tools to suggest how the climate system might respond under various circumstances. This is not only true when studying the past and on-going climate changes discussed above, but also for many other applications, such as climate response to vegetation and land-use changes, or modified geography and orography, or any other factor one might be interested in. They allow to isolate and study physical processes and their role in the climate system, eliminating possible complicating factors that are active in the real world. Also, they are used to investigate the effects of alternative parameterizations of physical processes. Model simulations used to explore all these topics, together with many others, are generally referred to as *sensitivity experiments*.

When working with coupled atmosphere-ocean simulations, one should always keep in mind that there is not a one-to-one correspondence between model years and actual years. That holds true also in the case of simulations driven by observation-derived boundary conditions (such as CMIP5 historical experiments forced by reconstructed atmospheric composition and solar forcing for the period 1850-2005), because the internal climate variability (i.e. climatic oscillations and quasiperiodic fluctuations such as the El Niño Sothern Oscillation and the North Atlantic Oscillation discussed in section 4) of the model is not in phase with the real one. As a consequence, temporal correlations or comparisons of a single month from a particular year between model simulations and observations are meaningless: any comparison must be performed in a statistical sense (mean and variability over a certain period).

In addition to coupled atmosphere-ocean experiments, in the next chapters I will also refer to atmospheric-only experiments. With respect to the former, atmospheric-only simulations need additional boundary conditions at the interface between the oceans and the atmosphere (typically sea surface temperatures and sea-ice coverage). While this can be a limiting factor for climate change studies because boundary conditions at the sea surface are not always available (e.g. for future climate projections), they require significantly smaller computational efforts and can be efficiently used to study atmospheric processes.

1.5   Mountains and climate: a two-fold challenge for modellers

> *"Mountains are important sources of water, energy, minerals, forest and agricultural products and areas of recreation. They are storehouses of biological diversity, home to endangered species and an essential part of the global ecosystem. From the Andes to the Himalayas, and from Southeast Asia to East and Central Africa, there is serious ecological deterioration. Most mountain areas are experiencing environmental degradation"*
> *From the Final Text of Agreements Negotiated by Governments at the United Nations Conference on Environment and Development* (UNCED), 3-14 June 1992, Rio de Janeiro (UN, 1992).

Mountain regions occupy close to 25% of the continental area of the Earth (Kapos et al., 2000). Although only about 26% of the world's population resides within mountains or in their foothills, mountain-based resources provide sustenance for over half (Beniston, 2003). Mountains play a central role in the hydrological cycle of the planet. They store water in the form of snow and ice and give birth to more than 50% of the globe's rivers, being crucial for ecosystems, agriculture, industrial and domestic supply, hydropower, sediment loads and nutrient balance. Since they supply disproportional runoff as compared to the adjacent lowland areas, mountains are often referred to as natural "water towers" (Viviroli et al., 2007). Mountain environments also represent important hotspots of biodiversity and serve as habitat for a number of species, many of which are endemic (i.e. species that are only found in that region and nowhere else in the world), being key elements of the global biosphere (Korner and Spehn, 2002).

Although mountains considerably differ from one region to another, a common feature to all mountain systems is the combination of vertical extent and extremely complex topography, showing the sharpest gradients found on land, which makes them unique in the climate system. Climate varies much more rapidly with height than with latitude, e.g. the typical lapse rate (i.e. the decrease of temperature with height) is of about 6°C/km, about three orders of magnitude higher than the change of temperature with latitude. In addition, the complex topography determines even more rapid changes in climatic parameters — such as temperature, precipitation, winds, clouds, radiation, soil and vegetation types and associated albedo, and so on — over very short distances. The heterogeneity of terrains and climate inevitably reflects in mountain biosphere, cryosphere and hydrosphere, being at the base of their importance and uniqueness discussed above. Also, sharp

gradients and rapid transitions make mountain ecosystems potentially very vulnerable to climatic changes, with implications for the environment, economy and society worldwide (see for example Diaz et al., 2003; Beniston, 2003). Furthermore, the complex topography constitutes a major constraint for climatic and meteorologic monitoring (see sections 4.1 and 5.1 for issues regarding precipitation and temperature measurements in mountain areas).

Such a complex environment represents a two-fold challenge for climate modellers, who always have to deal with finite spatial resolutions. On the one hand, it is necessary to represent the effect of mountains on the large-scale atmospheric circulation: orography interacts with the atmospheric flow by creating obstacles, additional turbulence and waves, represents an elevated source of heat and moisture, traps low-level clouds within valleys, strongly impacts on precipitation distribution and influences the radiative budget (Bougeault, 2001). Current spatial resolution of state-of-the-art GCMs is still too coarse to adequately represent the steep and complex topography of most mountain regions and their impact on climatic processes and variables. The spatial resolution needed to solve orographic details would require a computational effort that is still unattainable, even with currently-available computational resources. Thus, sub-grid scale orographic forcings must be necessarily parameterized in GCMs (e.g. Miller et al., 1989, see also 1.2.2). On the other hand, climate information on spatial scales that are much finer than GCM output resolution is typically needed for a number of applications, including climate change impact assessments, hydrological studies, coupling of atmospheric and soil-vegetation dynamics, and so on. While this limitation holds true everywhere on Earth, it is particularly evident in mountain regions, where climatic parameters may vary on shorter scales than anywhere else. Downscaling techniques exist to overcome the mismatch between the spatial scale solved by GCMs and the "local" scale (e.g. Maraun et al., 2010).

Two main downscaling methods have been developed: one is *statistical downscaling*, and consists in establishing statistical relationships between large scale variables solved by the GCM (the predictors) and a local variable (the predictand); the other is *dynamical downscaling*, where large-scale GCM outputs are used as boundary and initial conditions to drive a Regional Climate Model (RCM) over a given area for a specific period. RCMs are high-resolution versions of GCMs but limited to a given area (e.g. Giorgi et al., 1993), and as such can be run at higher resolution. For this reason, RCMs capture regional details — such as orography, but also land-sea boundaries, large lakes and others — and their forcing on regional climate processes in a more realistic manner than GCMs, and can be an advantage in mountain areas. However, both statistical and dynamical downscaling have a number of drawbacks, in particular the fact that the process is usually "one-way" (i.e., the climatic forcing occurs only from the larger to the finer scales and the advantages of the fine-scale simulation do not feed back into the larger scales, Beniston, 2003). Moreover, it is worth to remember that any downscaling

technique always relies on large scale climate information from GCM simulations: even the most sophisticated RCM cannot be used alone to run simulations of climate change, because a representation of the global climate system is needed to this aim and only GCMs can provide it. A number of works exists addressing climate change in mountain environments using GCM output data without downscaling (see for example Palazzi et al., 2014; Rangwala et al., 2015, and references therein). For these reasons, it is very important to analyze and evaluate also GCM outputs in mountain regions, always keeping in mind their limitations.

1.5.1   Complex topography in GCMs: the Tibetan Plateau-Himalayas case study

One of the most important mountain regions in the world is the Tibetan Plateau-Himalayan region. This area is dominated by the high-altitude regions of the Tibetan Plateau, with an average elevation exceeding 4,500 meters, surrounded by the highest mountain peaks of the world such as the Himalayas, Hindu-Kush, Karakoram and Pamir systems. The Tibetan Plateau-Himalayan region is often referred to as the "Third Pole" of the Earth, because it hosts the largest amount of snow and ice outside the polar regions. It constitutes a crucial reserve of fresh water and it is source of several major Asian rivers, supporting a population of more than 1 billion people (Bookhagen and Burbank, 2010). Part of the work of this thesis — presented in chapters 4 and 5 — is devoted to the study of some relevant climatic issues related to the Third Pole environment. In this section I consider the Third Pole region as a case study to show how the state-of-the-art coupled GCMs represent the complex topography of mountain areas.

Fig. 1.6a shows a high-resolution reconstruction of the topography of the Tibetan Plateau-Himalayas from the ETOPO1 Global Relief Model from the NOAA's National Geophysical Data Center (NGDC) available at `www.ngdc.noaa.gov/mgg/global/global.html`. ETOPO1 is a digital elevation model (DEM) available for the whole globe with a grid spacing of 1 arc-minute (approximately 0.008 degrees).

For what concerns model orographic data, I consider the orography fields from an ensemble of 27 coupled GCMs participating in the Coupled Model Intercomparison Project phase 5 (CMIP5, see section 1.4). This ensemble is the same that will be used in chapter 5, and a complete list of the models, along with their horizontal resolution and a key reference, is given in table 5.1.

The average orography of the CMIP5 ensemble — i.e. the multi-model mean (MMM) orography computed after regridding all individual orography fields onto a common 2×2 degrees resolution grid — is shown in Fig. 1.6b. With respect to the observed orography shown in Fig. 1.6a, the MMM orography is dramatically less detailed, because the lower spatial resolution flattens most of ridges and valleys. This feature is not an artifact of the multi-model mean, but it is evi-
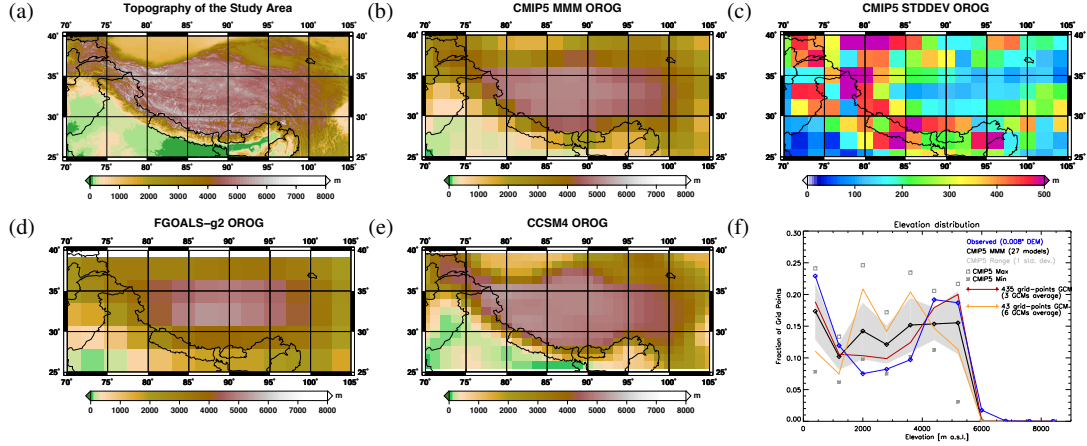
Figure 1.6: (a) Topography of the Tibetan Plateau-Himalayas from observations (0.008°
resolution). (b)–(c) CMIP5 model ensemble orography (2×2° res.): (b) multi-model
mean (MMM) and (c) inter-model standard deviation. (d) Original model orography from
FGOALS-g2 (2.8125° res.). (e) Original model orography from CCSM4 (1.25×0.9° res.).
(f) Elevation distribution across the region from observations (blue line), CMIP5 MMM
(black line), GCMs with the highest resolution (red line) and GCMs with the lowest
resolution (orange line). Gray shading indicates the CMIP5 spread. Empty squares and
stars are the maximum and minimum values across the model ensemble.

dent also in the orography fields from the individual models, as can be seen from
Figs. 1.6d and 1.6e showing the orographies from one of lowest-resolution member
(FGOALS-g2) and one of the highest-resolution members (CCSM4) of the CMIP5
ensemble. Moving from Fig. 1.6d to 1.6e, and then from 1.6e to 1.6a, the reader
should get an idea about the improvements we have as we move towards finer
resolutions. Unfortunately, with current computational resources, we are still far
from a detailed representation of mountain topography (compare 1.6e and 1.6a).

Fig. 1.6c shows the inter-model standard deviation of the CMIP5 ensemble,
computed after regridding all individual orography fields onto a 2×2 degrees grid
as for the MMM. As expected, the models agree less with each other (i.e. the stan-
dard deviation is higher) in the regions of strongest altitudinal gradients, such as
along the Himalayan chain, while the standard deviation is smaller in the more ho-
mogeneous regions (central Tibetan Plateau and flatter regions of central Pakistan
and northern India).

Figure 1.6f shows the elevation distribution of orography data in the Tibetan
Plateau-Himalayas. Shown is the fraction of grid cells falling in each 800 m bin
across the latitude and longitude range of the study area (Fig. 1.6a) from the
observed elevation (blue line) and the CMIP5 MMM (black line). The CMIP5
spread, defined as 1 standard deviation above and below the MMM, is shown with
grey shading. The figure also shows the mean elevation distribution of the three

highest-resolution models (CCSM4, CESM1-BGC, CESM1-CAM5, red line) and of the six lowest-resolution models (MIROC-ESM-CHEM, MIROC-ESM, bcc-csm1-1, BNU-ESM, CanESM2, FGOALS-g2, orange line). Of course, the higher the model resolution, the greater the number of high-elevation grid points in the region of interest. The highest-resolution GCMs have an elevation distribution that is closer to observations than the CMIP5 average. The CMIP5 MMM overestimates the fraction of grid points into the altitudinal bins at elevations between about 1000 and 4000 m a.s.l., while it underestimates the fraction of grid points at lower and higher elevations.

These results highlight how current GCM spatial resolution is still far from accurately capturing orographic features. However, while the finer-scale details are evidently impossible to be caught, many studies show that GCMs are able to reproduce various climatic features of mountain regions, such as the annual cycle of climatic variables as well as their dependence on the elevation (see for example Palazzi et al., 2014; Rangwala et al., 2013). Moreover, observational data in mountain areas are often scarce and inaccurate, and some studies suggest that GCMs outputs can be at least as reliable as observations (e.g. Palazzi et al., 2013). Finally, it is worth pointing out that there is a huge effort in the climate community towards higher-resolution GCMs (e.g. Jung et al., 2012; Mizielinski et al., 2014; Bell et al., 2013). The spatial scales resolved by future generations of GCMs will likely get finer and finer, gradually improving the detail to which orographic features are captured.

Chapter 2

Tuning the EC-Earth Earth System Model

2.1   Tuning of climate models

A common feature to all climate models, from the simplest to the most complex, is that they inevitably make use of parameterizations, i.e. imprecise or semi-empirical representations of processes that are not explicitly included in the model equations (see section 1.2.2). Parameterizations involve the use of numerical parameters whose value must be specified. Some parameters can be measured — at least in principle — but most of them are poorly constrained by observations or even non-observable. It is therefore common to adjust parameter values in order to improve the model performance in reproducing some selected features of the climate system. This practice of calibrating model parameters is usually referred to as model *tuning*. Model tuning is an integral part of the model development process, and usually constitutes the last step of a broader development cycle, after structural enhancements, improved parameterizations and refined boundary conditions have been implemented (Mauritsen et al., 2012).

Despite there have been recent efforts to develop systematic methods for model tuning, there is not a unique standard procedure (Neelin et al., 2010). A crucial aspect at the base of any tuning effort is to identify the features of the modelled climate we aim to focus on — and possibly improve. These features are observable climate variables that we expect are of importance in determining an overall good representation of the climate system. For instance, targeting the global mean top-of-the-atmosphere (TOA) radiative balance is essential to prevent the climate system from drifting to an unrealistic state (IPCC AR5). In addition to TOA radiative fluxes, other key variables for model tuning tipically include — but are not limited to — surface (SFC) fluxes and surface temperatures, which are known to be essential for a successful representation of a number of processes, including the atmospheric circulation and the water cycle (e.g., Stephens et al., 2012;

Cayan, 1992; Rodwell et al., 1999; Czaja and Frankignoul, 1999). Once the model features we aim to improve have been chosen, it is necessary to identify the model parameters that have an influence on them. In some cases, it is relatively straight-forward to understand the impact of a model parameter on the variable of interest. As an example, it is quite intuitive that model average surface temperature can be increased by reducing directly surface albedo (for instance the diffusive albedo of the ocean, see sections 2.2 and 2.3), as well as by decreasing low-level cloud coverage (for instance increasing the precipitation efficiency), thus reflecting less solar radiation. However, in most cases the effect of model parameters on modelled climate is much more complex and far from being easily predictable, and we do not know exactly how to tune the model features we are interested in. In these cases, there is no other option but to proceed by trial and error, investigating the sensitivity of model variables to different values of model parameters, and making decisions on the basis of a weak understanding of the relationship between model formulation and model behavior (Mauritsen et al., 2012).

After tuning a climate model, the tuned model has to undergo model evaluation. During this practice, it is importnant to include not only the verification of the improvements in the variables targeted by tuning, but also — and more importantly — the evaluation of quantities that were not directly targeted. Indeed, evaluating models based on their ability to represent a tuning target variable usually reflects how closely the models were tuned to that particular target, rather than the model overall qualities (Mauritsen et al., 2012).

It is worth to stress that improved performance arising from any tuning effort usually occurs not because selected parameters match their intrinsic values, even though this would clearly be desirable, but rather because error compensation is taking place. As an example, cloud-related parameters are the preferred knobs to tune a number of processes, because of the considerable uncertainty they are affected by. However, not only cloud parameter values are uncertain, but cloud processes themselves are poorly understood and misrepresented in climate models. Any improvement in target variables arising from a calibration of cloud related parameters does not imply that the representation of cloud processes has improved too, but more likely that we are compensating other errors hidden somewhere else in the code. An interesting demonstration of this has been given by (Mauritsen et al., 2012), who showed that different combinations of model parameter values can yield to the same improvements in the simulated climate. Hence, the need for model tuning may increase model uncertainty. For these reasons, the "a posteriori" and empirical nature of model tuning has raised a number of criticisms (see for example Randall and Wielicki, 1997). However, tuning is needed because climate models, and in particular the parameterizations of physical processes, are only approximate representation of reality (Hourdin et al., 2013b). Finite computational resources limit the number of processes that can be explicitly included and force modellers to introduce parameterizations. Furthermore, even if we had unlimited

computational resources, still tuning would be unavoidable, since a number of processes exist that are inadequately understood and for which we do not know the basic equations needed to model them explicitly and to get rid of parameterizations.

Part of the work of my thesis has been devoted to the tuning of the third version of the Earth System Model (ESM) EC-Earth (see section 1.3 for a description of the model and its components). This activity has been carried out in the framework of the Tuning Working Group of the EC-Earth Consortium. In section 1.2 we mentioned that ESMs are a collection of individual models simulating the main components of the climate system. When developing an ESM, tuning tipically takes place at two different levels. On the one hand, individual model components (e.g., the atmosphere, the ocean, etc.) are tuned in isolation. For instance, the atmospheric component can be run by prescribing sea surface temperatures (atmospheric-only simulations, see section 1.4) or the ocean and land components by prescribing atmospheric conditions. On the other hand, also the fully coupled model has to be tuned, through coupled simulations of the climate system. Moreover, tuning is needed each time a major structural change occurs, such as the addition of a new component or the upgrading of an existing component to a newer version.

The EC-Earth tuning activity presented here has been performed after three major model components (namely the atmospheric module IFS, the ocean module NEMO and the sea-ice module LIM) have been upgraded to a newer version (see section 1.3), leading from EC-Earth V2 to EC-Earth V3. My contribution to the tuning of the model can be divided into two parts. The first part has focused on the tuning of the new EC-Earth V3 in its coupled atmosphere+land-surface+ocean+sea-ice configuration. This tuning effort has been primarily devoted to improve the energy balance (TOA and SFC energy fluxes), the hydrological balance (precipitation and evaporation) and surface and tropospheric temperatures. During this work, a number of issues have emerged requiring actions other than just parameter calibration. Some errors in the code have been found and fixed. Also, as discussed in the next sections, an advection mass fixer has been implemented in order to conserve water vapour during atmospheric transport. While these actions lie outside the strict definition of model tuning (i.e. parameter calibration), they are included in the present discussion since they constitute an essential part of my activity within the EC-Earth Tuning Working Group. This activity has concluded with the release of the EC-Earth 3.1 version, the first tuned version of EC-Earth V3, and is described in section 2.2. Secondly, once the tuning of the model in coupled configuration has concluded, I focused on the individual atmospheric component of EC-Earth V3 (namely the IFS cy36r4 model), with the aim of further improving the representation of atmospheric energy fluxes. The results of this atmospheric tuning will be implemented in the next version of the coupled model, namely EC-Earth 3.2b. This activity is described in section 2.3.

2.2 Tuning EC-Earth V3 in coupled configuration

This section provides an overview of the activities aimed at tuning EC-Earth V3 in its coupled configuration. The tuning effort has focused on improving the early (non-tuned) EC-Earth 3.0.1 release — the first official release of EC-Earth V3 — and has leaded to the release of the tuned EC-Earth 3.1 version. Following the approach of Mauritsen et al. (2012), first the tuning goals are defined, based on the main biases of the original EC-Earth 3.0.1 release (section 2.2.1). Then the methodology adopted to tackle the main issues is illustrated in sections 2.2.2– 2.2.6. Finally, the differences and the improvements obtained in the new version (EC-Earth 3.1) are presented in section 2.2.7.

2.2.1 Issues and the tuning strategy

The official release of EC-Earth 3.0.1 presents the following two outstanding issues:

- A strong net energy flux directed from the atmosphere to the ocean (about 1.3 W m^{-2}), resulting in a dramatic warming of the oceans, leading to an equilibrium sea surface temperature (SST) much higher than observed. In EC-Earth 3.0.1 this has been addressed by introducing a multiplicative heat flux correction (`oas_qs_fluxcorr`=0.985) that reduces the heat flux directed to the ocean by the OASIS coupler.

- A positive Precipitation minus Evaporation (P-E) bias of about 0.03 mm/day (should be zero in equilibrium conditions), associated with an increase in sea surface height (SSH) of about 1 meter in about 100 years of simulations. In EC-Earth 3.0.1 this has been addressed by introducing a multiplicative correction to the runoff flux (`oas_rnf_fluxcorr`=0.985) which avoids the increase in SSH.

Note that the two flux corrections affect only coupled runs.

Flux corrections are non-conservative, unphysical practices consisting in adding or extracting heat and freshwater from the model. They were invented in the early days of coupled climate modelling to avoid that models quickly drifted away from the observed climatic state because of strong radiative and hydrological imbalances (Sausen et al., 1988). However, the presence of these unphysical knobs is highly not recommended for any state-of-the-art climate model. For this reason, the tuning strategy presented here is mainly based on two levels:

1. First of all, a first-order tuning aimed at improving the energy fluxes and the P-E, in order to get rid of the flux corrections mentioned above. As discussed in the next sections, this goal is mainly achieved by the introduction of an advection mass fixer — and not through parameter calibration (i.e. bug fixing/model development rather than proper model tuning).

2. In second place, once the first-order tuning has been achieved, a proper tuning (i.e. parameter calibration) in order to improve specific fields of the model. Given the importance of the temperature distribution on many physical processes, main attention is devoted to the surface and tropospheric temperatures, in analogy of what done by Mauritsen et al. (2012).

2.2.2   Methods and observational datasets

If it is not stated differently in the text, simulations are carried out with constant greenhouse gas (GHG) concentration and aerosols for year 2000. Most of the experiments are coupled simulations. In atmosphere-only simulations, the SST boundary conditions are obtained computing the monthly climatology for the 1979-2010 period from observations. In order to evaluate the improvements of the main physical fields, the Performance Indices (PIs) introduced by Reichler and Kim (2008) are used, a measure of the aggregated errors in simulating the observed climatological mean states of many different climate variables.

For what concerns climatic observations, a number of observational datasets are used. These datasets include sea surface temperatures and sea ice concentration data from Hadley Centre Global Sea Ice and Sea Surface Temperature dataset (HadISST, Rayner et al., 2003); surface air temperatures over land from the Climatic Research Unit temperature dataset (CRU, Harris et al., 2013); precipitation estimates from the Global Precipitation Climatology Project (GPCP, Adler et al., 2003); radiative fluxes from the Clouds and the Earth's Radiant Energy System (CERES, Wielicki et al., 1996); atmospheric three-dimensional and two-dimensional fields from two different reanalysis products: the ERA-Interim (Dee et al., 2011) and the NCEP/NCAR (Kalnay et al., 1996) atmospheric reanalyses. Atmospheric reanalyses are estimates of atmospheric temperatures, winds and other quantities, created by processing available observational data using a state-of-the-art atmospheric GCM with data assimilation techniques (definition from IPCC AR5).

Throughout the analysis the energy fluxes — shortwave and longwave radiation, sensible and latent heat — are defined to be positive when downward (i.e. towards the center of the Earth) and negative when upward. The TOA net energy flux — also referred to as TOA net radiative flux — is computed as the sum of the net shortwave and longwave radiation fluxes at the top of the atmosphere. The SFC net energy flux is computed as the sum of the net shortwave radiation, longwave radiation, sensible heat and latent heat fluxes at the surface, including the contribution of snowfall.

In the following, the official EC-Earth 3.0.1 release with the two flux corrections described above will be named **standard**.

2.2.3 The energy balance and the hydrological balance

A first attempt to reduce the surface heat flux toward the ocean and to get rid of the heat flux correction was to increase the diffusive oceanic surface albedo (**RALBSEAD**) from 0.06 to 0.07, thus reflecting more incident solar radiation. This allowed the SST to reach an equilibrium temperature closer to the observations even without the introduction of any heat flux corrector. Also, PI values are improved (i.e. smaller) with respect to the standard EC-Earth 3.0.1 version and in many instances better than the ones shown by EC-Earth V2 and by the best CMIP3 model (reported by Hazeleger et al., 2012). For this reason, this new release of the model has been used as reference scenario for the main tuning activities, and will be defined as **ocean-albedo baseline** in the following. However, the ocean-albedo baseline version shows an imbalance in the TOA net radiative flux of about -2 W m^{-2}. In other words, the increase of surface albedo has moved the energy imbalance from the surface to the TOA, without resolving it.

After running several simulations — either coupled or atmosphere-only, transient or with fixed GHG concentration, with or without heat flux correction, changing albedo and/or other model parameters — it has been noted that the model always shows a constant relation connecting the values of the net energy fluxes at TOA and at the SFC: whatever value is obtained individually for the two, the difference between the TOA and the SFC net energy fluxes (TOA-SFC imbalance) is always about -1.6 – -1.7 W m^{-2}, where the minus indicates that the atmosphere is losing energy (i.e. this energy is exiting the atmosphere).

Due to the presence/absence of a heat flux correction and to a change in ocean albedo, the way this heat is lost from the atmosphere changes among different runs: in the purely atmospheric run this imbalance is mainly at TOA; in the standard EC-Earth 3.0.1, which includes the heat flux correction, about 1.3 W m^{-2} are lost to the ocean (and then destroyed by the flux correction) and the residual 0.3 – 0.4 W m^{-2} are lost at TOA; in the ocean-albedo baseline experiments, the surface imbalance is over-reduced by the higher albedo and 0.3 – 0.4 W m^{-2} are entering the atmosphere from the ocean, but 2 W m^{-2} are then lost at TOA, the net loss being always of about 1.6 – 1.7 W m^{-2}. Interestingly, the average atmospheric temperature does not change significantly in any of these experiments, even over decades: more than 100-year long experiments show no significant cooling, even if a loss of more than 1.5 W m^{-2} should cool the atmosphere by some degrees over this timespan.

To summarize, the atmosphere loses radiation but does not cool, suggesting that the model has an internal heat source producing 1.6 – 1.7 W m^{-2}, which is matched by the same total net energy loss at TOA and at the surface. An important consideration regards the presence of different boundary conditions. Simulations carried out with higher-than-present GHG gas concentrations (in prticular with RCP8.5 year 2100 GHG concentrations, see section 1.4) still show the same

TOA-SFC imbalance (-1.6 – -1.7 W m^{-2}), suggesting that the source of heat found in IFS is independent from the external forcing.

The above considerations are focused on the energy budget of the atmosphere, and on the fact that the model is not energy-conserving. At the same time, however, we know that the standard version of the model does not conserve also water mass: P-E is about 0.03 mm/day in all experiments. The reason of the non-conservation of water mass may reside in the transport scheme of the atmospheric model IFS. Indeed, a well known drawback of semi-Lagrangian advection schemes, such as the one used by IFS, is that they do not formally conserve mass (Diamantakis and Flemming, 2014). If the model artificially creates water vapour, for example in the advection routine, the associated condensation will release latent heat, introducing a source of heat in the atmosphere. A quick calculation shows that the condensation of 0.03 Kg m^{-2} day^{-1} of water produce about 0.9 W m^{-2} (the latent heat of condensation for water is about 2.5 MJ Kg^{-1}). This is a significant source that is unaccounted for in our balance and it is of the same order of magnitude of what we are missing. If there are issues with the transport of other wet species this amount may be even greater.

To test this idea, a proportional advection mass fixer for water species in the atmosphere has been implemented. The mass fixer has been derived backporting a proportional mass fixer developed in a newer version of the IFS model (IFS cycle 38) that was not yet included in the IFS version used in EC-Earth V3 (IFS cycle 36) and adapting it to the different model configuration. In practice, the proportional advection mass fixer computes the global mass of each water species before and after the advection step. Then, each grid-point value is multiplied by the ratio of the mass before and after advection, in order to eliminate the global mass conservation error (see also Diamantakis and Flemming, 2014). Different experiments have been performed, implementing the mass fixer within the ocean-albedo baseline version and the standard version in both atmosphere-only and coupled configuration. In all the considered experiments, the TOA-SFC imbalance is successfully reduced to about -0.3 W m^{-2} (values range between -0.2 and -0.4 W m^{-2}). Moreover, P-E is over-reduced from 0.03 mm/day to about -0.016 mm/day. This suggests the presence of a further error, associated with a sink of water species somewhere in the atmosphere that is not connected with the transport. Note that the improvement of about 1.3–1.4 W m^{-2} obtained in the TOA-SFC imbalance is in good agreement with the simple estimation of the latent heat release given by the observed change in P-E (about 0.046 Kg m^{-2} day^{-1}) when considering the latent heat of condensation for water being about 2.5 MJ Kg^{-1}.

Given the improvements obtained in both the energy budget and in the hydrological budget, including the mass fixer in EC-Earth V3 is clearly desirable. Unfortunately, the mass-fixer routine leads also to a reduced heat flux directed to the surface, which implies that in a long run the coupled model achieves a new equilibrium at a lower surface temperature. The best results with operative mass

fixer are obtained when it is applied to the standard version without heat flux correction (indeed, the original heat flux correction would cause a further cooling because it deletes part of the heat flux entering the ocean). In this case, the equilibrium average surface temperature is of 286.37 K, i.e. 0.6 K lower than the equilibrium temperature of the ocean-albedo baseline version without mass fixer (286.95 K), which is at present the simulation showing the best match with observations. Such a 0.6 K difference leads to a considerable worsening of the Reichler and Kim (2008) PIs for the case when the mass fixer is applied. The adoption of the mass fixer in the ocean-albedo baseline version causes a supplementary cooling for the ocean temperature, due to the fact that ocean diffusive albedo is higher there, indicating that the ocean-albedo change and the mass-fixer implementation are mutually exclusive. In the following we refer to the case when the mass-fixer is applied to the original EC-Earth 3.0.1 release (standard version) without the heat flux correction as the **mass-fixer** version. For the considerations mentioned above, further tuning on temperatures is still needed to improve this version.

2.2.4 The residual atmospheric energy imbalance

A number of experiments have been carried out in order to further investigate the residual TOA-SFC imbalance of about -0.3 W m^{-2} that is obtained when the mass fixer is operative. Since this is a problem that is specific for IFS, we addressed this issue in atmosphere-only experiments with and without operative mass fixer. Many possibilities have been investigated, including changes in the radiative scheme, in the timestep of integration and various horizontal and vertical resolutions. The horizontal resolution is identified by the truncation number (T), i.e. the wave number at which the spherical harmonics expansion is truncated (spectral method, see for example Machenhauer, 1979). The vertical resolution is identified by the number of vertical levels (L). As an example, the standard resolution of EC-Earth V3 is T255L91, indicating a horizontal resolution with truncation at wave number 255 and 91 vertical levels. Results can be summarized as it follows:

- **Horizontal resolution**: in general, an increase in horizontal resolution leads to a change of the residual TOA-SFC imbalance towards more positive values. A mass-fixer run with T511L91 resolution leads to a TOA-SFC imbalance of +0.7 – +0.8 W m^{-2} while the P-E is little affected (-0.020 mm/day). Importantly, this occurs only when the mass fixer is operational. Otherwise, the TOA-SFC imbalance at T511L91 resolution remains similar (about -1.6 – -1.7 W m^{-2}) even though P-E increases strongly (+0.063 mm/day). This means that the mass fixer has a much stronger effect on high resolution runs, in agreement with what reported by Diamantakis and Flemming (2014), where it is stated that the transport error is inversely proportional to the timestep (T255 has a timestep of 2700s, while T511 of 900s). Furthermore, it

suggests that the other unknown sources of error causing the residual TOA-SFC imbalance strongly depend on the model resolution.

- **Vertical resolution**: a decrease in the vertical resolution from L91 to L62 affects the residual TOA-SFC imbalance by about $+0.6$ W m^{-2}. This occurs independently from the horizontal resolution. Therefore, a mass-fixer run at T255L62 resolution has TOA-SFC imbalance of $+0.3$ W m^{-2}. Even if we performed only few tests and it is hard to extrapolate any statistical relationships between vertical levels and TOA-SFC imbalance, given that in L91 many levels are added in the stratosphere and that there is no change in the P-E, it could be likely that a part of the radiative imbalance originates from the stratosphere.

- **Timestep of integration**: reducing the timestep from 2700s to 900s without modifying the spatial resolution affects the residual TOA-SFC imbalance by about $+0.3$ W m^{-2} (experiments performed at T255L91 and at T255L62). In particular, the residual TOA-SFC imbalance of about -0.3 W m^{-2} at T255L91 with operative mass fixer observed when a timestep of 2700s is used (default value) basically disappears when the timestep is reduced to 900s, which is the best result obtained for the standard resolution of EC-Earth V3. However, the time needed for the integration is considerably larger, which should be weighed against an improvement of only 0.3 W m^{-2}.

- **Radiative scheme**: no significant changes are obtained when playing with the main knobs of the radiative scheme (timestep, grid resolution and even an old shortwave radiative scheme have been tested without any success).

2.2.5 The issue of the sea surface height drift

The ocean-albedo baseline and the mass-fixer versions are successful in getting rid of the heat flux correction. In this section I focus on the problem of the SSH drift and the associated runoff flux correction.

The runoff flux correction (`oas_rnf_fluxcorr`=0.985) implemented in the standard and in the ocean-albedo baseline versions reduces the original runoff (i.e. P-E over land) by artificially removing 1.5% of it. In the ocean-albedo baseline experiment, where the global P-E bias is of 0.03 mm/day, this results in an almost stationary SSH ($+0.12$ m/100y). Thus, in absence of other error sources, one would conclude that 1.5% of the original runoff roughly corresponds to 0.03 mm/day. However, the problem is not as trivial as it looks like.

A series of simulations have been run to estimate the role of `oas_rnf_fluxcorr` and to understand the observed differences in the SSH drift between the ocean-albedo baseline version (P-E=0.03 mm/day) and the mass-fixer version (P-E=-0.016 mm/day). Comparing similar experiments (either ocean-albedo baseline or mass-fixer) with different values of `oas_rnf_fluxcorr` it is found that the actual

contribution of the flux corrector is really small (about -0.10 m/100y). However, in the ocean-albedo baseline runs, the strong positive P-E imbalance (+0.03 mm/day) should imply an increase of the SSH of about +1.6 m/100y, which is not observed in the model outputs. Since the actual sea level rise in the ocean-albedo experiments where no runoff flux correction is operative is of only 0.26 m/100y, we conclude that there must be a sink of water, which is responsible for the loss of about 1.3–1.4 m/100y. Moreover, given that the P-E over land computed by the atmospheric component (IFS) is consistent with the observed runoff, it is likely that the source of error should be placed somewhere in the ocean component (NEMO) or in the coupler (OASIS).

These results are confirmed by simulations performed with the mass-fixer version. Here, the total P-E imbalance is -0.016 mm/day, which should lead to a decrease of the SSH of about -0.8 m/100y. Conversely, a decrease of SSH of about -2.1 m/100y is obtained, which is consistent with the existence of a sink of water of about -1.3 m/100y.

Finally, this hypothesis has been further tested by running the mass-fixer version but with `oas_rnf_fluxcorr`=1.17, a value that should balance the -2.1m/100y decrease observed in mass-fixer experiments without runoff flux correction. With this large runoff flux correction, the observed SSH is almost stationary, with a decrease of only -0.2 m/100y.

Further analyses have revealed two different problems that were causing a large part of the freshwater sink:

- **NEMO bug #897**: A bug in NEMO 3.3.1 (corrected in the more recent version of the oceanic model) was causing a sink of freshwater of about -0.6 m/100y. This has been successfully corrected. Details on the bug can be found at `https://forge.ipsl.jussieu.fr/nemo/ticket/897`.

- **Ridging effect**: A further bug has been found, suggesting that melted water coming from ridging (i.e. collision of sea-ice sheets) was not accounted in the freshwater flux. This bug was found to cause approximately -0.65 m/100y of SSH decrease. Also this bug has been successfully corrected.

Combing the two corrections together the improvement in the SSH drift is considerable. Given an expected SSH decrease caused by the P-E imbalance of about -0.8 m/100y, in the mass-fixer experiments it is now observed a decrease of about -0.9 m/100y, which is less than the half of the original drift (-2.1 m/100y).

Finally, a different approach to correct the residual SSH drift and obtain a stable SSH has been implemented: instead of applying the mass corrector to the runoff, it is applied to the liquid precipitation over the oceans. In this way the excess of freshwater input to the ocean is not localized in coastal areas and should not drastically affect the regional salinity patterns. The new key parameter has been defined as `oas_mb_fluxcorr` and after several tests it has been tuned on the value of 1.01622 for the mass-fixer version.

2.2.6   Tuning of the surface temperature

The analyses and tests described in the previous sections have been performed to improve the main biases of the standard version of EC-Earth 3.0.1 — and in particular its heat and runoff flux corrections. At this point, the two most promising versions are the ocean-albedo baseline and the mass-fixer, in which the changes presented in section 2.2.5 to solve the SSH drift have been included. The mass-fixer version is particularly advisable because it has a better energy budget (i.e. a much smaller TOA-SFC imbalance). However, it shows a cold bias in surface temperatures, resulting in worse PIs than the ocean-albedo baseline version. The target version should have the TOA-SFC imbalance of the mass-fixer version and the surface temperatures of the ocean-albedo baseline version.

To reach this goal, a number of experiments have been done to tune the surface temperatures of the mass-fixer version in order to solve its cold bias. Part of the problem has been addressed by reducing the diffusive albedo of the ocean (**RALBSEAD**) from 0.06 to 0.05, as it has already been shown in the development of the ocean-albedo baseline version that it is an efficient knob to tune the sea surface temperature. Then, cloud-related parameters have been investigated. In particular, a reduction of the entrainment rate in organized convection (**ENTRORG**) from $1.8{\times}10^{-4}$ to $1.5{\times}10^{-4}$, leading to a decrease in low-level cloud-cover and thus less reflection of incident solar radiation, has been shown to be quite effective and it has been implemented. Finally, a parameterization (namely the "warm ocean parameterization", **LOECWA**) that was causing an unphysical coupling between the ocean and the atmosphere has been disabled in coupled runs. When active, indeed, the atmospheric component (IFS) mimics the absorption of solar radiation by the uppermost layer of the ocean. This is very useful in atmosphere-only runs forced by fixed SSTs, because it simulates the diurnal cycle of solar heating. However, in coupled simulations the ocean already accounts for the absorption of solar radiation, so the warm ocean parameterization is actually a double counting of solar heating. It makes IFS to see a slightly warmer ocean than what it gets from the ocean model (NEMO), which then results in a larger longwave flux and subsequently a cooling of the ocean (in NEMO). Switching off this parameterization in coupled runs gives a warmer ocean. Now the LEOCWA parameterization is true only for atmosphere-only runs.

Once these changes have been applied to the mass-fixer version, the resulting equilibrium average surface temperature is of 287.56 K, which is even closer to the observed surface temperature (287.58 K from the ERA-Interim reanalysis) than the average surface temperature of the ocean-albedo baseline version (286.95 K). Given this very good result, the mass-fixer version including these modifications has been chosen to be the new official release of the EC-Earth V3 model, namely the EC-Earth 3.1 version.

2.2.7   The new EC-Earth 3.1 release

The tuning activity described in the previous sections has leaded to the release of the new EC-Earth 3.1 official version. Here below a summary of the main changes between versions 3.0.1 and 3.1 is given:

- Introduction of a proportional advection mass fixer for water species in the atmosphere

- The heat flux corrector (`oas_qs_fluxcorr`) has been removed

- The runoff flux correction used to balance P-E has been changed from a correction factor to runoff (`oas_rnf_fluxcorr`) to a correction factor for liquid precipitation over the oceans (`oas_mb_fluxcorr`=1.01622)

- Two different bugs causing a reduction of the SSH have been fixed

- Diffusive albedo for the ocean (**RALBSEAD**) is reduced from 0.06 to 0.05

- The parameter for entrainment in organized convection (**ENTRORG**) is reduced from 1.8×10^{-4} to 1.5×10^{-4}

- The warm ocean parameterization (**LEOCWA**) has been disabled in coupled runs

A spin-up run (900 years) has been performed with the new EC-Earth 3.1 version, and new initial conditions have been provided.

In order to evaluate the differences and improvements from EC-Earth 3.0.1 to EC-Earth 3.1, two different runs are compared in the following: one with EC-Earth 3.0.1 (referred to as v3.0.1) and the other with EC-Earth 3.1 (referred to as v3.1). These runs are performed under perennial year 2000 GHGs and aerosol forcing and the last 100 years of each run are considered. The evaluation of the two simulations includes a comparison against observational data. Since these runs have been performed under perennial year 2000 conditions, it is worth to keep in mind that the comparison with observations is not entirely fair: the EC-Earth climate is almost at equilibrium under constant forcing, while the real climate of the Earth is subject to an important transient.

Table 2.1 shows the global mean values for some selected variables from the two model versions. The major improvement introduced during the tuning of the model is the reduction of the bias in the TOA-SFC imbalance from -1.61 W m^{-2} (v3.0.1) to -0.22 W m^{-2} (v3.1), thanks to the introduction of the advection mass fixer. The use of the advection mass fixer also leads to a partial improvement in the P-E bias, which is reduced from 0.03 mm/day to -0.016 mm/day. A considerable issue that was present in v3.0.1 was a cold surface temperature bias, of the order of 1°C. In v3.1 this average bias is completely removed, although some inconsistencies with observations persist at regional scales (see below for further details). This

Field	v3.0.1	v3.1	OBSERVATIONS
TOA [W/m²]	-0.43	-0.92	Should be 0
SFC [W/m²]	1.18	-0.70	Should be 0
TOA-SFC [W/m²]	-1,61	-0.22	Should be 0
P-E [mm/day]	0.031	-0.016	Should be 0
SST [°C]	17.69	18.71	18.41 (HadISST 1990-2010)
T2M [°C]	13.24	14.41	14.43 (ERAInterim 1990-2010)

Table 2.1: Global averages of TOA net radiative flux (TOA), SFC net energy flux (SFC), TOA-SFC imbalance (TOA-SFC), precipitation minus evaporation (P-E), sea surface temperature (SST) and surface (2-meter) air temperature (T2M) from EC-Earth 3.0.1, EC-Earth 3.1 and observations. Values for the model version closer to observations are reported in blue.

Field	v3.0.1	v3.1
T2M	33.35	13.10
MSL	2.21	1.72
QNET	19.10	21.28
TP	22.34	26.80
SST	13.07	14.97
T	25.58	10.71
U	1.97	1.82
V	1.63	1.43
Q	23.85	16.55
Total PI	0.83	0.72

Table 2.2: Main performance Indices for EC-Earth 3.0.1 and EC-Earth 3.1. Better (i.e. lower) PIs between the two versions are reported in blue. *T2M* is 2-meter air temperature, *MSL* mean sea level pressure, *QNET* net surface energy flux, *TP* total precipitation, *SST* sea surface temperature, *T* atmospheric temperature, *U* zonal wind, *V* meridional wind, *Q* specific humidity. *T*, *U*, *V* and *Q* are three dimensional fields. *Total PI* is computed by taking into account for all these variables as well as others not reported here (see Reichler and Kim, 2008, for further details).

warming has been obtained removing the warm ocean parameterization, changing the entrainment rate parameter for organized convection and reducing the diffusive albedo of the ocean.

In agreement with these changes in the global mean values, the Reichler and Kim (2008) Performance Indices shown in Table 2.2 report considerable improvements for the surface temperature and for three-dimensional atmospheric temperature and specific humidity. Only slightly worse skills (i.e. larger PIs) are observed for the net surface energy flux, total precipitation and SST. Good values are obtained for the meridional and zonal wind and for the mean sea level pressure in both versions. The total PI, which takes into account for all the variables used to compute the individual PIs, indicates an overall improvement of v3.1 with respect to v3.0.1.

It has to be noted that both simulations reach an equilibrium temperature with SFC net energy fluxes different from zero (Table 2.1). After the release of EC-Earth 3.1 a bug has been found, namely that the ocean model NEMO does not take the latent heat of snowfall and associated snowmelt into account, resulting in a heat generation of roughly 0.7 W m^{-2} in the ocean. The correction of this bug will be implemented in the next version of EC-Earth, together with the results discussed in section 2.3. For this reason, v3.1 shows an equilibrium SFC net energy flux of -0.70 W m^{-2}. Vice versa, the equilibrium SFC net energy flux of 1.18 W m^{-2} in v3.0.1 is dominated by the heat flux correction, which deletes part of the heat flux entering the ocean overbalancing the effect of the heat generation due to problems with snowmelt. The TOA net radiative flux is then the sum of the SFC net energy flux plus the atmospheric heat generation (TOA-SFC imbalance).

Surface Temperatures and SSTs

The overall improvements described above reflect changes in the main dynamical fields. The major improvements are connected to the increased surface temperature of the Earth by about 1°C. This reduces considerably the biases of surface air temperature over land (Fig. 2.1, *left*) even though the tropics remain too cold and the polar region experience a too mild climate, particularly over Eastern Siberia. This warm high latitude bias is stronger during the winter season in both hemispheres, suggesting that it may be connected to a longwave radiative issue, perhaps involving cloud cover. A different situation is found for the distribution of Sea Surface Temperatures (Fig. 2.1, *right*). On one side the SST bias is reduced in v3.1 due to the average increase of global temperatures. However, it shows some peculiar features and large regional biases in v3.1. These are evident especially over the North Atlantic, where a cold pool is now found south of Greenland. This bias in the North Atlantic is similar to the one discussed by Keeley et al. (2012), and may be important for the quality of the simulation of the Northern Hemisphere climate variability. Furthermore, both simulations show a strong pos-
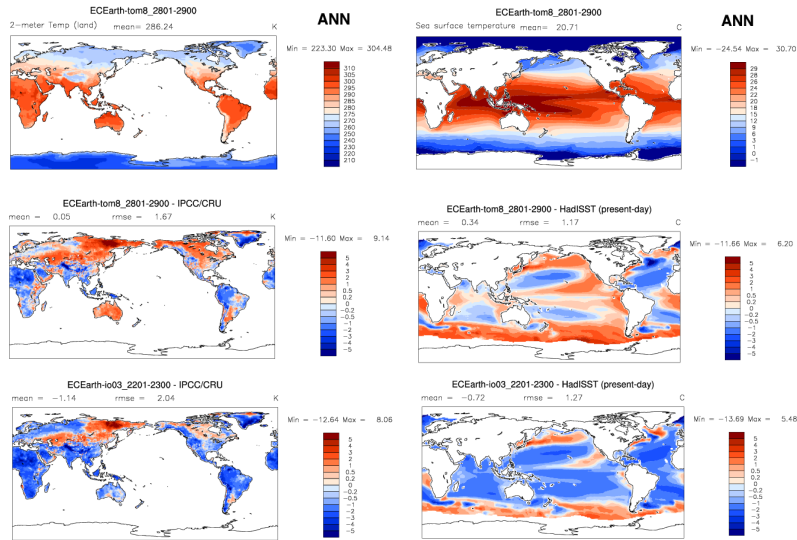
Figure 2.1: *Left:* annual mean surface air temperature over land: climatology from v3.1 (top), difference between v3.1 and observations (middle) and difference between v3.0.1 and observations (bottom). *Right:* the same but for sea surface temperatures. Observational fields are derived from CRU (surface air temperature over land) and HadISST (sea surface temperatures).

itive temperature bias in the Southern Ocean. This is likely associated with an underestimated cloud cover in that area.

Precipitation rate

Since the Earth is warmer in EC-Earth 3.1, also the precipitation rate is slightly increased (Fig. 2.2, *left*). This is also linked to the change in the parameter controlling the entrainment in organized convection, which leads to an increase of more than 10% in the tropical Western Pacific. A weak southward displacement of the Intertropical Convergence Zone (ITCZ) and a strengthening of the double ITCZ effect (e.g. Lin, 2007) can be seen in v3.1.

TOA net shortwave radiation

EC-Earth v3.0.1 and v3.1 both underestimate clouds over the Southern Ocean. As a consequence, there is too much incoming shortwave radiation (Fig. 2.2, *centre*) resulting in a stronger heating at the surface. This is likely one of the reasons why we observe a warm SST bias in the Southern Ocean. Clearly, this effect is stronger during the austral summer, when the solar radiation is stronger in the southern hemisphere. This problem is present both in v3.1 and v3.0.1 and it is common to
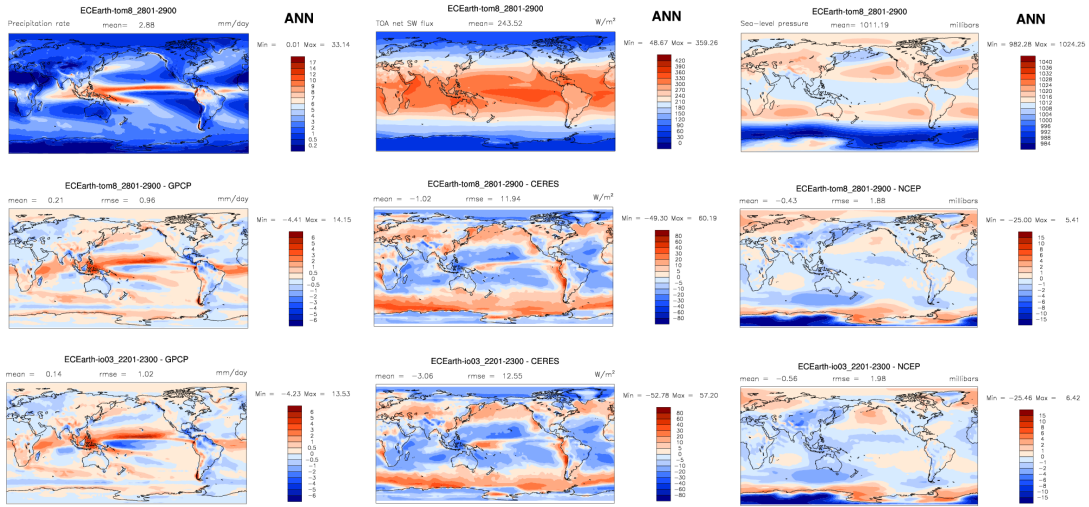
Figure 2.2: *Left:* Annual mean precipitation rate: climatology from v3.1 (top), difference between v3.1 and observations (middle) and difference between v3.0.1 and observations (bottom). *Centre:* the same but for TOA net shortwave radiation. *Right:* the same but for sea level pressure. Observational fields are derived from GPCP (precipitation rate), CERES (TOA net shortwave radiation) and NCEP/NCAR Reanalysis (sea level pressure).

many climate models. It is potentially associated also with the double-ITCZ effect and more generally to the tropical precipitation (see Hwang and Frierson, 2013).

Sea Level Pressure

Sea level pressure is well simulated by both versions of EC-Earth (Fig. 2.2, *right*). Biases are present in the proximity of Antarctica, likely associated with some issues regarding sea ice. No evident differences emerge between the two versions of EC-Earth.

Sea Ice Extent

The sea ice extent shows a moderate decrease from v3.0.1 to v3.1, approaching values closer to the observed ones (Figs. 2.3 and 2.4). Values for the end-of-summer Northern Hemisphere sea ice extent are around 8 millions of Km^2 for v3.0.1 and about 7 millions for v3.1 (Fig. 2.4). However, on the annual average, large positive biases compared to observations are still present in both the Northern and the Southern Hemispheres (Fig. 2.3). This seems somehow in contrast with the warm polar bias in the cold season discussed above, suggesting that ice dynamics and surface temperatures may be affected by two different issues.
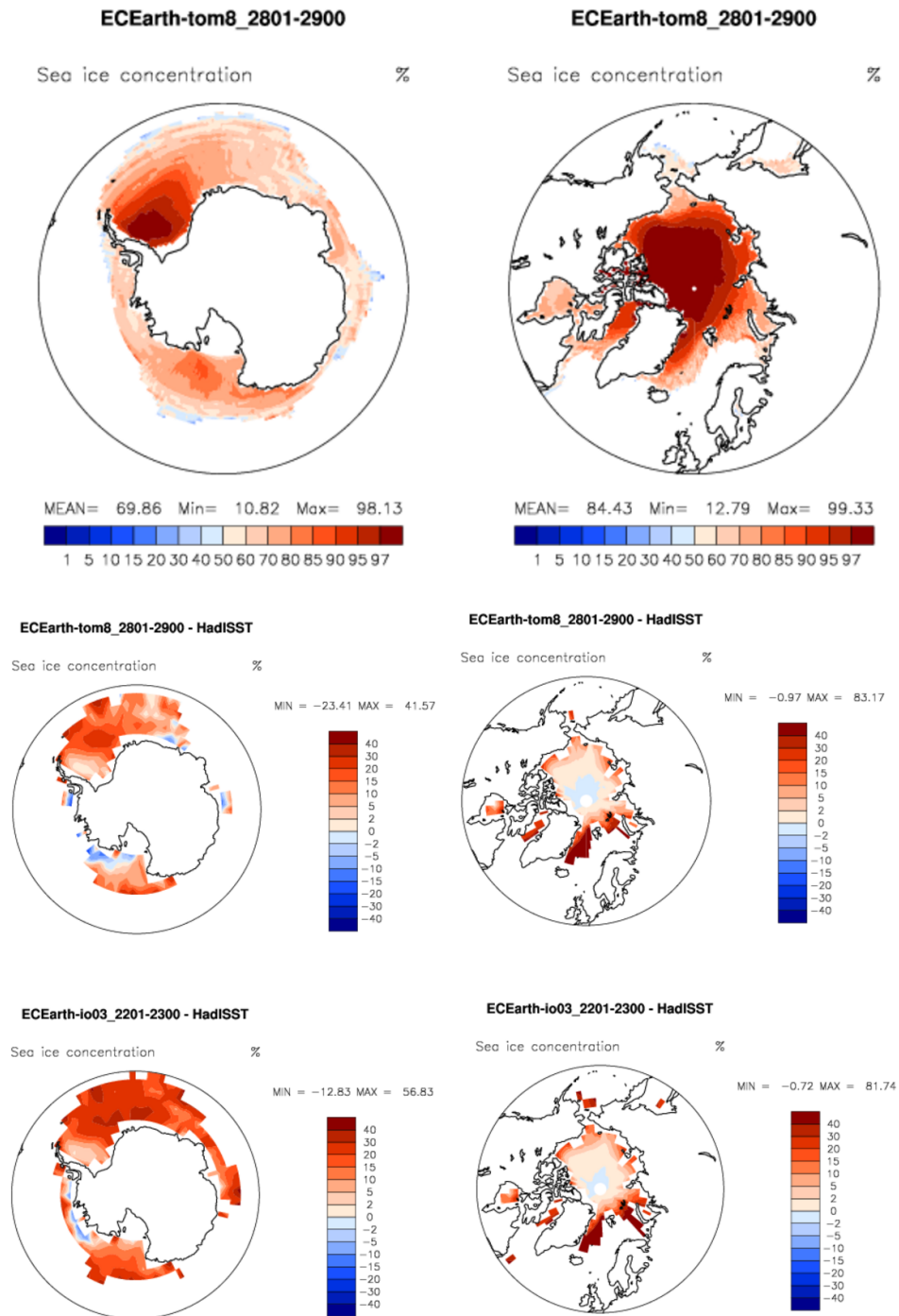
Figure 2.3: Annual mean sea ice concentration in the Southern Hemisphere (left) and in the Northern Hemisphere (right): climatology from v3.1 (top), difference between v3.1 and observations (middle) and difference between v3.0.1 and observations (bottom). Observational fields are derived from HadISST.
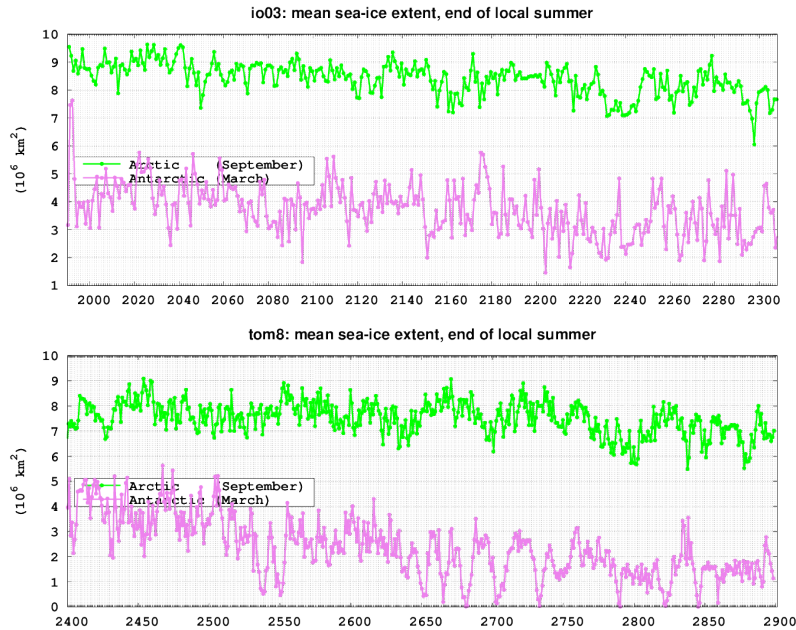
Figure 2.4: Time series of mean sea ice extent at the end of local summer in the Arctic (green) and in the Antarctic (purple) for v3.0.1 (top) and v3.1 (bottom).

Meridional profiles of three dimensional atmospheric fields

Vertical profiles of zonally averaged atmospheric quantities show an improvement for temperature and specific humidity in v3.1 with respect to v3.0.1 (Fig. 2.6, top and middle panels respectively), in agreement with the changes at the surface discussed above. However, even though the profile of temperature in v3.1 is particularly good in the troposphere, there are evident discrepancies emerging in the stratosphere. This should be addressed in the next versions, considered also that specific experiments with different vertical levels suggest that a part of the TOA-SFC radiative imbalance may be located in the stratosphere as well (see section 2.2.4). On the other hand, the zonal wind patterns are not significantly changed from v3.0.1 to v3.1 (Fig. 2.6, bottom panels). In both versions the model shows a good agreement with observations. A minor bias can be noticed in an underestimation of the jet stream in the southern hemisphere.

Atlantic Meridional Overturning Circulation

A final mention must be reserved to the Atlantic Meridional Overturning Circulation (AMOC), which shows a decrease of its intensity of the order of 2 Sv, moving from about 20 Sv to approximately 18 Sv (Fig. 2.6). Both values are within the range of existing estimates of the AMOC. The value of v3.1 provides the best agreement with a recent valid estimate of about 18.7 Sv (Cunningham et al., 2007).
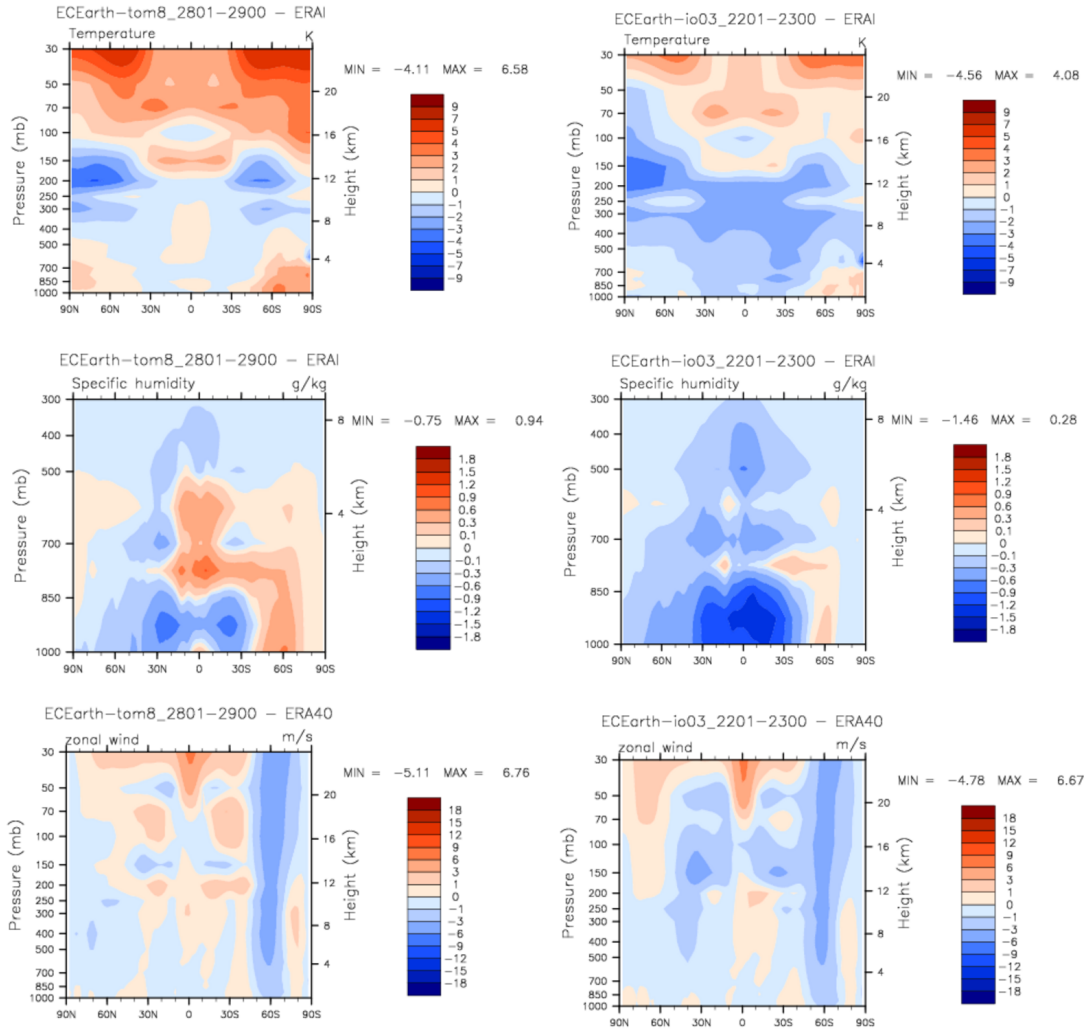
Figure 2.5: Differences of zonally averaged atmospheric temperature (top), specific humidity (middle) and zonal wind (bottom) between EC-Earth and observations. Left panels refer to EC-Earth v3.1, right panels to v3.0.1. Observational fields are derived from the ERA-Interim Reanalysis.
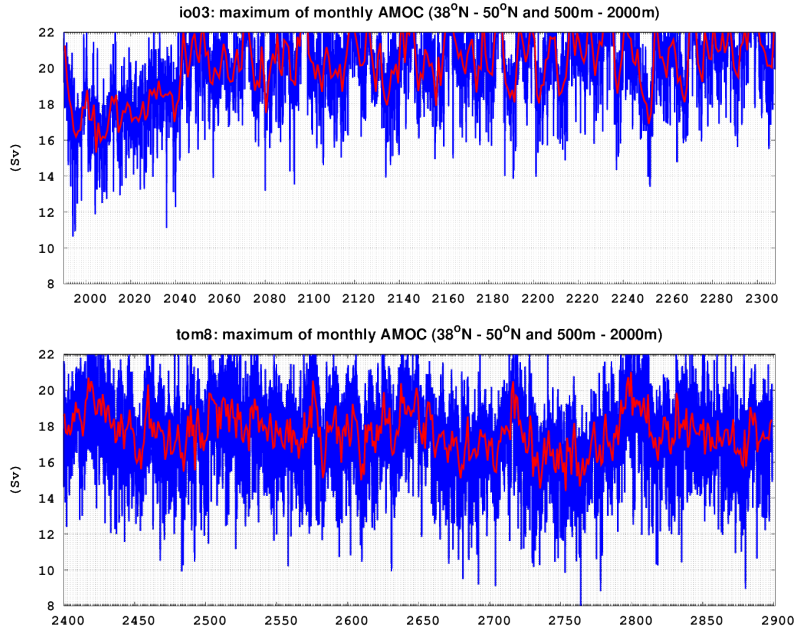
Figure 2.6: Maximum of the Meridional Overturning Streamfunction in the Atlantic Ocean from v3.0.1 (top) and from v3.1 (bottom).

2.3   Atmospheric sensitivity tests

After the tuning of the EC-Earth model in its coupled configuration described in section 2.2 and the release of the EC-Earth 3.1 version, I focused on the tuning of the atmospheric model, IFS cy36r4. The sensitivity of EC-Earth atmosphere to different model parameters has been explored, with the main purpose of improving the representation of the main energy fluxes. The results of this atmospheric tuning will be implemented in the next version of the coupled EC-Earth model, namely EC-Earth 3.2b. EC-Earth 3.2b will include, among the other things, an updated version of the ocean model NEMO, version 3.6, that will replace the version 3.3.1 included in the current EC-Earth 3.1 release. Since this new version of the NEMO model has not been implemented yet within EC-Earth, the tuning activity presented in this section is purely atmospheric, and the results will need to be tested in coupled configuration once the EC-Earth 3.2b including the new NEMO version will be released.

The current EC-Earth 3.1 version shows three main issues regarding the representation of energy fluxes:

- EC-Earth 3.1 has unrealistic high TOA net shortwave and longwave fluxes (about 243 W m^{-2} vs. observed fluxes of about 240 W m^{-2}).

- Longwave cloud radiative forcing shows unrealistic low values (about 24 W

40

m^{-2} vs. observed of about 26 W m^{-2}).

- EC-Earth 3.1 shows a too low net surface energy flux in simulations of present day climate driven by transient boundary conditions inferred from observations (atmospheric composition and solar forcing). At present day, the flux is estimated about 0.6 W m^{-2}.

Thus, the main goal is to tune these three aspects in order to get acceptable values, without worsening the representation of other key variables.

Twelve different parameters affecting convection, clouds, precipitation, and other various water-cycle-related features have been investigated. Some of them have been already introduced in section 2.2. All of them are described in detail in the IFS documentation available at `https://goo.gl/mTfwRe`. The complete list is given here below:

1. **ENTRORG**: it controls the organized entrainment in deep convection

2. **RPRCON**: it controls the rate of conversion of cloud water to rain

3. **DETRPEN**: it controls the detrainment rate in penetrative convection

4. **ENTRDD**: it controls the average entrainment rate for downdrafts

5. **RMFDEPS**: it controls the fractional massflux for downdrafts

6. **RVICE**: it regulates fall speed of ice particles

7. **RLCRITSNOW**: it affects the critical autoconversion threshold for snow in large scale precipitation

8. **RSNOWLIN2**: it is the snow autoconversion constant in large scale precipitation

9. **RLCRIT**: it is the critical autoconversion threshold for rain

10. **RTAUMEL**: it controls the relaxation time that affects the melting of falling solid particles for large scale precipitation

11. **RALBSEAD**: it controls the albedo for diffusive radiation over the ocean

12. **COND-LIMITER**: it is a code modification that affects the vertical humidity distribution

The analysis includes a number of atmosphere-only simulations, forced with standard climatological SSTs and with perennial present day forcing. The atmospheric tuning activity has been performed through two consecutive steps. First, 40 short atmospheric runs (6 years each) have been performed, by changing each

41

time only one of the 12 parameters of interest, exploring both increasing and decreasing values. The admissible bounds of parameter changes have been taken from Mauritsen et al. (2012) as well as from specific recommendations given by IFS development group at ECMWF. Years 2 to 6 of the simulations have been evaluated to assess the sensitivity of model selected fields to different parameters. After this first group of experiments, once the model sensitivity to individual parameters has been assessed, different parameter modifications have been combined together in order to find the best parameter configuration to improve the representation of the main radiative fluxes mentioned above. Evaluation of model behavior has been done through the comparison of global averages of model fields against available observations as well as through the use of Reichler and Kim (2008) PIs introduced in section 2.2 for the variables of interest. The latter include the energy fluxes we aim to improve, as well as other fields we aim not to worsen (mainly temperature, precipitation and dynamical fields).

Figs. 2.7–2.10 show the results of the sensitivity experiments to individual parameter changes for the TOA net shortwave and longwave radiation, longwave cloud radiative forcing and SFC net energy flux respectively. In general, the most efficient knobs to our purposes are found to be **RPRCON** and **RVICE**. Indeed, they have a significant effect on both TOA net shortwave and longwave fluxes (Figs. 2.7 and 2.8), since they operate on high cloud cover. For the same reason, they are the most efficient parameters in modifying the longwave cloud radiative forcing (Fig. 2.9). Finally, their are quite effective in regulating also the SFC net energy flux (Fig. 2.10). Interestingly, it is found that the **COND-LIMITER** has a strong effect in regulating the SFC net energy flux.

Results of the experiments in which different combinations of parameter values are merged together in order to find the best parameter configuration are reported in Figs. 2.11 and 2.12. They show the effect of 9 different configurations — the original one (baseline, *ca00*) and 8 modified versions — on global mean fields and PIs respectively. The green shading in Fig. 2.11 shows the range of acceptable values and the red lines are the "realistic" values available from literature, mainly derived from Trenberth et al. (2009). In both Figures, there are three experiments (namely *cac4*, *cac5* and *cac8*) showing parameter combinations with values similar to those used in a newer version of the IFS model, the IFS cy40r1 (see `https://goo.gl/4I4Q2l`), including the adoption of the condensation limiter (**COND-LIMITER**). These simulations are referred to as "Cy40-like" experiments. The TOA net shortwave and longwave radiative fluxes are successfully reduced by a number of different parameter setups. Indeed, 6 out of 8 modified parameter combinations lie within the range of admissible values for the TOA net longwave flux, while all the 8 modified combinations show acceptable values for the TOA net shortwave flux. The same can be said for the longwave cloud radiative forcing, even if in this case we do not have an estimate of the range of acceptable values. The situation is slightly different for the SFC net radiative flux, where only 4 parameter
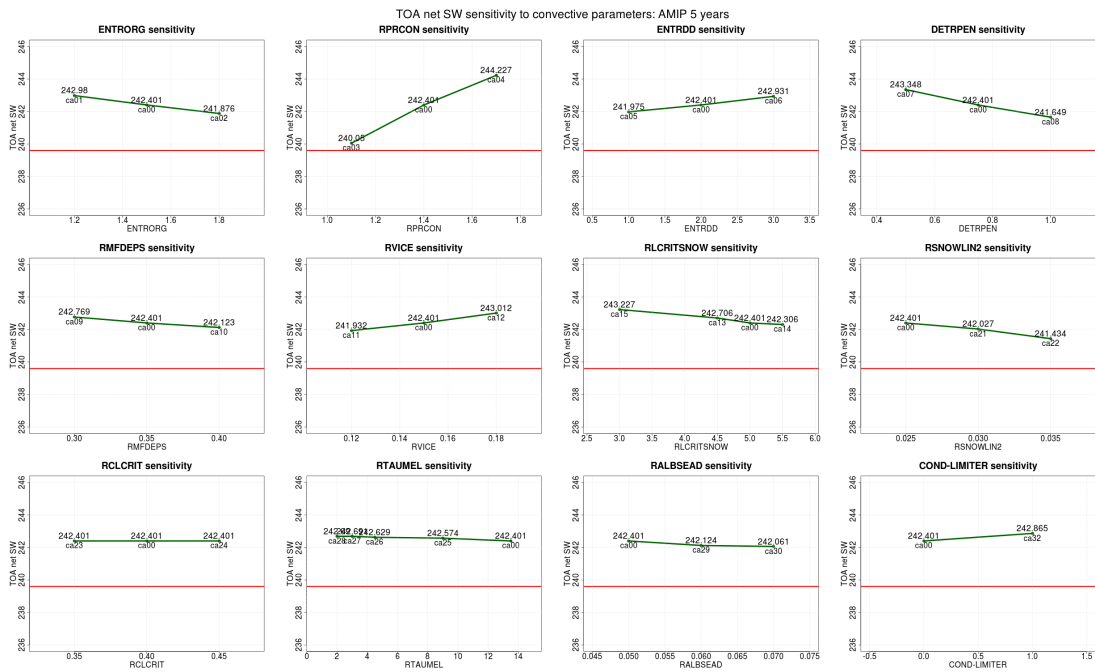
Figure 2.7: Sensitivity of TOA net shortwave radiation (y-axis) to individual model parameters (x-axis). Red line indicates the target (observed) value.
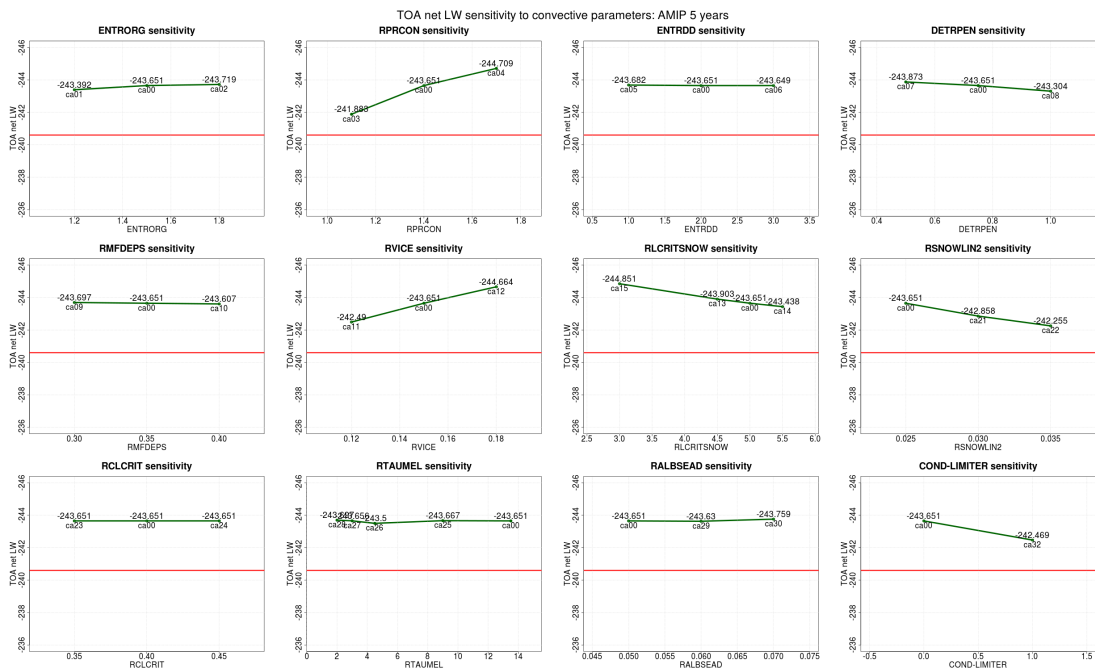
Figure 2.8: The same as in Fig. 2.7 but for TOA net longwave radiation.

43

Figure 2.9: The same as in Fig. 2.7 but for longwave cloud radiative forcing.
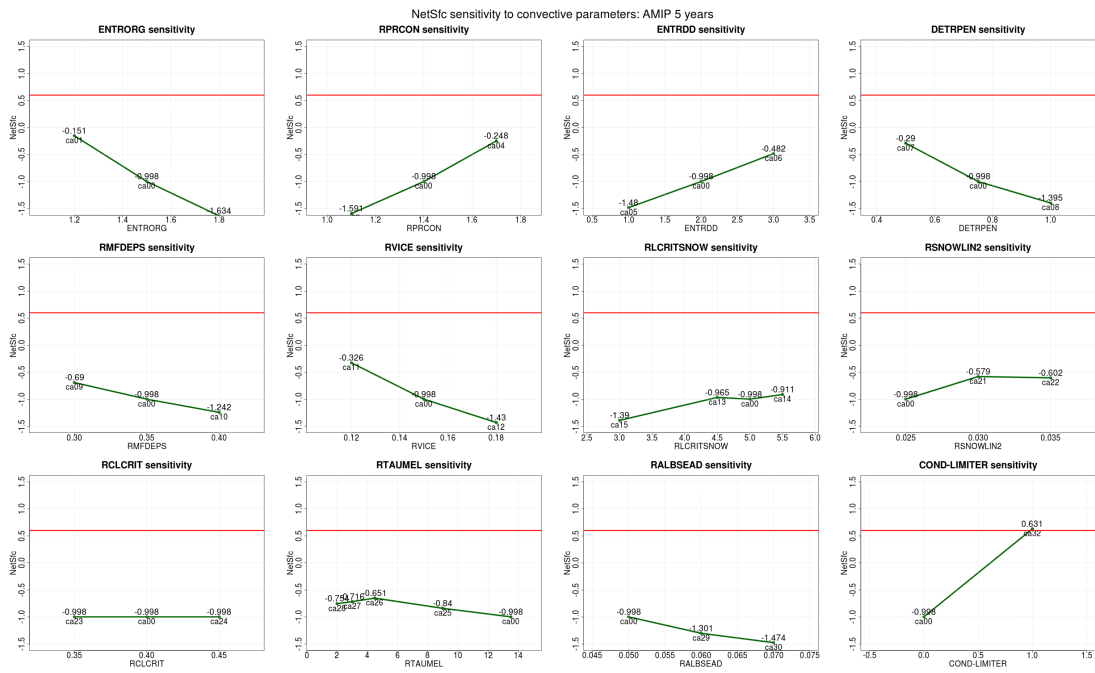
Figure 2.10: The same as in Fig. 2.7 but for SFC net energy flux.
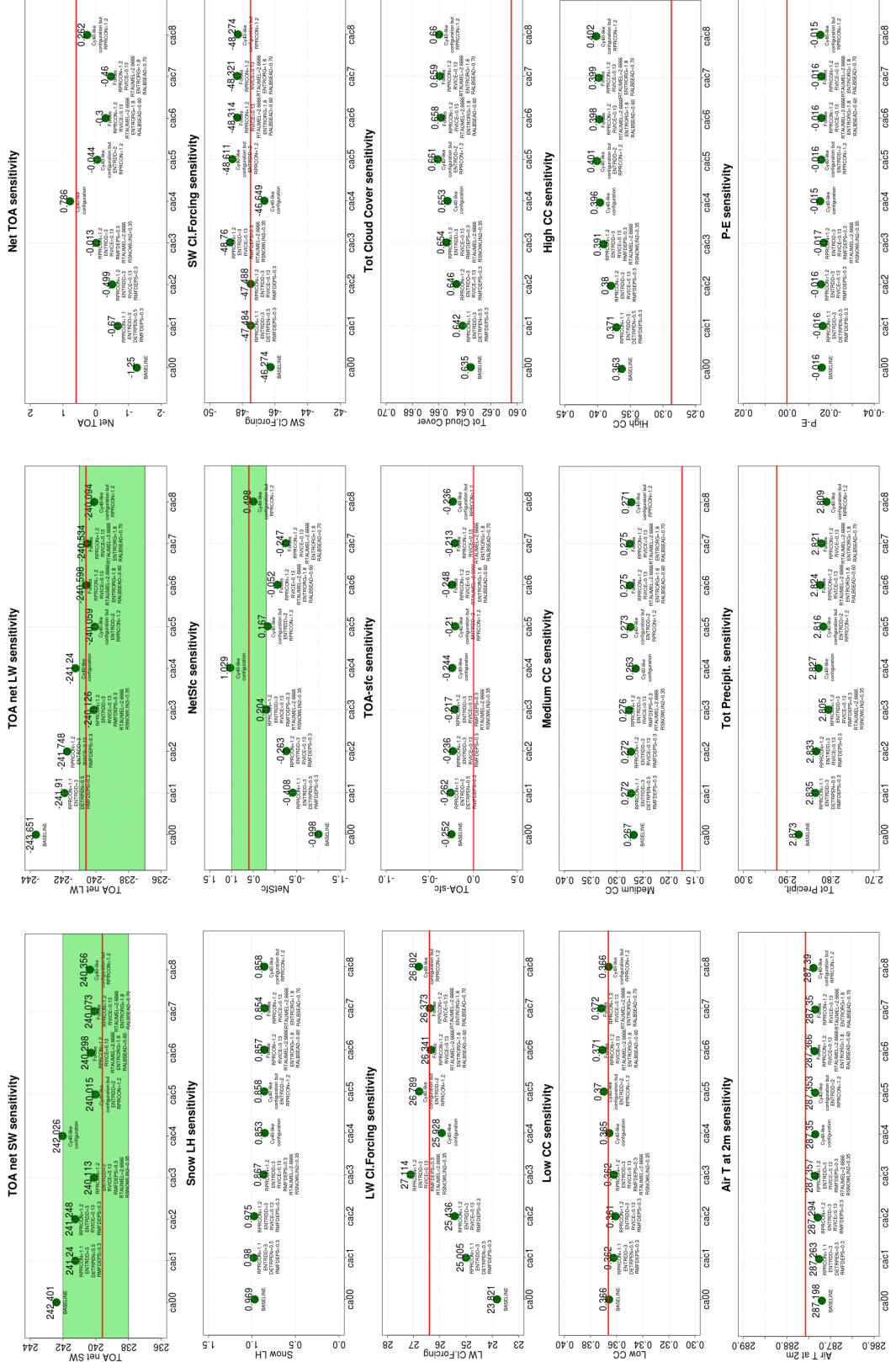
Figure 2.11: Effect of different parameter combinations on global mean values of selected fields. The green shading shows the range of acceptable values and the red lines are the "realistic" values from literature. For each configuration, parameters that have been modified are reported.

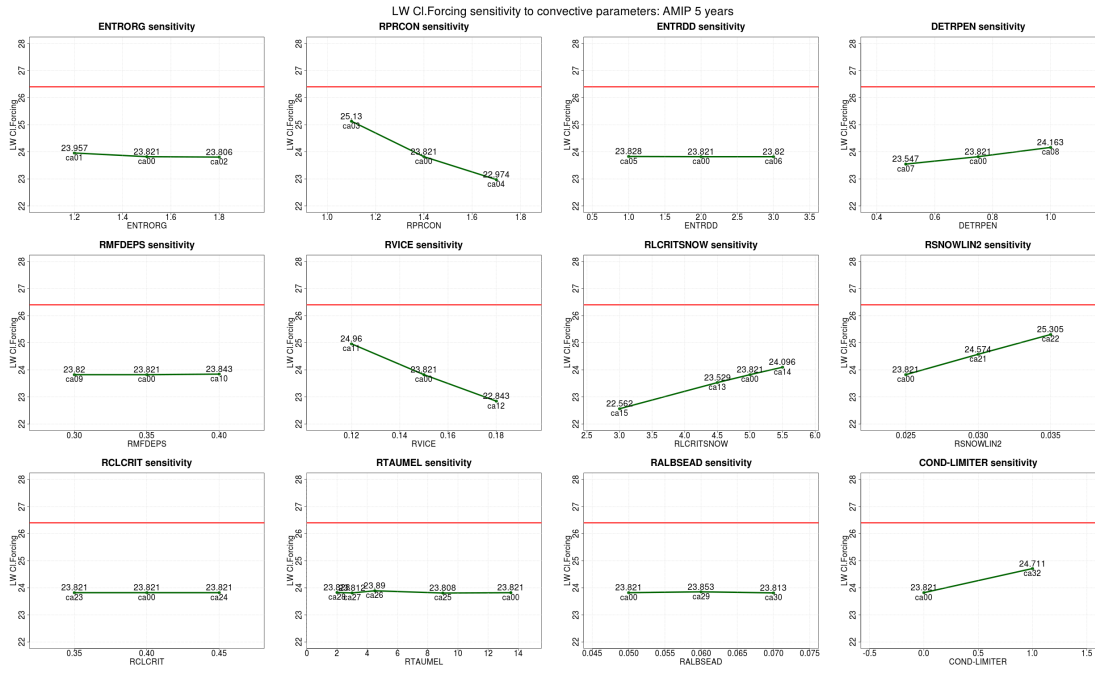Figure 2.12: Effect of different parameter combinations on Performance Indices of various fields. The *Partial PI* is the same as the *Total PI* of Table 2.2 but includes only atmospheric variables. For each configuration, parameters that have been modified are reported.

configurations lead to admissible values. In general, "Cy40-like" configurations provide very good results for the variable of interests, including TOA longwave and shortwave fluxes, SFC net energy flux and longwave c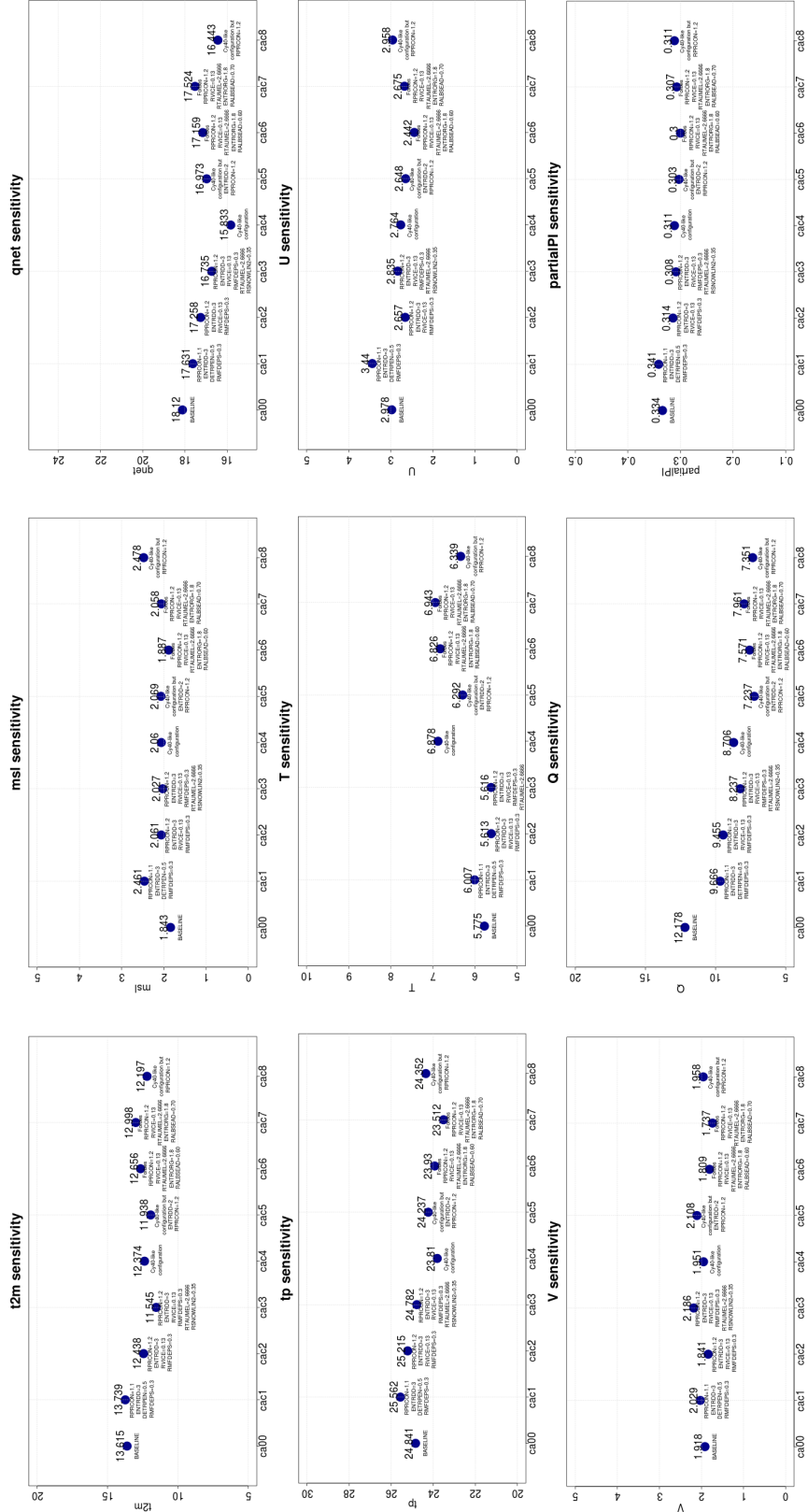loud radiative forcing. In particular, for what concerns the SFC net energy flux, a "Cy40-like" combination with reduced **RPRCON** (*cac8*) works best to achieve realistic current-day values. Interestingly, this simulation also shows an overall reduction of the PIs.

In conclusion of this analysis, the parameter configuration that accomplishes best the three main goals of this tuning activity has been identified in the "Cy40-like" combination with reduced **RPRCON** (*cac8*). However, these results hold true for the atmosphere-only model configuration. Thus, supplementary tuning will be likely needed to get optimal results once the model will be run in a coupled mode, in particular after the inclusion of the new version of the NEMO ocean model. In any case, the present analysis has allowed to identify the most efficient knobs to tune the variables of interest. The sensitivity of the considered knobs will hardly change, since they are all IFS parameters. For these reasons, it should be quite straightforward to apply these results to obtain rapidly a tuned atmosphere once the EC-Earth 3.2b, including the new ocean model, will be released.

A final consideration concerns the uncertainties that inevitably affect every tuning activity and constrain modellers to make choices on the basis of some assumptions. As an example, probably the most interesting feature emerging from Figs. 2.11 and 2.12 is that similar improvements can be achieved with different parameter configurations, and there is no obvious evidence of what is the best choice. In this case, a particular simulation (*cac8*) has been chosen because of its particularly good fit with the target value of the SFC net energy flux, but there are other three simulations (*cac3*, *cac4* and *cac5*) showing acceptable values for all the 4 variables of interest, and similarly improved PIs. Also, if the tuning had focused on other key variables — for example excluding the SFC net energy flux, rather than including precipitation or others — the resulting best configuration would have likely been a different one. These results highlight the importance of identifying and prioritizing the tuning goals in advance, taking in considerations which are the features we care to improve the most, as highlighted by Mauritsen et al. (2012).

Chapter 3

The Equable Climate Problem

3.1 Introduction

In one sentence, equable climates are defined as periods of roughly equal temperatures throughout the Earth. In particular, they are characterized by reduced temperature difference between the equator and the poles — i.e. polar temperatures much closer to equatorial ones than in present day climatic conditions — and low seasonality — i.e. only small temperature variations between the cold and the warm season.

Despite such homogeneous conditions are much different from the present climate, equable climates have been a recurrent feature during the past history of the Earth (Caballero and Lynch, 2011; Royer et al., 2004). Evidences of equable climate conditions span through the Mesozoic and the early Cenozoic eras (from about 250 Ma to 34 Ma). Most of the evidences refer to the most recent part of this long time span, corresponding to the late Cretaceous (about 100 to 65 Ma) and the early Paleogene (65 to 34 Ma) period. During that time the Earth was globally warmer than present, but polar regions were much warmer while tropical temperatures were only slightly higher than they are today (e.g. Greenwood and Wing, 1995; Zachos et al., 2001). The warmest period of the last 65 Ma was the Early Eocene (about 56 to 48 Ma), which is of particular interest also because it is relatively recent, and as such it is characterized by higher availability of paleontological data with respect to previous periods. The global average temperature during the equable climate of the Early Eocene was about 10 K higher than today and the meridional temperature gradient was deeply reduced. While tropical temperatures were only few degrees higher, high-latitude temperatures were up to 30 K higher than present (e.g. Wing and Greenwood, 1993; Sluijs et al., 2006; Huber and Caballero, 2011), polar ice sheets disappeared (Zachos et al., 1994) and the existence of frost-intolerant flora and fauna at high latitudes indicates winter temperatures above freezing also over continental areas during the polar night (Greenwood and Wing, 1995; Spicer and Parrish, 1990; Hutchison, 1982).

Among the other striking evidences, ancient crocodilians, relatives to present-day crocodiles and alligators, lived in Arctic islands close to Greenland, at paleolatitudes far to the north of the Arctic polar circle (Markwick, 2007; Eberle et al., 2014).

Paleoclimate reconstructions of equable climates of the late Cretaceous and the Eocene are based on proxy data — i.e. preserved physical characteristics of the environment that can stand in for direct measurements — including terrestrial flora and fauna as well as maritime fossils. While there is an increasing effort in studying and understanding proxies within the paleoclimate community, large uncertainties still persist in proxy interpretations. Source of uncertainties include the need to calibrate proxy data for environmental conditions far beyond modern values, issues related to proxy dating and paleolocation (including paleoelevation), undersampling of large regions including the coldest (such as Antarctica, Siberia and north-eastern North America) as well as the warmest (tropical land masses between 30°S and 30°N) climatic end-member, preferential temporal sampling (e.g. clipping seasonal or orbital scale cycles) and others (see for example Huber and Caballero, 2011, and references therein).

Given the number of issues affecting proxy data, climate models potentially represent a promising tool to better understand past climates and constrain uncertainties of paleoclimatic reconstructions. Moreover, application of climate models to paleoclimates provides a particularly stringent test of model robustness and reliability, with implications for future climate projections. While the quantitative assessment of future climate change relies very heavily on global climate models, the latter are normally tested over the only time period for which extensive instrumental records of climate are available, that is the recent past (typically the last 100 years). However, climate variations occurred over this period are small relative to the variations predicted for the next 100 years (see for example IPCC AR5), and as such they likely provide only a weak constraint on future projections. Paleoclimates offer the opportunity to test climate models under climatic conditions that are very different from the present ones (see for example Caballero and Lynch, 2011). In particular, Lunt et al. (2012) argued that the Early Eocene is likely the time period showing the most similarities to the projected climate for the end of the 21st century, because of its warmer temperatures associated with higher-than-present greenhouse gas concentrations. It is known that CO_2 concentrations where higher during the Early Eocene (e.g. Pearson and Palmer, 2000; Pagani et al., 2005; Fletcher et al., 2008; Doria et al., 2011). Although data are relatively sparse and a wide uncertainty range exists, recent atmospheric CO_2 reconstructions indicate reasonable values up to about 2000 ppm (Beerling and Royer, 2011), to be compared against a present-day value of about 390 ppm in 2010 (Value from the Scripps CO_2 program, `http://scrippsco2.ucsd.edu/`).

Previous modelling studies of past warm equable climates, such as the Early Eocene, have consistently failed in reproducing the warm temperatures of high

latitudes and in particular the above freezing winter temperatures over continental interiors. A number of hypotheses have been advanced in order to explain the model-data discrepancies, including: increased oceanic and/or atmospheric poleward heat transport (Covey and Barron, 1988; Sloan et al., 1995; Caballero and Langen, 2005), polar stratospheric clouds (Sloan and Pollard, 1998; Kirk-Davidoff et al., 2002), high-latitude convective clouds (Abbot et al., 2009b), altered vegetation (Sewall et al., 2000; Shellito and Sloan, 2006), altered topography and ocean gateways (Sewall et al., 2000), higher model resolution (Sewall and Sloan, 2006), different sea surface temperature distributions (Sloan et al., 2001; Sewall and Sloan, 2004), large lakes (Sloan, 1994; Morrill et al., 2001), altered orbital parameters (Lawrence et al., 2003; Sewall and Sloan, 2004) and higher CO_2 concentrations (Huber and Caballero, 2011). However, none of these studies succeeded in reproducing above freezing winter temperatures over continental interiors, unless imposing unrealistically high CO_2 concentrations, far beyond the upper limit of the range of acceptable values (Huber and Caballero, 2011). Despite all efforts, warm high-latitude annual mean and above freezing winter temperatures remain one of the great unsolved problems in paleoclimate, an issue that is referred to as the "equable climate problem" (Sloan and Barron, 1990; Huber and Caballero, 2011).

In the present study the EC-Earth Earth System Model is used to investigate the equable climate problem. Details on the simulation setup are given in section 3.2. The model ability in reproducing equable climate conditions with appropriate boundary conditions is tested in section 3.3. Results show that EC-Earth is at least as reliable as other models that have been used for equable climate simulations, but nonetheless still fails in reproducing above freezing winter temperatures over continental interiors. Thus, in sections 3.4 and 3.5 hypotheses are explored trying to get closer to the solution of the equable climate problem. Final considerations are discussed in section 3.6.

3.2 Simulation setup

Rather than targeting a specific time period of the past were equable climate conditions occurred (such as the late Cretaceous or the Early Eocene), the aim here is to simulate equable climate conditions on the Earth with present-day geography and topography. While a detailed geography may be crucial to accurately reproduce regional features of a particular period, evidences of past equable climates span a variety of geographical configurations, and it is reasonable to assume that geography itself is not a limiting factor for the occurrence of equable climate conditions (e.g. Bice et al., 2000). Similar considerations can be done for orbital parameters (Huber and Caballero, 2011). The atmospheric CO_2 concentration is raised up to 1680 ppm (i.e. 6 times its preindustrial value), a reasonable value according to Early Eocene CO_2 reconstructions. Even if this value is much higher
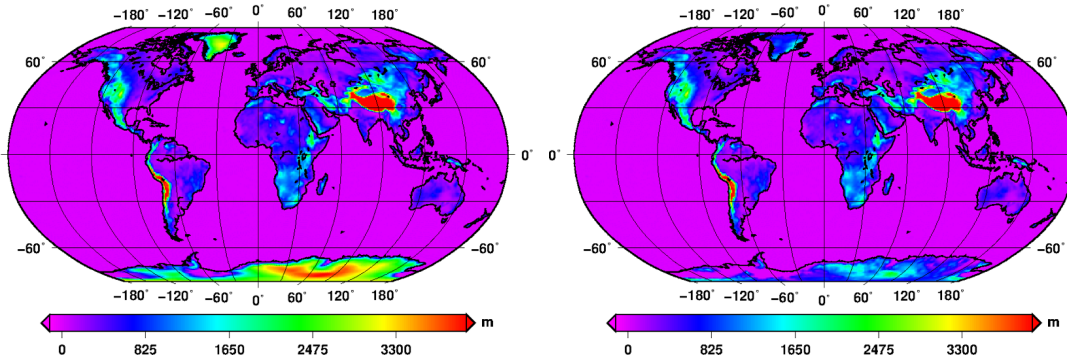
Figure 3.1: Left: original EC-Earth topography. Right: modified topography used in equable climate simulations.

than the present-day concentration (about 390 ppm in 2010), it is not beyond the realm of possibility for the Earth's future: projections of atmospheric CO_2 concentration do not exclude values as high 1000 ppm by the end of the 21st century (see for example the extreme RCP8.5 emission scenario, Riahi et al., 2011, and section 1.4 of the present work), and known fossil fuel reserves ensure that humanity can increase the CO_2 concentration to 2000 ppm over the next 100–200 years with just a little sprint in fuel consumption (Archer and Brovkin, 2008). In other words, the equable climate experiments discussed below can be also interpreted as follows: "What if humans burn all fossil fuel on Earth and then extinguish (i.e. stop to interact with the climate system)?"

The simulations are performed with the Earth System Model EC-Earth V3 (see section 1.3 for a description of the model). The EC-Earth 3.1 version is used, which has been released after the tuning activity described in section 2.2. The model is run at atmospheric horizontal resolution of T255, corresponding to a grid spacing of about 0.7°, and with 91 vertical levels. Ocean has approximately 1° horizontal resolution and 46 vertical levels.

As anticipated, the equable climate experiments run with EC-Earth aim at simulating equable climate conditions on the Earth with present-day geography. To this purpose, three changes in the model boundary conditions are applied with respect to the standard EC-Earth setup, regarding atmospheric composition, land ice and vegetation. These changes are described here below.

- Atmospheric composition. Atmospheric CO_2 is raised up to 1680 ppm (i.e. 6 times the preindustrial value). This value is in the range of the estimations of CO_2 concentration occurred during past equable climates, and in particular during the Early Eocene (e.g. Beerling and Royer, 2011). All other greenhouse gases and aerosols are set to their preindustrial values (CMIP5 year 1850).

- Land ice. Since EC-Earth has no dynamical representation of continental
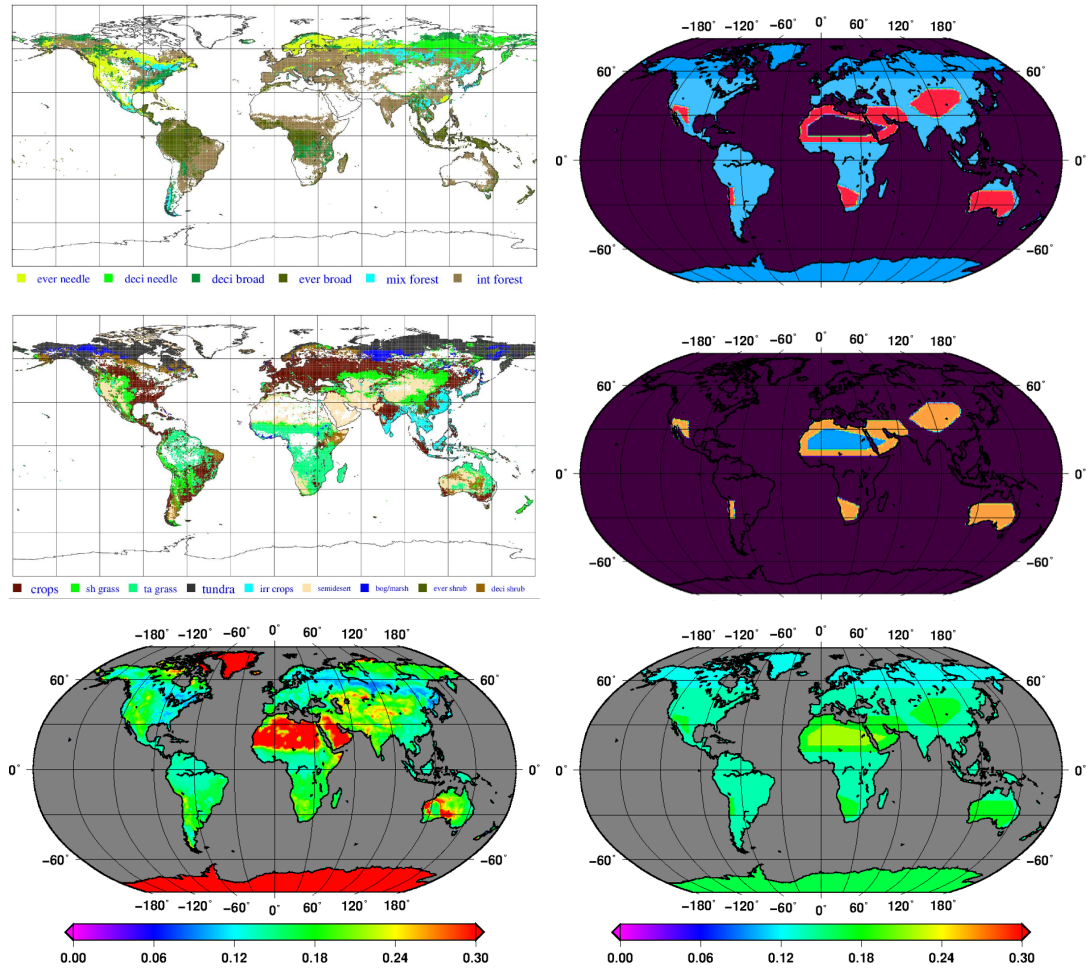
Figure 3.2: High vegetation types (top), low vegetation types (middle) and July surface albedo (bottom) from the EC-Earth original boundary conditions (left) and the modified boundary conditions used in equable climate experiments (right). High vegetation types used in equable climate experiments (top-right panel) are deciduous broadleaf trees (dark blue), evergreen broadleaf trees (light blue), interrupted forest (red), while purple indicates no high vegetation. Low vegetation types used in equable climate experiments (middle-right panel) are high grass (yellow), low grass (blue) while purple indicates no low vegetation.

ice, the land ice has to be removed manually. In the standard configuration, EC-Earth has fixed amount of land ice over Greenland and Antarctica integrated within the orography boundary condition. All the land ice from both Greenland and Antarctica is removed by taking into account the isostatic rebound (assuming that the bedrock is in equilibrium). To do this, I have considered the ice-surface topography and the bedrock topography of the ETOPO1 dataset, interpolated on the EC-Earth grid, taken from the NOAA web site (`http://www.ngdc.noaa.gov/mgg/global/global.html`). The ice-surface topography includes land ice, while the bedrock does not. The thickness of the ice is estimated as the difference between the ice-surface and the bedrock. The isostatic rebound $[\Delta h]$ is computed as the product between ice thickness $[h(ice)]$ and the ratio of the average densities of ice and Earth's mantle $[rho(ice)/rho(mantle)]$:

$$\Delta h = h(ice) * rho(ice)/rho(mantle),$$

where I set rho(ice)=0.91 Mg m^{-3} and rho(mantle)=3.37 Mg m^{-3} (Letreguilly et al., 1991). The ice-free, unloaded bedrock after isostatic rebound is then obtained as the sum of the bedrock and the isostatic rebound Δh. Over Greenland and Antarctica the original topography is replaced with the ice-free, unloaded bedrock computed as described above. In all the other regions, the standard EC-Earth topography is used. This modified topography used in equable climate simulations is shown in Fig. 3.1 together with the standard EC-Earth topography.

- Vegetation. Vegetation boundary conditions are modified according to the reconstructions of plausible vegetation during equable climate conditions. As a reference, the global vegetation distribution for the Early Eocene introduced by Sewall et al. (2000) is considered. Since present-day Earth geography and topography show significant differences from the ones of the Early Eocene, the direct implementation of Sewall's vegetation in the equable climate experiments presented here is impossible. Thus, a new global vegetation distribution has been produced, which is inspired by Sewall et al. (2000) but rearranged to take these differences into account. The new vegetation distribution consists of four different ecosystems, each one characterized by a low and a high vegetation type: deciduous broadleaf forest (100% coverage of deciduous broadleaf trees, no low vegetation), evergreen broadleaf forest (100% of evergreen broadleaf trees, no low vegetation), savanna (60% of tall grass and 40% of interrupted forest) and grassland (100% of low grass, no high vegetation). The spatial distribution of high and low vegetation types used in the equable climate experiments is shown in Fig. 3.2 (top and middle panels), together with the original high and low vegetation distributions from the standard EC-Earth boundary conditions. In addition to high and

low vegetation types, the model also requires boundary conditions for the Leaf Area Index (LAI). For each vegetation type, the LAI is computed as the average LAI corresponding to that vegetation type in the original EC-Earth boundary condition file. For deciduous broadleaf trees, the average LAI is computed monthly to preserve the annual cycle. For all the other vegetation types (evergreen broadleaf trees, interrupted forest, tall and low grass) the average LAI is computed from the annual mean and there is not an annual cycle. Since also the surface albedo is read as a boundary condition (the model does not compute it dynamically), it has to be changed in agreement with the new vegetation. As for the LAI, the albedo of each vegetation type is computed as the average albedo associated with that vegetation type in the original EC-Earth boundary conditions. Consistently with the LAI computation, average albedo is computed from monthly fields over deciduous broadleaf forest and from the annual mean in all the other cases. The surface albedo fields for July from the original and the modified boundary conditions are shown in the bottom panels of Fig. 3.2.

A **standard equable climate simulation** (*leqf*) has been run including the aforementioned three changes and no other changes. Other equable climate simulations including additional modifications are introduced and discussed in section 3.4. To compare the results of the equable climate experiments run with EC-Earth, additional simulations have been performed, including a preindustrial simulation, a present-day simulation, a 6xCO$_2$ simulation and a preindustrial simulation with Eocene-like vegetation. The **preindustrial simulation** (*tome*) uses preindustrial (CMIP5 year 1850) concentration of GHG gases and aerosols. All the other boundary conditions (e.g. land ice, vegetation, etc.) are the standard EC-Earth boundary conditions, distributed by the EC-Earth community. The **present-day simulation** (*tomc*) uses present day (CMIP5 year 2000) concentration of GHG gases and aerosols. As for the preindustrial simulation, all the other boundary conditions are standard. The other two experiments are "intermediate" simulations between the equable climate and the preindustrial one, aiming to isolate the effect of individual changes in the boundary conditions applied in the equable climate experiments. The **6xCO$_2$ simulation** (*leq2*) is identical to the preindustrial one, but with atmospheric CO$_2$ concentration set to 1680 ppm as in the equable climate experiments. The **preindustrial simulation with Eocene-like vegetation** (*leqp*) is identical to the preindustrial simulation, but with the modified vegetation distribution (and associated albedo) used in the equable climate experiments.

The simulation time required to reach the equilibrium when the atmospheric CO$_2$ concentration is raised up to 1680 ppm from present day — as well as from preindustrial — conditions can be quite long, due to the long time scales of the deep ocean. Previous studies that simulated the climate during the Early Eocene needed from hundreds to thousands of coupled simulation years to reach the equilibrium

(Lunt et al., 2012). To reduce computational cost, I have taken advantage of previous simulations performed with EC-Earth to estimate the average warming of the deep ocean (below 1000 m depth) when atmospheric CO_2 is set to 1680 ppm. Three different runs have been considered — a preindustrial simulation (CO_2 at 280 ppm), a present-day simulation (CO_2 at 368 ppm) and a simulation with doubled CO2 with respect to present — and the dependence of deep ocean temperature to the change in the CO_2 concentration has been investigated. The temperature of the deep ocean corresponding to 1680 ppm has been estimated by applying a linear fit, finding roughly 3 K more than in the doubled CO_2 simulation. Finally, new initial conditions have been created, starting from the doubled CO_2 simulation and adding 3 K everywhere to the temperature three-dimensional field of the whole ocean. These new initial conditions have been used for the equable climate as well as for the 6xCO_2 simulations. These simulations have been then run for more than another 500 years to reach equilibrium.

If not stated differently in the text, the last 50 years of simulation from each experiment are considered. Seasonal averages are computed using the standard definition of the seasons for the Northern Hemisphere mid-latitudes: winter (December to February, DJF), spring (March to May, MAM), summer (June to August, JJA), and autumn (September to November, SON).

3.3   The EC-Earth standard equable climate simulation

In this section, results from the standard equable climate simulation — characterized by present-day geography, 1680 ppm CO_2 concentration, no land ice and equable-like vegetation — are presented and compared against the preindustrial simulation, the present-day simulation, the 6xCO_2 simulation and the preindustrial simulation with Eocene-like vegetation. First, the surface temperature distribution is discussed. Then, the reasons for the observed temperature changes are investigated, considering possible mechanisms suggested by the previous literature.

3.3.1   Meridional temperature gradient and seasonality in the EC-Earth equable climate

In general, the standard equable climate simulation (*leqf*) shows a much more equable climate than all the other simulations considered here. The global annual mean temperature is about 10 K higher than in the present-day simulation (*tomc*) and 12.3 K higher than in preindustrial one (*tome*), in absolute agreement with proxy data for global mean temperature during the Early Eocene. The warming is stronger at high latitudes (see Figs. 3.3 and 3.4): the equator-to-north-pole temperature difference is reduced to 26.6 K in *leqf*, while it is 46.4 K in *tome* and 42.4 K in *tomc* based on an annual mean.

tomc tas ANN

leqf tas ANN

leqf–tomc tas ANN
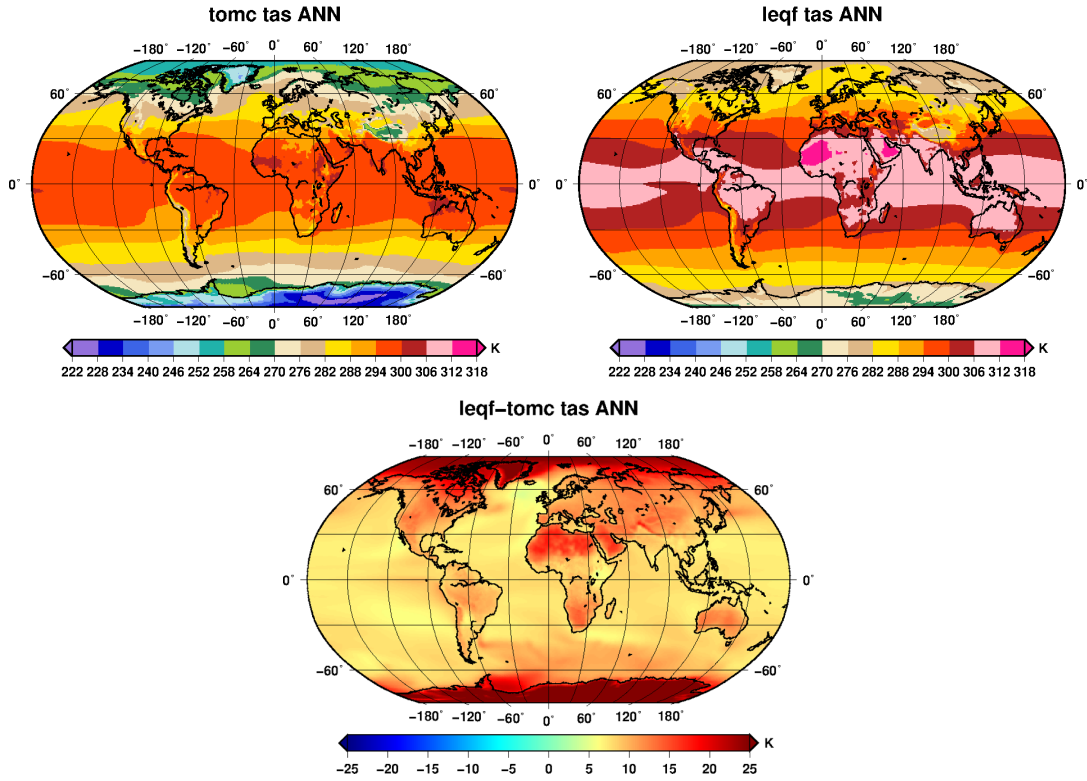
Figure 3.3: Annual mean surface air temperature from the present-day simulation *tomc* (top-left), the equable climate simulation *leqf* (top-right) and the difference between *leqf* and *tomc* (bottom).

tas

DJF

MAM

JJA

SON

Figure 3.4: Zonally averaged surface air temperature from the equable climate simulation *leqf* (blue), the 6xCO$_2$ simulation *leq2* (green) and the preindustrial simulation *tome* (red). Shown is the annual mean (left) and the seasonal means (right).

leqf tas DJF

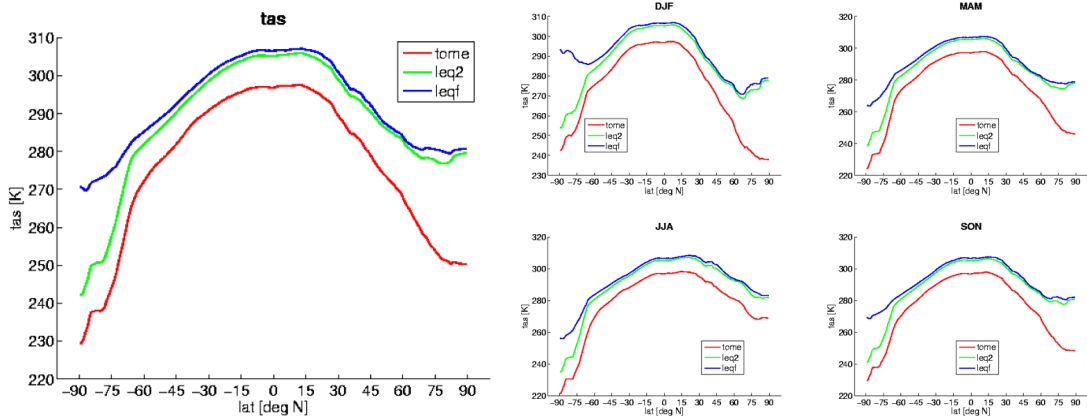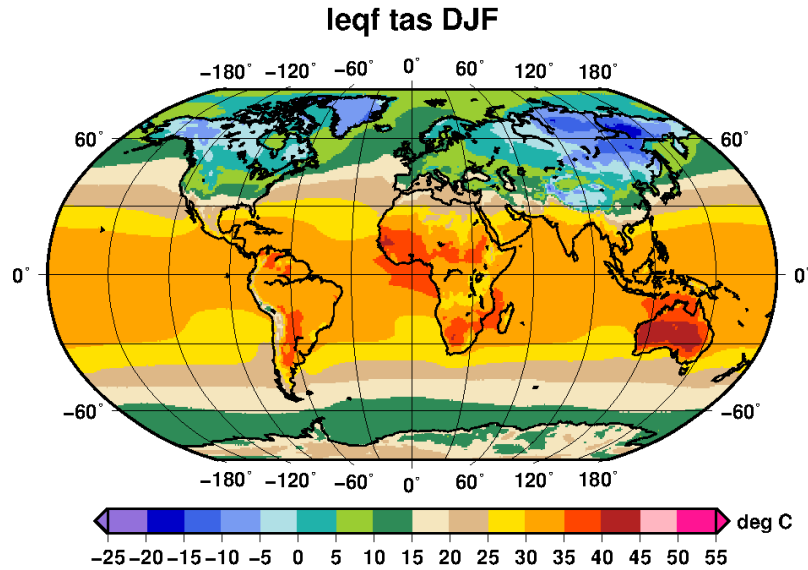Figure 3.5: Climatology of surface air temperature during the NH winter (DJF) from the equable climate simulation *leqf*.

Right panels of Fig. 3.4 show that the stronger warming of high latitudes is more evident during DJF both in the Northern Hemisphere (NH) and in the Southern Hemispheres (SH). In the SH the extra warming of high latitudes is likely due to the removal of the Antarctica ice sheets, resulting in lower albedo and lower elevations. This is confirmed by the fact that the $6xCO_2$ simulation with original land ice and vegetation boundary conditions (*leq2*) does not show this dramatic warming in the SH during any season (Fig. 3.4). Both the changes in albedo and elevation potentially contribute to the higher temperatures. The change in elevation is expected to contribute roughly equally during all the seasons, while the change in albedo is more relevant during the polar day. From these considerations, the dramatic warming of the southern pole in DJF (i.e. during the SH summer) has to be attributed to the changes in albedo. The situation in the NH is greatly different from the one in the SH. In the NH the strongest warming of high latitudes occurs during the polar night, suggesting that the albedo changes are not the leading mechanism here. In this hemisphere, the temperature profiles of *leq2* and *leqf* are only slightly different, with the second experiment being one or two degrees warmer than the first one. A somewhat higher difference occurs around 75°N, where Greenland is located, but also here the difference between *leqf* and *leq2* in terms of meridional profiles is very limited (below 4K). Over Greenland the same considerations made for the Antarctic do apply. However, the smaller geographical extent of Greenland results into a very limited effect on the zonally averaged temperature profiles.

It is interesting to compare the EC-Earth standard equable climate simula-
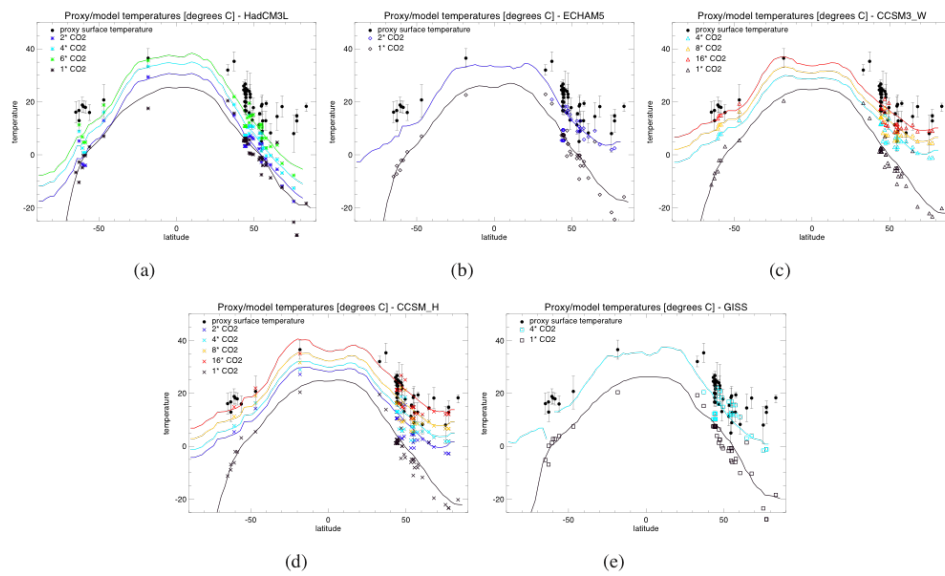
Figure 3.6: Zonally averaged surface air temperatures from model simulations of the Early Eocene available from literature. Models are HadCM3L (a), ECHAM5 (b), two versions of the CCSM3 model (c and d) and GISS (e). Proxy-derived temperatures are also reported (black dots with error bars). For the model results, the continuous lines represent the zonal mean, and the symbols represent the modelled temperature at the same location (longitude, latitude) as the proxy data. Figure 7 from Lunt et al. (2012).

tion *leqf* with previous simulations of equable climates, and in particular of the Early Eocene. By doing this, it is worth to remind that we are using current topography while Eocene simulations presented in literature used Eocene topography reconstructions. For this reason, a point-by-point comparison cannot be done. However, it is reasonable to assume that the different topography can influence only marginally the results, and a comparison can be done in terms of meridional gradient as well as large scale features. Like previous simulations of equable climates made with other climate models, also *leqf* fails to reproduce warm winter temperatures (i.e. above the freezing point of water) over the continental interiors at high latitudes (see Fig. 3.5). However, the comparison of zonally averaged annual mean surface air temperature in the NH shows that *leqf* is one of the simulations performing the lowest equator-to-pole temperature difference (CO_2 concentration being equal, compare Figs. 3.4 and 3.6). It approximately behaves like the CCSM3 model at 8x CO_2 concentration. This is very good result since (1) CCSM3 is the best model among EoMIP models in reproducing equable climate conditions (see Lunt et al., 2012), and (2) EC-Earth is run with 6x CO_2 concentration (i.e. lower than 8x). Vice versa, *leqf* seems to have more problems in reproducing the weakening of the temperature gradient in the SH: while other Eocene simulations show an almost symmetric situation in the two hemispheres, the equator-to-pole temperature difference in *leqf* is about 10 K higher in the SH, and the annual mean temperature is below the freezing point over the south pole. The reason for the differences between *leqf* and the other Eocene simulations could lie in the different geography. During the Eocene the Drake Passage was still closed and by consequence oceanic meridional heat transport in the SH was higher (e.g. Livermore et al., 2005). Since *leqf* has modern topography, it cannot include this effect. Moreover, Bice et al. (2000) suggested Eocene geography should not only increase the oceanic transport in the SH (closed Drake Passage) but also decrease it in the Northern one with respect to the present, while it should not affect atmospheric transport directly. If true, these impacts of geography on oceanic heat transport could explain why *leqf* is so good in the NH but not in the SH.

A last consideration should be spent about seasonality. It has been anticipated that the stronger high-latitude warming in *leqf* occurs during DJF in both hemispheres. In the NH, this implies a reduction of the temperature seasonal cycle, in line with both porxy data evidences and previous modelling studies. In the SH, conversely, this implies an amplification of the seasonal cycle. While this result sounds somehow unexpected, and even in contradiction to the definition of equable climates, it is important to note that (1) also previous modelling studies do not show an evident reduction of the high-latitude temperature annual cycle in the SH (see for example Huber and Caballero, 2011) and (2) most of the evidences from high-latitude proxy records are limited to the NH. Finally, the different configuration of the Drake Passage can also have an influence on the annual cycle of SH high-latitude temperatures (and not just on the annual mean), possibly explaining
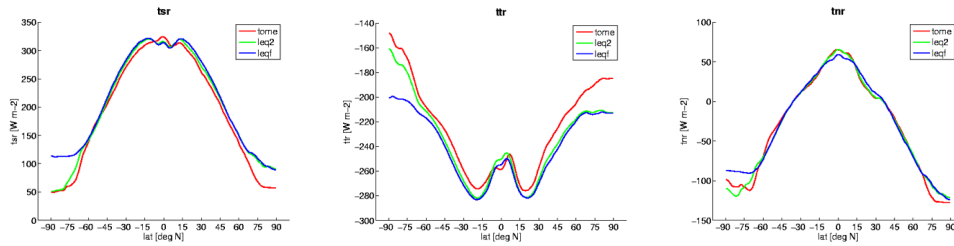
Figure 3.7: Zonally averaged TOA net shortwave radiation (TSR, left), TOA net long-wave radiation (TTR, middle) and TOA net radiative flux (TNR=TSR+TTR, right) from the equable climate simulation *leqf* (blue), the $6xCO_2$ simulation *leq2* (green) and the preindustrial simulation *tome* (red). Shown is the annual mean.

the rest of this unexpected behavior.

3.3.2   Energy balance and meridional energy transport

To investigate the active mechanisms contributing to the amplification of the warming signal at high latitudes in the EC-Earth standard equable climate simulation, a good starting point is to consider the top-of-the-atmosphere (TOA) energy balance. Fig. 3.7 shows the net flux of TOA solar (i.e. shortwave) radiation (TSR), of TOA thermal (i.e. longwave) radiation (TTR) and of TOA net radiation (TNR=TSR+TTR). Positive values indicate a downward net flux. The net incoming solar radiation at TOA (TSR) shows an increase at high latitudes in the standard equable climate simulation, due to changes in surface albedo (i.e. lower albedo due to ice-free conditions). Obviously, this effect is more important during the polar summer, while it has no effect during the polar night when there is not incident solar radiation. The net outgoing thermal radiation (TTR) is also increased, particularly at high latitudes, because of the stronger warming occurring there. The seasonality of this signal follows the seasonality of the changes in temperature: since in both the hemispheres the strongest warming occurs in DJF, the same happens for the TTR. Note that in the SH the strongest increase of TSR and TTR occur in the same season because albedo is the leading mechanism determining the warming, while in the NH it is the opposite. On an annual basis, the combination of these changes in TSR and TTR gives a TOA net radiative flux (TNR) that is substantially unchanged in the standard equable climate simulation with respect to preindustrial one (there is just a small decrease of net incoming radiation at the equator and net outgoing radiation at poles). Interestingly, also the net energy flux at the surface (SNEF=SSR+STR+SLHF+SSHF) is almost unchanged between the two simulations (Fig. 3.8): at low latitudes, the change in STR is balanced by higher evaporation (SLHF) and lower incoming solar radiation over the Equator (SSR); at high latitudes, the higher SSR is mainly balanced by increased SLHF and decreased SSHF.
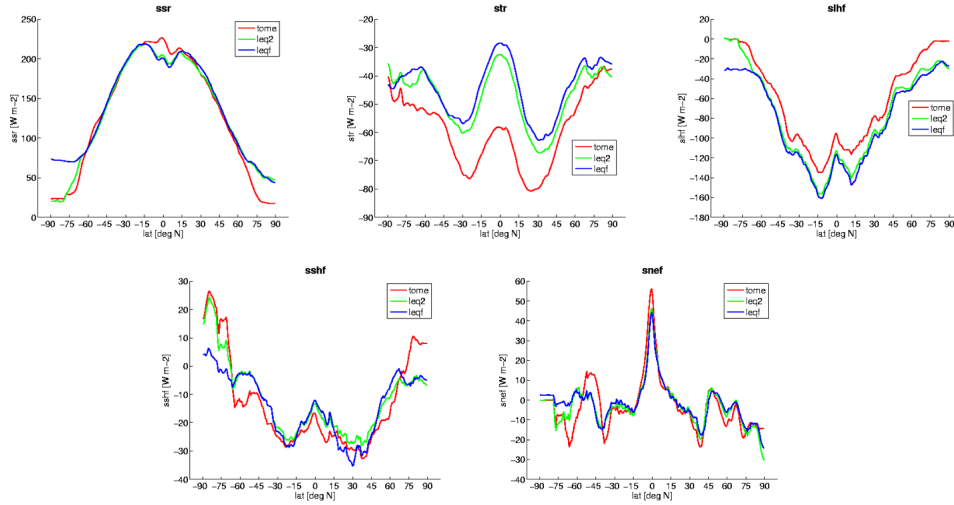
Figure 3.8: Zonally averaged SFC net shortwave radiation (SSR, top-left), SFC net longwave radiation (STR, top-middle), SFC latent heat flux (SLHF, top-right), SFC sensible heat flux (SSHF, bottom-left) and SFC net energy flux (SNEF=SSR+STR+SLHF+SSHF, bottom-right) from the equable climate simulation *leqf* (blue), the 6xCO$_2$ simulation *leq2* (green) and the preindustrial simulation *tome* (red). Shown is the annual mean.
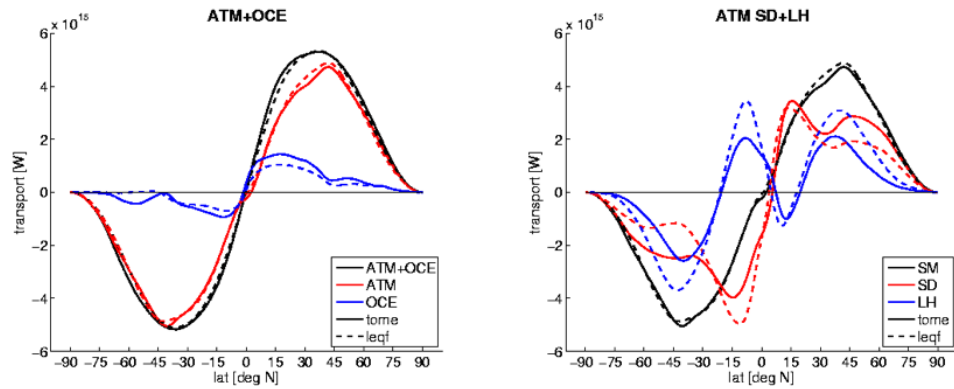
Figure 3.9: Left: Annual mean meridional energy transport by the atmosphere (red), the ocean (blue) and the total atmosphere+ocean system (black). Right: annual mean meridional energy transport in the atmosphere (black) and its subdivision into static dry (red) and latent heat (blue) components. In both figures the preindustrial simulation *tome* is indicated by continuous lines, the equable climate simulation *leqf* by dashed lines.

These results have important implications for the meridional energy transport. In equilibrium conditions, indeed, the annual mean meridional energy transport of the atmosphere and the oceans can be inferred from the energy fluxes at TOA and SFC (e.g. Zhang and Rossow, 1997): if the latitudinal dependence of the zonally averaged net energy fluxes does not change, also the overall meridional energy transport of both the oceans and the atmosphere will remain unchanged. Fig. 3.9 (left) shows the total meridional energy transport by the whole ocean+atmosphere system, and its partitioning into atmospheric and oceanic transport. As anticipated, the total poleward energy transport (ocean+atmosphere) is essentially equivalent in preindustrial *tome* and equable *leqf* experiments. Only minor changes occur in the partitioning of transport between ocean and atmosphere: in the NH the atmospheric transport is slightly increased and the oceanic slightly decreased in *leqf* with respect to *tome*; in the SH changes are less evident. It is interesting to divide the atmospheric meridional energy transport into its two main components: the dry static energy (sensible heat and potential energy) transport and the latent heat (water vapor) transport (right panel of Fig. 3.9). In the standard equable climate simulation, the latent heat (LH) transport is increased of about 1 PW in the mid-latitudes, while the static dry (SD) energy transport is reduced by the same amount. This is a significant change, since the order of magnitude of both LH and SH transport at these latitudes is between 2 and 3 PW in both hemispheres. The increase of LH is related to the increased atmospheric humidity due to higher temperatures. The decrease of the SD transport is a consequence of the weaker meridional temperature gradient, resulting in weaker mid-latitude eddies. Meridional transport in the tropics is almost unchanged in the NH, while changes of the order of 1 PW occur in the SH (higher poleward SD and equatorward LH transport), indicating a different response of the Hadley cells in the two hemispheres. Changes in the SH can be related to increased atmospheric humidity and higher Hadley cell, resulting in stronger LH and potential energy fluxes. These results are in general agreement with previous modelling studies, showing that higher temperatures and weaker meridional gradients result into stronger LH transport and weaker mid-latitude eddies respectively, the two effect compensating each other (e.g. Heinemann et al., 2009; Caballero and Langen, 2005; Frierson et al., 2007). For these reasons, meridional energy transport itself cannot be the leading mechanism producing the stronger warming of high-latitudes in the EC-Earth standard equable climate simulation.

3.3.3 Cloud radiative effect

Clouds, through they interactions with both longwave and shortwave radiation, have been often indicated as potential drivers for differential heating of high and low latitudes (e.g. Sloan et al., 1999; Abbot et al., 2009a). In Fig. 3.10 (top panels) the zonally averaged annual mean cloud cover is shown for both total
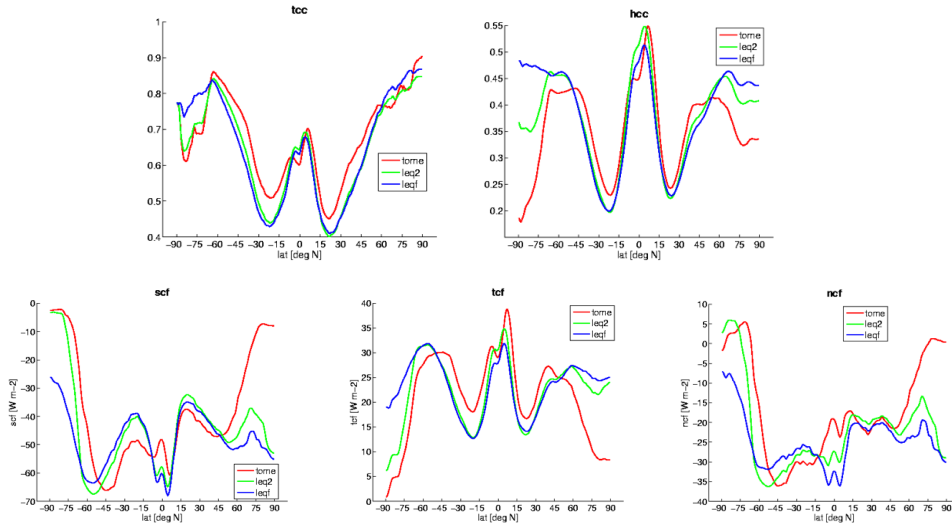
Figure 3.10: Top: Zonally averaged annual mean total cloud cover (left) and high cloud cover (right) expressed as fraction of covered area. Bottom: Zonally averaged annual mean cloud radiative forcing on solar radiation (left), thermal radiation (middle) and net (i.e. solar+thermal) radiation (right). The equable climate simulation *leqf* is shown in blue, the 6xCO$_2$ simulation *leq2* in green and the preindustrial simulation *tome* in red.
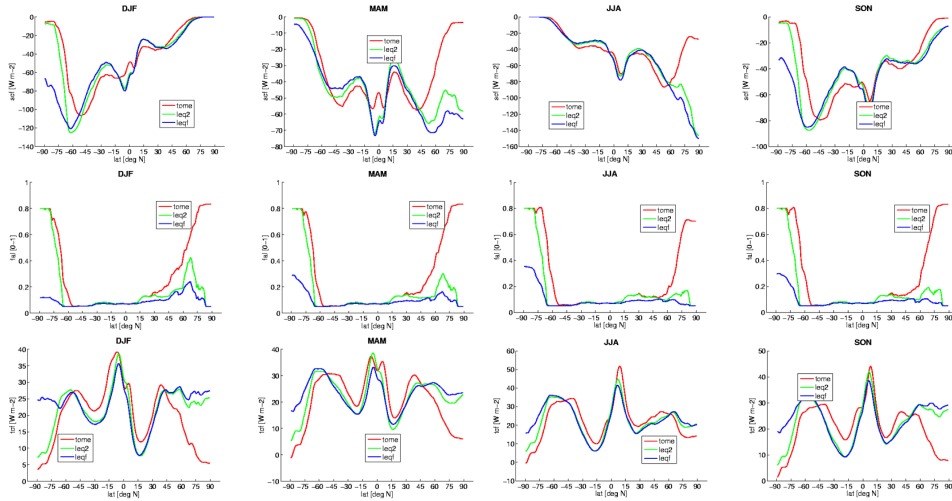
Figure 3.11: Zonally averaged solar cloud forcing (top), surface albedo (middle) and thermal cloud forcing (bottom) in the four seasons considered here from the equable climate simulation *leqf* (blue), the 6xCO$_2$ simulation *leq2* (green) and the preindustrial simulation *tome* (red).

clouds (including low, middle and high clouds) and high clouds only. While the total cloud cover does not show significant changes between the standard equable climate simulation and the preindustrial simulation, apart from an increase of about 0.1 over the southern pole, high cloud cover is significantly increased at high latitudes and becomes almost as high as over the equator (0.5) in the equable climate simulation *leqf*. This increase in high-latitude high cloud cover is stronger during winter in the NH, while it is almost equivalent throughout the year over the SH. This indicates a change in the type of clouds over polar regions and could potentially affect the effect of clouds on radiation.

The effect of clouds on radiation is measured by the cloud radiative forcing, computed as the difference between the net radiative flux at the top of the atmosphere in all-sky and clear-sky conditions. On an annual basis, the effect of clouds on both shortwave radiation (solar cloud forcing - SCF) and longwave radiation (thermal cloud forcing - TCF) is amplified at poles in the standard equable climate simulation (see Fig. 3.10, bottom panels). SCF is increased of more than 20 W m^{-2} to the south of 60°S and about 40 W m^{-2} to the north of 60°N (cooling effect). TCF is increased in both hemispheres by about 15-20 W m^{-2} (warming effect). The net result (net cloud forcing - NCF) is a stronger cooling effect of clouds of about 10 W m^{-2} over the South and 25 W m^{-2} over the North Pole in *leqf* with respect to *tome*. Nevertheless, there are important seasonal changes in the cloud radiative forcing.

Since the shortwave radiation over poles is present only in summer, changes in SCF between *leqf* and *tome* affect only this season (Fig. 3.11, top panels). The change is of about 60 W m^{-2} in the SH and more than 100 W m^{-2} in the NH during DJF and JJA respectively. This indicates an increased reflecting power of clouds. However, the absolute values of the change in SCF are so high also because there is a strong difference of surface albedo between *leqf* and *tome* (see Fig. 3.11, middle panels): in *leqf* there is no ice (both over land and sea) and albedo is dramatically lower than in *tome*, where Antarctica is covered by ice sheets and the Arctic Ocean by sea ice also in summer. SCF is computed as the difference between the TOA net shortwave radiation in all-sky and clear-sky conditions. Since clouds have a stronger effect on the net shortwave radiation at TOA when they occur over a dark surface — a white cloud over a white surface does not change the background reflectivity — the huge increase in the SCF absolute values reflects also the reduction of the surface albedo, and not only the actual increase of the reflecting power of clouds. Fig. 3.7 (left panel) shows that the net flux of TOA solar radiation is higher over the poles in *leqf* than in *tomc*, i.e. more solar energy is entering the Earth at these latitudes. Since the incident solar radiation is the same in the two simulations, this implies that less solar radiation is reflected by the total Earth system (atmosphere + surface) in *leqf*. In other words, the increased reflectivity of clouds (SCF - cooling effect) is overbalanced by the reduced reflectivity of the surface (lower albedo - warming effect).
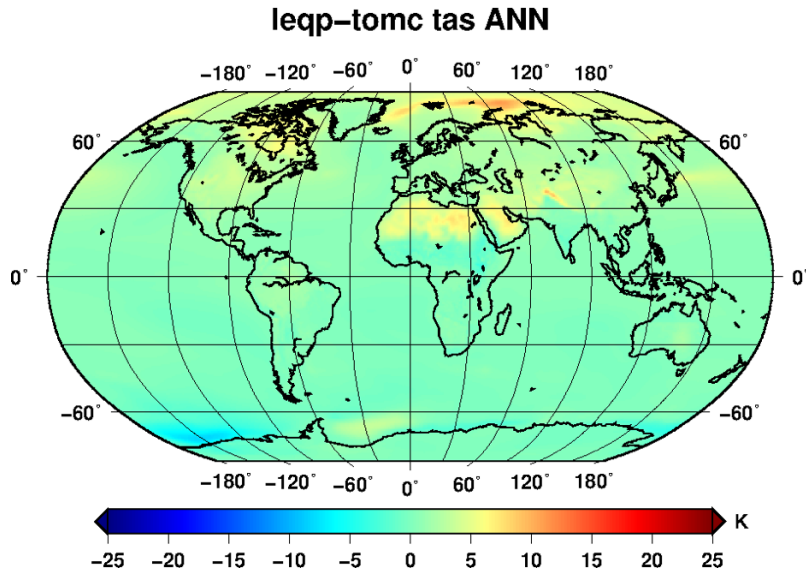
leqp–tomc tas ANN

Figure 3.12: Difference of annual mean surface air temperature between the preindustrial simulation with Eocene-like vegetation (*leqp*) and the preindustrial simulation with standard vegetation (*tomc*).

Vice versa, the NCF profile during winter is dominated by the TCF. TCF shows an increase of 20 W m^{-2} in the NH high-latitudes during DJF and of about 15 W m^{-2} in the SH high-latitudes during JJA (Fig. 3.11, bottom panels). This increase in cloud forcing can help in maintaining higher temperatures during the polar night (even if it is lower than the 50 W m^{-2} of cloud radiative forcing found by Abbot and Tziperman, 2008, using a single-column model). As discussed in section 3.3.5, this change in TCF corresponds to about 1/3 of the higher increase of greenhouse effect occurring at poles with respect to lower latitudes on an annual basis.

3.3.4   Effect of vegetation distribution on surface temperatures

The effect of the different vegetation distributions used in the preindustrial (as well as present-day) and in the standard equable climate simulations can be estimated by comparing the preindustrial simulation *tomc* and the preindustrial simulation with modified Eocene-like vegetation *leqp*. Note that both simulations have land ice over Greenland and Antarctica, and as such the vegetation changes discussed in this section do not include changes over these two regions (which are dominated by the removal of ice and the reduced orography, rather than the vegetation coverage). Results shown in Fig. 3.12 indicate that vegetation changes have no influence on the SH, which is mainly occupied by oceans. In the NH the vegetation change leads to a slight warming of about +1–2 K at latitudes below 50°N. Interestingly,
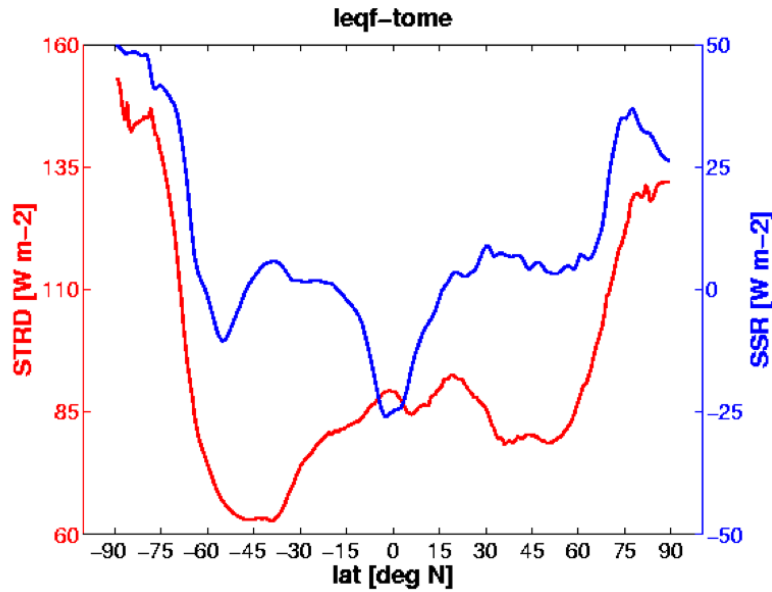
Figure 3.13: Change (i.e. difference) of zonally averaged downward thermal radiation at surface (STRD, red) and surface net solar radiation (SSR, blue) between the equable climate simulation *leqf* and the preindustrial simulation *tome*. Note that STRD and SSR have different y-axis.

to the north of 50°N the difference between *leqp* and *tomc* increases (up to +5 K at latitudes greater than 75°N), showing a sort of Arctic amplification. However, it is worth to note that the different vegetation distribution cannot explain the dramatic warming of NH high latitudes in the equable climate experiment *leqf*, since a comparable signal of Arctic amplification is found in the 6xCO$_2$ simulation *leqf* that uses the original EC-Earth vegetation (see section 3.3.1).

3.3.5 Who is warming the surface: thermal and solar radiation

It has been shown in the previous sections that both the meridional energy transport and the different vegetation distribution are unable to explain the strong warming of high latitudes in the standard equable climate simulation run with EC-Earth. Conversely, the observed changes of both thermal radiation (e.g. due to cloud radiative forcing) and solar radiation (e.g. due to ice-free conditions and associated lower albedo) favor equable climate conditions (warmer temperatures and a weaker equator-to-pole temperature gradient). Thermal radiation contributes through the greenhouse effect, while solar radiation through changes in albedo. Here these two contributions are investigated, with the goal of understanding which effect is more important in determining the observed change in surface temperatures. To this aim, the variables of interest are the amounts of ther-

mal and solar radiation entering the surface, thus warming it. If we assume that all the thermal radiation reaching the surface is absorbed, thus the best measure for thermal radiation is the surface thermal radiation downward (STRD), representing the amount of thermal radiation reflected back by the Earth's atmosphere (i.e. the greenhouse effect). Vice versa, not all the surface solar radiation downward (SSRD) enters the surface, because a fraction of it is reflected back by the Earth's surface. The fraction of solar radiation entering the surface is $(1-albedo)*SSRD$. This corresponds to the definition of the SFC net solar radiation (SSR), which is taken now as the appropriate measure of the solar radiation warming the surface.

  Fig. 3.13 shows the change of STRD and SSR (zonally averaged) between the standard equable climate simulation and the preindustrial simulation. From this figure, it becomes clear that:

1. STRD changes (green house effect) strongly contribute to the overall warming, since its global mean change is of $+84$ W m^{-2}. Vice versa, SSR changes (surface+cloud albedo) do not contribute (the global mean SSR is of $+1$ W m^{-2}). The almost null contribution of shortwave radiation to the global mean warming could be surprising, since we know that surface albedo has been strongly decreased in *leqf*. However, there is an increase in cloud reflectivity that globally balances the warming effect of changed surface albedo: the net effect of solar radiation changes is to cool the equator and to warm the poles.

2. Both SSRD and SSR changes contribute to reduce the equator-to-pole temperature difference of a similar amount (the change in both cases is about 50–60 W m^{-2} higher at high latitudes than at low ones), even if they have strongly different meridional profiles. The solar contribution is due to the higher surface albedo at high latitudes and the higher cooling effect of clouds over the Equator. The attribution of the thermal radiation contribution to the reduced meridional temperature gradient — i.e. the amplification of the increase in the greenhouse effect at high latitudes — is more challenging. In section 3.3.3 it has been mentioned that thermal cloud forcing is increased of about 15–20 W m^{-2} at high latitudes, thus contributing approximately to about 1/3 of the stronger increase of STRD at high latitudes. Other possible explanations may include changes in atmospheric water vapour (see for example Ruckstuhl et al., 2007), different CO_2 loads and temperature feedbacks. Finally, it is important to stress that solar radiation effects act only during the polar summer. Thus, the importance of the thermal radiation mechanisms resides also in the fact that they are active also (if not mainly) during the polar night.

3.4   Tropical Low Cloud Feedback

Tropical low clouds (TLCs) — and in particular marine stratocumulus clouds that are prominent over subtropical eastern oceans — play a crucial role in the Earth's energy balance through their reflection of high amounts of solar radiation (cooling effect, Hartmann et al., 1992; Klein and Hartmann, 1993; Rozendaal et al., 1995; Chen et al., 2000; Wood, 2012). Temporal variability of TLCs is related to the underlying surface temperature. TLCs decrease when the surface warms, resulting in less shortwave reflection and hence a further warming of the surface (positive feedback, see Clement et al., 2009; Eitzen et al., 2011; Zhou et al., 2013; Bellomo et al., 2014; Qu et al., 2015). This amplifying effect is hereafter referred to as tropical low cloud feedback (TLC feedback).

   As for many cloud-related processes, TLC variability is poorly represented by climate models (Soden and Vecchi, 2011; Zelinka et al., 2012; Webb et al., 2013; Qu et al., 2014), which generally tend to underestimate the associated TLC feedback with respect to observations (i.e. underestimate the sensitivity of TLCs to temperature changes, see Bony and Dufresne, 2005; Brient and Schneider, 2016). Differences in the representation of the TLC feedback among climate models have been proved to account for more than half of the spread in equilibrium climate sensitivity, i.e. the equilibrium average surface warming after doubling CO_2 concentrations (Vial et al., 2013; Brient and Schneider, 2016). In particular, if models underestimate the TLC feedback, they will also underestimate the increase in temperatures due to higher CO_2 concentrations. This can have significant implications for simulations of warm equable climates, in which atmospheric CO_2 concentrations and surface temperatures are so high that TLCs should likely disappear. Also, the strong dependence of model equilibrium climate sensitivity — which accounts for global temperatures and not only for tropical ones — on the strength of the TLC feedback suggests that model problems in simulating TLCs may potentially affect not only tropics but also the mid-to-high latitudes.

   Here I test the hypothesis that a stronger TLC feedback — i.e. a higher sensitivity of TLCs to temperature changes — may lead to high-latitude warming in equable climate simulations run with EC-Earth. To simulate the effect of a stronger TLC feedback in a warmer climate, a set of simulations have been run in which the TLC cover seen by the radiative scheme is artificially reduced. Reduction is obtained by multiplying by a factor $LBDA$ ($0 < LBDA < 1$) the cloud fraction and water content of TLCs. TLCs are defined as clouds occurring at latitudes between 30°S and 30°N at atmospheric levels below model hybrid level 76 — corresponding to pressure levels $p > 800$ hPa when surface pressure is of 1000 hPa (see Appendix A). Results from three experiments are discussed in the following. The three experiments are:

- **Standard equable climate simulation** (*lec1*): the setup is identical to the *leqf* experiment discussed in sections 3.2 and 3.3 (1680 ppm atmospheric
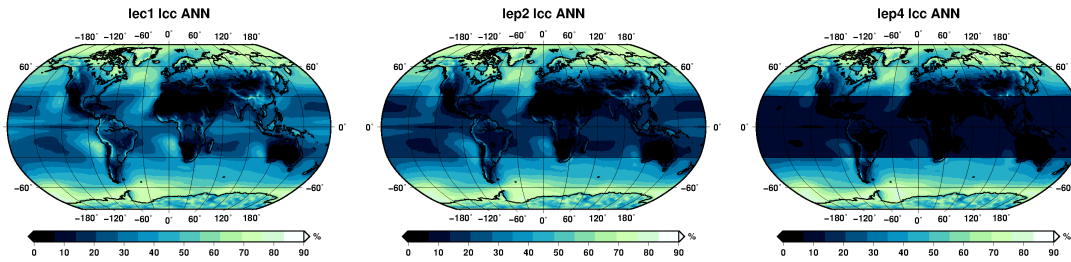
Figure 3.14: Annual mean low cloud cover seen by the radiative scheme from (left) the standard equable climate simulation *lec1*, (middle) the intermediate-modified simulation *lep2* and (right) the extreme-modified simulation *lep4*.

CO_2, equable-like vegetation and no ice over land). Initial conditions have been derived from the end of the *leqf* simulation.

- **Intermediate-modified equable climate simulation** (*lep2*): the same as *lec1*, but with TLC cover artificially reduced to 0.65 times the original one ($LBDA = 0.65$).

- **Extreme-modified equable climate simulation** (*lep4*): the same as *lec1*, but with TLC cover artificially reduced to 0.35 times the original one ($LBDA = 0.35$).

The three experiments have been run for 41 model years. The last 30 years of simulation are analyzed.

Fig. 3.15 shows the distribution of low cloud cover from the three experiments. The standard equable climate simulation still shows TLCs, in particular over eastern subtropical oceans, approximatively between 10 and 30 degrees latitude in both hemispheres, which are reduced in the other two simulations as a direct effect of the imposed modifications. Implications for cloud radiative forcing on both solar and net (i.e. solar+thermal) radiation are shown in Fig. 3.15. The main effect of reducing TLCs is a reduction of the solar cloud forcing (i.e. positive anomaly) in the subtropical eastern oceans, where most of the TLCs are located (see Fig. 3.15). Since TLCs have almost no effect on thermal radiation, the drop in solar cloud forcing results into a similar decrease of the net cloud forcing in the low cloud regions, and as such a net decrease of the cooling radiative effect of clouds.

Fig. 3.16 shows the differences in surface air temperature between the two modified simulations and the standard equable climate simulation. The effect of the stronger TLC feedback — represented by the imposed reduction of TLCs in *lep2* and *lep4* — results into a general increase of surface temperatures, which is not limited to the tropics but significantly affects also regions far outside of the tropical latitudes. The two modified simulations show similar spatial patterns of the warm anomaly either for annual, DJF and JJA temperatures, with higher

69
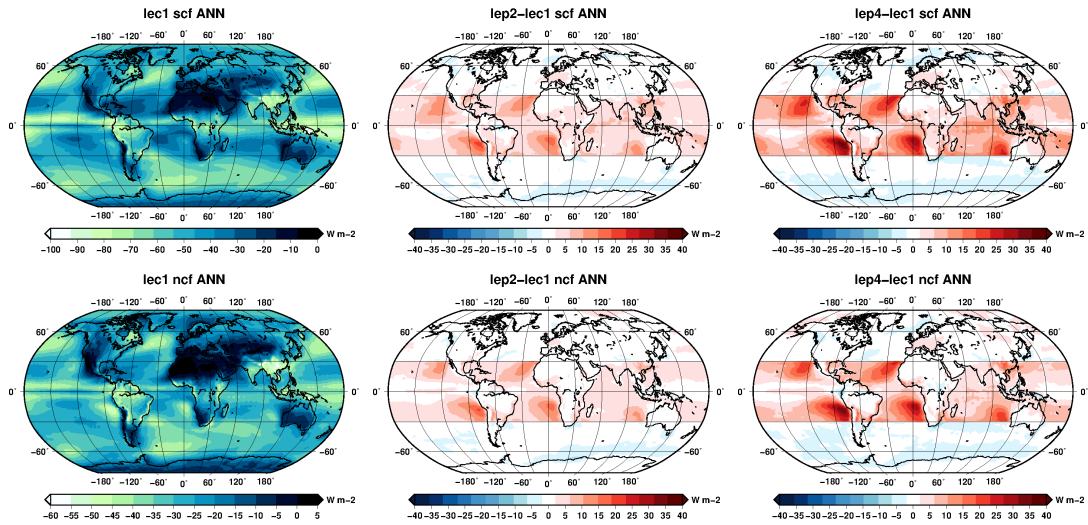
Figure 3.15: Top panels: annual mean solar cloud forcing from the standard equable climate simulation (*lec1*, left), difference between the intermediate-modified simulation and the standard equable climate simulation (*lep2-lec1*, middle) and difference between the extreme-modified simulation and the standard equable climate simulation (*lep4-lec1*, right). By definition, a negative cloud forcing indicates a cooling radiative effect of clouds. Bottom panels are the same as top panels but for the net cloud forcing.

Figure 3.16: Surface air temperature anomaly induced by the reduction of TLCs. Shown is the difference between the intermediate-modified and the standard equable climate simulation (*lep2-lec1*, top) and between the extreme-modified and the standard equable climate simulation (*lep4-lec1*, bottom). Left column refers to annual mean values, middle is the NH summer (JJA) and right the NH winter (DJF).

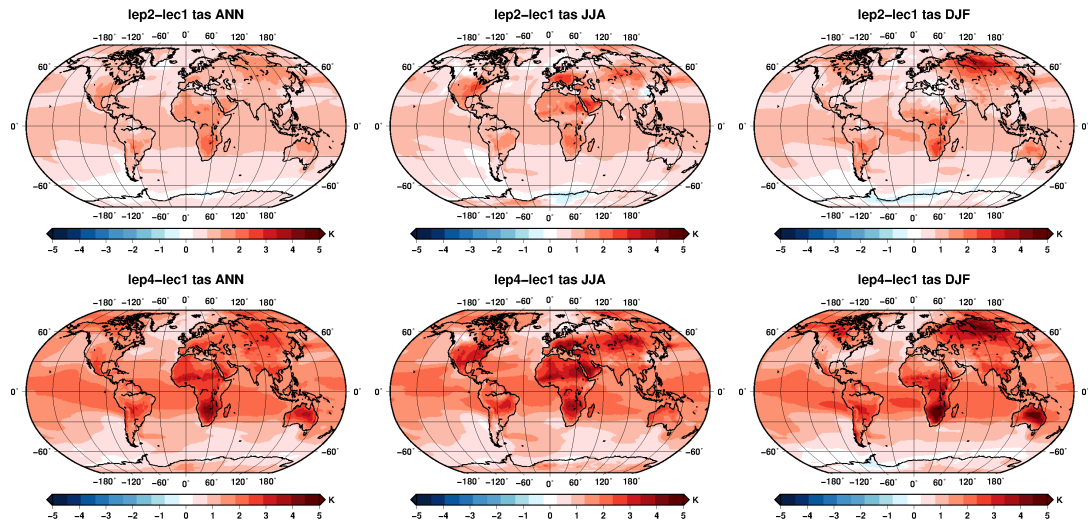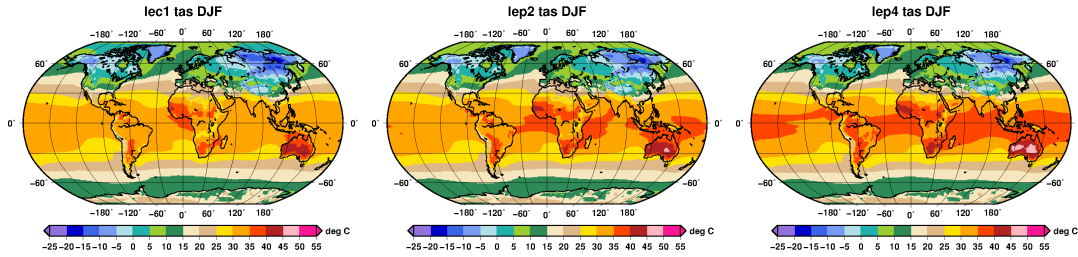Figure 3.17: Climatology of surface air temperature during the NH winter (DJF) from the standard equable climate simulation (*lec1*, left), the intermediate-modified simulation (*lep2*, middle) and the extreme-modified simulation (*lep4*, right).

values occurring in *lep4* due to the stronger forcing applied there. In general, the strongest warming occurs in the tropics and over the NH extratropical continents. The anomaly is weaker in the SH (both over oceans and Antarctica). The warm anomaly over NH extratropical continents shows a seasonal shift, being centered in the mid-latitudes during the warm season (JJA) and in the high-latitudes during the cold one (DJF). Interestingly, the winter high-latitude continental warming is of the same order of magnitude than the subtropical one, indicating that a stronger TLC feedback may lead to temperature increases right in the regions and during the season most affected by the equable climate problem. However, it is worth to note that winter temperatures over some regions in the high-latitude continental interiors still go below freezing also in the warmest simulation (*lep4*, see Fig. 3.17).

A final consideration concerns the strength of the TLC feedback "imposed" in the modified simulations through the reduction of TLC cover. Brient and Schneider (2016) quantified the strength of the TLC feedback computing the covariance of solar reflection by TLCs with the underlying surface temperature (the higher the covariance, the stronger the TLC feedback). They found that reasonable values for this measure are as high as 3 W m^{-2} K^{-1} under global warming (see that paper for details). Using the same method, I have found a covariance between TLC reflection and temperature in the extreme-modified simulation of about 2.6 W m^{-2} K^{-1}, which is inside the range of reasonable values defined in that paper. Obviously, the other two simulations considered here show smaller values of TLC feedback. In other words, the imposed reduction of TLCs is within the range of plausible values under warm equable climate conditions even in the most extreme case considered here.

3.5 Comments on the maritime influence on continental temperatures

Results presented in section 3.4 indicate that a subtropical warming because of stronger tropical low cloud feedbacks can lead to high-latitude warming, especially over continents during the winter season. However, this warming is not enough not to go sub-freezing in model simulations run with EC-Earth. Here some considerations are drawn, suggesting that problems of state-of-the-art climate models in representing the maritime influence (i.e. the mitigating effect of oceans) on continental winter temperatures may help to explain the additional degrees required to be above freezing in winter.

Existing literature about terrestrial proxy data during past warm equable climates indicates that continental regions where fossils clearly point to winter temperature above freezing are mostly close to oceans or large lakes (e.g. Greenwood and Wing, 1995; Markwick, 2007; Huber and Caballero, 2011; Eberle et al., 2014).

I have analyzed how EC-Earth and other state-of-the-art coupled climate models from the CMIP5 ensemble (see section 1.4) reproduce winter surface temperatures and the temperature annual cycle over oceans and land in present-day simulations, with a particular focus on continental regions exposed to oceanic influence. The main results are summarized in Fig. 3.18. These statistics suggest that models tend to underestimate winter temperatures — and, by consequence, to overestimate the amplitude of the annual cycle — in the western portion of mid-latitudes continents, i.e. in the regions whose climate is mitigated by the influence of an upstream ocean. The latter can be inferred from Fig. 3.18d: areas experiencing maritime influence exhibit an annual cycle with small amplitude and zonal gradient, conversely to areas affected by deep continental climates showing large amplitudes and meridional gradients. The pattern of negative and positive winter temperature anomalies over NH continents follows this division into maritime versus continental climates (top panels of Fig. 3.18). On average, the cold bias over continental areas exposed to oceanic influence is of the order of two or more degrees Celsius (clearly it is model dependent). At the highest latitudes, the switch from negative to positive model temperature bias over land corresponds with the absence/presence of sea-ice in the Arctic ocean (Figs. 3.18a and 3.18b). There was no sea-ice in the Arctic during past warm equable climates, thus also the northernmost edge of NH continents was likely exposed to maritime influence. Concluding, if present models tend to underestimate the maritime influence on winter temperatures, they are likely biased low in their winter temperatures for the regions with fossil records.

tomc−eraint tas DJF   (a)

tomc−eraint tas JAN   (b)

cmip5ens−era40 tas DJF   (c)

eraint AMPx2   (d)

tomc−eraint AMPx2   (e)

cmip5ens−era40 AMPx2   (f)
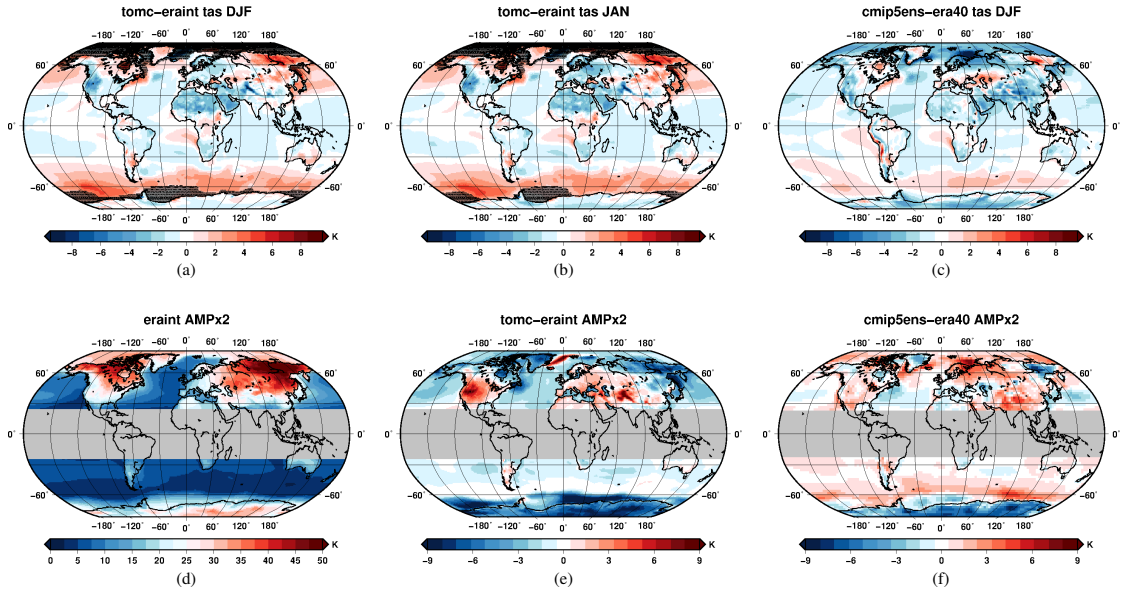
Figure 3.18: Present-day surface air temperatures (top) and amplitude of the annual cycle (bottom) in model and reanalysis data. (a) Difference of surface air temperature between the EC-Earth present-day simulation (*tomc*) and the ERA-Interim reanalysis (period 1980-2014) during the NH winter (DJF). Superimposed black dots indicate sea-ice coverage during DJF from *tomc*. (b) The same as (a) but for January only (coldest month over NH continents). (c) Difference of NH winter (DJF) surface air temperature between the CMIP5 multi-model mean (average between 30 historical simulations performed with different models from the CMIP5 ensemble) and the ERA40 reanalysis during the period 1958-2001. (d) Amplitude of surface air temperature annual cycle (computed as the amplitude of the yearly-period sinusoidal component of surface air temperature) from the ERA-Interim reanalysis. Latitudes between 23.5° North and South are masked because there is no significant annual cycle there. (e) Difference in the amplitude of surface air temperature annual cycle between *tomc* and ERA-Interim. (f) Difference in the amplitude of surface air temperature annual cycle between the CMIP5 multi-model mean and ERA40. See sections 2.2.2 and 4.2 for more informations on the ERA-Interim and ERA40 reanalyses.

3.6 Conclusions

Evidences from climatic observations of recent climate (i.e. over the last decades) indicate that the the Arctic is warming faster than the lower latitudes, an issue that has been known as "Arctic amplification" (e.g. Serreze and Barry, 2011). Arctic amplification being observed today is expected to become stronger in coming decades, and the future of the Earth could be not so different from past warm equable climates, such as the Early Eocene equable climate, with their reduced meridional temperature gradient and weak seasonality (Lunt et al., 2012). Future climatic projections heavily rely on climate models. However, model simulations of past warm equable climates consistently fail in reproducing their warm high latitudes and in particular above-freezing winter temperatures over continental interiors, an issue that has been referred to as the "equable climate problem". Understanding why models suffer for this problem is crucial to constrain uncertainties about future projections of the Earth's climate.

In the present study, the equable climate problem has been investigated using the Earth system model EC-Earth. A long simulation of equable climate conditions using appropriate boundary conditions — including atmospheric CO_2 concentration 6 times higher than its preindustrial value, no land ice and equable-like vegetation — has been run and analyzed. Results indicate that EC-Earth is at least as reliable as previous climate models used to simulate past warm equable climates. In particular, EC-Earth shows a very strong reduction of the meridional temperature gradient and of the high-latitude annual cycle in the Northern Hemisphere. This result is mostly an effect of albedo changes — mainly due to the extinction of polar ice sheets, leading to a reduction of high-latitude albedo, and the increase in cloud reflectivity over the equator — and of the amplification of the greenhouse effect at high latitudes — due to, among the others, increased cloud forcing on longwave radiation. The differential changes of albedo and greenhouse effect between the low and the high latitudes contribute to the reduction of the meridional temperature gradient by a similar amount on an annual mean. However, it is worth to note that albedo changes affect high-latitudes only during the polar summer. Thus, the importance of the amplified greenhouse effect resides also in the fact that it is active also (if not mainly) during the polar night.

Despite these positive results, also EC-Earth is affected by the equable climate problem: as well as other climate models, it fails in reproducing above freezing winter temperatures over high-latitude continents. New hypotheses have been explored to solve the equable climate problem. The most promising result refers to tropical low clouds, whose response to warmer-than-present climatic conditions is known to be poorly represented by climate models. Observations indicate that tropical low clouds decrease when the surface warms, resulting in less reflection of solar radiation and as such a positive feedback on surface temperatures (tropical low cloud feedback). This feedback is generally underestimated by climate mod-

els. The analysis with EC-Earth presented here shows that subtropical warming, because of stronger tropical low cloud feedbacks, can lead to significant warming over high-latitude continents during winter, that is right in the regions and during the season most affected by the equable climate problem. This result is achieved by imposing a reduction of tropical low clouds in warm climatic conditions which is consistent with reliable estimates given by the existing literature (based on both observations and model simulations, see Brient and Schneider, 2016). As a final consideration, the analysis presented here suggests that problems of state-of-the-art climate models in reproducing the maritime influence on continental temperatures may explain the additional degrees required to be above freezing during winter in model simulations of warm equable climates.

Chapter 4

On the relationship between the North Atlantic Oscillation and winter precipitation in the Hindu-Kush Karakoram

4.1 Overview

The Hindu-Kush Karakoram (HKK), encompassing parts of Afghanistan, Pakistan, India and China, is at the western edge of the Himalayan range, the largest mountain region in the world (see section 1.5 for issues concerning mountains and climate).

The whole Himalayan region is exposed to three main circulation patterns — the Indian Summer Monsoon, the East Asian Monsoon and Western Weather Patterns (WWPs, Archer and Fowler, 2004; Syed et al., 2006; Yadav et al., 2009b; Pal et al., 2014) — leading to different precipitation climatologies in the western, central and eastern portions of the mountain chain (Bookhagen and Burbank, 2010). The HKK in the west is strongly impacted by westerly perturbations (WWPs) originating from the Mediterranean/Atlantic regions during winter and it is affected, at least in part, by the monsoon during summer. As a result, precipitation in the HKK is characterized by a bimodal annual cycle (Palazzi et al., 2013). In the western Himalaya and in the Karakoram, WWPs are primarily responsible for the build-up of seasonal snow cover, which represents a crucial water reservoir and a significant source for some of the major river basins in the region, such as the Indus River and its tributaries (Archer and Fowler, 2004). Bookhagen and Burbank (2010) showed that snowmelt constitutes up to 50% of the total annual discharge in this area.

The North Atlantic Oscillation (NAO) is the dominant pattern of atmospheric variability in the North Atlantic sector and it refers to changes in the intensity
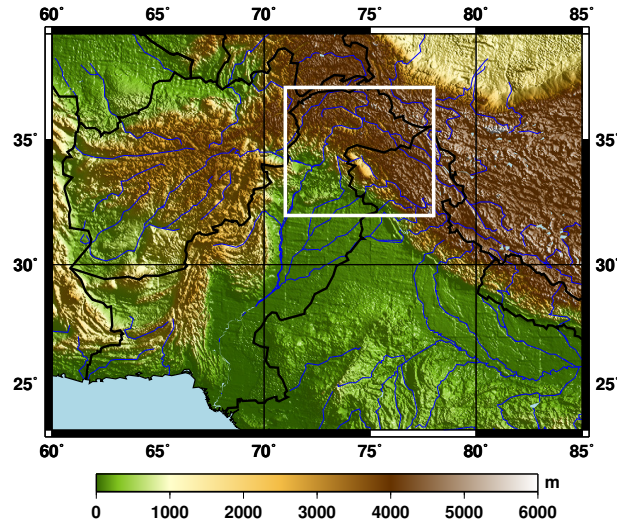
Figure 4.1: Map of the Hindu-Kush Karakoram region and its surroundings. The white rectangle highlights the HKK domain.

and location of the Azores pressure high in the subtropical Atlantic and of the Icelandic low in the Arctic. It strongly affects climate across much of the Northern Hemisphere during winter (Hurrell et al., 2003). Some authors have regarded the NAO as the regional expression of a hemispheric, zonally symmetric mode of variability known as the Arctic Oscillation (AO) or Northern Hemisphere Annular Mode (NAM, see for example Thompson and Wallace, 2001). While there is an on-going debate about the relationship between the NAO and AO (Wallace, 2000; Ambaum et al., 2001), their time series show strong similarities and Deser (2000) found a temporal correlation of 0.95 between the two for monthly data. For this reason, here I focus on the North Atlantic Oscillation but I reasonably expect similar findings if an index measuring the AO would be adopted instead.

Recently the NAO has been indicated as an important regulating factor also in the Karakoram region (Syed et al., 2006; Yadav et al., 2009b). Previous work has focused on the effects of the NAO on winter precipitation in the HKK based on the analysis of data from individual in-situ stations (Archer and Fowler, 2004), spatial averages of ground measurements (Yadav et al., 2009b), or gridded datasets (Syed et al., 2006). All studies agreed in showing that winter precipitation and the NAO are correlated with above (below) normal precipitation over the HKK area during the positive (negative) NAO phase.

Two mechanisms have been proposed to explain the link between the NAO and precipitation in the HKK. Syed et al. (2010) observed an increase in the number and intensity of eastern Mediterranean storms reaching northern Pakistan during the positive NAO phase, as the result of deeper surface and 500 hPa troughs over central-southwestern Asia in that phase. They also noticed that the transport

of extra moisture during the positive NAO phase from the Mediterranean, the Caspian and the Arabian Sea contributes to the NAO-related precipitation signal in northern Pakistan. Another mechanism was proposed by Yadav et al. (2009b), in which WWPs are intensified over northwestern India by the strengthening of the westerly jet stream over the Middle East during the positive NAO phase.

The relationship between the NAO and precipitation in the HKK underwent secular variations during the 20th century. Yadav et al. (2009b) investigated the temporal evolution of this relationship, finding significant correlations between the NAO and precipitation in the period from 1940 to 1980 and non-significant ones in the first and last part of the century. The recent drop in the NAO control was accompanied by a simultaneous strengthening of the relationship between the El Niño Southern Oscillation (ENSO) and precipitation in this area, which was not significant in the period 1940–1980. Yadav et al. (2010) showed that the intensification of the ENSO signal in recent decades was associated with a change in the strength of the tropical atmospheric response to ENSO. This result can, at least in part, explain also the recent weakening of the NAO-precipitation relationship. However, it is not clear if the secular variations in the NAO-precipitation relationship can be attributed entirely to changes in the intensity of the ENSO signal. Figure 2 in Yadav et al. (2009b) shows periods (before 1920 and between 1930 and 1940) when neither the NAO nor ENSO were statistically linked to precipitation in this area, suggesting that ENSO could be a factor, but there must be also other processes able to determine such variations.

The NAO underwent notable changes in the late 1970s. In particular, it shifted from a predominance of the negative phase in the 1960s to a predominance of the positive phase in the 1990s. Many studies showed that this trend is outside the range of internal atmospheric variability (Thompson et al., 2000; Feldstein, 2002; Gillett et al., 2003). At the same time, Hilmer and Jung (2000) and Lu and Greatbatch (2002) documented an eastward displacement of the centers of action (COAs) of interannual variability of the NAO in the period 1978-1997 compared to the previous decades. The extent to which these concurrent changes are linked to each other is still a matter of debate (see for example Luo et al., 2010). In any case, a spatial shift in the NAO variability has strong implications for different climatic parameters (Jung et al., 2003; Pinto and Raible, 2012). Wang et al. (2012) investigated the spatial displacements of the NAO COAs on decadal timescales from the end of the 19th century onwards. They introduced a new climate index (Angle Index, AI) to quantify the relative position of the COAs in 20-year running windows and showed that the AI provides additional information which cannot be represented by a standard, fixed-in-space NAO index. All these changes, at least in principle, may have played a role also in the secular variations of the NAO-precipitation signal.

In this work, I investigate the relationship between the NAO and precipitation in the HKK region (shown in Fig. 4.1) using both observational datasets and

simulation results from the Earth System Model (ESM) EC-Earth.

I consider an ensemble of currently available observational precipitation datasets, including three gridded archives based on the interpolation of in-situ rain gauge measurements (GPCC, CRU and APHRODITE), TRMM satellite observations and the ERA40 reanalysis. The complex orography of the region, the sparse coverage of ground stations, usually limited to lower altitudes, and issues in properly measuring solid precipitation are major constraints for precipitation estimates in this area (Immerzeel et al., 2012; Rasmussen et al., 2012). Gridded archives based on in-situ observations interpolate available data, which are often sparse and limited to lower altitudes. Additionally, rain gauges tend to underestimate total precipitation, owing to the difficulty in properly recording solid precipitation. Also satellite observations do not correctly estimate snow, owing to problems in identifying snow crystals (Rasmussen et al., 2012). Reanalysis products provide estimates of solid and liquid precipitation; however, biases in the models and possible changes in the observing systems can affect the output fields (Bengtsson et al., 2004b). Therefore, gridded precipitation data are always biased. While previous work already demonstrated a link between the NAO and precipitation, here I opt for a multi-dataset approach to estimate the differences that could arise in the representation of this signal by using different large-scale data archives.

I focus on the processes which are responsible for the link between the NAO and precipitation in the HKK. Particular emphasis is given to the study of the NAO-associated changes in evaporation from the main moisture reservoirs, which were not considered in previous work and can help to gain a more complete view of the whole mechanism. Moreover, I address the secular variations that occurred in the NAO-precipitation signal and investigate if the spatial shifts in the NAO variability help to understand the observed changes, using the Twentieth Century Reanalysis data (Compo et al., 2011) to reconstruct the atmospheric variability from 1871 to the present.

The whole analysis is repeated using the EC-Earth ESM (see section 1.3) to assess its ability to reproduce WWPs and the associated mechanisms and, at the same time, to have a further tool to investigate these processes.

This chapter is structured as follows: in section 4.2 I discuss data and methods employed in this study; results from the analysis with observational datasets are presented in sections from 4.3 to 4.6, where I analyze WWPs trajectories, the NAO-precipitation signal, the mechanisms responsible for this signal and the role of the position of the NAO COAs in determining the strength of the NAO-precipitation relationship; the analysis with EC-Earth in discussed in section 4.7. Final considerations are discussed in section 4.8. Contents of this chapter have been published in Filippi et al. (2014).

79

4.2 Data and metodology

Datasets

The precipitation datasets employed here include satellite TRMM observations, three rain-gauge-based archives (APHRODITE, CRU and GPCC) and the ERA40 reanalysis. Evaporation, specific humidity, sea surface temperature (SST) and wind data from ERA40 are also analyzed. To study multi-decadal variations that occurred in the atmospheric response to the NAO, I analyze sea level pressure (SLP) and wind fields from the Twentieth Century Reanalysis, which provides information from the end of the nineteenth century. For what concerns the analysis with EC-Earth, outputs from a historical simulation produced for CMIP5 (see section 1.4) are considered.

- Asian Precipitation Highly-Resolved Observational Data Integration Towards Evaluation of Water Resources (APHRODITE). APHRODITE, a project of the Research Institute for Humanity and Nature (RIHN) and the Meteorological Research Institute of the Japan Meteorological Agency (MRI/JMA), produces precipitation data primarily obtained from a rain gauge observation network (Yatagai et al., 2012), available at `http://goo.gl/SNcqAs`. I use the APHRO_MA (Monsoon Asia) V1101, characterized by a spatial resolution of 0.25° latitude-longitude, covering an area from 60°E-150°E in longitude and 15°S-55°N in latitude during the period 1951-2007.

- Global Precipitation Climatology Centre (GPCC). This product, created by the Deutscher Wetterdienst (DWD, National Meteorological Service of Germany), in the framework of the World Climate Research Program (WCRP), consists of monthly precipitation fields over land obtained from a rain-gauge-based dataset. I use the GPCC version 6 release (Schneider et al., 2011), having a spatial resolution of 0.5° latitude-longitude and a temporal coverage from 1901 to 2010.

- Climate Research Unit (CRU). The CRU precipitation dataset, produced by the University of East Anglia, consists of monthly gridded fields over land from in-situ rain gauge data. Here I use the version CRU TS 3.21, characterized by a temporal coverage from 1901 to 2012 and a spatial resolution of 0.5° latitude-longitude.

- Tropical Rainfall Measuring Mission (TRMM). I use the TRMM 3B42 product (Huffman et al., 2007), available through the NASA Mirador interface (`http://mirador.gsfc.nasa.gov`), which supplies satellite-based precipitation estimates from 1998 onwards. The data have a spatial resolution of 0.25° latitude-longitude and a 3-hour temporal resolution, covering a global belt extending approximately from 50°S to 50°N latitude.

- ERA40 reanalysis. ERA40 is a global atmospheric reanalysis for the period 1958-2002 developed by the European Center for Medium-Range Weather Forecast (ECMWF) (Uppala et al., 2005). From ERA40, I analyze total precipitation (daily resolution); evaporation and sea surface temperature (monthly resolution); U and V wind components, specific humidity and 10m wind speeds (6-hour temporal resolution). All variables are on a 1.125° latitude-longitude regular grid. Precipitation and evaporation are not assimilated in the reanalysis but they are produced by the forecast model and, as such, they may be susceptible to systematic model errors (Bengtsson et al., 2004b). I consider the three-dimensional specific humidity and wind fields at 1000, 925, 850, 775, 700, 600, 500, 400, 300 and 250 hPa pressure levels. For the definition of atmospheric reanalysis see section 2.2.2.

- Twentieth Century Reanalysis (20CR). 20CR is a global atmospheric circulation reanalysis assimilating only surface pressure data and using observed monthly SST and sea-ice distributions as boundary conditions (Compo et al., 2011). I use the second version of the 20CR, available from 1871 to the present with a $2° \times 2°$ spatial resolution, considering monthly SLP and horizontal wind fields. The 20CR data are provided by the NOAA/OAR/ESRL PSD, Boulder, Colorado, USA, from their Web site at `http://www.esrl.noaa.gov/psd/`.

- EC-Earth. The Earth System Model EC-Earth is described in section 1.3. Here, outputs from the historical simulation run at ISAC-CNR in the context of the Coupled Model Intercomparison Project Phase 5 (CMIP5, Taylor et al. (2012)) are analysed. The run is forced by reconstructed solar variability and anthropogenic forcing during the period 1850-2005. This simulation has been run with the EC-Earth v2.3 release, at T159 horizontal spectral resolution (corresponding to a grid of about 1.125° latitude-longitude) with 62 vertical levels in the atmosphere.

Analysis methods

The analysis is performed using observational data first (sections 4.3–4.6) and then repeated using modelling results from EC-Earth (section 4.7).

The winter season is defined as the period from December to March (DJFM), when both WWPs and the NAO are more active. This choice is consistent with other studies analyzing the relationships between teleconnection patterns and precipitation in this area (Syed et al., 2006, 2010; Yadav et al., 2009b). Each winter is labelled by the calendar year of its January, so that winter 2000 includes months from December 1999 to March 2000.

The analysis of the NAO-precipitation signal and related mechanisms presented in sections 4.4 and 4.5 refers to the period 1958-2002, during which all datasets

overlap. To investigate the mechanisms by which the NAO regulates precipitation (section 4.5) I use the ERA40 reanalysis. In section 4.6, in order to enlarge the temporal coverage to study multi-decadal variations occurring in the NAO-precipitation relationship, I use the 20CR reanalysis, covering the period from winter 1872 to winter 2012.

I adopt the DJFM station-based NAO index (NAOI, Hurrell (1995)). This NAO index calculation is based on the difference between the normalized average winter SLP in Lisbon (Portugal) and in Stykkisholmur/Reykjavik (Iceland); normalization is obtained by removing the long-term mean and by dividing by the long-term standard deviation, to prevent the series from being dominated by the larger variability of the northern station. For observations, I use the observation-derived NAO index (OBS-NAOI) available from NCAR at `http://goo.gl/opvFM`, using SLP data from in-situ meteorological stations. Long-term means and standard deviations used for normalization of the OBS-NAOI are based on the period 1864-1983. Since the oscillation patterns (such as the NAO) in global climate model simulations are not in phase with the observed oscillations (see section 1.4), a NAO index for EC-Earth is calculated with the same method using sea level pressure data from the model output fields (MOD-NAOI). For this index, long-term means and standard deviations for normalization are computed over the whole period of the simulation (1851-2005). The temporal evolution of these indices from 1958 to 2002 is shown in Fig. 4.2. I consider a winter season to be in a positive (negative) NAO phase if the NAOI is more than one standard deviation above (below) the averaged NAOI for the period 1958-2002. I have verified that the results presented here are independent of the choice of the NAOI, by repeating the analysis using a NAO index based on Empirical Orthogonal Functions (EOFs). The details are not reported for the sake of conciseness.

Statistical analyses are performed mostly through 1) the computation of the correlations between the NAOI time series and other key variables, such as precipitation, evaporation, SST, wind and moisture transport; and 2) the inspection of positive and negative NAO composites of the different variables (that is, climatological averages conditioned on the NAO phase). Correlations are computed using the Pearson's linear correlation coefficient and their significance is assessed using a standard two tailed t-test. A time-shuffling method is used to assess the significance of the differences between the positive and the negative NAO composites (Pollard et al., 1987; Ciccarelli et al., 2008).

The vertically integrated water vapor (moisture) transport and the precipitable water in the air column are computed following the approach by Chen (1985). The seasonal mean precipitable water $\overline{W}$ is given by the vertical integral over pressure levels of the seasonal mean specific humidity ($\overline{q}$), normalized by the gravity acceleration g:

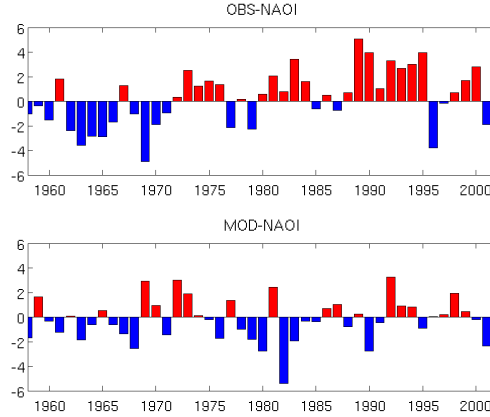$$\overline{W} = \frac{1}{g} \int \overline{q} dp.$$

Figure 4.2: Time series of DJFM NAO indices computed as the difference between normalized SLP in Lisbon and Stykkisholmur/Reykjavik from (top) observations and (bottom) EC-Earth.

The seasonal mean moisture transport $\overline{\mathbf{Q}}$ is given by

$$\overline{\mathbf{Q}} = \frac{1}{g} \int \overline{q\mathbf{v}} dp, \tag{4.1}$$

where $\mathbf{v}$ is the horizontal wind and the overbar represents time average over the season. ERA40 and EC-Earth 6-hour 3-dimensional fields of specific humidity and horizontal wind are used for this computation, considering only tropospheric levels (250–1000 hPa). Different variants for the choice of the upper level (here 250 hPa) exist in literature. I have tested different choices of the upper bound and found that they do not influence the results, as the moisture content is extremely low above 250 hPa. Note, also, that in high-elevation areas the lower levels are below the Earth surface. ERA40 and EC-Earth fields take values very close to zero below the surface (although not exactly zero). I tested the contribution of such spurious levels in the vertical integral (4.1) and found that it is negligible for our purposes.

I investigate the slow movements of the NAO centers of action (Hilmer and Jung, 2000; Lu and Greatbatch, 2002), using the Angle Index (AI) introduced by Wang et al. (2012). I consider 21-year running windows such that each subsequent window is moved over by one year. The 21-year periods are labelled by their 11th year. For each of the 21-year long periods, the NAO pattern is computed as the first Empirical Orthogonal Function (EOF1) of monthly SLP anomalies over the region 20-80°N, 90°W-40°E. The centers of action (or nodes) of the NAO are the positions of the absolute minimum and maximum of EOF1. The sign of EOF1 is fixed so that the northern node of the NAO is always negative. The AI is computed as the angle between the axis connecting the two nodes of the NAO and its mean climatological orientation, and normalized to unit standard deviation. The AI has
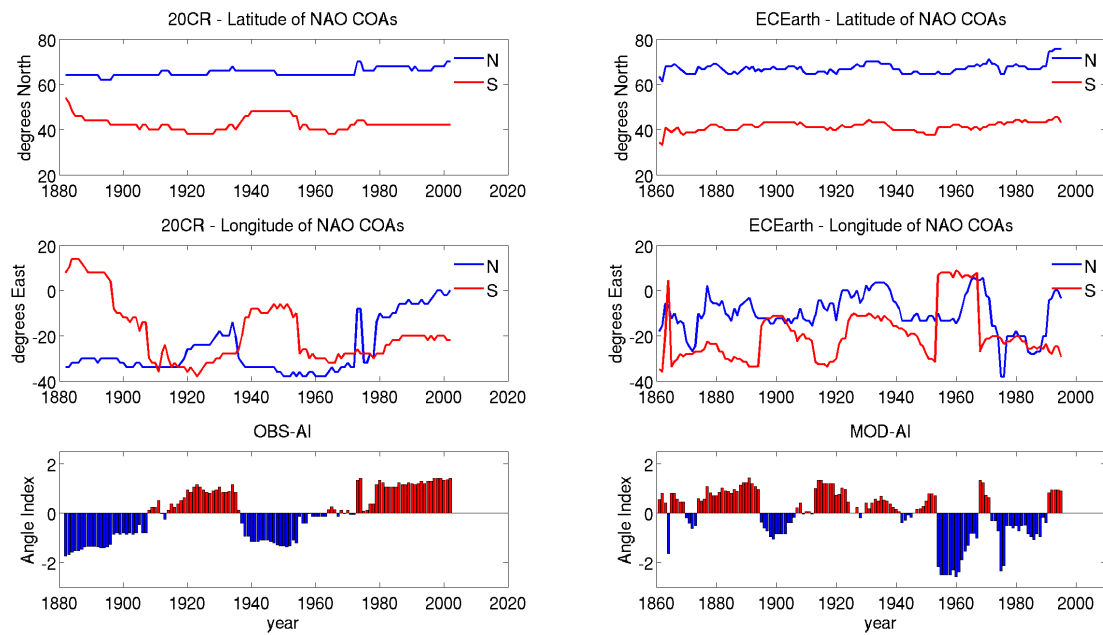
Figure 4.3: Temporal evolution of the position of the NAO COAs and the resulting Angle Index from (left) 20CR and (right) EC-Earth. Top: latitude of the northern node (blue) and the southern node (red) in 21-yr windows where neighboring windows have 20 years in common. Center: longitude of the northern node (blue) and the southern node (red) in the same 20-yr windows. Bottom: Time series of the Angle Index.
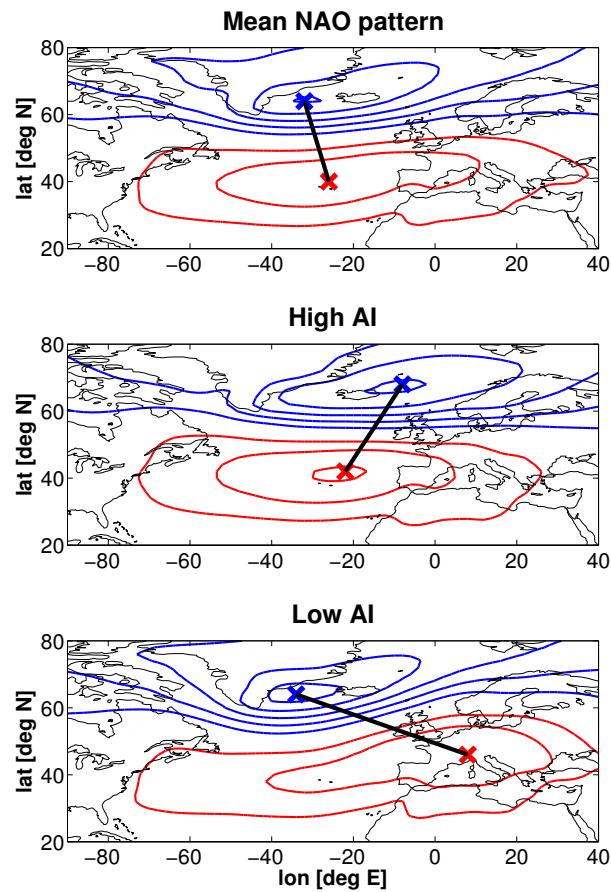
Figure 4.4: Top: mean spatial pattern of the NAO from 20CR during 1872-2012, computed as EOF1 of monthly SLP anomalies in 21-yr windows where neighboring windows have 20 years in common. Center: mean spatial pattern of the NAO during periods of high AI (1 standard deviation above the mean). Bottom: mean spatial pattern of the NAO during periods of low AI (1 standard deviation below the mean). For each pattern, the northern and southern nodes are indicated by blue and red crosses respectively. The axis connecting the two nodes is indicated by a black line.

a positive value, and we say that the NAO has a positive tilt, when this north-south axis is tilted clockwise compared to its mean climatological orientation. In the opposite case, we say that the NAO has a negative tilt. As the NAOI, also this index has to be computed separately for observations and model simulations. Monthly SLP fields from the 20CR are considered for the computation of the observation-derived AI (OBS-AI). SLP data from EC-Earth outputs are used to compute the model AI (MOD-AI). The temporal evolution of the NAO COAs and the resulting AI are shown in Fig. 4.3 for both the 20CR and the model EC-Earth. The spatial pattern of the NAO corresponging to periods of positive and negative tilt of the NAO is shown if Fig. 4.4.

4.3   WWP trajectories

Winter precipitation in the HKK is associated with the arrival of westerly perturbations (WWPs) originating from the Atlantic and the Mediterranean regions (Archer and Fowler, 2004; Syed et al., 2006). The space-time propagation of these systems is illustrated in Fig. 4.5, which shows the meridionally-averaged daily precipitation for one winter season (the year 2001 is taken as an example) from TRMM (left) and ERA40 (right), plotted as a function of longitude and time. Precipitation is averaged over the latitude band from 30 to 45°N, while longitude ranges from the Mediterranean basin to the HKK region, as shown in the top panels. WWPs appear as intermittent rainy systems propagating eastward, with alternating intensified and weakened precipitation, with a marked association with orographic features (see, for example, the intensified precipitation at about 50°E and 75°E, corresponding to the mountain regions of western Iran and the HKK, respectively). Figure 4.5 shows that the number of systems reaching the longitudes corresponding to the HKK region is higher during February-March than December-January and, as a consequence, conspicuous precipitation amounts in this area occur during late winter (see for example Palazzi et al., 2013).

The main features of WWP tracks are qualitatively captured by precipitation from TRMM and ERA40. The two datasets provide a similar longitudinal distribution of mean precipitation, as shown by the bottom panels of Fig. 4.5. TRMM shows slightly lower precipitation values over the Atlantic and higher values over the Mediterranean and the Middle East (up to about 50°E), while ERA40 shows a peak in total precipitation at HKK longitudes, between about 70°E and 80°E. This enhanced precipitation is not visible in the TRMM data, probably owing to the fact that the snow component of precipitation is neglected in the satellite estimates. The liquid-only precipitation from ERA40, shown as the green line in the bottom-right panel of Fig. 4.5, is much closer to the satellite-derived precipitation values.
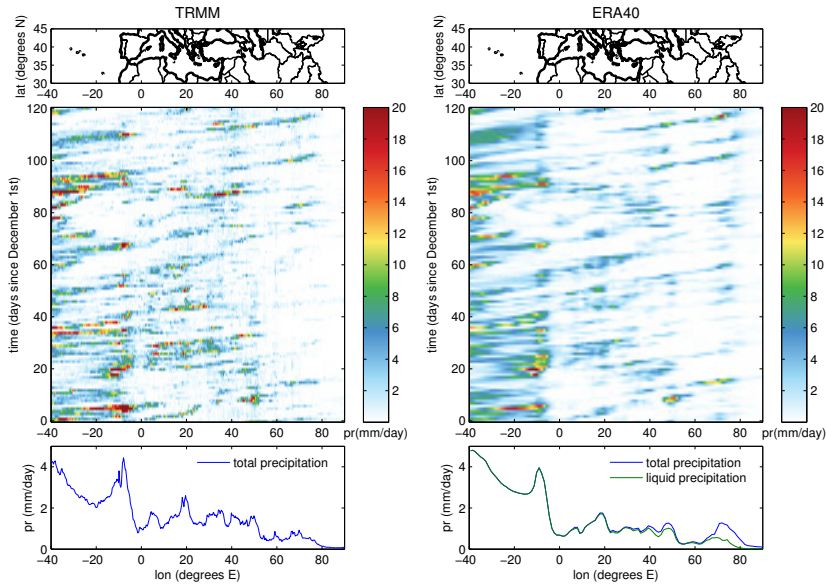
Figure 4.5: Top: Maps showing the region considered in the analysis. Center: Daily precipitation in winter 2001 from TRMM (left) and ERA40 (right) averaged over the latitudes from 30 to 45°N and plotted as a function of longitude and time. Bottom: Mean daily precipitation in winter 2001 averaged over latitudes from 30 to 45°N.

4.4 NAO-precipitation signal

I explore the correlation between the NAO and precipitation by plotting the spatial distribution of the statistically significant correlations (at the 95 percent confidence level) between DJFM precipitation and DJFM OBS-NAOI time series (Fig. 4.6) and the difference between positive and negative composites of precipitation from the GPCC, CRU, APHRODITE and ERA40 datasets conditioned on the phase of the NAO (Fig. 4.7) during the period 1958-2002. The strongest signal emerging from these plots is a European precipitation dipole, discussed by Wibig (1999) and by Trigo et al. (2002), in which strong positive NAO phases tend to be associated with above-average precipitation over northern Europe in winter, and with below-average precipitation over southern and central Europe, while opposite patterns of precipitation anomalies are observed during strong negative NAO phases. Another area displaying statistically significant positive correlations is located at the border between northeastern Pakistan and northwestern India, corresponding to the HKK region, though differences in the spatial extent arise between the datasets. In the three rain-gauge-based datasets (GPCC, CRU and APHRODITE) significant correlations are limited to a very small area and the weakest signal is found in CRU. Conversely, ERA40 shows significant positive correlations over a broad area encompassing central and northern Afghanistan and Pakistan, and the greater
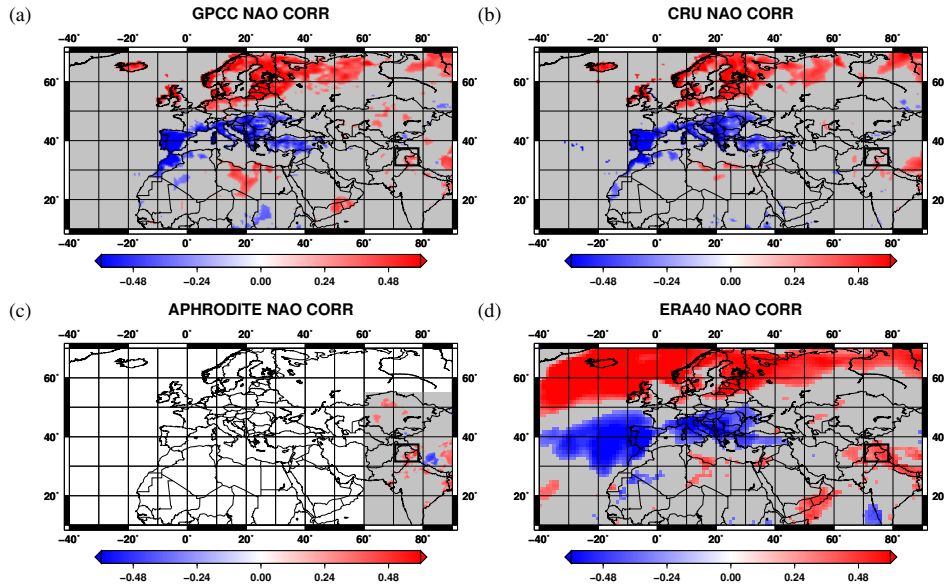
Figure 4.6: Correlation maps between the OBS-NAOI and winter precipitation from (a) GPCC, (b) CRU, (c) APHRODITE and (d) ERA40 during 1958-2002. Colors indicate statistically-significant values at the 95 percent confidence level. Non-significant values are marked in gray. The black rectangle highlights the HKK region.

Himalayan chain. This picture is confirmed by Fig. 4.7, where northern Pakistan and northern India display the strongest signal outside the European domain. All datasets show a positive (negative) precipitation anomaly during the positive (negative) NAO phase, but with differences both in the spatial extent and intensity of the anomaly. The composites in this area are statistically significant in ERA40, while they are not in the three rain-gauge-based datasets.

These results are consistent with previous works. Syed et al. (2010) observed that the non-significance of the NAO-precipitation signal in this area is due to the high variability of precipitation. These regions receive low precipitation amounts and exhibit high noise levels (Palazzi et al., 2013). The weak NAO-precipitation signal suggests that the NAO is not the only factor regulating precipitation, but there is high interannual variability due to other sources, including other teleconnection patterns such as ENSO (Syed et al., 2006, 2010; Yadav et al., 2009b, 2010; Dimri, 2013), Indian Ocean sea surface temperatures (Yadav et al., 2007), convection over the warm pool region (Yadav et al., 2009a) and random atmospheric variability. Differences between the datasets highlight current problems in having reliable precipitation estimates in this region and the importance of using multiple datasets to estimate uncertainties. The lower correlation signal in station-based datasets, compared to ERA40, may be associated with the underestimation of total precipitation in the observations (Palazzi et al., 2013) where winter snowfall is
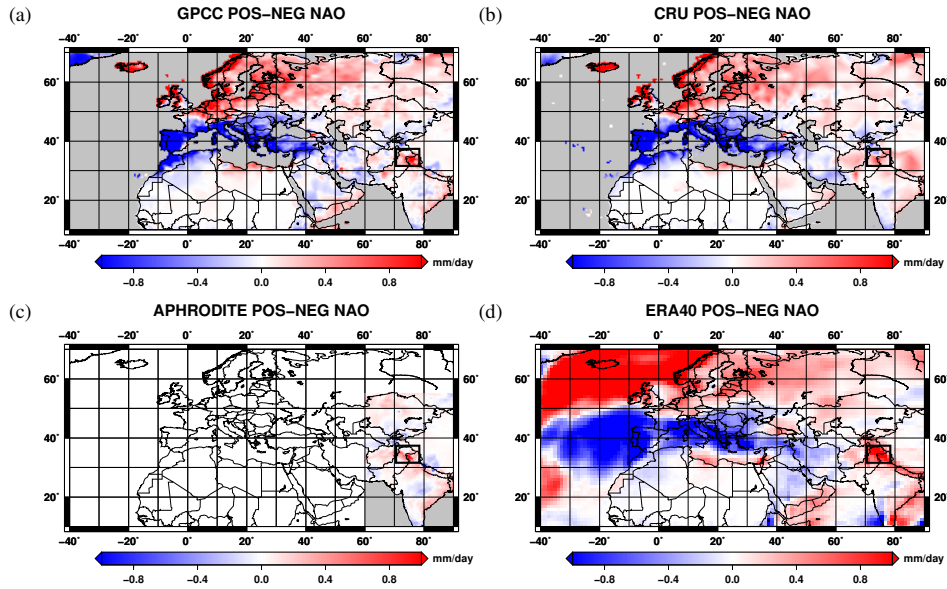
Figure 4.7: Difference between the positive and the negative NAO composites of winter precipitation from (a) GPCC, (b) CRU, (c) APHRODITE and (d) ERA40 during the period 1958-2002. The black rectangle highlights the HKK region.

not adequately captured. However, one should note that reanalysis precipitation outputs should be regarded with care, as they are susceptible to model errors and inhomogeneities in the data used in the assimilation procedure.

4.5 Mechanisms

The secondary maximum of the Asian subtropical jet stream, which is located climatologically over northern Egypt and Saudi Arabia (Middle East jet stream, MEJS), has been recognised as an important factor in determining climate over southern Asia, and the NAO can exert its effects on this region through modifications of the jet (Yang et al., 2004). Yadav et al. (2009b) suggested that the NAO regulates winter precipitation in northern India by strengthening the MEJS from North Africa to southeastern Asia during its positive phase. To study the effects of the NAO on tropospheric westerlies over this region, in the vertical cross section of Fig. 4.8 I show the correlation coefficients between the OBS-NAOI and zonal wind (averaged between 40°E and 70°E) in the Northern Hemisphere. This meridional band corresponds to the longitudes of greater importance for the transport of humidity towards the HKK (see below). Significant positive correlations are found from the lower to the higher troposphere at latitudes between 20°N and 30°N, where the climatological jet is located. The jet stream core in

Figure 4.8: Filled colored contours: correlation coefficients between the OBS-NAOI and winter zonal wind averaged over longitudes between 40 and 70°E during the period 1958-2002. Only correlations which ar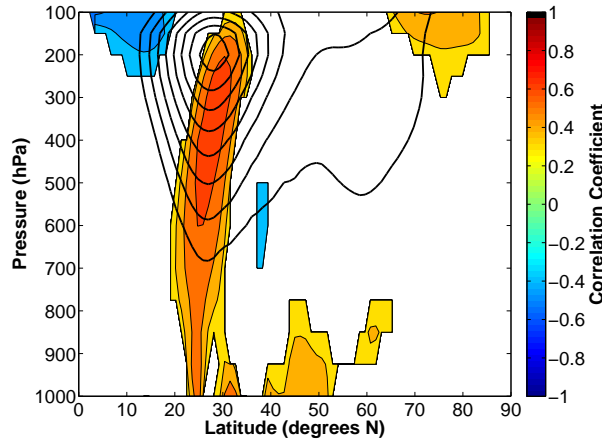e statistically significant at the 95 percent confidence level are reported. Black contours: climatology (1958-2002) of winter zonal wind averaged over longitudes between 40 and 70°E, identifying the position of the Middle East jet stream. Only values above 10 m s^{-1} are reported. Contour interval is 5 m s^{-1}.

the upper troposphere (around 200 hPa) is intensified and slightly shifted to the north during the positive NAO phase. The strengthening of the westerlies at these latitudes is marked throughout the troposphere and weakens slightly only at the lower levels (below 800-850 hPa), where surface effects become important and the mean circulation increasingly deviates from the zonal flow. NAO-related changes of middle-tropospheric westerlies are consistent with the deeper 500 hPa trough observed by Syed et al. (2006, 2010), highlighting the link between their findings and the ones by Yadav et al. (2009b).

I explore the extent to which this anomaly in westerly winds affects moisture transport towards the HKK. A first step is to identify the major sources of the humidity transported to the HKK region. Fig. 4.9 shows the climatology of vertically integrated moisture transport (vectors) superimposed on the spatial map of the significant correlations between the OBS-NAOI and the intensity of moisture transport (that is, the modulus of the transport vector). The climatology shows that moisture, originating mainly from the northern Arabian Sea and the Red Sea, is transported towards the HKK through the Persian Gulf. This result is consistent with Yadav et al. (2010). A comparatively smaller moisture contribution comes from the Mediterranean area, though, on average, moisture from that area deviates north-eastwardly and affects mainly the regions north of the HKK. As expected, in the correlation map (colored filled contours in Fig. 4.9) significant positive correlations occur over central-western Europe, while negative correlations
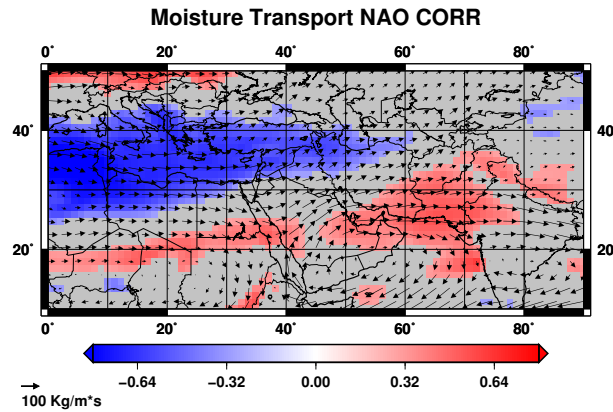
Figure 4.9: Climatology of moisture transport during winter (vectors) and correlation coefficients between the OBS-NAOI and the intensity of moisture transport (color map) during the period 1958-2002. Colors are used for statistically significant correlations at the 95 percent confidence level; gray indicates non-significant correlations.

occur across all the Mediterranean area, as shown by Hurrell (1995). This map also shows that the intensity of moisture transport from the Arabian Peninsula towards Pakistan and western India is significantly larger during the positive NAO phase. Significant positive correlations are found also over a thin zonal strip in eastern Africa, between about 15°N and 25°N. The contiguity of this region to the Arabian Peninsula may suggest an inter-dependence between the two signals but, as shown by the vectors of moisture transport superimposed on the correlation map, on average, humidity from this region deviates southward and does not flow directly into the Arabian Peninsula.

The strengthening of moisture transport from the Arabian Peninsula towards Pakistan during the positive NAO phase sustains wetter than normal conditions in winter in the HKK, as observed by Syed et al. (2010) and shown in Fig. 4.10a. This figure shows the difference between positive and negative NAO composites of precipitable water from ERA40. The Mediterranean region is characterized by a negative anomaly (that is, drier conditions during the positive NAO phase), which is mainly caused by the weaker advection of moisture from the Atlantic (Hurrell, 1995). Conversely, positive anomalies are found over the southern and south-western side of the greater Himalayan chain. This extra-moisture accumulating at the foot of the Himalayas during the positive NAO phase is available to WWPs that release more precipitation as they reach the HKK slopes.

While changes in tropospheric circulation play a major role in determining the enhanced moisture transport from Arabia to Pakistan during positive NAO periods, wind is not the only variable influencing moisture transport. In Fig. 4.10b I show the difference between the positive and the negative NAO composites of evaporation: during the positive NAO phase, enhanced evaporation occurs
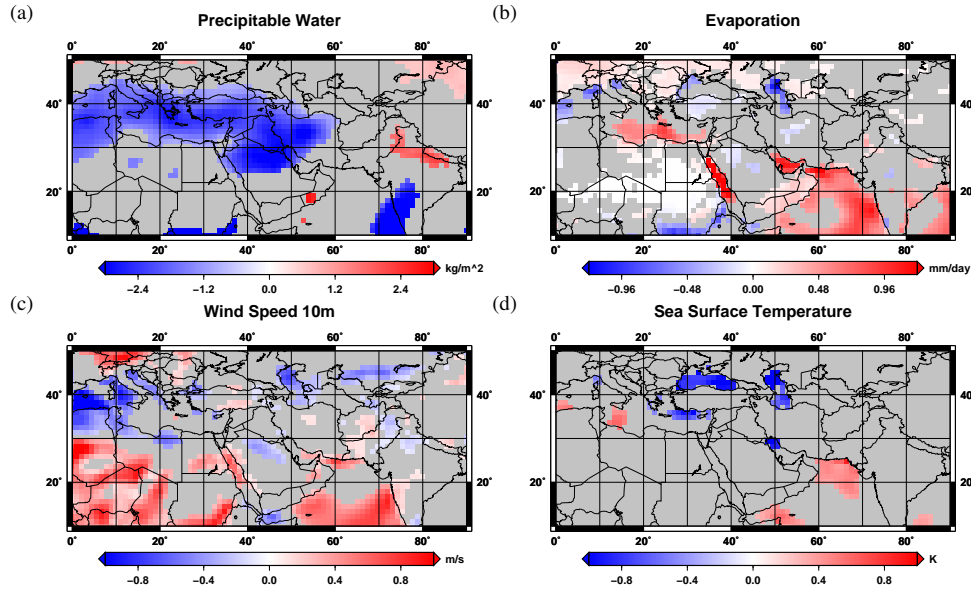
Figure 4.10: Difference between the positive and the negative NAO composites of (a) precipitable water, (b) evaporation, (c) 10m wind speed and (d) sea surface temperature during the period 1958-2002. Colors indicate statistically significant values at the 95 percent confidence level; gray indicates non-significant values.

from the Red Sea, the Persian Gulf, the northern Arabian Sea and the south-eastern Mediterranean. As mentioned above, these basins constitute the major moisture sources for the HKK. The evaporation anomaly found in the southeastern Mediterranean is associated with dry air conditions during the positive NAO phase (4.10a). The evaporation signal from the Red Sea, the Persian Gulf and the northern Arabian Sea is associated with coherent signals in surface wind speed and SST, as shown in Fig. 4.10c and Fig. 4.10d, respectively. During the positive NAO phase, ERA40 shows high surface wind speed over the Red Sea (note the good correspondence with evaporation anomalies), the Persian Gulf (significant correlations in the southern part, where the evaporation anomaly is stronger than elsewhere), and the northern Arabian Sea (significant correlations in the northernmost part of the region and south of about 20-15°N). High SSTs occur in a portion of the northern Arabian Sea. The whole picture provided by Figs. 4.10c and 4.10d matches well with the evaporation signal reported in Fig. 4.10b. The reader should note that the SST anomaly in the northern Arabian Sea is relatively confined, and I did not find a clear explanation for this effect. The results reported here suggest that the dominant path through which the NAO induces higher evaporation is the intensification of surface winds. This intensification might ensue from the NAO-induced strengthening of tropospheric westerlies over this region, as discussed above (see Fig. 4.8), although the link between the two is not trivial
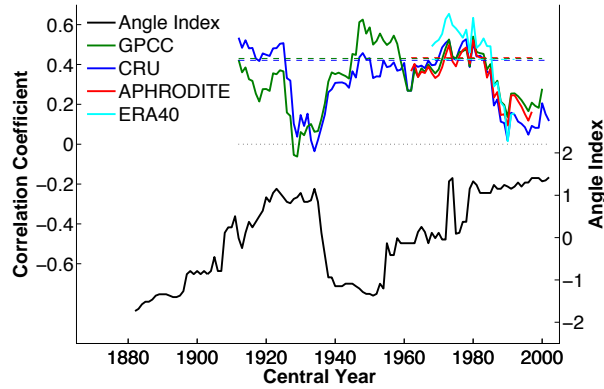
Figure 4.11: Sliding correlations on 21-year moving windows between the OBS-NAOI and the time series of precipitation averaged in the HKK domain (71-78°N/32-37°E) from GPCC (green), CRU (blue), APHRODITE (red) and ERA40 (cyan). Dashed lines indicate the 95 percent significance level and the dotted line indicates zero correlation. The black line is the time series of the Angle Index. Sliding correlations and the Angle Index have different y-axes on the left and right side respectively. Values are plotted at the 11th year of each 21-year window.

due to the strong influence of surface conditions.

4.6 Secular variations in the NAO-precipitation relationship

Yadav et al. (2009b) observed for the first time, using station data from the Indian Meteorological Department (IMD), that the relationship between the NAO and precipitation in north-west India underwent multi-decadal changes during the 20th century. To see if these changes are detectable also in the large-scale datasets used here, in Fig. 4.11 I show the sliding correlations over 21-year moving windows between the OBS-NAOI and the time series of precipitation averaged in the HKK domain from GPCC, CRU, APHRODITE and ERA40. The HKK domain is defined, as in Palazzi et al. (2013), in the range 71-78°E/32-37°N and is highlighted by the white rectangle in Fig. 4.1. Note that this domain slightly differs from the one used in Yadav et al. (2009b), who focused on a larger portion of north-western India and did not include northern Pakistan.

The various datasets have different temporal coverages, but they all show consistent changes in the NAO-precipitation relationship during their overlapping periods. Correlation coefficients between the NAO and precipitation are significant in the period between 1940 and 1980, while they are not significant after 1980 and between 1920 and 1940. The two datasets extending to the first years of the 20th century show a stronger signal before 1920 with respect to the following decade (the correlations are statistically significant in CRU, not in GPCC) and seem to
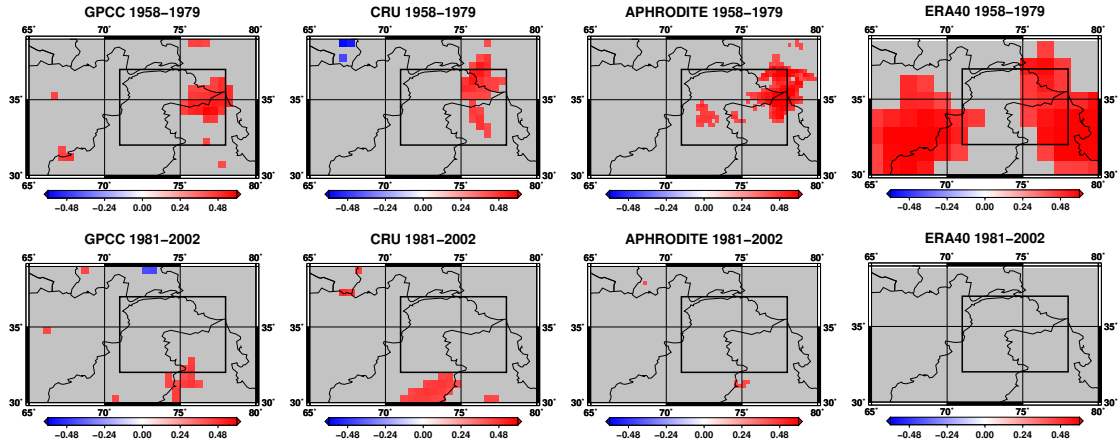
Figure 4.12: Correlation coefficients between the OBS-NAOI and winter precipitation from (left to right) GPCC, CRU, APHRODITE and ERA40 during the periods 1958-1979 (top) and 1981-2002 (bottom). Colors indicate statistically-significant correlations at the 95 percent confidence level. Non-significant correlations are marked in gray. The black rectangle highlights the HKK domain.

suggest a decline of the NAO control on precipitation during these years. However, it is worth pointing out that precipitation estimates are less and less reliable as we move back to the beginning of the century, as the number of stations in this area decreases and the gridded datasets are obtained by interpolating data from stations which are quite far from each other.

As a further check, Fig. 4.12 shows the spatial distribution of the correlations between the OBS-NAOI and precipitation from the different datasets during the periods 1958-1979 and 1981-2002, i.e. before and after 1980. In the HKK region, all datasets indicate a more widespread area of statistically significant correlations during 1958-1979 than during 1981-2002 (when significant correlations almost disappear), consistent with the drop of the correlation occurring around 1980 shown in Fig. 4.11. These changes in the intensity of the NAO-precipitation correlations are in good agreement with the results of Yadav et al. (2009b), giving robustness to our findings and showing that the large-scale datasets describe multi-decadal variations in a consistent manner.

Fig. 4.11 shows the time series of the Angle Index, measuring the spatial displacements of the NAO pattern in the North Atlantic on decadal timescales. The temporal evolution of the AI shows interesting similarities with the time series of the correlation between the NAO and precipitation, and the two seem to evolve in antiphase: in the two periods with non-significant correlations (1920-1940 and 1980-onwards) the AI shows the highest values (that is, the NAO has a positive tilt). Vice versa, the period with significant correlations (1940-1980) is characterized by lower values of the AI, which was strongly negative before the mid-50s

(when GPCC shows its highest correlations) and approximately zero afterwards. At the beginning of the 20th century, when CRU and GPCC suggest a weakening of the NAO-precipitation relationship, the AI is moving from negative to positive values. As discussed in section 4.4, there are sources of variability other than the NAO for precipitation in this area. These factors add noise to the record of sliding correlations, potentially worsening the synchronization with the time series of the AI. However, these results support the view that the position of the NAO COAs regulates the strength of the NAO-precipitation relationship in the HKK region. In particular, Fig. 4.11 suggests that when the NAO has a positive tilt, the NAO-precipitation correlation is weaker, while suitable conditions for the NAO-precipitation correlation are found when the NAO shows a negative — or at least very small — tilt.

Previous work showed that shifts of the NAO COAs have significant implications for the circulation response to the NAO phase in the North Atlantic and European sectors (Jung et al., 2003; Wang et al., 2012), with possible implications also outside these domains. In section 4.5 we have discussed how the NAO control on precipitation in the HKK occurs through the regulation of westerlies in the region of the MEJS, including changes in evaporation. To investigate whether the different configurations of the spatial pattern of the NAO shown in Fig. 4.4 have an effect on the way the NAO regulates westerlies in this region, I compute composites of the correlation coefficients between the OBS-NAOI and 250 hPa zonal winds conditioned on periods when the AI is high or low (that is, more than one standard deviation above or below the mean). To have a larger temporal coverage, from winter 1872 to winter 2012, I use the 20CR wind data. Correlation fields are computed on 21-year windows, to be consistent with the definition of the AI. Results are shown in Figs. 4.13a and 4.13c for low and high values of the AI respectively. The dots highlight grid points where the correlation coefficients are statistically significant at the 95 percent confidence level in all the 21-year periods considered in the composite. The figures show four domains of influence of the NAO: negative values are found over Greenland and over a zonal band extending from southern US to Mediterranean Europe, while positive values are found at about 60°N from western Canada to Scandinavia and to the south from tropical North Atlantic to southeastern Asia. The latter region corresponds to the intensification of the MEJS. When the NAO has a negative tilt (Fig. 4.13a), significant correlations over Greenland are displaced more to the west and the bands of positive and negative correlation in the extratropical North Atlantic have a more southwest-northeast orientation. In the region of the MEJS, significant positive correlations are found from North Africa to Pakistan, indicating that the NAO exerts a strong control on the jet mainly when the AI is low. When the NAO has a positive tilt (Fig. 4.13c), negative correlations over Greenland are displaced more to the east and the two bands of significant correlations in the extratropical North Atlantic have a more zonal orientation. During these periods,
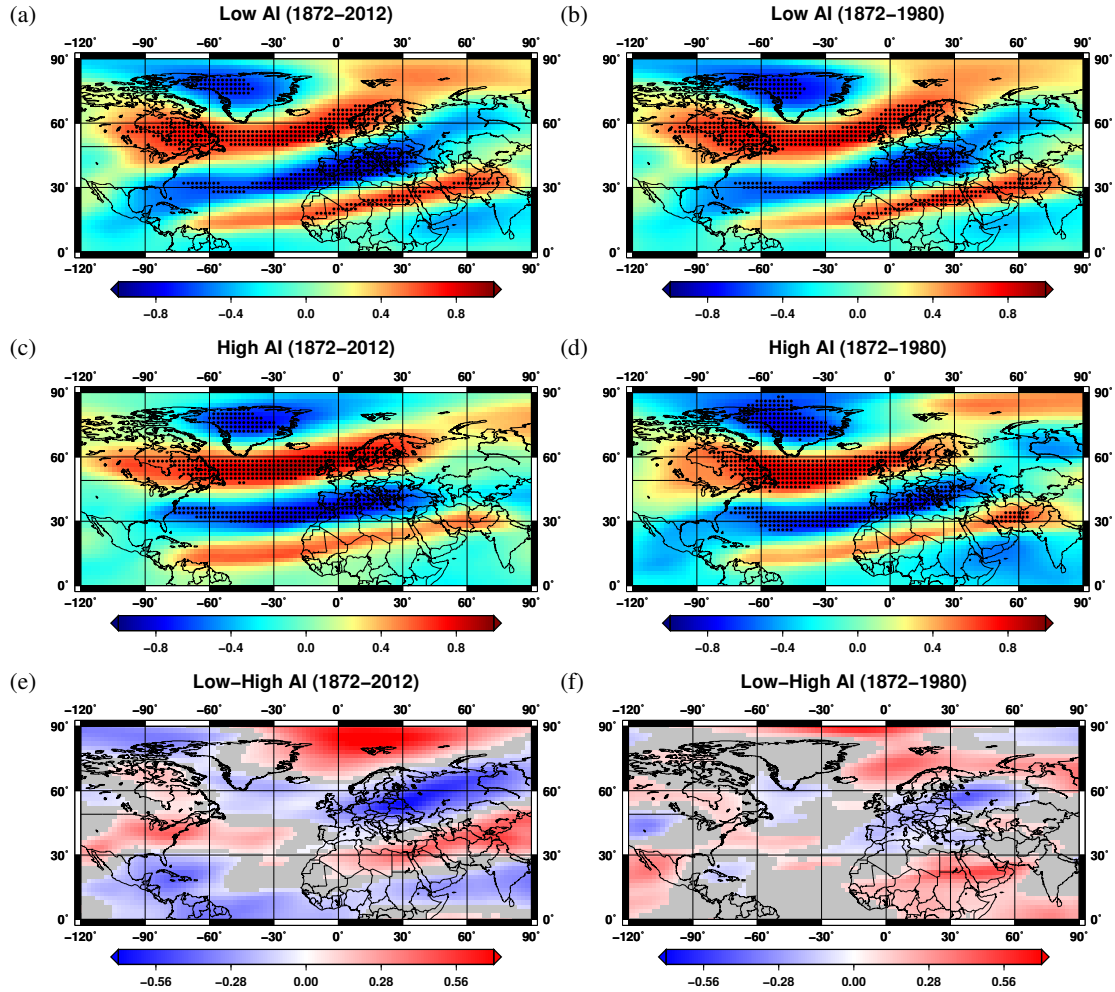
Figure 4.13: Composites of the correlation fields between the OBS-NAOI and 250 hPa zonal wind corresponding to (a) low and (c) high values of the Angle Index for the period 1872-2012. Correlation fields are computed on 21-year windows to be consistent with the definition of the Angle Index. Dots indicate grid points where the correlation coefficients are statistically significant at the 95 percent confidence level in all the 21-year periods considered in the composite. (e) Difference between the composites at low and high Angle Index, (a)-(c). Colors indicate statistically significant values at the 95 percent confidence level; gray indicates non-significant values. Significance of the difference is assessed using a time-shuffling method. (b), (d) and (f) are the same as (a), (c) and (e) respectively, but for the period 1872-1980.

characterized by high values of the AI, the NAO exerts only a weak control on the MEJS, with a drop of the statistical significance of the signal. In Fig. 4.13e I show the difference between Figs. 4.13a and 4.13c to further highlight the changes occurring between periods of low and high values of the AI. The significance of the difference is assessed using a time-shuffling method (Ciccarelli et al., 2008). The significant positive values occurring in the region of the MEJS indicate that differences between Figs. 4.13a and 4.13c in this area are large enough not to be just due to random sampling differences. The fact that, when the AI is high, the NAO does not project — or projects weakly — onto the MEJS can explain why the NAO-precipitation relationship weakens. Vice versa, suitable conditions for a significant NAO-precipitation signal occur when the AI is low because the NAO exerts a strong control on the jet.

Figs. 4.13a, 4.13c and 4.13e show the results obtained by considering all winters covered by 20CR data (1872-2012). After 1980, the atmospheric response to ENSO has strengthened; ENSO has started to influence also the intensity and position of the MEJS and consequently precipitation in the HKK. A stronger control of ENSO could weaken the NAO signature. Since this period shows high values of the AI, one might ask if the weaker signal in Fig. 4.13c could ensue from this change in ENSO. To investigate this issue, Figs. 4.13b, 4.13d and 4.13f are obtained exactly in the same way as Figs. 4.13a, 4.13c and 4.13e, but excluding the years after 1980 from the analysis. I anticipate that weaker differences are expected between low and high AI values during the period 1872-1980 than during 1872-2012, since I am excluding periods of strong positive AI. However, also in this case the differences in the NAO control of the jet associated with opposite values of the AI are evident. In Fig. 4.13d (high AI), significant positive correlations are found in a limited area over Iran, but the overall signal in the region of the MEJS is weak and non-significant. In Fig. 4.13b (low AI), the signal is stronger and statistically significant from North Africa to Pakistan. The differences between low and high AI shown in Fig. 4.13f are not significant over Iran, but they are significant over North Africa and Saudi Arabia. From these results, it can be stated that differences in the relationship between the NAO and the MEJS observed when the AI is high or low are independent of the changes that could have occurred in the period post-1980, and thus they are not a direct product of ENSO.

The AI is a measure of the relative position of the NAO COAs and considers both the northern and the southern node of the NAO. To understand if one of the two nodes is more important than the other, I have repeated the same analysis presented in Fig. 4.13 but using indices measuring the position of a single NAO COA instead of the AI (Fig. 4.14). Results are consistent with the considerations drawn from Fig. 4.13 for the AI and they indicate that both indices play a role in determining the strength of the NAO influence on the jet.
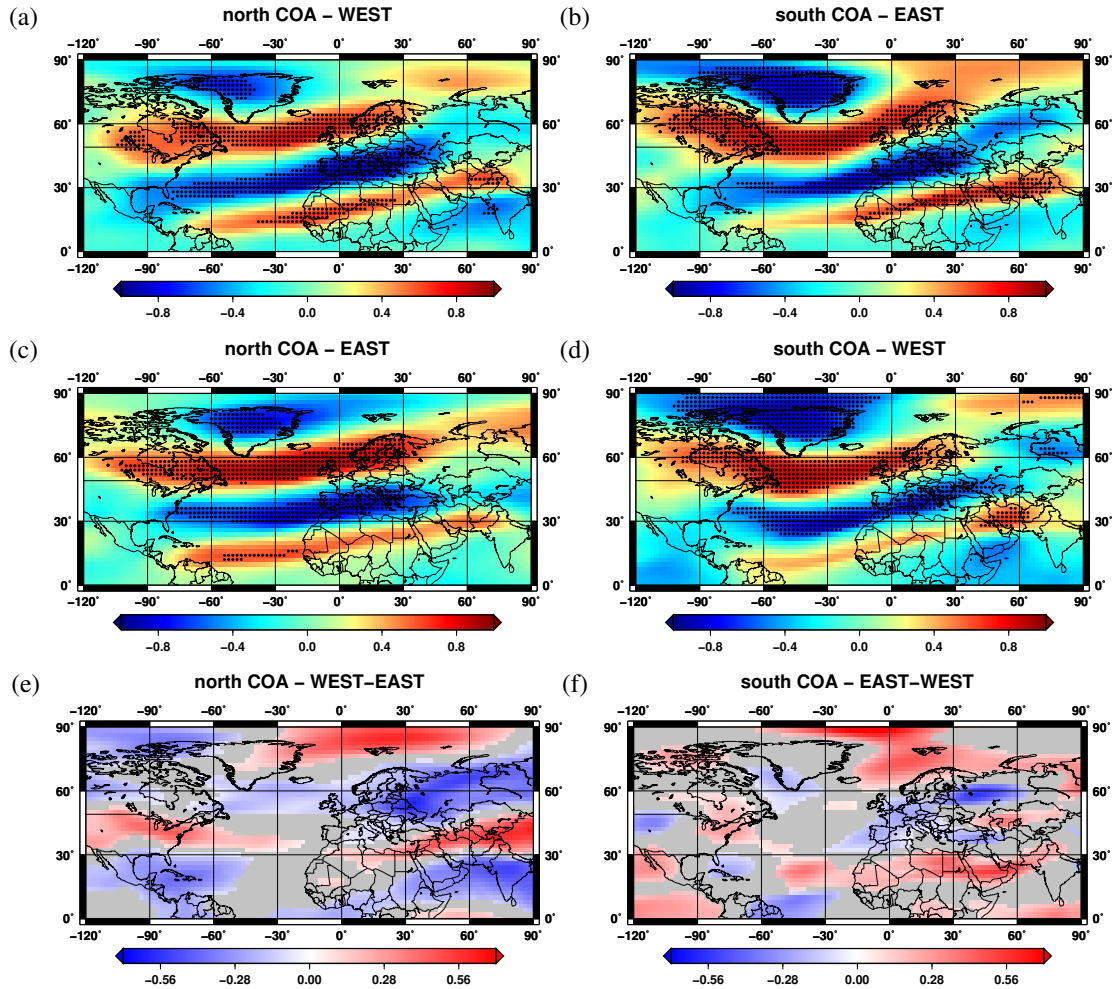
Figure 4.14: Same as in Fig. 4.13 but using the longitude of a single NAO COA instead of the Angle Index during the period 1872-1980. (a) corresponds to a westward displacement of the northern COA, (c) an eastward displacement and (e) the difference (a)-(c). (b) corresponds to an eastward displacement of the southern COA, (d) a westward displacement and (f) the difference (b)-(d).
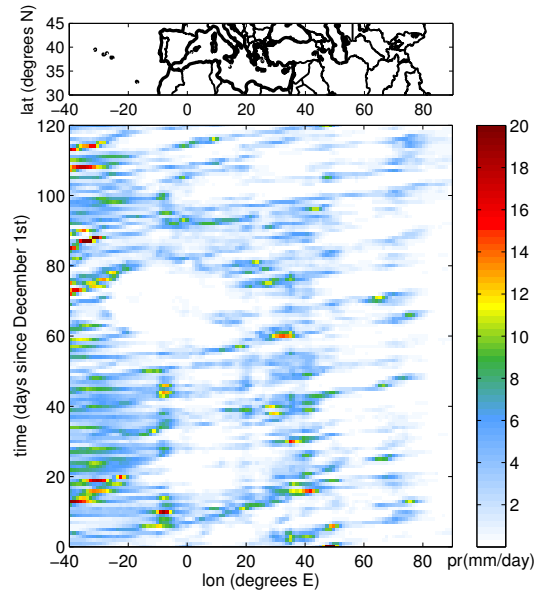
Figure 4.15: Top: Map showing the region considered in the analysis. Bottom: Daily precipitation during a winter season (model year 2001) from EC-Earth averaged over latitudes from 30 to 45°N and plotted as a function of longitude and time.

4.7 WWPs in the EC-Earth model

Discussion in the previous sections of this chapter embraces both well established concepts in climate science (e.g. the NAO interannual variability and westerly perturbations affecting the HKK during winter) as well as newer and less studied aspects of climate dynamics (e.g. mechanisms controlling WWPs and concurrent variations between the NAO spatial structure and the NAO-precipitation signal). Also, results presented in section 4.6 refer to variability over multi-decadal timescales, and longer data records — which are often not available from observations — are needed to discriminate between noise and significant signals. For these reasons, the topics of this chapter constitutes an intriguing framework where to use a climate model like EC-Earth, to check if the model is able to reproduce well-known features of the climate system and to give robustness to the new findings.

A first step is to establish if the model is able to reproduce the main climatic features of winter precipitation in the HKK. In section 1.5 I stressed that GCM performance in mountain regions may be limited by finite spatial resolution. In a previous study, Palazzi et al. (2013) already showed that precipitation climatology and annual cycle from EC-Earth are in reasonable agreement with observations in this region. Fig. 4.15 shows that also the WWPs dynamics on the synoptic time and spatial scales is well reproduced. Winter precipitation events in the HKK have
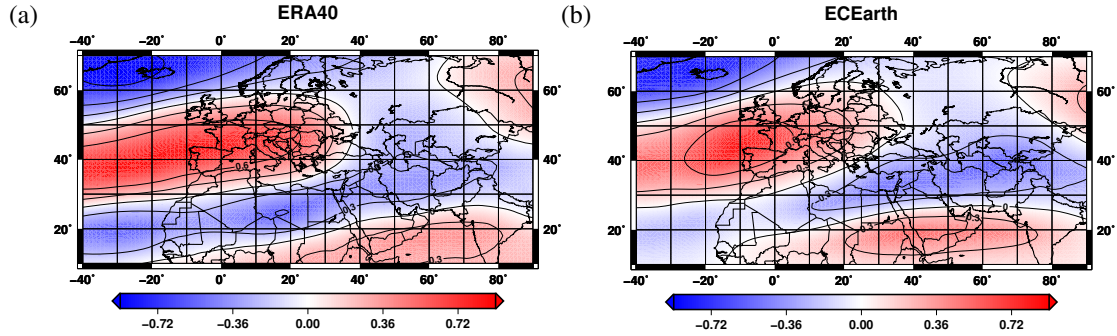
Figure 4.16: Correlation coefficients between (a) OBS-NAOI and 500 hPa geopotential from ERA40 and (b) MOD-NAOI and 500 hPa geopotential from EC-Earth during 1958-2002.

an average periodicity of about 1 week and are associated with weather systems generating in the Middle East, in the Mediterranean or even in the western North Atlantic. The slope of raining systems in Fig. 4.15 is consistent with Fig. 4.5, confirming the overall agreement between EC-Earth and observations.

Anstey et al. (2013) discussed the problems of CMIP5 models in reproducing Northern Hemisphere winter blocking and, consequently, the NAO (see for example Woollings et al., 2008). They showed that simulation skills improve with increasing model resolution, and EC-Earth (which is included in that study) resulted among the best performing CMIP5 models. Fig. 4.2 shows the temporal evolution of the EC-Earth NAOI (MOD-NAOI) and observation-derived NAOI (OBS-NAOI) used in this study. To verify that the two indices catch the same atmospheric features, in Fig. 4.16 I show the correlation map between MOD-NAOI and 500 hPa geopotential field from EC-Earth and compare it with the same metric but using OBS-NAOI and ERA40 500 hPa geopotential data over the region of interest. Correlation fields show that both indices are able to grab the main circulation anomalies associated with the NAO, including the Icelandic low, the Azores high and the 500 hPa trough over central-southwestern Asia described by Syed et al. (2010).

The NAO-precipitation signal in EC-Earth is shown in Fig. 4.17. The model performs well in reproducing the European precipitation dipole, with negative correlations over southern Europe and positive ones over northern Europe. The main difference from observational datasets (Fig. 4.6) is that significant positive correlations over northern Europe are limited to western Scandinavia in the model, while they extend deeper in the continent in observations. EC-Earth shows significant positive correlations in the HKK region: modelled signal is within the range of the signals displayed by the observational datasets, showing that it reliably reproduces the effects of the NAO on precipitation in this area.

In section 4.5 we discussed the mechanisms by which the NAO regulates pre-

ECEarth NAO CORR
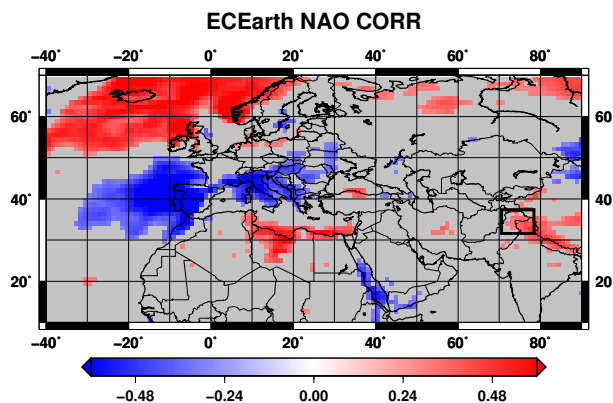
Figure 4.17: Correlation coefficients between the MOD-NAOI and winter precipitation from EC-Earth during model years 1958-2002. Colors indicate statistically-significant correlations at the 95 percent confidence level. Non-significant correlations are marked in gray. The black rectangle highlights the HKK region.
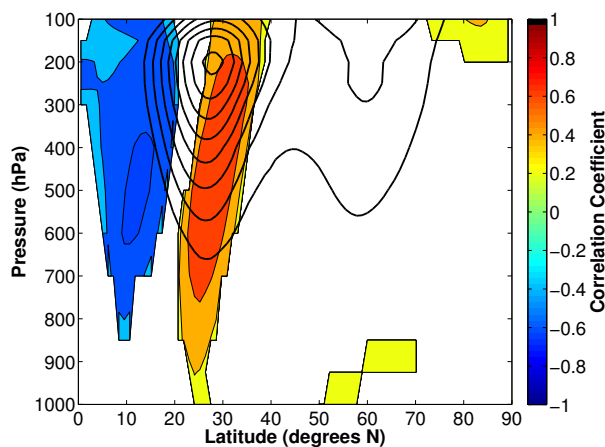
Figure 4.18: Filled colored contours: correlation coefficients between the MOD-NAOI and winter zonal wind from EC-Earth averaged over longitudes between 40 and 70°E during model years 1958-2002. Only correlations which are statistically significant at the 95 percent confidence level are reported. Black contours: climatology (1958-2002) of winter zonal wind averaged over longitudes between 40 and 70°E, identifying the position of the Middle East jet stream. Only values above 10 m s^{-1} are reported. Contour interval is 5 m s^{-1}.
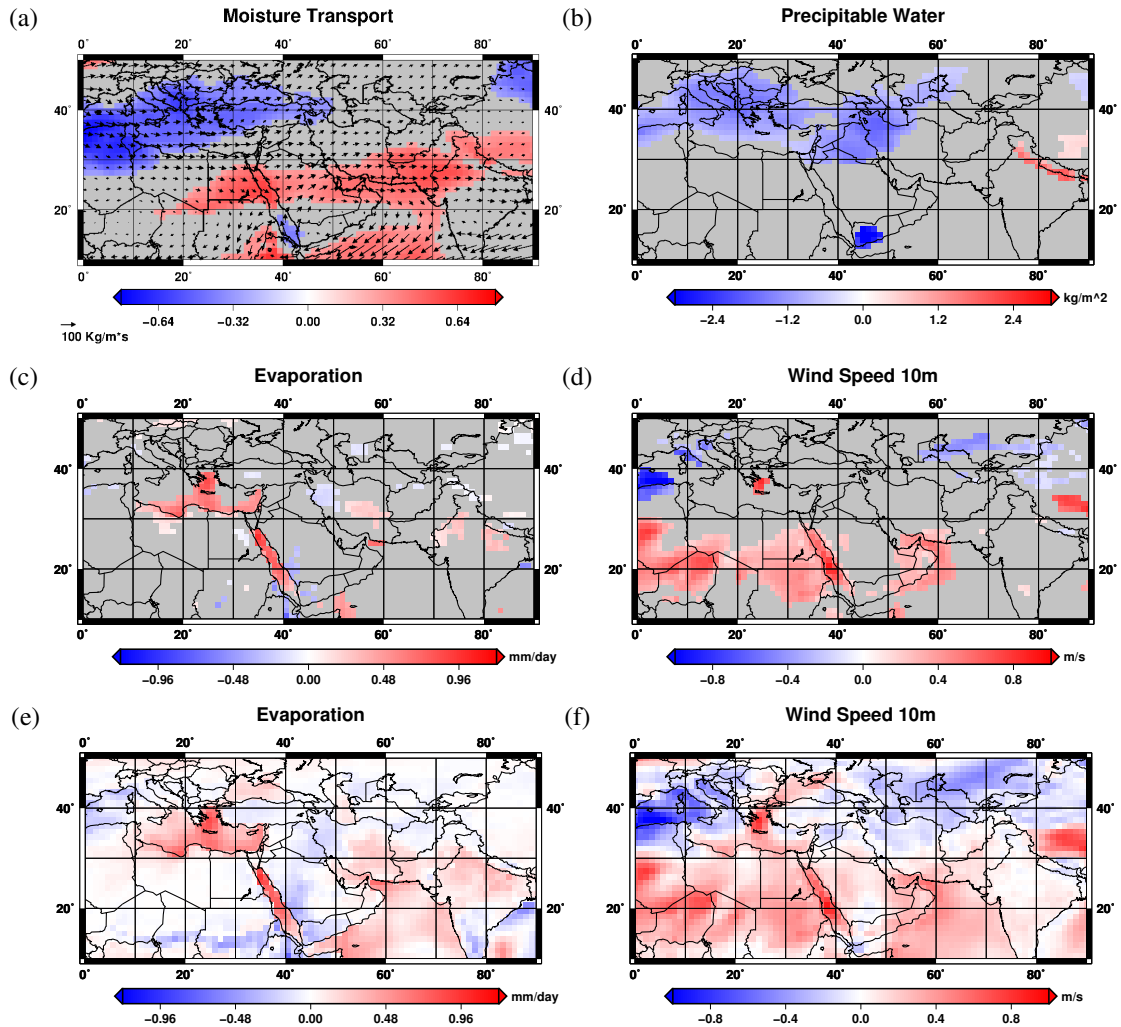
Figure 4.19: (a) Climatology of EC-Earth moisture transport during winter (vectors) and correlation coefficients between the MOD-NAOI and the intensity of moisture transport (color map) during model years 1958-2002. Colors are used for statistically significant correlations at the 95 percent confidence level; gray indicates non-significant correlations. (b), (c) and (d) Difference between the positive and the negative NAO composites of (b) precipitable water, (c) evaporation and (d) 10m wind speed from EC-Earth during model years 1958-2002. Colors indicate statistically significant values at the 95 percent confidence level; gray indicates non-significant values. (e) and (f) The same as (c) and (d) but displaying also non-significant values with colors.

cipitation in the HKK and we emphasized the role of the MEJS and moisture transport. Fig. 4.18 shows the MEJS in EC-Earth (black contours) and the effect of the NAO on westerly winds in this region. First, note that the model reliably reproduces both the location and the average intensity of the MEJS; second, the NAO effect on westerlies in EC-Earth is totally consistent with the picture drawn from observations (compare Figs. 4.18 and 4.8). Fig. 4.19a (arrows) shows the climatology of vertically integrated moisture transport from EC-Earth. The model underestimates the intensity of moisture transport with respect to ERA40 in some regions (see for example the length of arrows over the Mediterranean Sea as well as in the region from Arabia towards Pakistan), but overall moisture trajectories from the model are in very good agreement with observations (Fig. 4.10). Moreover, EC-Earth reproduces well the effects of the NAO on moisture transport discussed in section 4.5, with negative correlations over the Mediterranean Sea and significant positive correlations from the Arabian Peninsula towards Pakistan and western India (colors in Fig. 4.19a). Also in EC-Earth the intensification of moisture transport in this area produces an accumulation of humidity at the foot of the Himalayas during the positive NAO phase (Fig. 4.19b).

Observation analysis suggests that the strengthening of moisture transport from Arabia towards Pakistan is sustained by higher evaporation from the southeastern Mediterranean, the Red Sea, the Persian Gulf and the northern Arabian Sea, mainly associated with an intensification of surface winds. This hypothesis is further supported by simulation results from the EC-Earth model. Figs. 4.19e and 4.19f show the difference between the positive and the negative NAO composites of evaporation and 10m wind speed respectively, and positive values occur everywhere over these basins. However, the statistical significance of this signal in EC-Earth is lower than in observations (compare Figs. 4.19c and 4.19d with Figs. 4.10b and 4.10c). The evaporation signal in the model is statistically significant at the 95 percent confidence level over the southeastern Mediterranean and the Red Sea, but it is generally not significant in the Arabian Sea and the Persian Gulf. Similarly, the portion of the Arabian Sea affected by statistically significant anomalies of surface wind speed is largely reduced. Finally, EC-Earth does not show NAO-associated signals of SST over these basins. On the one hand, this could partly explain the weaker evaporation signal in the model. On the other hand, it suggests that higher SSTs are not the dominant path through which the NAO regulates evaporation and, by consequence, moisture transport in this area.

Section 4.6 discusses how changes in the spatial structure of the NAO in the North Atlantic have implications in the relationship between the NAO and precipitation in the HKK over multi-decadal timescales. Fig. 4.3 compares the temporal evolution of the NAO COAs from observations (20CR) and EC-Earth. The range of positions covered by the COAs in the model is in agreement with observations. Latitude changes are relatively confined, with the northern COA centered between 60 and 70°N and the southern one between 40 and 50°N. Vice versa, longitudinal
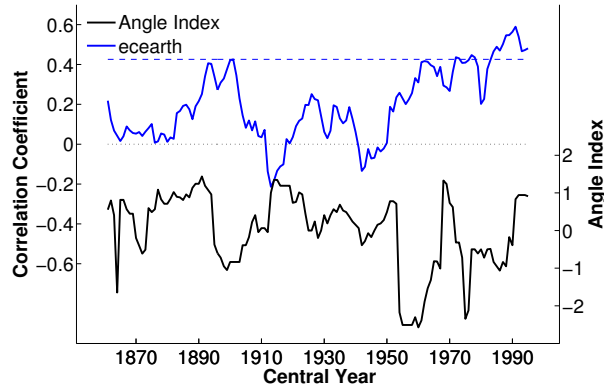
Figure 4.20: Sliding correlations on 21-year moving windows between the MOD-NAOI and the time series of precipitation averaged in the HKK domain (71-78°N/32-37°E) from EC-Earth (blue). The dashed line indicates the 95 percent significance level and the dotted line indicates zero correlation. The black line is the time series of the MOD-AI. Sliding correlations and the Angle Index have different y-axes on the left and right side respectively. Values are plotted at the 11th year of each 21-year window.

changes are higher, varying between 40°W and 0–20°E for both COAs. The main difference between model and observations is related to the longitude of the northern node, which generally resides in the western part of the domain in the model while it spends much more time in the eastern part in observations. However, as stated before, the range of longitudinal variability is consistent between model and observations, and this difference is probably just a consequence of the fact that we have to deal with finite time series. Another difference is that time series from the model are generally noisier (i.e. they show variability over shorter timescales) than observations, and this is reflected by the temporal evolution of the MOD-AI and the OBS-AI shown in the bottom panels of Fig. 4.3.

Despite its noisier behaviour, also the evolution of the MOD-AI is synchronized with the time series of sliding correlations between the NAO and HKK precipitation from EC-Earth (Fig. 4.20), with significant correlations occurring during periods of low values of the Angle Index. In section 4.6 I discussed how this synchronization ensues from the different way the NAO regulates the the MEJS during periods of positive and negative tilt. In Fig. 4.21 the composites of the correlation coefficients between the MOD-NAOI and 250 hPa zonal wind from EC-Earth conditioned on periods when the MOD-AI is high or low are shown. The model is able to catch the main differences in the NAO-associated circulation response corresponding to opposite phases of the Angle Index. The bands of positive and negative correlation in the extratropical North Atlantic have a more southwest-northeast orientation when the MOD-AI is low, while they are more zonal when the MOD-AI is high. Moreover, the NAO has a strong control on the
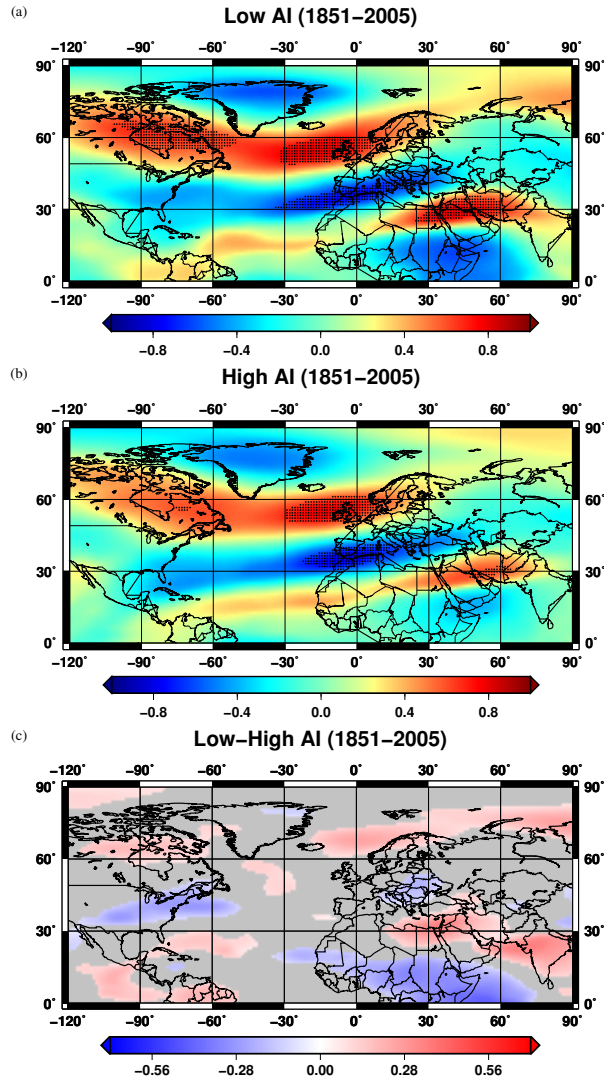
Figure 4.21: Composites of the correlation fields between the MOD-NAOI and 250 hPa zonal wind from EC-Earth corresponding to (a) low and (b) high values of the MOD-AI during the whole simulation period (1851-2005). Correlation fields are computed on 21-year windows to be consistent with the definition of the Angle Index. Dots indicate grid points where the correlation coefficients are statistically significant at the 95 percent confidence level in all the 21-year periods considered in the composite. (c) Difference between the composites at low and high Angle Index, (a)-(b). Colors indicate statistically significant values at the 95 percent confidence level; gray indicates non-significant values. Significance of the difference is assessed using a time-shuffling method.

MEJS when the MOD-AI is low, while the significance of the signal in this region drops when the MOD-AI is high. Thus, also in the model EC-Earth the strength of the relationship between the NAO and precipitation in the HKK is regulated by the relative position of the NAO COAs, through the control of the intensity of westerlies in the region of the MEJS. As highlighted before, observations are constrained by their temporal coverage and become less and less reliable as we move back in time. Since the model simulation constitutes an independent experiment, this result gives robustness to the findings of section 4.6.

4.8   Conclusions

Winter precipitation in the Hindu-Kush Karakoram (HKK), an essential water input for the area, is associated with the arrival of westerly perturbations, the Western Weather Patterns (WWPs), originating from the Mediterranean and northeastern Atlantic regions. The existence of correlations between the NAO and winter precipitation in the HKK is well known (Syed et al., 2006, 2010; Yadav et al., 2009b). Here I have used an ensemble of large-scale precipitation datasets, showing that they coherently reproduce the NAO-precipitation link, and I have discussed the processes responsible for the relationship between the NAO and winter precipitation in the HKK. I have also addressed the issue related to the multi-decadal variations occurring in the NAO-precipitation relationship and I have argued that these changes are related to the spatial structure of the NAO pattern in the North Atlantic basin. The whole analysis has been repeated using a historical simulation from EC-Earth (1850-2005), showing that the model reliably reproduces the main processes considered here and giving robustness to the new findings.

The analysis of the relationship between the NAO and precipitation estimates from three rain-gauge-based datasets (APHRODITE, CRU and GPCC) and the ERA40 reanalysis confirms that the NAO influences the amount of precipitation in the HKK. All datasets show that years in the positive (negative) NAO phase are characterized by above (below) normal precipitation over the target area in winter (December to March). Differences among the datasets arise in the spatial extent, intensity and significance level of the NAO-associated precipitation anomalies. Compared to the three rain-gauge-based datasets, ERA40 shows a stronger link between the NAO and precipitation. The weaker signal found in the rain-gauge-based datasets can be due to the difficulty of rain gauges to detect the snow component of precipitation and biases arising from the sparse station coverage.

The relationship between precipitation and the NAO is maintained through the control exerted by the NAO on the westerlies in the region of the Middle East jet stream (MEJS), from North Africa to southeastern Asia. At longitudes between 40°E and 70°E, where the majority of moisture transport towards the HKK takes place, the intensification of the westerlies during the positive NAO phase is evident from the upper-tropospheric jet to the lower-level westerlies. The stronger jet in-

tensifies the WWPs (Yadav et al., 2009b) and faster westerlies in the middle-lower troposphere intensify moisture transport towards the HKK (Syed et al., 2010). In addition to this, evaporation plays an important role in the mechanism. The main moisture sources for precipitation in the HKK are in the northern Arabian Sea, the Red Sea, the Persian Gulf and, to a lesser extent, the Mediterranean. During the positive NAO phase, enhanced evaporation occurs from these reservoirs, mainly related to higher surface wind speed. Surface wind anomalies might be associated with the strengthening of westerlies in this region during the positive NAO phase, even if the link with upper level circulation is not trivial owing to the strong effects of surface topography. The increased humidity arising from evaporation combines with the intensification of westerlies to give enhanced moisture transport towards the HKK. As a consequence, wetter conditions are found over northern Pakistan and northern India and larger precipitation amounts are released as the WWPs reach this region.

The precipitation datasets used in this study show significant multi-decadal variations in the relationship between the NAO and precipitation, consistent with observations of Yadav et al. (2009b). I have used the NAO Angle Index (AI) introduced by Wang et al. (2012) to measure the slow movements of the NAO centers of action. Results show that high values of the AI (positive tilt of the NAO) are associated with non-significant correlations between the NAO and precipitation in the HKK, while significant correlations occur when the AI is negative. Shifts in the position of the NAO COAs have significant implications for the NAO-associated circulation anomalies in the troposphere. In particular, when the AI is low, the NAO exerts a strong control on the MEJS and, as a consequence, the mechanism of regulation of the HKK precipitation by the NAO is activated. The opposite occurs when the AI is high. The AI considered here is one of the possible indices measuring the changes in the NAO spatial pattern, and others can be defined that capture slightly different features (such as considering only one of the two centers of action). What is important here is that changes in the spatial structure of the NAO pattern can be crucial in determining the strength of the relationship between the NAO and other climatic parameters, and as a consequence in determining precipitation in the HKK.

The analysis with EC-Earth further supports conclusions drawn from observations. The model is able to reliably reproduce well-known processes considered here (such as the NAO effects on circulation and precipitation over the European sector) as well as the new findings (such as processes underlying the NAO-precipitation relationship in the HKK and the associated variability over multi-decadal timescales), attesting it is a valuable tool to investigate these aspects and giving robustness to the results presented here. Sometimes the analysis of the NAO-associated anomalies in the model has shown slightly weaker signals than in the observation-derived datasets (see for example the evaporation response to the NAO phase), possibly suggesting that the NAO control on some variables

in the model is not as strong as in observations. However, note that the NAOI adopted here is obtained according to the station-based definition introduced by Hurrell (1995), which is widely used when analyzing observations because of the long-standing availability of in-situ station data, but less common when working with modern GCMs. While I have tested that other NAOI definitions do not affect significantly the results presented here, different NAO indices exist that can potentially give stronger signals in the model. Finally, one should always keep in mind that also observations can be biased, they are available over limited time spans and different data sources are needed to constrain uncertainties related to observed signals.

Chapter 5

Elevation Dependent Warming

5.1 Overview

Climate change in mountain regions has received increasing attention in recent years, owing to the crucial role that mountains play on environments, economies and societies worldwide (see section 1.5). In this framework, there is growing evidence that the rate of temperature change with increased levels of greenhouse gases (GHG) in the atmosphere is amplified with elevation, i.e. that mountainous regions are warming faster than adjacent lowlands, similarly to the warming amplification observed in the Arctic (Screen and Simmonds, 2010; Serreze and Barry, 2011). This phenomenon has been referred to as Elevation-Dependent Warming (EDW). Evidences of EDW have emerged from a number of studies using different methods and data sources, including in-situ observations, satellites estimates, reanalyses products and outputs of climate models. A review of existing studies is presented by Rangwala and Miller (2012). However, there is not a general consensus and some studies exist that show either no relationship or a more complex situation, suggesting a seasonal dependence of the rate of warming with elevation, asymmetry in the response of daytime and night-time temperatures to GHG increase as well as regional differences (MRI, 2015). Typically, observational studies tend to be less in agreement than model simulations, probably also because models are integrated over longer time periods and can be used to project changes in the future, when EDW may become more widespread than it has been so far.

It is extremely difficult to determine the rate of warming in mountainous regions from available observations for a number of reasons. As discussed also for precipitation measurements in section 4.1, in-situ stations are extremely sparse at high altitudes, and regions above 5000 m are mostly unexplored. Conversely to other areas, mountain temperatures show strong local variability on small spatial scales due to topography, slope, vegetation coverage and exposure. Satellite data have the advantage of being spatially homogeneous, but they are limited by their temporal coverage, which is typically too short to study long-term trends, and

they are still poorly validated in high-elevation regions where clouds are common. Also reanalysis data should be treated with care, since they are not homogenized for climate trend analysis (Bengtsson et al., 2004a). Model simulations, on the other hand, do not suffer of most of problems affecting observations, but they are generally limited by poor spatial resolution (see also section 1.5 for issues concerning climate modelling in mountainous regions). Furthermore, they require observational data for validation, making it difficult to be sure that simulations are accurate.

Since temperature at the Earth's surface is primarily a response to the energy balance, potential drivers for EDW are those factors that preferentially increase the net flux of energy to the surface along an elevation gradient. These factors include, but are not limited to, the snow/ice-albedo feedback, the water vapour feedback and the cloud-radiation feedback. Also aerosols have been indicated as potential drivers for EDW, but their net contribution is less clear. An overview of possible mechanisms driving EDW is given by MRI (2015). Climate models are the preferred tools to investigate the possible mechanisms responsible for EDW, mainly because they allow to study a number of variables for which observations are often not available.

One of the regions showing the strongest signal of elevation dependent warming in both observations and model simulations is the Tibetan Plateau area (Rangwala et al., 2013; Yan and Liu, 2014), which constitutes, together with the surrounding chains of the Himalayas, the largest mountain region in the world (the so called "Third Pole" of the Earth, see section 1.5.1). Rangwala et al. (2015) analysed the outputs of several coupled GCMs from the CMIP5 experiment (see section 1.4) to investigate EDW in the latitude band between 27.5°N and 40°N, encompassing the Tibetan Plateau-Himalayas in Asia and the Rocky Mountains in north America. They found an amplification of the warming rates in the mountainous regions, particularly for the minimum temperatures in the cold season, and they ascribed it to an increase in downward longwave radiation at higher elevations, associated with increases in atmospheric water vapour. These results are consistent with a previous study by Liu et al. (2009), which used both observations and model projections for the Tibetan Plateau region and observed a stronger EDW in winter and spring, likely caused by a combination of cloud-radiation and snow-albedo feedbacks.

The present analysis focuses on the EDW in the region encompassing the Tibetan Plateau, Hindu-Kush, Karakoram and Himalayan mountains and the surrounding lower-lying regions using an ensemble of model simulations from the CMIP5 archive. Historical simulations as well as future projections under a high-range emission scenario (RCP8.5) according to the IPCC Fifth Assessment Report (IPCC AR5, see also section 1.4) are considered. The possible mechanisms leading to EDW in this region are investigated and a multiple regression model is used to evaluate their relative contribution to the simulated change in either the minimum and the maximum temperature.

Topography of the Study Area
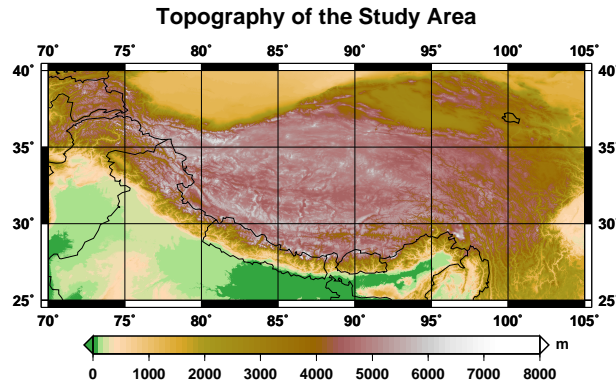
Figure 5.1: Topography of the study area, corresponding to panel (a) of Fig. 1.6

This chapter is structured as follows: section 5.2 presents the climate models and methods employed in this study; section 5.3 gives an overview of the average warming and of the spatial distribution of the temperature change in the Tibetan Plateau-Himalayan region; section 5.4 discusses the EDW signal emerging from the ensemble of climate models considered here; the mechanisms leading to EDW are investigated in section 5.5; final considerations are drawn in section 5.6.

5.2   Data and methods

The area considered in this study extends from 70°E to 105°E longitude and from 25°N to 40°N latitude (Fig. 5.1), covering the Tibetan Plateau-Himalayas and their surroundings, including the Hindu-Kush Karakoram region discussed in chapter 4. A detailed description of the area, including a comparison between the actual topography and CMIP5 model orographies, is presented in section 1.5.1.

Outputs from 27 coupled GCMs participating in the Coupled Model Intercomparison Project phase 5 (CMIP5) are considered. This set includes only models for which the relevant variables for this study — surface altitude (*orog*), daily maximum and minimum near surface air temperature (*tasmax* and *tasmin*, respectively), surface downwelling longwave radiation (*rlds*), surface downwelling shortwave radiation (*rsds*), surface upwelling shortwave radiation (*rsus*), near surface specific humidity (*huss*) — are available from the Earth Science Grid Federation archive data portals (`esgf.llnl.gov`). Surface *albedo* is computed as the ratio between *rsus* and *rsds*. For each climate model only one member (the so called "r1i1p1" member) is considered. These models, along with their horizontal resolution and a key reference, are listed in table 5.1. Further model details and information on their configurations can be found in the PCMDI data portal (`www-pcmdi.llnl.gov`) and in Chapter 9 of the IPCC Fifth Assessment Report (IPCC AR5).

Table 5.1: The CMIP5 models used in this study, ordered by increasing resolution.

Model ID	Institution ID	Resolution Lon×Lat° Lev	Grid points (TP-Him)	Key reference
FGOALS-g2	LASG-CESS	2.8125×2.8125L26 (T63)	65	Li et al. (2013)
CanESM2	CCCMA	2.8125×2.8125L35 (T63)	65	Arora et al. (2011)
BNU-ESM	GCESS-BNU	2.8125×2.8125L26 (T42)	65	Ji et al. (2014)
bcc-csm1-1	BCC	2.8125×2.8125L26 (T42)	65	Wu et al. (2013)
MIROC-ESM	MIROC	2.8125×2.8125L80 (T42)	65	Watanabe et al. (2011)
MIROC-ESM-CHEM	MIROC	2.8125×2.8125L80 (T42)	65	Watanabe et al. (2011)
IPSL-CM5B-LR	IPSL	3.75×1.9L39	80	Hourdin et al. (2013a)
IPSL-CM5A-LR	IPSL	3.75×1.89L39	80	Hourdin et al. (2013a)
GISS-E2-R	NASA/GISS	2.5×2L24	112	Schmidt et al. (2006)
GISS-E2-H	NASA/GISS	2.5×2L24	112	Schmidt et al. (2006)
GFDL-ESM2M	GFDL	2.5×2L24 (M45)	112	Delworth et al. (2006)
GFDL-ESM2G	GFDL	2.5×2L24 (M45)	112	Delworth et al. (2006)
GFDL-CM3	GFDL	2.5×2L48 (C48)	112	Delworth et al. (2006)
NorESM1-M	NCC	2.5×1.9L26 (F19)	120	Bentsen et al. (2013)
CSIRO-Mk3-6-0	CSIRO-QCCCE	1.875×1.875L18 (T63)	152	Rotstayn et al. (2012)
INM-CM4	INM	2×1.5L21	180	Volodin et al. (2010)
IPSL-CM5A-MR	IPSL	2.5×1.2587L39	180	Hourdin et al. (2013a)
HadGEM2-CC	MOHC	1.875×1.24L60 (N96)	247	Martin et al. (2011)
ACCESS1-3	CSIRO-BOM	1.875×1.25L38	247	Bi et al. (2013)
ACCESS1-0	CSIRO-BOM	1.875×1.25L38 (N96)	247	Bi et al. (2013)
MIROC5	MIROC	1.40625×1.40625L40 (T85)	275	Watanabe et al. (2010)
CNRM-CM5	CNRM-CERFACS	1.40625×1.40625L31 (T127)	275	Voldoire et al. (2013)
MRI-CGCM3	MRI	1.125×1.125L48 (T159)	434	Yukimoto et al. (2012)
bcc-csm1-1-m	BCC	1.125×1.125L26 (T106)	434	Wu et al. (2013)
CESM1-CAM5	NSF-DOE-NCAR	1.25×0.9L27	435	Hurrell et al. (2013)
CESM1-BGC	NSF-DOE-NCAR	1.25×0.9L27	435	Hurrell et al. (2013)
CCSM4	NCAR	1.25×0.9L27 (T63)	435	Meehl et al. (2012)

For each CMIP5 ensemble member considered here, I analyse outputs from the historical experiment (1870-2005) and the future projection under the emission scenario RCP8.5 (2006-2100), corresponding to an anthropogenic radiative forcing of 8.5 Wm^2 by the end of the 21st century (Riahi et al., 2011). Previous studies showed that projected temperature changes in the Tibetan Plateau region are similar among different RCPs, with differences occurring just in the magnitude of the change (being strongest in the most extreme RCP8.5 scenario).

Throughout this chapter, the analysis of individual models is performed using model outputs at their native resolution (without remapping). In addition, a Multi-Model Mean (MMM) of the considered ensemble is computed after regridding all individual model outputs onto a common 2×2 degrees resolution grid. To investigate possible seasonal asymmetries in the EDW signal suggested by previous studies on this topic, the whole analysis presented here refers to seasonal averages, using the standard definition of the seasons for the Northern Hemisphere mid-latitudes: winter (December to February, DJF), spring (March to May, MAM), summer (June to August, JJA), and autumn (September to November, SON).

Seasonal changes in minimum and maximum temperatures and other variables are computed as the difference of the 30-year climatology between the periods 1971-2000 and 1871-1900 ("historical" changes) and between the periods 2071-2100 and 1971-2000 (future changes under the RCP8.5 scenario). Minimum and maximum temperatures are considered separately because they are likely affected differently by various climate drivers (see for example Rangwala et al., 2013). The relationship between temperature — or other variable — changes and elevation is explored by using simple linear regressions and correlation coefficients and assessing their statistical significance. The latter is determined using a Monte Carlo "shuffling" method to test against the null-hypothesis of no elevational gradients (Pollard et al., 1987; Schreiber and Schmitz, 2000). A significance level of 95% is always used.

To study the mechanisms leading to EDW, I consider the seasonal changes of *rlds*, *rsds*, *huss* and *albedo* and I analyse their dependence on elevation. Their relative importance in driving the temperature change in the study area is assessed using a multiple linear regression model. Further details on these procedures are given in section 5.5.

5.3 Warming in the Third Pole environment

Before digging deep into the question of the EDW, in this section a brief overview of the average signal and the spatial pattern of the temperature change in the Tibetan Plateau-Himalayan region is given.

Figure 5.2 shows the average change of minimum and maximum temperatures in the study area for the four seasons in the historical period and in the RCP8.5 scenario from the MMM. Independently from the season and the period, both
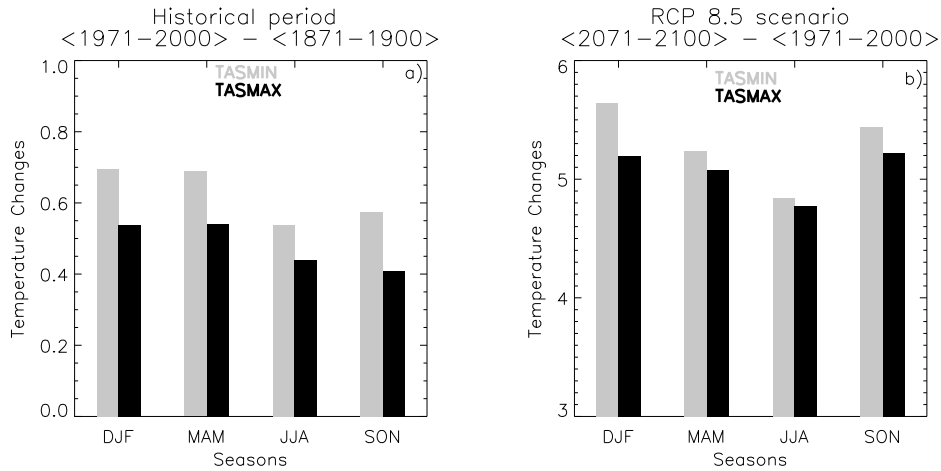
Figure 5.2: Seasonal temperature changes in the Tibetan Plateau-Himalayas (70°E-105°E; 25°N-40°N) in the historical period (left) and in the scenario simulations (right) from the multi-model ensemble mean. Seasons are defined as winter (DJF), spring (MAM), summer (JJA) and autumn (SON).

minimum and maximum temperatures indicate an average warming. Projected changes show higher values, being one order of magnitude higher than the historical ones. An interesting feature emerging Fig. 5.2a is that the minimum temperatures exhibit a stronger absolute change than the maximum temperatures in the historical period. This finding is consistent with previous studies highlighting the asymmetric nature of the warming rates during daytime and nighttime in the Tibetan Plateau (e.g., Liu et al., 2009). However, this asymmetry weakens in the future simulations, being evident only during DJF. Seasons showing the strongest changes of both *tasmin* and *tasmax* during the historical period are DJF and MAM. In future projections, the strongest signals occur during SON, DJF and MAM, while the average warming is something weaker during JJA.

Figs. 5.3 and 5.4 show the spatial maps of the changes in minimum and maximum temperatures from the MMM for the historical period and the RCP8.5 scenario respectively. Note that all changes are greater than zero, and they are statistically significant at the 95% confidence level. While these figures further support the considerations about the average warming in the Tibetan Plateau-Himalayas drawn from Fig. 5.2, they clearly highlight that there is not a unique spatial pattern of warming common to all seasons, variables (i.e. *tasmin* and *tasmax*) and time periods, indicating that different drivers may be at play during day and night, winter and summer, and different historical periods. The only feature that is relatively consistent among the various panels — at least in the RCP8.5 scenario (Fig. 5.4) — is that smaller changes generally occur to the south of the Himalayan chain and stronger ones to the north of it, suggesting a tendency of

Figure 5.3: Spatial maps of the change between the period 1971-2000 and the period 1871-1900 of the minimum temperature (left) and of the maximum temperature (right) for each season and for the CMIP5 MMM.

Figure 5.4: Spatial maps of the change between the period 2071-2100 and the period 1971-2000 of the minimum temperature (left) and of the maximum temperature (right) for each season and for the CMIP5 MMM.
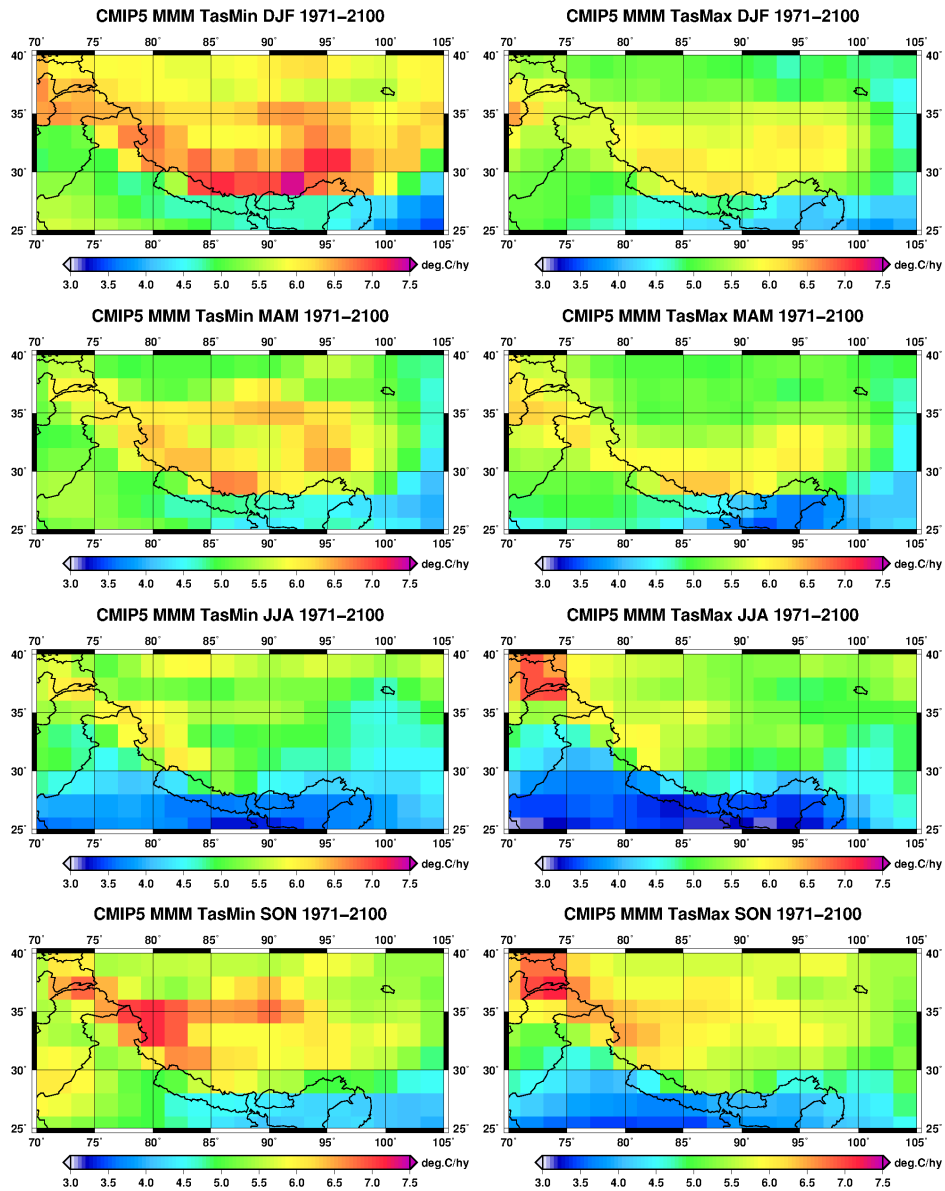
Figure 5.5: Spatial maps of linear trends $\left[°C/100 \text{ years}\right]$ of minimum temperatures (left) and maximum temperatures (right) computed during the whole period 1971-2100 for each season and for the CMIP5 MMM.

high-elevation regions to warm more than the adjacent lowlands.

Fig. 5.5 shows the spatial maps of linear trends of the minimum and maximum temperatures from the MMM during the period 1971-2100, corresponding to the whole time span considered to compute changes for the RCP8.5 scenario (Fig. 5.4). Linear trends are calculated using the least-square method. The strong similarities between panels of Fig. 5.5 and of Fig. 5.4 demonstrate that the same results are obtained when using linear trends instead of changes to evaluate the temporal variations of *tasmin* and *tasmax* in the study area. This is true also for the historical simulation. For this reason, in the next chapters temporal variations are computed as changes (i.e. differences of the 30-year climatologies between the periods 1971-2000 and 1871-1900 for the historical simulations and between the periods 2071-2100 and 1971-2000 for the RCP8.5 scenarios, see section 5.2), but the same results are expected if using linear trends instead.

5.4   Elevational dependence of surface warming

Fig. 5.6 shows, for the four seasons, the change of minimum temperature (left) and of maximum temperature (right) during the historical period as a function of the elevation for the MMM of the CMIP5 ensemble. Data points have been fitted with a linear regression over the whole altitude range (red line) and from 1500 m upwards (blue line). The slopes of the two regression lines (in °C km^{-1}) are reported in each panel. As already observed for Fig. 5.3, all grid points show positive changes (i.e., warming trend) and the absolute values are larger for the minimum than for the maximum temperature. In addition, Fig. 5.6 shows that the absolute value of the change tends to be higher at higher elevations (i.e., elevational trend). The elevational trends are generally enhanced when assessed over an altitude range that excludes the elevations lower than 1500 m. The minimum temperature shows the strongest elevational trend of warming in spring and autumn and the weakest in summer. For the maximum temperature the seasonal differences in the elevational trend are, in general, less important than for the minimum temperature. Overall, the EDW signal is stronger for *tasmin* than for *tasmax* in spring, while the opposite is found in summer.

Fig. 5.7 is the same as Fig. 5.6 but for future projections under the RCP8.5 scenario. We have already mentioned that the average warming of the Tibetan Plateau-Himalayan region is higher in the RCP8.5 scenario than in the historical simulation. Fig. 5.7 shows that also the elevational trends are much higher in the scenario simulation than in the historical one. Considering only trends calculated over the whole range of altitudes (red lines in Figs. 5.6 and 5.7) the values of the projected slope are from about 10 (minimum temperatures in spring and maximum temperatures in winter) to about 30 (minimum temperatures in winter and maximum temperatures in summer and autumn) times higher than those evaluated for the historical period.
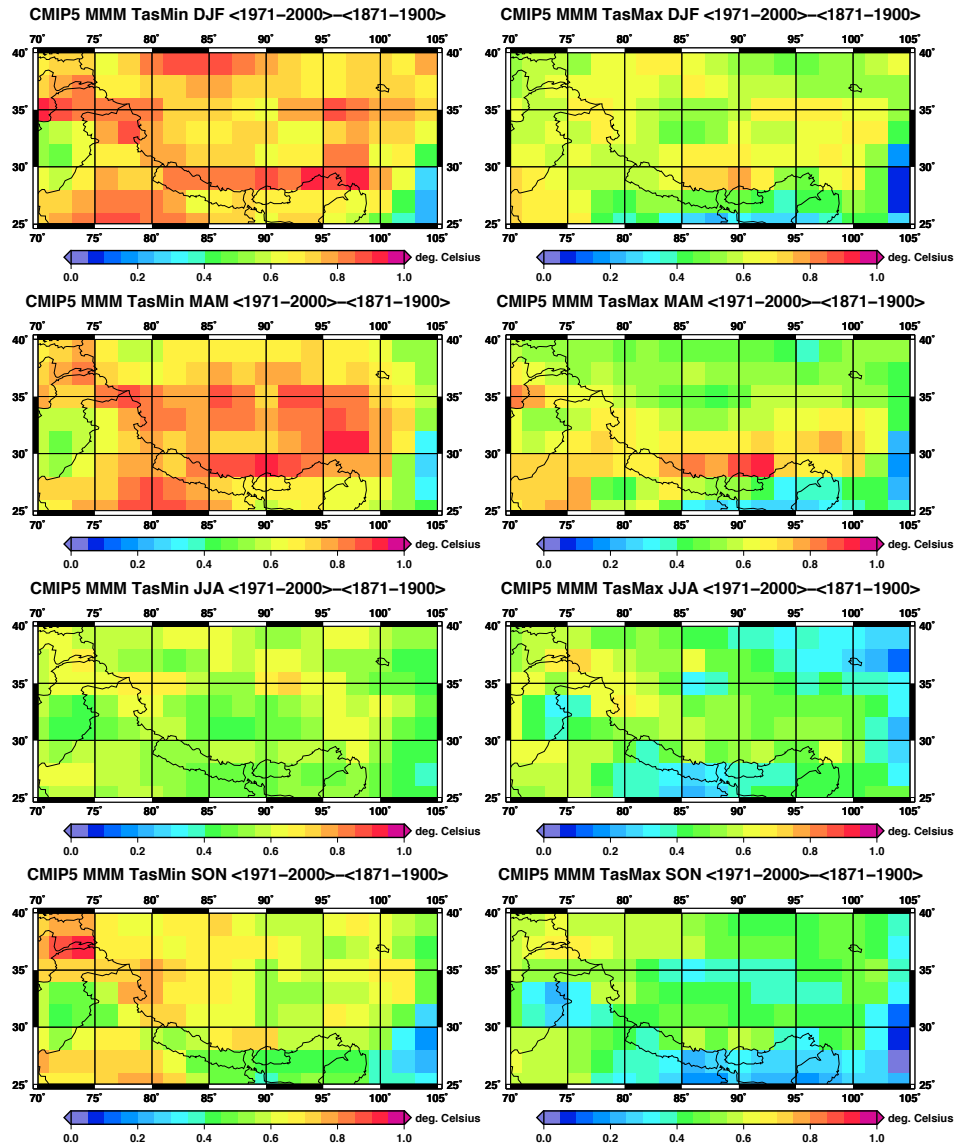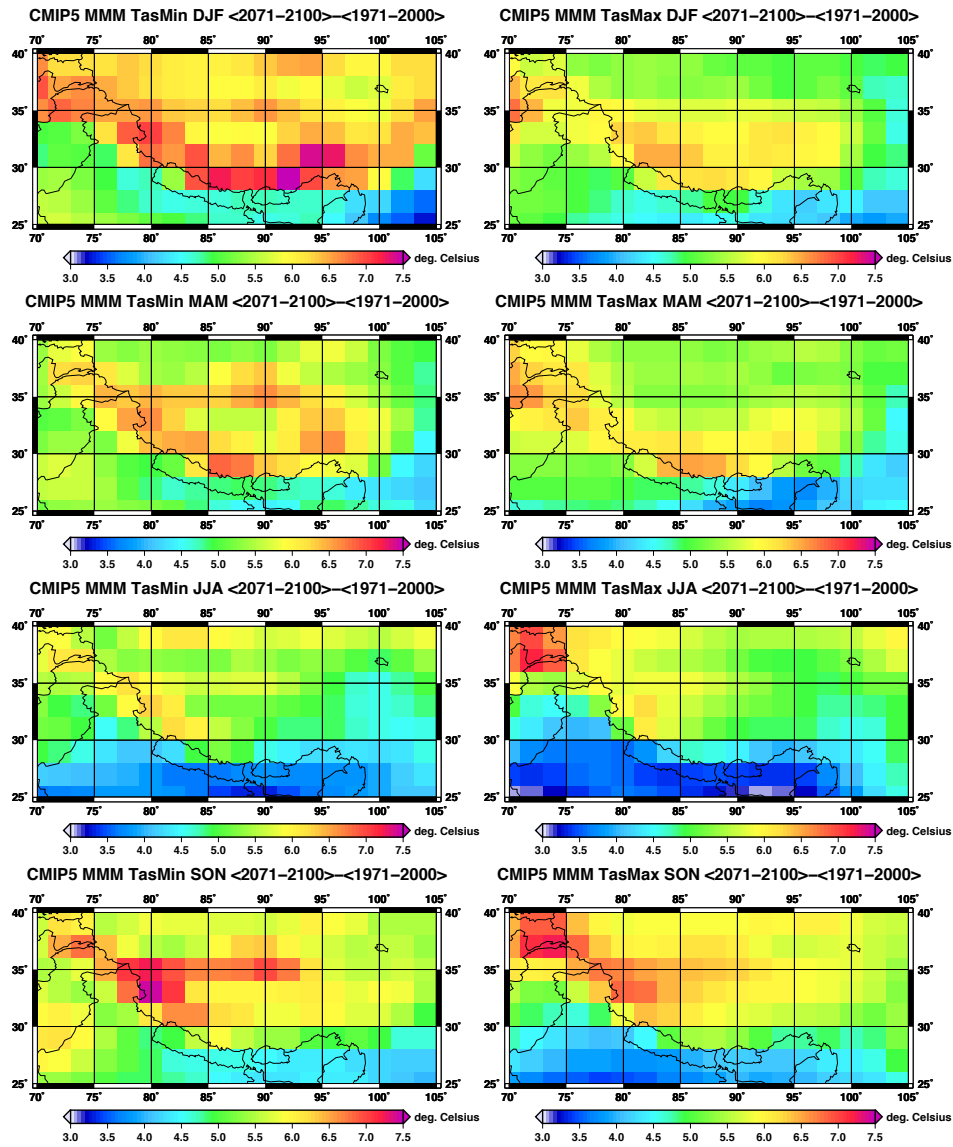
Figure 5.6: Change between the period 1971-2000 and the period 1871-1900 of the minimum temperature (left) and of the maximum temperature (right) as a function of surface elevation for each season and for the CMIP5 MMM. The slope of linear regression (°C km^{-1}) is indicated (see text for details); a star in parentheses indicates the statistical significance of the elevational trend.
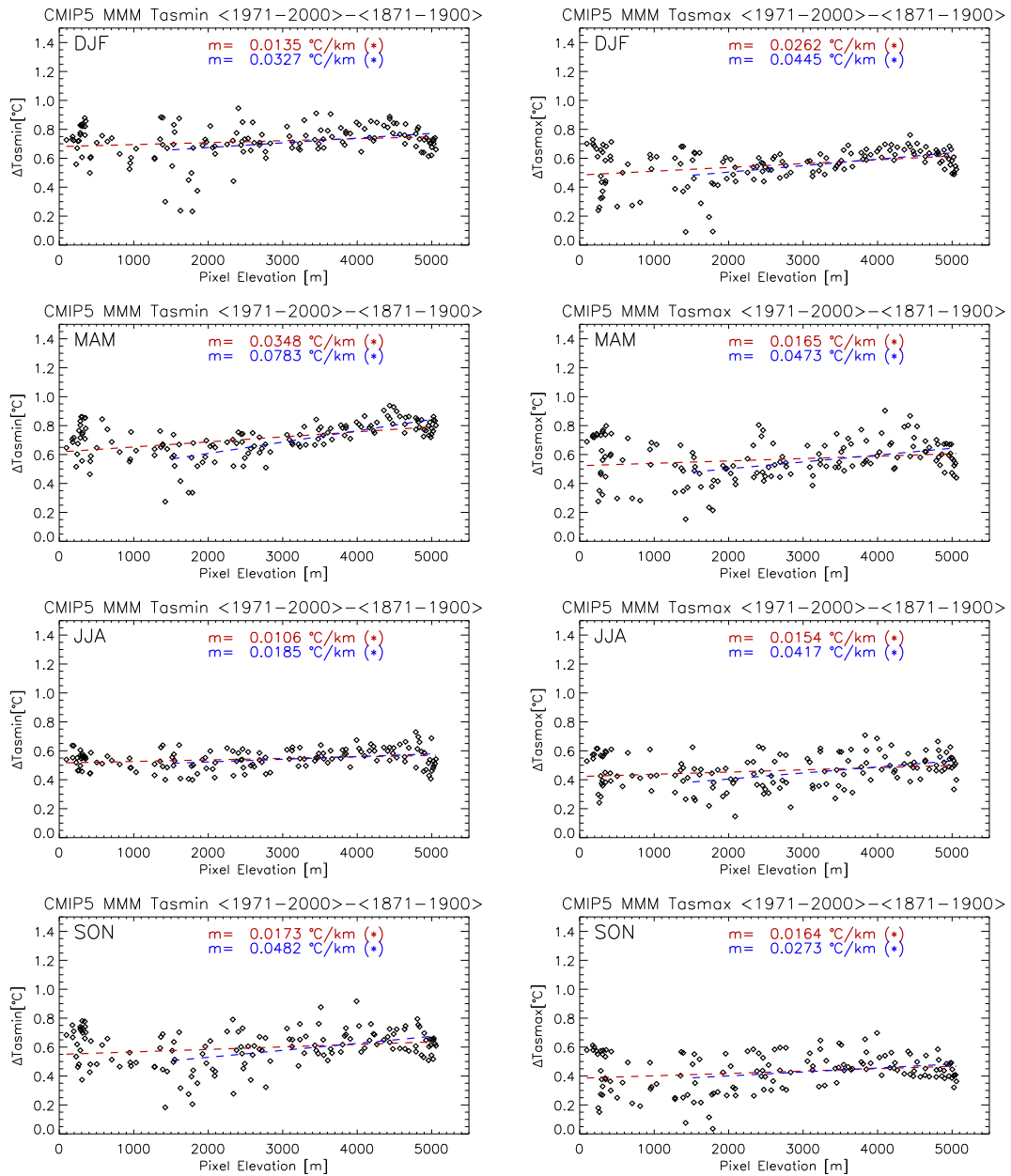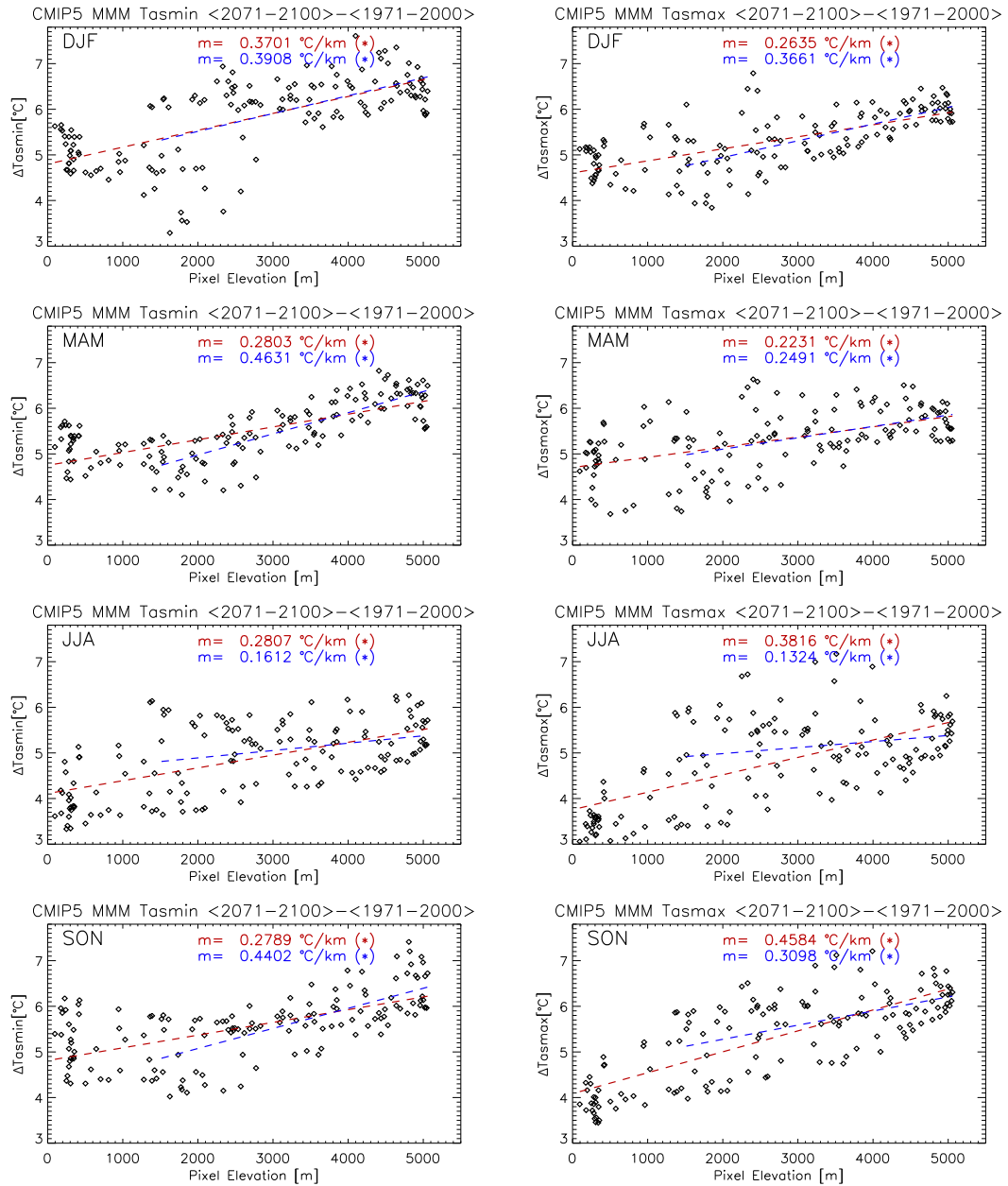
Figure 5.7: Change between the period 2071-2100 and the period 1971-2000 of the minimum temperature (left) and of the maximum temperature (right) as a function of surface elevation for each season and for the CMIP5 MMM. The slope of linear regression (°C km^{-1}) is indicated (see text for details); a star in parentheses indicates the statistical significance of the elevational trend.

Table 5.2 shows, for each GCM, the slope of the linear regression ($^{\circ}$C km^{-1}) describing the 20th century changes (1971-2000 climatology minus 1871-1900 climatology) of minimum temperatures as a function of the surface elevation for each season in the Tibetan Plateau-Himalayan region. For completeness, values from the MMM are also reported. Stars in parentheses indicate statistically significant (p<0.05) elevational gradients of warming rates. Most of the models show statistically significant elevational gradients of the minimum temperature changes. For most of them (67% in winter, 70% in spring and 65% in autumn) the slopes are positive, denoting higher warming rates as the altitude increases. During summer, the 55% of the models indicate a negative slope instead (i.e., reduced warming rate with the elevation), even if the slope of the MMM is positive. Table 5.3 shows the same as Table 5.2, but for the maximum temperature. In this case, the 67% of the models showing statistically significant elevational gradients during winter have a positive slope; during spring the percentage is 69%, 65% in summer, and 61% in autumn. Therefore, while the MMM indicates statistically significant warming trends with elevation for both minimum and maximum temperatures and in all seasons, there are noticeable inter-model differences, such that some models agree very well with the MMM but others do not and even exhibit a trend of opposite sign.

Tables 5.4 and 5.5 show the same as Tables 5.2 and 5.3 but for the scenario simulations. In this case, there are many more models that show positive slopes of either the minimum and maximum temperature change with the elevation with respect to the historical model simulations. Almost the 90% of the models for which the slopes are statistically significant indicate positive elevational gradients of the minimum temperature change in all seasons. For the maximum temperature change, this situation is even amplified: in autumn, all models give rise to statistically significant elevational gradients and all of them are positive; the percentage of models giving rise to statistically significant positive slopes is very high also in the other seasons (95% in winter, 88% in spring, 96% in summer). However, the inter-model spread in the scenario simulations remains very high, even larger than for the historical simulations. As an example, the inter-model standard deviation of the elevational gradients of *tasmax* during autumn is of 0.0998 $^{\circ}$C km^{-1} for the historical simulations and of 0.2535 $^{\circ}$C km^{-1} for the scenario simulations, even if all models show statistically significant positive elevational trends in the scenario and both positive and negative trends in the historical period. Similar considerations can be drawn for the other seasons and for *tasmin*.

It is worth pointing out that both Fig. 5.6 and Fig. 5.7 suggest that a simple linear fit describing the relationship between the temperature changes and the elevation is likely to be a simplistic approach. Indeed, a more complex situation is noticeable, and at least two patterns are discernible from those figures (also depending on the variable and season that are considered) indicating a different behaviour below and above about 1500 m. Fig. 5.6 in particular shows that

Table 5.2: Slope of linear regressions (°C km^{-1}) describing the elevational gradients of changes in minimum temperature between 1971-2000 and 1871-1900 in the Tibetan Plateau-Himalayas for each season and for each CMIP5 model. Stars in parentheses indicate statistically significant slopes (red if positive, blue if negative; p<0.05). The table also shows the slope of the linear regression and its significance for the CMIP5 Multi-Model Mean.

Model ID	DJF	MAM	JJA	SON
CCSM4	0.0725(∗)	0.0770(∗)	−0.0323(∗)	0.0809(∗)
CESM1-BGC	−0.0618(∗)	0.0059	−0.0226	0.0421(∗)
CESM1-CAM5	0.0464(∗)	0.0909(∗)	0.2278(∗)	0.0843(∗)
bcc-csm1-1-m	0.1649(∗)	0.0287(∗)	−0.0346(∗)	0.0618(∗)
MRI-CGCM3	−0.1008(∗)	−0.0448(∗)	−0.0438(∗)	−0.0285(∗)
CNRM-CM5	0.0610(∗)	0.0726(∗)	−0.0442(∗)	0.1205(∗)
MIROC5	0.0383(∗)	0.0491(∗)	−0.0855(∗)	0.0658(∗)
ACCESS1-0	0.0626(∗)	0.0053	−0.0158(∗)	−0.0016
ACCESS1-3	−0.0758(∗)	−0.0252(∗)	−0.0026	−0.0927(∗)
HadGEM2-CC	−0.1832(∗)	−0.0843(∗)	0.1542(∗)	0.1871(∗)
IPSL-CM5A-MR	0.1883(∗)	0.2250(∗)	0.2368(∗)	0.1867(∗)
INM-CM4	0.0157	0.2423(∗)	0.0967(∗)	0.1797(∗)
CSIRO-Mk3-6-0	0.1022(∗)	0.1013(∗)	−0.0145	−0.0218(∗)
NorESM1-M	0.0228	0.0458(∗)	−0.0177	−0.0540(∗)
GFDL-CM3	0.0208	−0.0154	−0.0602(∗)	0.0191
GFDL-ESM2G	0.0162	−0.0973(∗)	0.0132	−0.1478(∗)
GFDL-ESM2M	0.0874(∗)	−0.0132	0.0187	0.0562(∗)
GISS-E2-H	−0.1519(∗)	−0.1212(∗)	−0.1755(∗)	−0.0869(∗)
GISS-E2-R	0.0174	−0.0401	0.0429(∗)	0.0958(∗)
IPSL-CM5A-LR	0.0216	0.1572(∗)	0.2619(∗)	0.0696
IPSL-CM5B-LR	0.0643	0.0366	0.0878(∗)	0.0108
MIROC-ESM-CHEM	0.1034(∗)	0.2060(∗)	−0.0125	0.2179(∗)
MIROC-ESM	0.1634(∗)	0.2742(∗)	−0.0713	0.2292(∗)
bcc-csm1-1	0.0516	0.0567(∗)	−0.0326(∗)	−0.1093(∗)
BNU-ESM	−0.0253	0.009	0.1730(∗)	0.1528(∗)
CanESM2	−0.2605(∗)	−0.0727(∗)	−0.0791(∗)	−0.0966(∗)
FGOALS-g2	0.1469(∗)	0.1083(∗)	0.0354(∗)	0.0843(∗)
MMM	0.0135(∗)	0.0348(∗)	0.0106(∗)	0.0173(∗)

Table 5.3: The same as Table 5.2 bur for changes in maximum temperature.

Model ID	DJF	MAM	JJA	SON
CCSM4	0.0923(∗)	0.0742	0.0050(∗)	0.1051(∗)
CESM1-BGC	0.0061	−0.0161	0.1071(∗)	0.0630(∗)
CESM1-CAM5	0.1523(∗)	0.1201(∗)	0.2443(∗)	0.0672(∗)
bcc-csm1-1-m	0.1570(∗)	0.0162(∗)	0.0434(∗)	0.0483(∗)
MRI-CGCM3	0.0236(∗)	0.0251(∗)	−0.0395(∗)	−0.0051
CNRM-CM5	−0.0281(∗)	−0.0151	−0.0715(∗)	0.0667(∗)
MIROC5	0.0321(∗)	0.0488(∗)	−0.0563(∗)	0.0113
ACCESS1-0	0.1117(∗)	−0.0228	−0.0022	0.0118
ACCESS1-3	−0.0491(∗)	−0.0659(∗)	0.0289(∗)	−0.1185(∗)
HadGEM2-CC	−0.3635(∗)	−0.3967(∗)	−0.1294(∗)	−0.1774(∗)
IPSL-CM5A-MR	0.1887(∗)	0.2745(∗)	0.1049(∗)	0.0653(∗)
INM-CM4	0.2734	0.0439	0.0314	0.1488
CSIRO-Mk3-6-0	0.0987(∗)	0.0609(∗)	−0.0201(∗)	0.0308(∗)
NorESM1-M	0.0612(∗)	0.0719(∗)	−0.0247	−0.0721(∗)
GFDL-CM3	0.1184(∗)	0.1070(∗)	−0.0184	0.0896(∗)
GFDL-ESM2G	0.0401	0.0111	0.0008	−0.2052(∗)
GFDL-ESM2M	0.1171(∗)	−0.0466(∗)	−0.0470	0.0384
GISS-E2-H	−0.0776(∗)	−0.0102	0.0543	0.0770(∗)
GISS-E2-R	0.0123	−0.0026	0.0579(∗)	0.0113
IPSL-CM5A-LR	0.0043	0.1164(∗)	0.1816(∗)	0.0929(∗)
IPSL-CM5B-LR	0.0259	0.0059	0.0851(∗)	−0.0208
MIROC-ESM-CHEM	−0.0191	0.2179(∗)	−0.0155	0.1213
MIROC-ESM	−0.0091	0.2574(∗)	−0.1692	0.1716(∗)
bcc-csm1-1	0.0071	−0.0551(∗)	0.0563(∗)	−0.1421(∗)
BNU-ESM	−0.0253(∗)	0.009	0.1730(∗)	0.1528(∗)
CanESM2	−0.2370(∗)	−0.2007(∗)	−0.1648(∗)	−0.1025(∗)
FGOALS-g2	0.0426(∗)	−0.0354	0.0097	0.0051
MMM	0.0262(∗)	0.0165(∗)	0.0154(∗)	0.0164(∗)

Table 5.4: The same as Table 5.2 but for changes in minimum temperature between 2071-2100 and 1971-2000 under the RCP8.5 emission scenario.

Model ID	DJF	MAM	JJA	SON
CCSM4	0.2877(∗)	0.2522(∗)	0.1173(∗)	0.4709(∗)
CESM1-BGC	0.3746(∗)	0.2861(∗)	0.1395(∗)	0.5024(∗)
CESM1-CAM5	0.2215(∗)	0.2969(∗)	0.1856(∗)	0.5270(∗)
bcc-csm1-1-m	0.0666(∗)	0.3218(∗)	0.0215	0.2655(∗)
MRI-CGCM3	0.2180(∗)	0.2963(∗)	−0.1597(∗)	0.1996(∗)
CNRM-CM5	0.0845(∗)	0.0725(∗)	0.3768(∗)	0.3715(∗)
MIROC5	0.5820(∗)	0.6507(∗)	0.7439(∗)	0.6464(∗)
ACCESS1-0	0.5868(∗)	0.3837(∗)	0.1200(∗)	0.3559(∗)
ACCESS1-3	0.0634	−0.1024(∗)	0.0262	−0.1568(∗)
HadGEM2-CC	0.4784(∗)	0.1657(∗)	−0.0205	−0.0667
IPSL-CM5A-MR	0.5710(∗)	0.9932(∗)	0.7807(∗)	0.7555(∗)
INM-CM4	0.4045(∗)	0.3555(∗)	0.2390(∗)	0.0788
CSIRO-Mk3-6-0	−0.1364(∗)	−0.0168	−0.3181(∗)	−0.2246(∗)
NorESM1-M	0.0228	0.1197(∗)	0.1292(∗)	0.4294(∗)
GFDL-CM3	0.8013(∗)	0.2334(∗)	0.4409(∗)	0.0311
GFDL-ESM2G	0.2719(∗)	−0.0862	0.0591	0.5960
GFDL-ESM2M	0.1237	−0.1202(∗)	−0.0986	−0.1100
GISS-E2-H	0.2650(∗)	0.2967(∗)	0.4443(∗)	0.2420(∗)
GISS-E2-R	0.2810(∗)	0.3123(∗)	0.3612(∗)	0.2227(∗)
IPSL-CM5A-LR	0.7722(∗)	0.9205(∗)	0.6992(∗)	0.7080(∗)
IPSL-CM5B-LR	−0.3270(∗)	−0.1847	0.0073	−0.1412
MIROC-ESM-CHEM	1.0942(∗)	0.9205(∗)	0.9234(∗)	0.8005(∗)
MIROC-ESM	1.0143(∗)	0.6984(∗)	1.0271(∗)	0.9246(∗)
bcc-csm1-1	0.4102(∗)	0.0613	−0.07234	0.0260
BNU-ESM	0.3852(∗)	0.2155(∗)	0.0021	0.2584(∗)
CanESM2	0.1108	0.3518(∗)	0.3253(∗)	0.0294
FGOALS-g2	0.3648(∗)	0.4250(∗)	0.6463(∗)	0.5142(∗)
MMM	0.3701(∗)	0.2803(∗)	0.2807(∗)	0.2789(∗)

Table 5.5: The same as Table 5.2 but for changes in maximum temperature between 2071-2100 and 1971-2000 under the RCP8.5 emission scenario.

| Model ID	DJF	MAM	JJA	SON
CCSM4	0.1597(∗)	0.0256	0.1539(∗)	0.2769(∗)
CESM1-BGC	0.1860(∗)	0.1271(∗)	0.1808(∗)	0.2977(∗)
CESM1-CAM5	0.1345(∗)	0.1350(∗)	0.1658(∗)	0.3480(∗)
bcc-csm1-1-m	−0.0084	0.0280	0.3870(∗)	0.3276(∗)
MRI-CGCM3	0.2194(∗)	0.0436(∗)	−0.0833(∗)	0.1220(∗)
CNRM-CM5	0.0098	−0.0736(∗)	0.2748(∗)	0.3410(∗)
MIROC5	0.2943(∗)	0.3857(∗)	0.7418(∗)	0.7996(∗)
ACCESS1-0	0.3555(∗)	0.1849(∗)	0.0637	0.3403(∗)
ACCESS1-3	0.1934(∗)	0.0848(∗)	0.2664(∗)	0.2096(∗)
HadGEM2-CC	0.6138(∗)	0.3117(∗)	0.2235(∗)	0.5364(∗)
IPSL-CM5A-MR	0.3869(∗)	0.7101(∗)	0.0371	0.4038(∗)
INM-CM4	0.3845(∗)	0.5113(∗)	0.2300(∗)	0.3486(∗)
CSIRO-Mk3-6-0	0.0280	0.1143(∗)	0.1264(∗)	0.1791(∗)
NorESM1-M	−0.0225	0.0565	0.3158(∗)	0.3865(∗)
GFDL-CM3	1.1250(∗)	0.5482(∗)	0.8839(∗)	1.2325(∗)
GFDL-ESM2G	0.3624(∗)	0.0249	0.2318(∗)	0.4521(∗)
GFDL-ESM2M	0.2881(∗)	0.0448	0.0754	0.1881(∗)
GISS-E2-H	0.1846(∗)	0.3817(∗)	0.8583(∗)	0.3958(∗)
GISS-E2-R	0.3205(∗)	0.4212(∗)	0.8243(∗)	0.4876(∗)
IPSL-CM5A-LR	0.3232(∗)	0.5499(∗)	−0.0393	0.2591(∗)
IPSL-CM5B-LR	0.0066	0.0538	0.0918(∗)	0.1669(∗)
MIROC-ESM-CHEM	0.4030(∗)	0.1926	0.8054(∗)	0.7354(∗)
MIROC-ESM	0.3789(∗)	0.0925	1.0010(∗)	0.8286(∗)
bcc-csm1-1	−0.0040	−0.2446(∗)	0.3642(∗)	0.2016(∗)
BNU-ESM	−0.1067	0.3215(∗)	0.3774(∗)	0.5989(∗)
CanESM2	0.1286(∗)	0.1668	0.6585(∗)	0.1568(∗)
FGOALS-g2	−0.2748(∗)	−0.1021	1.0018(∗)	0.2257(∗)
MMM	0.2635(∗)	0.2231(∗)	0.3816(∗)	0.4584(∗)
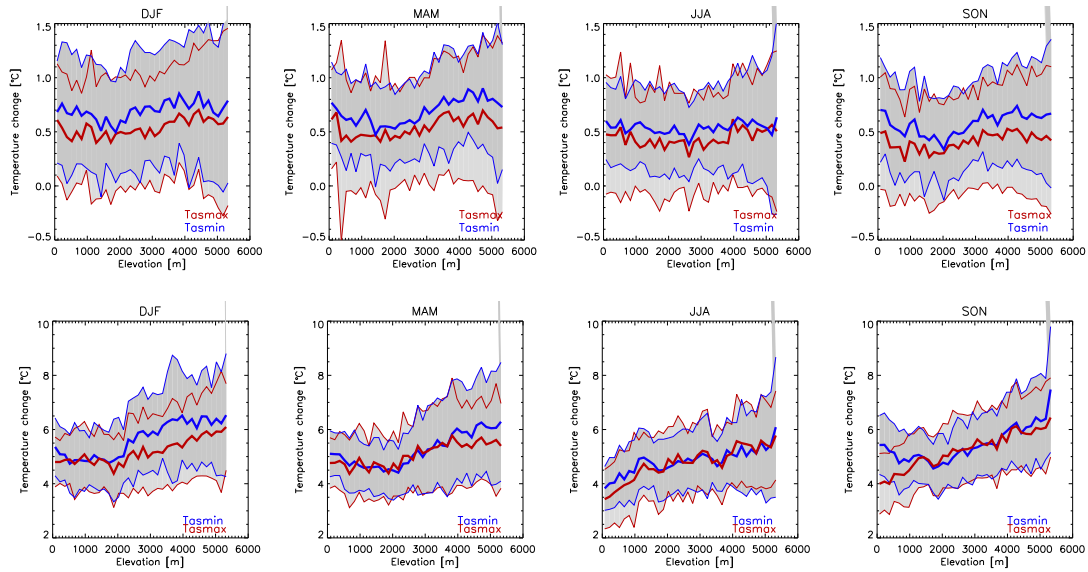
Figure 5.8: Minimum and maximum temperature change as a function of surface elevation in the historical period (1971-2000 climatology minus 1871-1900 climatology; top panels) and in the RCP8.5 scenario (2071-2100 climatology minus 1971-2000 climatology; bottom panels) for the CMIP5 ensemble, considering 150 m-thick bins for the four seasons. The blue (red) lines show the MMM and the dark (light) shaded areas represent the inter-model spread measured as one standard deviation above and below the MMM for the minimum temperature (maximum temperature).

the minimum temperature change (left column) tends to slightly decrease as a function of the elevation or to remain almost constant, depending on the season, until about 1500 m a.s.l. At higher elevations the elevational trend is positive and always statistically significant. Above about 4500 m the trend reverses again, giving rise to a cooling with elevation. A similar behaviour is observed for the change of the maximum temperature with the elevation (right column). Also results for the future projections (Fig. 5.7) confirm that the relationship between temperature changes and elevation is far from being simply linear, and different behaviour generally occur below and above about 1500 m a.s.l.

In order to make the non-linearity of the relationship between the temperature changes and the elevation clearer, Fig. 5.8 shows the minimum and maximum temperature changes as a function of the surface elevation in the CMIP5 ensemble for the four seasons and for both the historical and scenario simulations. Data have been averaged in 150 m-thick bins to compute the elevation distribution of the MMM and the range of variability of the models (inter-model spread, computed as one standard deviation above and below the MMM). The figure highlights the two-fold regime mentioned above, which is more evident during winter, spring, and autumn, particularly for the minimum temperatures: the elevational trend of
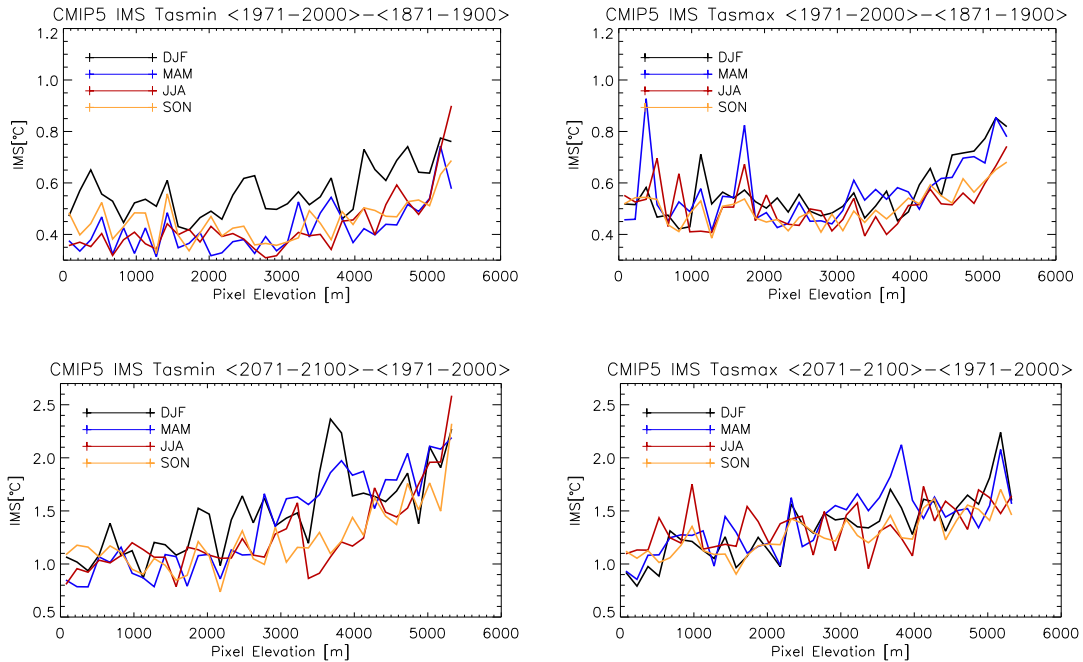
Figure 5.9: Inter-model standard deviation of the change of minimum temperatures (left panels) and of maximum temperatures (right panels) as a function of surface elevation (150 m-thick bins) in the CMIP5 ensemble for the four seasons from the historical simulations (top) and the RCP8.5 scenarios (bottom).

the temperature change is observed to change and even be reversed at altitudes around 1500-2000 m a.s.l., as also discernible from the slopes of the linear fit calculated over the two different altitude ranges shown in Figs. 5.6 and 5.7 (red and blue lines). This behaviour is emphasized in the scenario simulations, where the stronger warming likely allows to better separate the actual signals from the background noise.

The inter-model spread of the change of temperature at different elevations is relatively large. As it was for the elevational gradients of individual models shown in Tables 5.2–5.5, the spread is larger in the scenario simulations than in the historical ones (note the different y-axis in the top and bottom panels of Fig. 5.8; see also Fig. 5.9). Interestingly, the inter-model spread tends to increase as the elevation increases, particularly from ∼3000 m a.s.l. upward. This highlights that model simulated changes are less in agreement at higher altitudes, possibly because of problems in representing the complex orography of high-elevation regions (see section 1.5). Figs. 5.8 and 5.9 show the results for the multi-model mean and the inter-model standard deviation, but the same conclusions can be achieved if the multi-model median and percentiles were used instead.

Some interesting insights emerge when considering the minimum and maximum
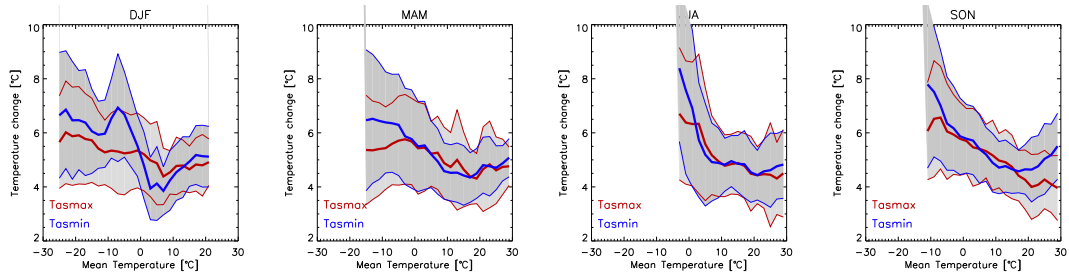
Figure 5.10: Minimum and maximum temperature change between the 2071-2100 climatology and the 1971-2000 climatology as a function of the mean temperature for the CMIP5 ensemble, considering 1°C-thick bins for the four seasons. The blue (red) lines show the MMM and the dark (light) shaded areas represent the inter-model spread measured as one standard deviation above and below the MMM for the minimum temperature (maximum temperature).
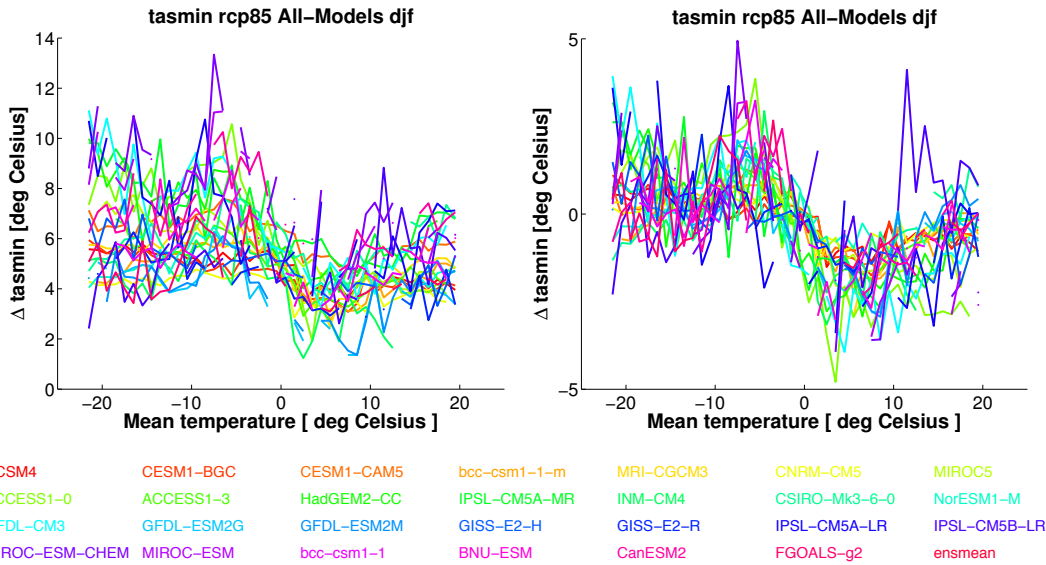
Figure 5.11: Minimum temperature change between the 2071-2100 climatology and the 1971-2000 climatology as a function of the mean temperature for individual CMIP5 models in the winter season, considering 1°C-thick bins. In the right panel, minimum temperature changes have been aligned by dividing by the average minimum temperature change computed for each model separately, to reduce the inter-model spread arising from different model climate sensitivities.

temperature changes as a function of the mean surface temperature — rather than as a function of the elevation. While the mean surface temperature is clearly related to the elevation, some differences exist since temperatures are influenced also by other factors, such as latitude and circulations regimes (e.g. Palazzi et al., 2013). Fig. 5.10 shows the results for the RCP8.5 scenario. Data have been averaged in 1°C-thick bins to compute the distribution of the MMM and the inter-model spread. The mean temperature is calculated as the average between *tasmin* and *tasmax* also averaged over the two 30-years long time periods. The two-fold behaviour mentioned above is clearly evident in Fig. 5.10. In particular, the wintertime signal in the minimum temperature is strongly emphasized, and the switch between the two regimes occurs close to the 0°C isotherm: the regions with temperatures below the freezing point of water show a much stronger warming than regions with temperatures above it, suggesting that the phase of water and/or the presence of snow may play a key role. It is interesting to note that these considerations hold true not only for the MMM and the inter-model spread, but also for each individual model, as shown in Fig. 5.11. The agreement between all individual models gives robustness to these findings.

The existence of different temperature responses in regions above and below the freezing point observed for the minimum temperatures in winter seems to occur also in the other seasons and for the maximum temperatures (Fig. 5.10), even if the signal is generally less evident and the switch between the two regimes is smoother and less localized across the 0°C isotherm. It has been mentioned that the two-fold behaviour in the relationship between temperature change and elevation is not evident during summer (see Fig. 5.8). Fig. 5.10 suggests that the two regimes might not exist in this season simply because there are (almost) no points with mean temperatures below zero.

5.5 Mechanisms

The analyses reported in section 5.4 indicate that the CMIP5 models and their multi-model mean depict a situation in which warming is amplified with elevation. Also, the link between temperature changes and elevation is described by a more complex relationship than a simple linear one and two main regimes can be distinguished, corresponding to temperatures above and below the zero-degree isotherm. In this section, the mechanisms leading to EDW in the Tibetan Plateau-Himalayas are further explored.

For the sake of conciseness, I consider only the cases (i.e. variables, seasons and periods) showing the strongest EDW signal, namely the minimum temperature during winter and the maximum temperature during autumn in the RCP8.5 scenario. I analyse CMIP5 model variables whose variations may be important for determining temperature variations and their dependence on the elevation. Following previous modelling studies of EDW (e.g. Rangwala et al., 2015), I focus

on surface albedo, the surface downwelling longwave radiation, the surface downwelling shortwave radiation and the near-surface specific humidity, which may affect the surface temperatures both directly and indirectly by means of, e.g., feedback mechanisms involving clouds. Changes of these variables between the end and the beginning of the century (hereafter called $\Delta albedo$, $\Delta rlds$, $\Delta rsds$ and $\Delta huss$) are computed in the same way as the minimum and maximum temperature changes and are considered as possible drivers of EDW. In addition, I include other three more possible drivers, namely the normalized changes (i.e., changes relative to a given climatology) in surface downwelling longwave and shortwave radiation ($\Delta rlds/rlds_0$, $\Delta rsds/rsds_0$) and in near-surface specific humidity ($\Delta huss/huss_0$) since they could be more effective in determining elevation-dependent temperature signals, as highlighted in previous studies (e.g. Rangwala et al., 2013, 2015). In particular, the authors of those studies pointed out that the normalized change in specific humidity is a more appropriate metric than the absolute change, because of the sensitivity of the downward longwave radiation to water vapour changes. For the same increase in atmospheric water vapour amount, indeed, the downward longwave radiation increases more when the mean state is drier (as in the high-elevation sites) and less when it is wetter (as in lower-elevation sites), leading to higher warming rates at higher elevations.

Summarizing, I consider the following seven possible drivers of EDW: $\Delta albedo$, $\Delta rlds$, $\Delta rsds$, $\Delta huss$, $\Delta rlds/rlds_0$, $\Delta rsds/rsds_0$, $\Delta huss/huss_0$. In order to understand if these changes may actually drive EDW in the Tibetan Plateau-Himalayas, I analyze their dependence on elevation and I study their covariance with the temperature changes. In particular, I check if the following three conditions are satisfied:

1. They have to exhibit a dependence on the elevation, as the temperature change does.

2. The sign of this dependence has to be consistent with the observed changes in surface temperatures, i.e. with the amplification of the warming rate at higher elevations.

3. They have to spatially correlate with the temperature change even when the dependence on the elevation is removed.

The first step is to check for the existence of a clear relationship between $\Delta albedo$, $\Delta rlds$, $\Delta rsds$, $\Delta huss$, $\Delta rlds/rlds_0$, $\Delta rsds/rsds_0$, $\Delta huss/huss_0$ and the elevation. Figure 5.12 shows, for each individual GCM and for their MMM, the correlation coefficients between each of the seven possible drivers and the elevation during winter; the correlation coefficient between $\Delta tasmin$ and the elevation is also displayed for completeness. The MMM shows that all correlations are statistically-significant except those involving the changes (both absolute and normalized) of the surface downward shortwave radiation. This is consistent with the
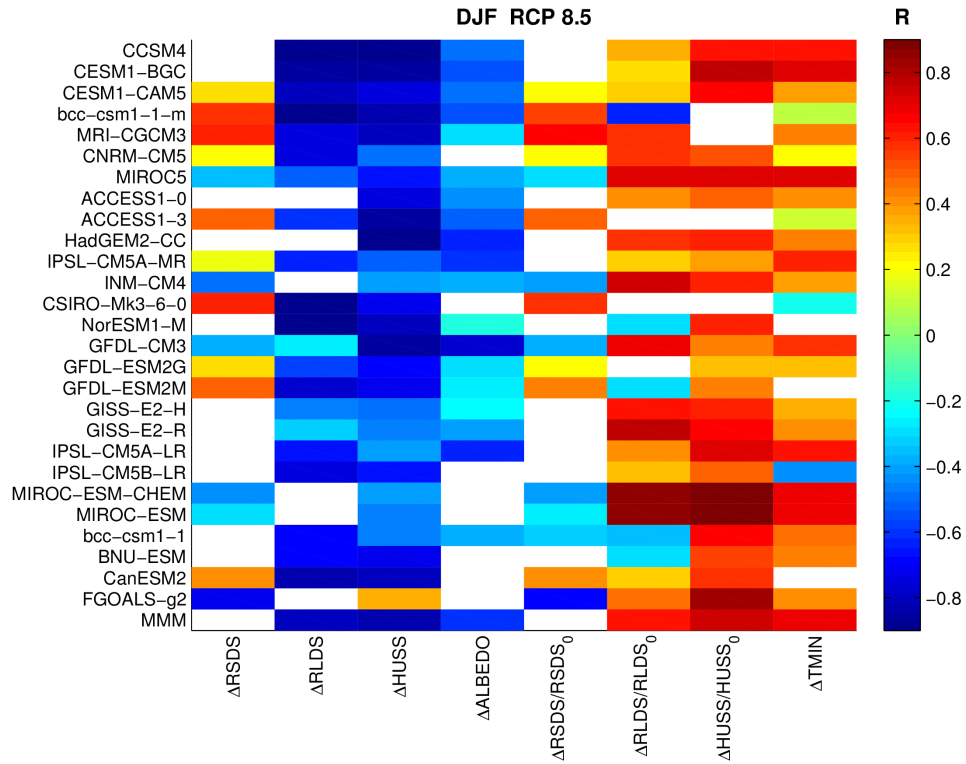
Figure 5.12: Correlation coefficients between the following variables — $\Delta albedo$, $\Delta rlds$, $\Delta rsds$, $\Delta huss$, $\Delta rlds/rlds_0$, $\Delta rsds/rsds_0$, $\Delta huss/huss_0$ and $\Delta tasmin$ — and the elevation for all CMIP5 models ad for their multi-model mean (MMM) in DJF for the RCP8.5 scenario. White boxes indicate correlation coefficients that are not statistically significant.
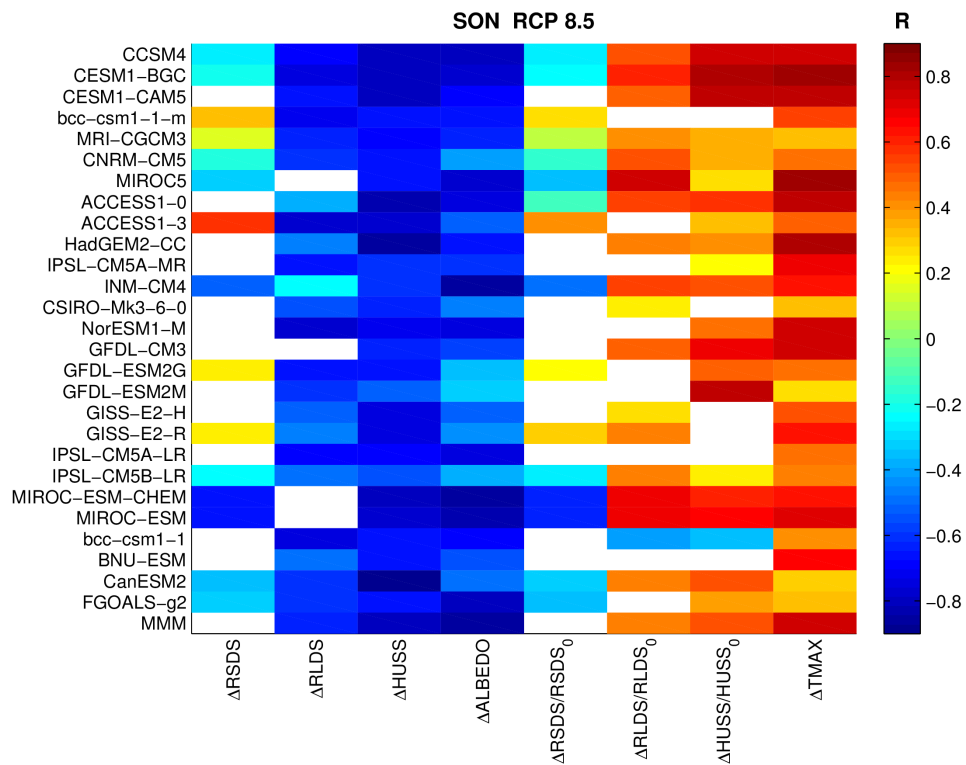
Figure 5.13: The same as Fig. 5.12 but during SON and displaying $\Delta tasmax$ instead of $\Delta tasmin$.

signal emerging from the individual GCMs, showing a general consensus in the sign of the correlation coefficients involving all variables but $\Delta rsds$ and $\Delta rsds/rsds_0$, for which correlations of either signs occur. The same result if found in autumn (Fig. 5.13). This first-level analysis suggests not to include the changes (both absolute and normalized) of *rsds* in the successive steps, since they do not show a clear dependence on the elevation (i.e. they do not satisfy the 1st condition considered here).

To verify the fulfillment of the second condition, the sign of the correlation coefficients has to be considered. Basic physical considerations imply that, in order to be consistent with the elevational gradient of the temperature change, changes of *rlds* and *huss* have to exhibit the same elevational dependence as the temperature change does, since an increase in these variables determines an increase in temperature as well. Vice versa, *albedo* changes have to exhibit an elevational gradient of opposite sing, since an increase in *albedo* determines a decrease in surface temperature. The temperature change is positively correlated with elevation. This holds true for both $\Delta tasmin$ and $\Delta tasmax$. Figs. 5.12 and 5.13 show that also $\Delta rlds/rlds_0$ and $\Delta huss/huss_0$ are positively correlated with elevation, while $\Delta albedo$, $\Delta rlds$ and $\Delta huss$ are negatively correlated. This excludes from the ensemble of the possible EDW predictors the absolute changes of *rlds* and *huss* ($\Delta rlds$ and $\Delta huss$) since their negative correlation with the elevation is not physically consistent with the enhanced warming at higher elevations.

The above considerations suggest that the three following variables, namely $\Delta albedo$, $\Delta rlds/rlds_0$ and $\Delta huss/huss_0$, may drive the positive elevational gradient of $\Delta tasmin$ in winter and of $\Delta tasmax$ in autumn, since they are all related to the elevation and their elevational gradient has the "right sign". Nonetheless, the covariance between these three possible drivers and temperature changes has not been addressed so far. To this end, spatial correlations could be used. However, since all of them show elevational gradients, their correlation with the temperature change could arise simply because they exhibit a dependence on the elevation as the temperature change does, independently whether they are actually driving the temperature change and the associated EDW in this area. For this reason, I require that $\Delta albedo$, $\Delta rlds/rlds_0$ and $\Delta huss/huss_0$ spatially correlate with the temperature change even when I "control for" elevation (i.e., when I remove the dependence of these variables and of the temperature change on the elevation).

To this end, a multiple regression model is used where the three possible EDW drivers are used as *predictors* for the seasonal change in either *tasmin* or *tasmax* (the *predictand*). Both the *predictors* and the *predictand* are "altitude-detrended" by removing their linear fit on elevation. The resulting multiple linear regression model can be written as:

$$\Delta T \;\; = \;\; a_1 \Delta albedo + a_2 \Delta huss/huss_0 + a_3 \Delta rlds/rlds_0 + a_0 \qquad (5.1)$$

where ΔT indicates the seasonal change in either *tasmin* or *tasmax*. Please note

that all predictors and predictands in Eq. 5.1 are standardized by dividing each value by the associated standard deviation.

This approach allows to test all the possible combinations of the three predictors by removing or keeping them time by time. Each combination leads to a different regression model. Overall, the possible combinations are $(2^n - 1) = 7$, with $n = 3$ predictors and include the three regression models made of one single predictor, the three models with the combinations of two predictors and the model with all three predictors. The predictive ability of the seven regression models is assessed by examining the proportion of the variance they can explain, which can be measured by the coefficient of determination R^2: the closer R^2 is to 1, the better the model predictive ability is. Since by construction the regression model including all predictors is associated with the highest value of R^2, the Akaike information criterion corrected for finite sample sizes is used to measure the relative quality of the models (AICc, Burnham and Anderson, 2003). This metric allows to rank the regression models with different number of predictors penalizing those with more and favoring those with less predictors. The lower the AICc, the better the model.

The seven multiple regression models are applied to all 27 GCMs and to their MMM. The resulting coefficients of determination are graphically shown in Fig. 5.14 (prediction of the minimum temperature change in DJF) and in Fig. 5.15 (prediction of the maximum temperature change in SON). For completeness, the average of the R^2 values across the different GCMs is also reported, $< R^2 >$. The bottom part of Figs. 5.14 and 5.15 indicates which predictors are "switched on" (black squares) or "switched off" (blank) in each regression model. To facilitate the interpretation of the results, Table 5.6 summarizes the results for the MMM. In this table, the seven regression models are ranked in order of increasing AICc values.

As a starting point, I consider the prediction of $\Delta tasmin$ in DJF and focus on the MMM of the CMIP5 models for conciseness (Fig. 5.14 and upper part of Table 5.6). In this case, $\Delta albedo$ emerges as the driver having a leading role for EDW. In fact, the four models including $\Delta albedo$ as a predictor show the highest values of R^2 among the seven regression models for the MMM. In particular, among the three single-predictor models, the one with $\Delta albedo$ shows the highest R^2. The three multi-predictor models including $\Delta albedo$ in conjunction with any other variable are capable of accounting for most of the variance of the predictand (more than the 75%). For what concerns the other predictors, they are generally less relevant than $\Delta albedo$ but nonetheless they play a role in the performance of the regression model. As mentioned, indeed, the multi-predictor models including $\Delta huss/huss_0$ and/or $\Delta rlds/rlds_0$ in addition to $\Delta albedo$ show higher R^2 than the single-predictor model including only $\Delta albedo$ and are the ones showing the best (i.e. the lowest) AICc values.

Similar considerations can be drawn for the prediction of $\Delta tasmax$ in SON (Fig.
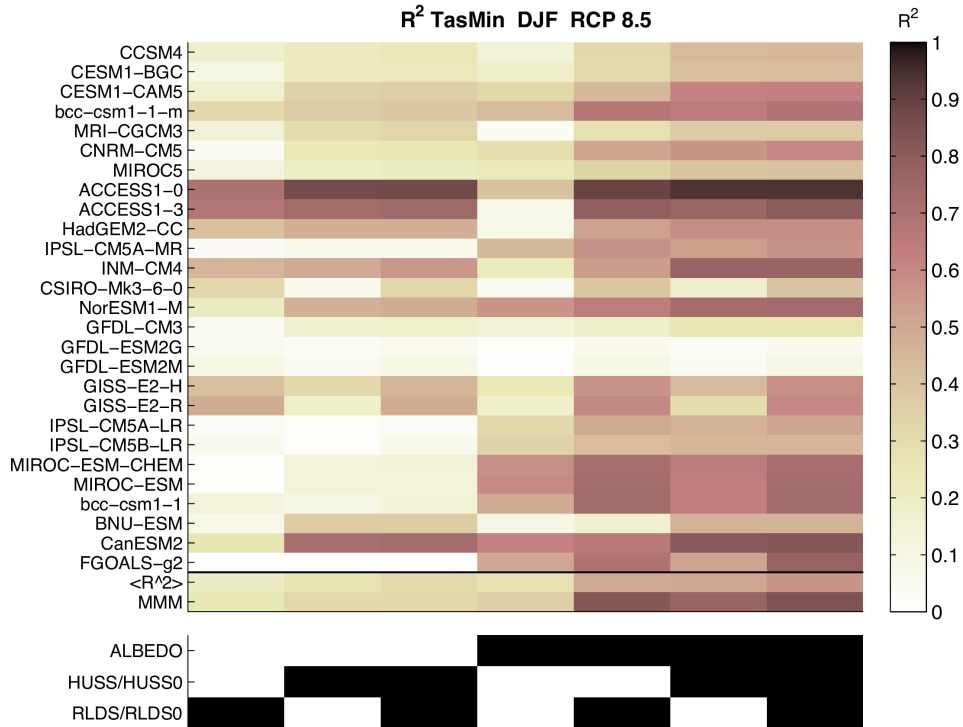
Figure 5.14: Top: Coefficients of determination R^2 of the seven regression models (columns) for $\Delta tasmin$ during DJF in the RCP8.5 scenario. Results are shown for each GCM and for the MMM (rows). The averaged value of R^2 across the various GCMs is also reported $< R^2 >$. Bottom: For each of the seven regression models (columns), a black box indicates which predictors (rows) are included.
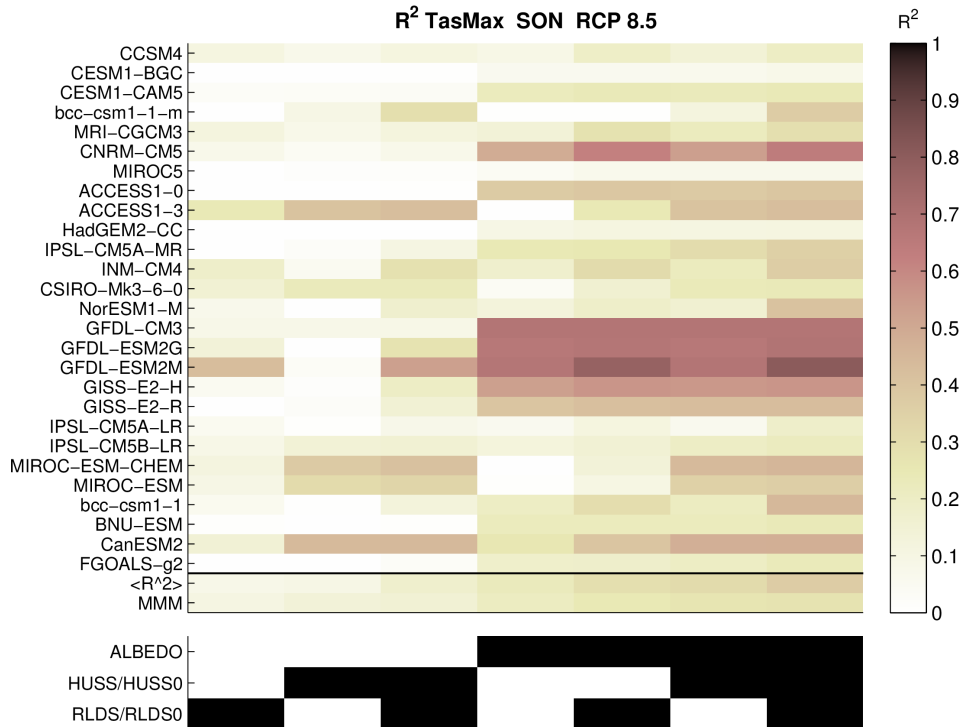
Figure 5.15: The same as in Fig. 5.14 but for $\Delta tasmax$ during SON.

Table 5.6: For each of the seven regression models, the top (bottom) part of the table shows the coefficient of determination R^2 and the AICc for the prediction of $\Delta tasmin$ in DJF ($\Delta tasmax$ in SON). The models are ranked according to the AICc values (the lower the AICc, the better the model). Predictors included in each model are marked with crosses. Results refer to the MMM.

		$\Delta tasmin$ DJF			
Model	$\Delta albedo$	$\Delta huss/huss_0$	$\Delta rlds/rlds_0$	R^2	AICc
1	X	X	X	0.84	-0.87
2	X		X	0.82	-0.80
3	X	X		0.77	-0.53
4	X			0.36	0.48
5		X		0.32	0.54
6		X	X	0.32	0.55
7			X	0.25	0.64

		$\Delta tasmax$ SON			
Model	$\Delta albedo$	$\Delta huss/huss_0$	$\Delta rlds/rlds_0$	R^2	AICc
1	X	X		0.26	-0.08
2	X	X	X	0.28	-0.08
3	X		X	0.25	-0.05
4	X			0.21	-0.02
5		X	X	0.15	0.06
6		X		0.14	0.06
7			X	0.10	0.10

5.15 and lower part of Table 5.6). Also in this case the four regression models including $\Delta albedo$ as a predictor show the highest values of R^2 for the MMM. Again, the other predictors are less relevant than $\Delta albedo$ but their presence still increase the variance explained by the regression model. However, in this case lower R^2 values are generally found. This holds true for the MMM as well as for most of the individual GCMs. The only exception is given by a group of GCMs including CNRM-CM5 and the GFDL and GISS "model families", for which the R^2 values of the regression models including $\Delta albedo$ are rather high. The low R^2 values shown by the regression models during SON indicate that the three predictors are not able to explain much of the variance of $\Delta tasmax$ in this season, and that some other relevant drivers may be at work. To this regard, it has to be noted that the predictors considered here have been chosen considering processes and variables suggested by previous studies, which have mainly focused on minimum temperatures and the winter season (see for example Liu et al., 2009; Rangwala et al., 2015). As such, lower R^2 for maximum temperatures and other seasons are not so surprising.

It is worth noting that the individual GCMs exhibit very large differences with

each other (see Figs. 5.14 and 5.15). This significant inter-model spread suggests that the processes associated with the temperature increase and driving the EDW signal are treated differently in the various GCMs. It is interesting to note that the GCMs belonging to the same "model family" provide more similar signals with each other than with other independent models (see Knutti et al., 2013, for an overview of the lineage connections among the climate models used in this study). The reasons for such inter-model discrepancies are not explored in the present study, but could be related, among the others, to a different description and treatment of aerosols and clouds, which can affect the radiation transfer in the atmosphere.

5.6   Conclusions

In this chapter, the Elevation Dependent Warming (EDW) in the Tibetan Plateau-Himalayan region has been investigated using an ensemble of twenty-seven global climate models participating in the Coupled Model Intercomparison Project phase 5 (CMIP5). Results indicate higher warming rates at higher elevations in this region, both in the historical model simulations and in the future projections under the RCP8.5 emission scenario. The EDW signal is amplified in the future simulations with respect to the historical period, and it is particularly strong for the minimum temperatures in winter and spring and for the maximum temperatures in summer and autumn.

The relationship between the maximum and minimum temperature changes and the elevation is not simply linear. At least two different regimes can be identified occurring below and above the zero-degree isotherm: the regions with temperatures below freezing show a much stronger warming than the regions with temperatures above, suggesting that the phase of water and/or the presence of snow play a key role.

To better understand the mechanisms that drive EDW in this region, the elevational gradients of a number of variables that may be relevant in determining the stronger warming of higher elevations have been investigated. The relative importance of these variables in determining temperature changes has been assessed using a multiple linear regression model. Here I have discussed the results for the two cases showing the strongest EDW signal, namely the minimum temperatures in winter and the maximum temperatures in autumn under the RCP8.5 scenario. It is found that changes in surface albedo — mainly due to a reduction of snow cover — atmospheric humidity and surface downward longwave radiation are relevant drivers of EDW in the Tibetan Plateau-Himalayas, with surface albedo being the leading driver in both cases discussed here.

A very important consideration refers to the fact that the individual GCMs exhibit very large differences with each other, suggesting that the processes associated with the temperature increase and the EDW are treated differently in the various GCMs. This implies that conclusions drawn from a single GCM should

be treated with care, and highlights the importance of using model ensembles in order to try to quantify, and possibly constrain, model uncertainties.

As a final remark, it is worth to stress that further research is needed to understand the inherent complexity of mountain regions and of the elevation dependent warming in particular, given the environmental and socio-economical impacts of a changing climate in the mountains. Modelling results do not still have a really solid observational counterpart because of the inadequacy or even the lack of measurements in high-elevation regions. More in-situ observatories, complemented by satellite data and appropriate analysis methods, would be necessary to measure EDW and to evaluate and validate the CMIP5 model performances, in order to be more confident in their projections of the future elevation dependent warming and its consequences.

Conclusions

State-of-the-art global climate models are based on general circulation models of the atmosphere and the ocean coupled together, possibly along with other modules simulating other major components or processes of the climate system, such as soil, vegetation, ice, chemistry and others. In this thesis I have addressed the optimization of a specific model, namely EC-Earth, as well as the application of this and other state-of-the-art global climate models to investigate some of the challenging questions in the context of climate dynamics and climatic changes.

The work of optimization of the EC-Earth model presented here refers to the model tuning. This activity has targeted both the model in its coupled configuration as well as its individual atmospheric component and has leaded to the release of the latest version of the model, namely EC-Earth 3.1. The tuning effort has been primarily devoted to improve the energy balance and the hydrological balance, as well as the representation of surface and tropospheric temperatures. Most of the improvements have been introduced through the implementation of an advection mass fixer in order to conserve water species during atmospheric transport, which has significantly enhanced both the hydrological and the energy balance of the model. In addition, fine calibration of model parameters, mainly affecting convection, clouds and precipitation but also the diffusive albedo of the ocean, has leaded to further improvements of simulated energy fluxes and temperature distribution. The analysis has also shown that similar enhancements can be achieved with different parameter configurations, and there is not obvious evidence of which is the "right" one. This result highlights that parameterizations inevitably introduce uncertainties in climate models. Model tuning may improve the representation of some selected fields, but cannot reduce such uncertainties which are necessarily there when representing some climatic processes by empirical statistical parameterizations.

Testing climate models under climatic conditions that are as different as possible from the present ones is an important task to constrain uncertainties about model projections of future climate. In this sense, paleoclimates offer a unique framework where to test model robustness and reliability. In this thesis I have used the EC-Earth model to study the so-called equable climates, i.e. warm periods characterized by weak meridional temperature gradients and low seasonality

that occurred during the past history of the Earth, such as during the late Cretaceous (about 100 to 65 million years ago) and the Early Eocene (about 56 to 48 million years ago). Model simulations driven by appropriate boundary conditions (including higher atmospheric CO_2 concentration, no land ice and modified vegetation) indicate that EC-Earth is able to detect the reduction of the meridional temperature gradient as well as the reduction of the annual cycle in the Northern Hemisphere high latitudes typical of warm equable climates, but nonetheless it fails in reproducing above freezing winter temperatures over high-latitude continental interiors. This issue, which is common to all climate models that have been used to study equable climates so far, has come to be known as the "equable climate problem" and clearly indicates that something fundamental is missing in current climate models and their representation of the climate system. Experiments have been carried out with EC-Earth showing that inadequacies of climate models in the representation of tropical low clouds may be crucial in determining their deficiency in reproducing warm equable climate conditions. In particular, it is found that a higher sensitivity of tropical low clouds to surface temperatures, which is supported by observations, may lead to significant temperature increases over high-latitude continents during winter, that is right in the regions and the season affected by the equable climate problem. Additional degrees required to be above freezing during winter in model simulations, then, may arise from model problems in reproducing the maritime influence on continental temperatures. This consideration is supported by the analysis of winter surface temperatures and the temperature annual cycle over oceans and land in present-day simulations from an ensemble of climate models including EC-Earth as well as other models participating in the Coupled Model Intercomparison Project phase 5.

In this thesis particular attention is given to mountain regions, due to the crucial role they play within the climate system. To this regard, I have focused on the Tibetan Plateau-Himalayan region, one of the most important mountain areas in the world.

Winter precipitation in the western Himalayas has been investigated, using an ensemble of observational datasets and model simulations run with EC-Earth. The teleconnection between precipitation in this area and the North Atlantic Oscillation has been explored over both the interannual as well as the multi-decadal time scales, and the underlying mechanisms have been enlightened. This study, encompassing both well established concepts as well as newer and less studied aspects of climate dynamics, represents an ideal framework where to test the EC-Earth model against observations. The overall agreement between modelling results and observational analysis indicates that the model is a valuable tool to investigate these aspects and gives robustness to the new findings. Future developments include the possibility to use EC-Earth to evaluate future scenarios in this region and to investigate if such mechanisms are expected to act in the same way in the next decades.

Finally, I have investigated the elevational dependence of surface warming occurred during the 20th century and projected for the 21st century in the Tibetan Plateau-Himalayan region using an ensemble of model simulations from the Coupled Model Intercomparison Project phase 5. Results indicate that regions at higher elevations have experienced a stronger warming than the adjacent lowlands in model simulations of the last century, and this behavior is expected to exacerbate in the next decades. The relationship between the warming trends and the elevation is not simply linear. In general, regions with temperatures below the freezing level of water show higher warming rates than the regions with temperatures above, indicating that the phase of water is of importance in determining the faster warming of higher elevations. The change in surface albedo, mainly affected by the reduction of snow cover at higher temperatures, is recognized as the most important driver for this elevation dependent warming, followed by changes in atmospheric humidity and downward longwave radiation. An important outcome of this analysis is that significant spread exists among individual models. While the multi-model mean clearly indicates that the rate of warming is faster in high-elevation areas, individual models exist showing either no or even opposite signals. Also, processes driving the temperature change and the associated elevation dependent warming in this region strongly differ among various climate models. These results indicate that conclusions drawn from individual models should be treated with care and highlight the importance of using multi-model ensembles to quantify model uncertainties.

Appendix A

Basic equations of the Integrated Forecasting System

The Integrated Forecasting System (IFS) is the atmospheric model of the ESM EC-Earth (see section 1.3). It uses the hybrid vertical coordinate $\eta(p, p_s)$ introduced by Simmons and Burridge (1981), which is a monotonic function of the pressure p and also depends on the surface pressure p_s in such a way that

$$\eta(0, p_s) = 0; \quad \eta(p_s, p_s) = 1 \tag{A.1}$$

The hybrid coordinate system is a combination of the pressure coordinate system, where the vertical variable is simply the pressure p, and the sigma coordinate system, where the vertical position is denoted by $\sigma = (p - p_T)/(p_s - p_T)$, p_T being the (constant) top-of-the-atmosphere pressure. It is characterized by sigma-denominated layers at the bottom (following terrain) and isobaric layers aloft.

In (λ, θ, η) coordinates, where λ is longitude and θ is latitude, basic equations of IFS corresponding to equations 1.1–1.5 are:

Horizontal momentum equations

$$\frac{\partial U}{\partial t} + \frac{1}{a \cos^2 \theta}\left\{U\frac{\partial U}{\partial \lambda} + V\cos\theta\frac{\partial U}{\partial \theta}\right\} + \dot{\eta}\frac{\partial U}{\partial \eta}$$
$$- fV + \frac{1}{a}\left\{\frac{\partial \phi}{\partial \lambda} + R_{dry}T_v\frac{\partial}{\partial \lambda}(\ln p)\right\} = P_U + K_U$$

$$\frac{\partial V}{\partial t} + \frac{1}{a \cos^2 \theta}\left\{U\frac{\partial V}{\partial \lambda} + V\cos\theta\frac{\partial V}{\partial \theta} + \sin\theta(U^2 + V^2)\right\} + \dot{\eta}\frac{\partial V}{\partial \eta}$$
$$+ fU + \frac{\cos\theta}{a}\left\{\frac{\partial \phi}{\partial \theta} + R_{dry}T_v\frac{\partial}{\partial \theta}(\ln p)\right\} = P_V + K_V$$

Thermodynamic equation

$$\frac{\partial T}{\partial t} + \frac{1}{a\,\cos^2\theta}\left\{U\frac{\partial T}{\partial \lambda} + V\cos\theta\frac{\partial T}{\partial \theta}\right\} + \dot{\eta}\frac{\partial T}{\partial \eta} - \frac{\kappa T_v \omega}{(1+(\delta-1)q)p} = P_T + K_T$$

Moisture equation

$$\frac{\partial q}{\partial t} + \frac{1}{a\,\cos^2\theta}\left\{U\frac{\partial q}{\partial \lambda} + V\cos\theta\frac{\partial q}{\partial \theta}\right\} + \dot{\eta}\frac{\partial q}{\partial \eta} = P_q + K_q$$

Continuity equation

$$\frac{\partial}{\partial t}\left(\frac{\partial p}{\partial \eta}\right) + \nabla\cdot\left(\mathbf{v}_H\frac{\partial p}{\partial \eta}\right) + \frac{\partial}{\partial \eta}\left(\dot{\eta}\frac{\partial p}{\partial \eta}\right) = 0$$

Hydrostatic equation

$$\frac{\partial \phi}{\partial \eta} = -\frac{R_{dry}T_v}{p}\frac{\partial p}{\partial \eta}$$

Where:
$(U,V) = (u,v)\cos\theta$,
$\mathbf{v}_H = (u,v) =$ horizontal wind,
$t =$ time,
$a =$ radius of the Earth,
$\dot{\eta} = \eta$-coordinate vertical velocity $(\dot{\eta} = d\eta/dt)$,
$f = 2\Omega\sin\theta$,
$\Omega =$ Earth's angular velocity,
$\phi =$ geopotential,
$R_{dry} =$ gas constant for dry air,
$T_v =$ virtual temperature $(T_v = T[1 + \{(R_{vap}/R_{dry}) - 1\}q])$,
$T =$ temperature,
$q =$ specific humidity,
$R_{vap} =$ gas constant for water vapour,
P_U, P_V, P_T and $P_q =$ contributions of the parametrized physical processes,
K_U, K_V, K_T and $K_q =$ horizontal diffusion terms,
$\kappa = R_{dry}/c_{p_{dry}}$,
$\delta = c_{p_{vap}}/c_{p_{dry}}$
$c_{p_{dry}} =$ specific heat of dry air at constant pressure,
$c_{p_{vap}} =$ specific heat of water vapour at constant pressure,
$\omega =$ pressure-coordinate vertical velocity $(\omega = dp/dt)$.

Details about discretization and the semi-Lagrangian formulation can be found in the official IFS documentation available at `https://goo.gl/mTfwRe`.

Bibliography

Abbot, D. S., M. Huber, G. Bousquet, and C. C. Walker, 2009a: High-CO2 cloud radiative forcing feedback over both land and ocean in a global climate model. *Geophysical Research Letters*, **36 (5)**.

Abbot, D. S. and E. Tziperman, 2008: Sea ice, high-latitude convection, and equable climates. *Geophysical Research Letters*, **35 (3)**.

Abbot, D. S., C. C. Walker, and E. Tziperman, 2009b: Can a convective cloud feedback help to eliminate winter sea ice at high CO2 concentrations? *Journal of Climate*, **22 (21)**, 5719–5731.

Adler, R. F., et al., 2003: The version-2 global precipitation climatology project (GPCP) monthly precipitation analysis (1979-present). *Journal of hydrometeorology*, **4 (6)**, 1147–1167.

Ambaum, M. H., B. J. Hoskins, and D. B. Stephenson, 2001: Arctic Oscillation or North Atlantic Oscillation? *J. Climate*, **14 (16)**, 3495–3507, doi:10.1175/1520-0442(2001)014<3495:AOONAO>2.0.CO;2.

Anstey, J. A., et al., 2013: Multi-model analysis of Northern Hemisphere winter blocking: Model biases and the role of resolution. *Journal of Geophysical Research: Atmospheres*, **118 (10)**, 3956–3971.

Archer, D. and V. Brovkin, 2008: The millennial atmospheric lifetime of anthropogenic CO2. *Climatic Change*, **90 (3)**, 283–297.

Archer, D. R. and H. J. Fowler, 2004: Spatial and temporal variations in precipitation in the Upper Indus Basin, global teleconnections and hydrological implications. *Hydrol. Earth. Syst. Sc.*, **8 (1)**, 47–61, doi:10.5194/hess-8-47-2004.

Arora, V., et al., 2011: Carbon emission limits required to satisfy future representative concentration pathways of greenhouse gases. *Geophysical Research Letters*, **38 (5)**.

Beerling, D. J. and D. L. Royer, 2011: Convergent Cenozoic CO2 history. *Nature Geoscience*, **4 (7)**, 418–420.

Bell, R., J. Strachan, P. L. Vidale, K. Hodges, and M. Roberts, 2013: Response of tropical cyclones to idealized climate change experiments in a global high-resolution coupled general circulation model. *Journal of Climate*, **26 (20)**, 7966–7980.

Bellomo, K., A. C. Clement, J. R. Norris, and B. J. Soden, 2014: Observational and model estimates of cloud amount feedback over the indian and pacific oceans. *Journal of Climate*, **27 (2)**, 925–940.

Bengtsson, L., S. Hagemann, and K. I. Hodges, 2004a: Can climate trends be calculated from reanalysis data? *Journal of Geophysical Research: Atmospheres (1984–2012)*, **109 (D11)**.

Bengtsson, L., K. I. Hodges, and S. Hagemann, 2004b: Sensitivity of large-scale atmospheric analyses to humidity observations and its impact on the global water cycle and tropical and extratropical weather systems in ERA40. *Tellus A*, **56 (3)**, 202–217, doi:10.3402/tellusa.v56i3.14412.

Beniston, M., 2003: Climatic change in mountain regions: a review of possible impacts. *Climate Variability and Change in High Elevation Regions: Past, Present & Future*, Springer, 5–31.

Bentsen, M., et al., 2013: The Norwegian earth system model, NorESM1-M – Part 1: description and basic evaluation of the physical climate. *Geosci. Model Dev*, **6 (3)**, 687–720.

Bi, D., et al., 2013: The ACCESS coupled model: description, control climate and evaluation. *Aust. Meteorol. Oceanogr. J*, **63 (1)**, 41–64.

Bice, K. L., C. R. Scotese, D. Seidov, and E. J. Barron, 2000: Quantifying the role of geographic change in Cenozoic ocean heat transport using uncoupled atmosphere and ocean models. *Palaeogeography, Palaeoclimatology, Palaeoecology*, **161 (3)**, 295–310.

Bony, S. and J.-L. Dufresne, 2005: Marine boundary layer clouds at the heart of tropical cloud feedback uncertainties in climate models. *Geophysical Research Letters*, **32 (20)**.

Bookhagen, B. and D. W. Burbank, 2010: Toward a complete Himalayan hydrological budget: Spatiotemporal distribution of snowmelt and rainfall and their impact on river discharge. *J. Geophis. Res.*, **115 (F3)**, doi:10.1029/2009jf001426.

Bougeault, P., 2001: Sub-grid scale orography parametrizations. *Key issues in the parametrization of subgrid physical processes, 3-7 September 2001*, ECMWF, Shinfield Park, Reading, ECMWF, 53–70.

Brandt, M., 2010: *IS-ENES, InfraStructure for the European Network for the Earth System Modelling, is an FP7-Project funded by the European Commission under the Capacities Programme, Integrating Activities.*

Brient, F. and T. Schneider, 2016: Constraints on climate sensitivity from space-based measurements of low-cloud reflection. *Climate Dynamics.*

Burnham, K. P. and D. R. Anderson, 2003: *Model selection and multimodel inference: a practical information-theoretic approach.* Springer Science & Business Media.

Caballero, R. and P. L. Langen, 2005: The dynamic range of poleward energy transport in an atmospheric general circulation model. *Geophysical Research Letters*, **32 (2)**.

Caballero, R. and P. Lynch, 2011: Climate modelling and deep-time climate change. *Climate Change, Ecology and Systematics*, 44.

Cayan, D. R., 1992: Latent and sensible heat flux anomalies over the northern oceans: The connection to monthly atmospheric circulation. *Journal of climate*, **5 (4)**, 354–369.

Chen, T., W. B. Rossow, and Y. Zhang, 2000: Radiative effects of cloud-type variations. *Journal of climate*, **13 (1)**, 264–286.

Chen, T. C., 1985: Global water vapor flux and maintenance during FGGE. *Mon. Wea. Rev.*, **113**, 1801–1819, doi:10.1175/1520-0493(1985)113<1801:GWVFAM>2.0.CO;2.

Ciccarelli, N., J. Von Hardenberg, A. Provenzale, C. Ronchi, A. Vargiu, and R. Pelosini, 2008: Climate variability in north-western Italy during the second half of the 20th century. *Global Planet. Change*, **63 (2)**, 185–195, doi:10.1016/j.gloplacha.2008.03.006.

Clement, A. C., R. Burgman, and J. R. Norris, 2009: Observational and model evidence for positive low-level cloud feedback. *Science*, **325 (5939)**, 460–464.

Compo, G. P., et al., 2011: The Twentieth Century Reanalysis Project. *Quart. J. Roy. Meteor. Soc.*, **137 (654)**, 1–28, doi:10.1002/qj.776.

Covey, C. and E. Barron, 1988: The role of ocean heat transport in climatic change. *Earth-Science Reviews*, **24 (6)**, 429–445.

Cunningham, S. A., et al., 2007: Temporal variability of the Atlantic meridional overturning circulation at 26.5 N. *science*, **317 (5840)**, 935–938.

Czaja, A. and C. Frankignoul, 1999: Influence of the North Atlantic SST on the atmospheric circulation. *Geophysical Research Letters*, **26 (19)**, 2969–2972.

Dee, D., et al., 2011: The ERA-Interim reanalysis: Configuration and performance of the data assimilation system. *Quarterly Journal of the Royal Meteorological Society*, **137 (656)**, 553–597.

Delworth, T. L., et al., 2006: GFDL's CM2 Global Coupled Climate Models. Part I: Formulation and Simulation Characteristics. *Journal of Climate*, **19 (5)**, 643–674.

Deser, C., 2000: On the teleconnectivity of the Arctic Oscillation. *Geophys. Res. Lett.*, **27 (6)**, 779–782, doi:10.1029/1999gl010945.

Diamantakis, M. and J. Flemming, 2014: Global mass fixer algorithms for conservative tracer transport in the ECMWF model. *Geoscientific Model Development*, **7 (3)**, 965–979.

Diaz, H. F., M. Grosjean, and L. Graumlich, 2003: *Climate variability and change in high elevation regions: past, present and future*. Springer.

Dimri, A., 2013: Relationship between ENSO phases with Northwest India winter precipitation. *Int. J. Climatol.*, **33 (8)**, 1917–1923, doi:10.1002/joc.3559.

Doria, G., D. L. Royer, A. P. Wolfe, A. Fox, J. A. Westgate, and D. J. Beerling, 2011: Declining atmospheric CO2 during the late Middle Eocene climate transition. *American Journal of Science*, **311 (1)**, 63–75.

Eberle, J. J., M. D. Gottfried, J. H. Hutchison, and C. A. Brochu, 2014: First Record of Eocene Bony Fishes and Crocodyliforms from Canada's Western Arctic. *PloS one*, **9 (5)**, e96 079.

Eitzen, Z. A., K.-M. Xu, and T. Wong, 2011: An estimate of low-cloud feedbacks from variations of cloud radiative and physical properties with sea surface temperature on interannual time scales. *Journal of Climate*, **24 (4)**, 1106–1121.

Feldstein, S. B., 2002: The recent trend and variance increase of the Annular Mode. *J. Climate*, **15 (1)**, 88–94, doi:10.1175/1520-0442(2002)015<0088:TRTAVI>2.0.CO;2.

Filippi, L., E. Palazzi, J. von Hardenberg, and A. Provenzale, 2014: Multidecadal Variations in the Relationship between the NAO and Winter Precipitation in the Hindu Kush–Karakoram. *Journal of Climate*, **27 (20)**, 7890–7902.

Fletcher, B. J., S. J. Brentnall, C. W. Anderson, R. A. Berner, and D. J. Beerling, 2008: Atmospheric carbon dioxide linked with Mesozoic and early Cenozoic climate change. *Nature Geoscience*, **1 (1)**, 43–48.

Frierson, D. M., I. M. Held, and P. Zurita-Gotor, 2007: A gray-radiation aquaplanet moist GCM. Part II: Energy transports in altered climates. *Journal of the atmospheric sciences*, **64 (5)**, 1680–1693.

Ghil, M., 2002: Natural climate variability. *Encyclopedia of global environmental change*, **1**, 544–549.

Gillett, N. P., H. F. Graf, and T. J. Osborn, 2003: Climate change and the North Atlantic Oscillation. *Geoph. Monog. Series*, **134**, 193–209, doi:10.1029/134gm09.

Giorgi, F., M. R. Marinucci, and G. T. Bates, 1993: Development of a second-generation regional climate model (Re.g.CM2). Part I: Boundary-layer and radiative transfer processes. *Monthly Weather Review*, **121 (10)**, 2794–2813.

Greenwood, D. R. and S. L. Wing, 1995: Eocene continental climates and latitudinal temperature gradients. *Geology*, **23 (11)**, 1044–1048.

Harris, I., P. Jones, T. Osborn, and D. Lister, 2013: Updated high-resolution grids of monthly climatic observations–the CRU TS3.10 Dataset. *Int. J. Climatol.*, **34 (3)**, 623Ð642, doi:10.1002/joc.3711.

Hartmann, D. L., M. E. Ockert-Bell, and M. L. Michelsen, 1992: The effect of cloud type on Earth's energy balance: Global analysis. *Journal of Climate*, **5 (11)**, 1281–1304.

Hazeleger, W. and R. Bintanja, 2014: Accomplishments, current status and future plans of EC-Earth: a European Earth System Model. Tech. rep., Royal Netherlands Meteorological Institute.

Hazeleger, W., et al., 2012: EC-Earth V2. 2: description and validation of a new seamless earth system prediction model. *Climate Dynamics*, **39 (11)**, 2611–2629.

Heinemann, M., J. Jungclaus, and J. Marotzke, 2009: Warm Paleocene/Eocene climate as simulated in ECHAM5/MPI-OM. *Climate of the Past*, **5**, 785–802.

Hilmer, M. and T. Jung, 2000: Evidence for a recent change in the link between the North Atlantic Oscillation and Arctic sea ice export. *Geophys. Res. Lett.*, **27 (7)**, 989–992, doi:10.1029/1999gl010944.

Hourdin, F., et al., 2013a: Impact of the LMDZ atmospheric grid configuration on the climate and sensitivity of the IPSL-CM5A coupled model. *Climate Dynamics*, **40 (9-10)**, 2167–2192.

Hourdin, F., et al., 2013b: LMDZ5B: the atmospheric component of the IPSL climate model with revisited parameterizations for clouds and convection. *Climate Dynamics*, **40 (9-10)**, 2193–2222.

Huber, M. and R. Caballero, 2011: The early Eocene equable climate problem revisited. *Climate of the Past*, **7 (2)**, 603–633.

Huffman, G. J., et al., 2007: The TRMM Multisatellite Precipitation Analysis (TMPA): Quasi-global, multiyear, combined-sensor precipitation estimates at fine scales. *J. Hydrometeor*, **8**, 38–55, doi:10.1175/JHM560.1.

Hurrell, J. W., 1995: Decadal trends in the North Atlantic Oscillation: Regional temperatures and precipitation. *Science*, **269 (5224)**, 676–679, doi:10.1126/science.269.5224.676.

Hurrell, J. W., Y. Kushnir, G. Ottersen, and M. Visbeck, 2003: An Overview of the North Atlantic Oscillation. *Geoph. Monog. Series*, **134**, 1–35, doi:10.1029/134gm01.

Hurrell, J. W., et al., 2013: The community earth system model: a framework for collaborative research. *Bulletin of the American Meteorological Society*, **94 (9)**, 1339–1360.

Hutchison, J., 1982: Turtle, crocodilian, and champsosaur diversity changes in the Cenozoic of the north-central region of western United States. *Palaeogeography, Palaeoclimatology, Palaeoecology*, **37 (2)**, 149–164.

Hwang, Y.-T. and D. M. Frierson, 2013: Link between the double-Intertropical Convergence Zone problem and cloud biases over the Southern Ocean. *Proceedings of the National Academy of Sciences*, **110 (13)**, 4935–4940.

Immerzeel, W. W., F. Pellicciotti, and A. B. Shrestha, 2012: Glaciers as a proxy to quantify the spatial distribution of precipitation in the Hunza basin. *Mt. Res. Dev.*, **32 (1)**, 30–38, doi:10.1659/MRD-JOURNAL-D-11-00097.1.

IPCC AR5, 2013: Climate Change 2013: the physical science basis. Contribution of working group I to the fifth assessment report of the intergovernmental panel on climate change. Cambridge University Press.

Ji, D., et al., 2014: Description and basic evaluation of Beijing Normal University Earth System Model (BNU-ESM) version 1. *Geoscientific Model Development*, **7 (5)**, 2039–2064.

Jung, T., M. Hilmer, E. Ruprecht, S. Kleppek, S. K. Gulev, and O. Zolina, 2003: Characteristics of the recent eastward shift of interannual NAO variability. *J. Climate*, **16 (20)**, 3371Ð3382, doi:10.1175/1520-0442(2003)016<3371:COTRES>2.0.CO;2.

Jung, T., et al., 2012: High-resolution global climate simulations with the ECMWF model in Project Athena: Experimental design, model climate, and seasonal forecast skill. *Journal of Climate*, **25 (9)**, 3155–3172.

Kalnay, E., et al., 1996: The NCEP/NCAR 40-year reanalysis project. *Bulletin of the American meteorological Society*, **77 (3)**, 437–471.

Kapos, V., J. Rhind, M. Edwards, M. Price, C. Ravilious, N. Butt, et al., 2000: Developing a map of the world's mountain forests. *Forests in sustainable mountain development: a state of knowledge report for 2000. Task Force on Forests in Sustainable Mountain Development.*, 4–19.

Keeley, S., R. Sutton, and L. Shaffrey, 2012: The impact of North Atlantic sea surface temperature errors on the simulation of North Atlantic European region climate. *Quarterly Journal of the Royal Meteorological Society*, **138 (668)**, 1774–1783.

Kirk-Davidoff, D. B., D. P. Schrag, and J. G. Anderson, 2002: On the feedbaseck of stratospheric clouds on polar climate. *Geophysical Research Letters*, **29 (11)**.

Klein, S. A. and D. L. Hartmann, 1993: The seasonal cycle of low stratiform clouds. *Journal of Climate*, **6 (8)**, 1587–1606.

Knutti, R., D. Masson, and A. Gettelman, 2013: Climate model genealogy: Generation CMIP5 and how we got there. *Geophysical Research Letters*, **40 (6)**, 1194–1199.

Korner, C. and E. Spehn, 2002: *Mountain biodiversity: a global assessment.* CRC.

Lawrence, K., L. C. Sloan, and J. Sewall, 2003: Terrestrial climatic response to precessional orbital forcing in the Eocene. *Special Papers-Geological Society of America*, 65–78.

Letreguilly, A., P. Huybrechts, and N. Reeh, 1991: Steady-state characteristics of the Greenland ice sheet under different climates. *Journal of Glaciology*, **37 (125)**, 149–157.

Li, L., et al., 2013: The flexible global ocean-atmosphere-land system model, Gridpoint Version 2: FGOALS-g2. *Advances in Atmospheric Sciences*, **30**, 543–560.

Lin, J.-L., 2007: The double-ITCZ problem in IPCC AR4 coupled GCMs: Ocean-atmosphere feedback analysis. *Journal of Climate*, **20 (18)**, 4497–4525.

Liu, X., Z. Cheng, L. Yan, and Z.-Y. Yin, 2009: Elevation dependency of recent and future minimum surface air temperature trends in the Tibetan Plateau and its surroundings. *Global and Planetary Change*, **68 (3)**, 164–174.

Livermore, R., A. Nankivell, G. Eagles, and P. Morris, 2005: Paleogene opening of Drake passage. *Earth and Planetary Science Letters*, **236 (1)**, 459–470.

Lu, J. and R. J. Greatbatch, 2002: The changing relationship between the NAO and northern hemisphere climate variability. *Geophys. Res. Lett.*, **29 (7)**, 1148, doi:10.1029/2001gl014052.

Lunt, D. J., et al., 2012: A model–data comparison for a multi-model ensemble of early Eocene atmosphere–ocean simulations: EoMIP. *Climate of the Past*, **8**, 1717–1736.

Luo, D., Z. Zhu, R. Ren, L. Zhong, and C. Wang, 2010: Spatial Pattern and Zonal Shift of the North Atlantic Oscillation. Part I: A Dynamical Interpretation. *J. Atmos. Sci.*, **67 (9)**, 2805–2826, doi:10.1175/2010jas3345.1.

Machenhauer, B., 1979: *The spectral method. Numerical Methods Used in Atmospheric Models*, GARP Publication Series 17, Vol. II, 121–275. World Meteorological Organization, Geneva, Switzerland.

Maraun, D., et al., 2010: Precipitation downscaling under climate change: Recent developments to bridge the gap between dynamical models and the end user. *Reviews of Geophysics*, **48 (3)**.

Markwick, P., 2007: The palaeogeographic and palaeoclimatic significance of climate proxies for data-model comparisons. *Deep-time perspectives on climate change: marrying the signal from computer models and biological proxies*, 251–312.

Martin, G., et al., 2011: The HadGEM2 family of met office unified model climate configurations. *Geoscientific Model Development*, **4 (3)**, 723–757.

Mauritsen, T., et al., 2012: Tuning the climate of a global model. *Journal of Advances in Modeling Earth Systems*, **4 (3)**.

McGuffie, K. and A. Henderson-Sellers, 2005: *A climate modelling primer*. John Wiley & Sons.

Meehl, G. A., et al., 2012: Climate system response to external forcings and climate change projections in CCSM4. *Journal of Climate*, **25 (11)**, 3661–3683.

Miller, M., T. Palmer, and R. Swinbank, 1989: Parametrization and influence of subgridscale orography in general circulation and numerical weather prediction models. *Meteorology and Atmospheric Physics*, **40 (1-3)**, 84–109.

Mizielinski, M., et al., 2014: High-resolution global climate modelling: the upscale project, a large-simulation campaign. *Geoscientific Model Development*, **7 (4)**, 1629–1640.

Morrill, C., E. E. Small, and L. C. Sloan, 2001: Modeling orbital forcing of lake level change: Lake Gosiute (Eocene), North America. *Global and Planetary Change*, **29 (1)**, 57–76.

Moss, R. H., et al., 2008: Towards new scenarios for analysis of emissions, climate change, impacts, and response strategies. Tech. rep., Pacific Northwest National Laboratory (PNNL), Richland, WA (US).

MRI, M. R. I. E. W. G., 2015: Elevation-dependent warming in mountain regions of the world. *Nature Climate Change*, **5 (5)**, 424–430.

Neelin, J. D., A. Bracco, H. Luo, J. C. McWilliams, and J. E. Meyerson, 2010: Considerations for parameter optimization and sensitivity in climate models. *Proceedings of the National Academy of Sciences*, **107 (50)**, 21 349–21 354.

Pagani, M., J. C. Zachos, K. H. Freeman, B. Tipple, and S. Bohaty, 2005: Marked decline in atmospheric carbon dioxide concentrations during the Paleogene. *Science*, **309 (5734)**, 600–603.

Pal, I., A. W. Robertson, U. Lall, and M. A. Cane, 2014: Modeling winter rainfall in Northwest India using a hidden Markov model: understanding occurrence of different states and their dynamical connections. *Climate Dynamics*, doi:10.1007/s00382-014-2178-5.

Palazzi, E., J. von Hardenberg, and A. Provenzale, 2013: Precipitation in the Hindu-Kush Karakoram Himalaya: Observations and future scenarios. *J. Geophys. Res.*, **118 (1)**, 85–100, doi:10.1029/2012JD018697.

Palazzi, E., J. von Hardenberg, S. Terzago, and A. Provenzale, 2014: Precipitation in the Karakoram-Himalaya: a CMIP5 view. *Climate Dynamics*, **45 (1-2)**, 21–45.

Pearson, P. N. and M. R. Palmer, 2000: Atmospheric carbon dioxide concentrations over the past 60 million years. *Nature*, **406 (6797)**, 695–699.

Pinto, J. G. and C. C. Raible, 2012: Past and recent changes in the North Atlantic Oscillation. *WIREs Climate Change*, **3 (1)**, 79–90, doi:10.1002/wcc.150.

Pollard, E., K. Lakhani, and P. Rothery, 1987: The detection of density-dependence from a series of annual censuses. *Ecology*, **68 (6)**, 2046–2055, doi:10.2307/1939895.

Qu, X., A. Hall, S. A. Klein, and P. M. Caldwell, 2014: On the spread of changes in marine low cloud cover in climate model simulations of the 21st century. *Climate dynamics*, **42 (9-10)**, 2603–2626.

Qu, X., A. Hall, S. A. Klein, and A. M. DeAngelis, 2015: Positive tropical marine low-cloud cover feedback inferred from cloud-controlling factors. *Geophysical Research Letters*, **42 (18)**, 7767–7775.

Randall, D. A. and B. A. Wielicki, 1997: Measurements, models, and hypotheses in the atmospheric sciences. *Bulletin of the American Meteorological Society*, **78 (3)**, 399–406.

Rangwala, I. and J. R. Miller, 2012: Climate change in mountains: a review of elevation-dependent warming and its possible causes. *Climatic Change*, **114 (3-4)**, 527–547.

Rangwala, I., E. Sinsky, and J. R. Miller, 2013: Amplified warming projections for high altitude regions of the northern hemisphere mid-latitudes from CMIP5 models. *Environmental Research Letters*, **8 (2)**, 024 040.

Rangwala, I., E. Sinsky, and J. R. Miller, 2015: Variability in projected elevation dependent warming in boreal midlatitude winter in CMIP5 climate models and its potential drivers. *Climate Dynamics*, 1–8.

Rasmussen, R., et al., 2012: How well are we measuring snow: the NOAA/FAA/N-CAR winter precipitation test bed. *Bull. Amer. Meteor. Soc.*, **93 (6)**, 811–829, doi:10.1175/BAMS-D-11-00052.1.

Rayner, N., D. E. Parker, E. Horton, C. Folland, L. Alexander, D. Rowell, E. Kent, and A. Kaplan, 2003: Global analyses of sea surface temperature, sea ice, and night marine air temperature since the late nineteenth century. *Journal of Geophysical Research: Atmospheres*, **108 (D14)**.

Reichler, T. and J. Kim, 2008: How well do coupled models simulate today's climate? *Bulletin of the American Meteorological Society*, **89 (3)**, 303–311.

Riahi, K., et al., 2011: RCP 8.5 — A scenario of comparatively high greenhouse gas emissions. *Climatic Change*, **109 (1-2)**, 33–57.

Rodwell, M. J., D. P. Rowell, and C. K. Folland, 1999: Oceanic forcing of the wintertime North Atlantic Oscillation and European climate. *Nature*, **398 (6725)**, 320–323.

Rotstayn, L., S. Jeffrey, M. Collier, S. Dravitzki, A. Hirst, J. Syktus, and K. Wong, 2012: Aerosol- and greenhouse gas-induced changes in summer rainfall and circulation in the Australasian region: a study using single-forcing climate simulations. *Atmos. Chem. Phys*, **12 (14)**, 6377–6404.

Royer, D. L., R. A. Berner, I. P. Montañez, N. J. Tabor, and D. J. Beerling, 2004: CO2 as a primary driver of Phanerozoic climate. *GSA today*, **14 (3)**, 4–10.

Rozendaal, M. A., C. B. Leovy, and S. A. Klein, 1995: An observational study of diurnal variations of marine stratiform cloud. *Journal of climate*, **8 (7)**, 1795–1809.

Ruckstuhl, C., R. Philipona, J. Morland, and A. Ohmura, 2007: Observed relationship between surface specific humidity, integrated water vapor, and longwave downward radiation at different altitudes. *Journal of Geophysical Research: Atmospheres*, **112 (D3)**.

Sausen, R., K. Barthel, and K. Hasselmann, 1988: Coupled ocean-atmosphere models with flux correction. *Climate Dynamics*, **2 (3)**, 145–163.

Schmidt, G. A., et al., 2006: Present-day atmospheric simulations using GISS ModelE: Comparison to in situ, satellite, and reanalysis data. *Journal of Climate*, **19 (2)**, 153–192.

Schneider, U., A. Becker, P. Finger, A. Meyer-Christoffer, B. Rudolf, and M. Ziese, 2011: GPCC full data reanalysis version 6.0 at 0.5: monthly land-surface precipitation from rain-gauges built on GTS-based and historic data. Global Precipitation Climatology Centre at Deutscher Wetterdienst, doi:10.5676/DWD_GPCC/FD_M_V6_050.

Schreiber, T. and A. Schmitz, 2000: Surrogate time series. *Physica D: Nonlinear Phenomena*, **142 (3)**, 346–382.

Screen, J. A. and I. Simmonds, 2010: The central role of diminishing sea ice in recent Arctic temperature amplification. *Nature*, **464 (7293)**, 1334–1337.

Serreze, M. C. and R. G. Barry, 2011: Processes and impacts of Arctic amplification: A research synthesis. *Global and Planetary Change*, **77 (1)**, 85–96.

Sewall, J. O. and L. C. Sloan, 2004: Less ice, less tilt, less chill: The influence of a seasonally ice-free Arctic Ocean and reduced obliquity on early Paleogene climate. *Geology*, **32 (6)**, 477–480.

Sewall, J. O. and L. C. Sloan, 2006: Come a little bit closer: A high-resolution climate study of the early Paleogene Laramide foreland. *Geology*, **34 (2)**, 81–84.

Sewall, J. O., L. C. Sloan, M. Huber, and S. Wing, 2000: Climate sensitivity to changes in land surface characteristics. *Global and Planetary Change*, **26 (4)**, 445–465.

Shellito, C. J. and L. C. Sloan, 2006: Reconstructing a lost Eocene paradise: Part I. Simulating the change in global floral distribution at the initial Eocene thermal maximum. *Global and Planetary Change*, **50 (1)**, 1–17.

Simmons, A. J. and D. M. Burridge, 1981: An energy and angular-momentum conserving vertical finite-difference scheme and hybrid vertical coordinates. *Monthly Weather Review*, **109 (4)**, 758–766.

Sloan, L. C., 1994: Equable climates during the early Eocene: significance of regional paleogeography for North American climate. *Geology*, **22 (10)**, 881–884.

Sloan, L. C. and E. J. Barron, 1990: "Equable" climates during Earth history? *Geology*, **18 (6)**, 489–492.

Sloan, L. C., M. Huber, T. Crowley, J. Sewall, and S. Baum, 2001: Effect of sea surface temperature configuration on model simulations of "equable" climate in the Early Eocene. *Palaeogeography, Palaeoclimatology, Palaeoecology*, **167 (3)**, 321–335.

Sloan, L. C., M. Huber, and A. Ewing, 1999: Polar stratospheric cloud forcing in a greenhouse world. *Reconstructing Ocean History*, Springer, 273–293.

Sloan, L. C. and D. Pollard, 1998: Polar stratospheric clouds: A high latitude warming mechanism in an ancient greenhouse world. *Geophys. Res. Lett*, **25 (18)**, 3517–3520.

Sloan, L. C., J. C. Walker, and T. Moore, 1995: Possible role of oceanic heat transport in early Eocene climate. *Paleoceanography*, **10 (2)**, 347–356.

Sluijs, A., et al., 2006: Subtropical Arctic Ocean temperatures during the Palaeocene/Eocene thermal maximum. *Nature*, **441 (7093)**, 610–613.

Soden, B. J. and G. A. Vecchi, 2011: The vertical distribution of cloud feedback in coupled ocean-atmosphere models. *Geophysical Research Letters*, **38 (12)**.

Spicer, R. A. and J. T. Parrish, 1990: Late Cretaceous–early Tertiary palaeoclimates of northern high latitudes: a quantitative view. *Journal of the Geological Society*, **147 (2)**, 329–341.

Stephens, G. L., et al., 2012: An update on Earth's energy balance in light of the latest global observations. *Nature Geoscience*, **5 (10)**, 691–696.

Syed, F. S., F. Giorgi, J. S. Pal, and K. Keay, 2010: Regional climate model simulation of winter climate over Central-Southwest Asia, with emphasis on NAO and ENSO effects. *Int. J. Climatol.*, **30 (2)**, 220–235, doi:10.1002/joc.1887.

Syed, F. S., F. Giorgi, J. S. Pal, and M. P. King, 2006: Effect of remote forcings on the winter precipitation of central southwest Asia part 1: observations. *Theor. Appl. Climatol.*, **86 (1-4)**, 147–160, doi:10.1007/s00704-005-0217-1.

Taylor, K. E., R. J. Stouffer, and G. A. Meehl, 2012: An overview of CMIP5 and the experiment design. *Bulletin of the American Meteorological Society*, **93 (4)**, 485–498.

Thompson, D. W. and J. M. Wallace, 2001: Regional climate impacts of the Northern Hemisphere Annular Mode. *Science*, **293 (5527)**, 85–89, doi:10.1126/science.1058958.

Thompson, D. W., J. M. Wallace, and G. C. Hegerl, 2000: Annular Modes in the Extratropical Circulation. Part II: Trends. *J. Climate*, **13 (5)**, 1018–1036, doi:10.1175/1520-0442(2000)013<1018:AMITEC>2.0.CO;2.

Trenberth, K. E., 1992: *Climate system modeling.* Cambridge University Press.

Trenberth, K. E., J. T. Fasullo, and J. Kiehl, 2009: Earth's global energy budget. *Bulletin of the American Meteorological Society*, **90 (3)**, 311–323.

Trigo, R. M., T. J. Osborn, and J. M. C. Real, 2002: The North Atlantic Oscillation influence on Europe: climate impacts and associated physical mechanisms. *Climate Res.*, **20 (1)**, 9–17, doi:10.3354/cr020009.

UN, 1992: Earth Summit: Agenda 21. the United Nations Programme of Action from Rio, The Final Text of Agreements Negotiated by Governments at the United Nations Conference on Environment and Development (UNCED), 3–14 june 1992, Rio de Janeiro, Brazil. Tech. rep., UN.

Uppala, S. M., et al., 2005: The ERA-40 re-analysis. *Quart. J. Roy. Meteor. Soc.*, **131 (612)**, 2961–3012, doi:10.1256/qj.04.176.

Vallis, G. K., 2006: *Atmospheric and oceanic fluid dynamics: fundamentals and large-scale circulation.* Cambridge University Press.

Vial, J., J.-L. Dufresne, and S. Bony, 2013: On the interpretation of inter-model spread in CMIP5 climate sensitivity estimates. *Climate Dynamics*, **41 (11-12)**, 3339–3362.

Viviroli, D., H. H. Dürr, B. Messerli, M. Meybeck, and R. Weingartner, 2007: Mountains of the world, water towers for humanity: Typology, mapping, and global significance. *Water resources research*, **43 (7)**.

Voldoire, A., et al., 2013: The CNRM-CM5. 1 global climate model: description and basic evaluation. *Climate Dynamics*, **40 (9-10)**, 2091–2121.

Volodin, E., N. Dianskii, and A. Gusev, 2010: Simulating present-day climate with the INMCM4.0 coupled model of the atmospheric and oceanic general circulations. *Izvestiya, Atmospheric and Oceanic Physics*, **46 (4)**, 414–431.

Wallace, J. M., 2000: North Atlantic Oscillation/annular mode: Two paradigms — one phenomenon. *Quart. J. Roy. Meteor. Soc.*, **126 (564)**, 791–805, doi: 10.1256/smsqj.56401.

Wang, Y.-H., G. Magnusdottir, H. Stern, X. Tian, and Y. Yu, 2012: Decadal variability of the NAO: Introducing an augmented NAO index. *Geophys. Res. Lett.*, **39 (21)**, L21 702, doi:10.1029/2012gl053413.

Washington, W. M. and C. L. Parkinson, 2005: *An introduction to three-dimensional climate modeling.* University science books.

Watanabe, M., et al., 2010: Improved climate simulation by MIROC5: mean states, variability, and climate sensitivity. *Journal of Climate*, **23 (23)**, 6312–6335.

Watanabe, S., et al., 2011: MIROC-ESM 2010: model description and basic results of CMIP5-20c3m experiments. *Geoscientific Model Development*, **4 (4)**, 845–872.

Webb, M. J., F. H. Lambert, and J. M. Gregory, 2013: Origins of differences in climate sensitivity, forcing and feedback in climate models. *Climate Dynamics*, **40 (3-4)**, 677–707.

Wibig, J., 1999: Precipitation in Europe in relation to circulation patterns at the 500 hPa level. *Int. J. Climatol.*, **19 (3)**, 253–269, doi:10.1002/(sici)1097-0088(19990315)19:3<253::aid-joc366>3.0.co;2-0.

Wielicki, B. A., B. R. Barkstrom, E. F. Harrison, R. B. Lee III, G. Louis Smith, and J. E. Cooper, 1996: Clouds and the Earth's Radiant Energy System (ceres): an Earth observing system experiment. *Bulletin of the American Meteorological Society*, **77 (5)**, 853–868.

Wing, S. L. and D. R. Greenwood, 1993: Fossils and fossil climate: the case for equable continental interiors in the Eocene. *Philosophical Transactions of the Royal Society of London B: Biological Sciences*, **341 (1297)**, 243–252.

Wood, R., 2012: Stratocumulus clouds. *Monthly Weather Review*, **140 (8)**, 2373–2423.

Woollings, T., B. Hoskins, M. Blackburn, and P. Berrisford, 2008: A new Rossby wave-breaking interpretation of the North Atlantic Oscillation. *Journal of the Atmospheric Sciences*, **65 (2)**, 609–626.

Wu, T., et al., 2013: Global carbon budgets simulated by the Beijing Climate Center Climate System Model for the last century. *Journal of Geophysical Research: Atmospheres*, **118 (10)**, 4326–4347.

Yadav, R., K. R. Kumar, and M. Rajeevan, 2007: Role of Indian Ocan sea surface temperatures in modulating northwest Indian winter precipitation variability. *Theor. Appl. Climatol.*, **87 (1–4)**, 73–83, doi:10.1007/s00704005-0221-5.

Yadav, R., K. R. Kumar, and M. Rajeevan, 2009a: Out–of–phase relationships between convection over northwest India and warm pool region during the winter season. *Int. J. Climatol.*, **29 (9)**, 1330–1338, doi:10.1002/joc.1783.

Yadav, R. K., K. R. Kumar, and M. Rajeevan, 2009b: Increasing influence of ENSO and decreasing influence of AO/NAO in the recent decades over northwest India winter precipitation. *J. Geophys. Res.*, **114 (D12)**, 112, doi:doi:10.1029/2008JD011318.

Yadav, R. K., J. H. Yoo, F. Kucharski, and M. A. Abid, 2010: Why is ENSO influencing northwest India winter precipitation in recent decades? *J. Climate*, **23 (8)**, 1979–1993, doi:10.1175/2009jcli3202.1.

Yan, L. and X. Liu, 2014: Has climatic warming over the Tibetan Plateau paused or continued in recent years? *J. Earth Ocean Atmos. Sci*, **1**, 13–28.

Yang, S., K. Lau, S. Yoo, J. Kinter, K. Miyakoda, and C. Ho, 2004: Upstream subtropical signals preceding the Asian summer monsoon circulation. *J. Climate*, **17 (21)**, 4213–4229, doi:10.1175/jcli3192.1.

Yatagai, A., K. Kamiguchi, O. Arakawa, A. Hamada, N. Yasutomi, and A. Kitoh, 2012: APHRODITE: Constructing a long-term daily gridded precipitation dataset for Asia based on a dense network of rain gauges. *Bull. Amer. Meteor. Soc.*, **93 (9)**, 1401–1415, doi:10.1175/bams-d-11-00122.1.

Yukimoto, S., et al., 2012: A New Global Climate Model of the Meteorological Research Institute: MRI-CGCM3 – Model Description and Basic Performance. *Journal of the Meteorological Society of Japan*, **90**, 23–64.

Zachos, J., M. Pagani, L. Sloan, E. Thomas, and K. Billups, 2001: Trends, rhythms, and aberrations in global climate 65 Ma to present. *Science*, **292 (5517)**, 686–693.

Zachos, J. C., L. D. Stott, and K. C. Lohmann, 1994: Evolution of early Cenozoic marine temperatures. *Paleoceanography*, **9 (2)**, 353–387.

Zelinka, M. D., S. A. Klein, and D. L. Hartmann, 2012: Computing and partitioning cloud feedbacks using cloud property histograms. Part II: Attribution to changes in cloud amount, altitude, and optical depth. *Journal of Climate*, **25 (11)**, 3736–3754.

Zhang, Y. and W. Rossow, 1997: Estimating meridional energy transports by the atmospheric and oceanic general circulations using boundary fluxes. *Journal of climate*, **10 (9)**, 2358–2373.

Zhou, C., M. D. Zelinka, A. E. Dessler, and P. Yang, 2013: An analysis of the short-term cloud feedback using MODIS data. *Journal of Climate*, **26 (13)**, 4803–4815.

COMMISSIONE GIUDICATRICE

_____

Il dott. Luca Filippi ha discusso in data 26/05/2016 presso il Dipartimento di Ingegneria Meccanica e Aerospaziale del Politecnico di Torino la tesi di Dottorato avente il seguente titolo:

The fluid dynamics of climate: General circulation models and applications to past, present and future climatic changes.

Le ricerche oggetto della tesi sono l'applicazione e l'ottimizzazione di modelli climatici su scala globale.

Le metodologie appaiono adeguate ed innovative.

I risultati sono interessanti ed analizzati con senso critico.

Nel colloquio il candidato dimostra un'approfondita conoscenza delle problematiche trattate.

La Commissione unanime giudica positivamente il lavoro svolto

e propone che al dott. Luca Filippi venga conferito il titolo di **Dottore di Ricerca**.

Torino, 26/05/2016

Prof. Roberto Marsilio (Presidente)

Prof.ssa Antonella Abbà (Componente)

Prof.ssa Claudia Pasquero (Segretario)